

THESIS

EFFECTS OF MAXIMUM PARTICLE SIZE AND SAMPLE SCALING ON THE  
MECHANICAL BEHAVIOR OF MINE WASTE ROCK;  
A CRITICAL STATE APPROACH

Submitted By

Justin Neil Stoeber

Department of Civil and Environmental Engineering

In partial fulfillment of the requirements

for the Degree of Master of Science

Colorado State University

Fort Collins, Colorado

Spring 2012

Master's Committee:

Advisor: J. Antonio H. Carraro

Charles D. Shackelford

Derek L. Schutt

Copyright by Justin Neil Stoeber 2012

All Rights Reserved

## ABSTRACT

### EFFECTS OF MAXIMUM PARTICLE SIZE AND SAMPLE SCALING ON THE MECHANICAL BEHAVIOR OF MINE WASTE ROCK; A CRITICAL STATE APPROACH

A rigorous and systematic study on the effects of maximum particle size and sample scaling on the mechanical behavior of mine waste rock (*MWR*) is presented. Materials tested were obtained from a similar location within the open pit of Barrick Gold Corporation's Goldstrike gold mine approximately 60 km northwest of Elko, Nevada. The collected field gradation was scaled using the parallel gradation technique in order to most accurately reproduce the fabric of the collected field material in the laboratory. The two *MWR* materials were shown to have drastically different mineralogy, which may be due to varying levels of *in situ* hydrogeologic weathering. Mechanical behavior of two *MWR* materials was systematically evaluated on 70-mm-diameter, 140-mm-tall specimens with a maximum particle size equal to 11.2 mm in drained isotropic and monotonic axisymmetric compression using a conventional triaxial device. Results from conventional triaxial tests in drained isotropic and monotonic axisymmetric compression were systematically compared to results presented by Fox (2011) for 150-mm-diameter, 300-mm-tall specimens with a maximum particle size equal to 25.0 mm for the same *MWR* materials also scaled using the parallel gradation technique and tested at the same levels of mean effective stress ( $p'$ ) in a large-scale triaxial device.

Intrinsic critical state parameters were defined for each material in conventional scale triaxial testing. Results suggest the parallel gradation technique provides a reasonable

way to estimate values of intrinsic critical state parameters during isotropic compression in large-scale applications using conventional triaxial tests provided that the range of  $D_{R,Initial}$  is similar between scales. Values of the critical state friction angle ( $\phi_c$ ) were determined to be within  $2^\circ$  of the larger scale specimens. Dilatancy rates measured in conventional scale unweathered specimens was found to be, on average, approximately twice of that measured in the large-scale specimens of the same material. The weathered material indicated no significant changes in average dilatancy rates between scales. Bolton's (1986) fitting parameters  $Q$  and  $R$  were determined to decrease with decreasing particle size where Bolton's stress – dilatancy relationship was found to predict values of the peak friction angle ( $\phi_p$ ) more accurately using values of  $Q$  and  $R$  obtained in large-scale triaxial tests where conventional scale specimens yielded consistently unconservative predictions of  $\phi_p$  suggesting that conventional triaxial tests should not solely be used to characterize the mechanical behavior of large-scale materials. Particle breakage measured after each triaxial test indicated a relatively constant shift from pre to post test particle-size distribution curves between conventional and large-scale specimens. Additional results and comparisons of values such as fractal dimension ( $D$ ) and surface energy ( $\Gamma_{se}$ ) are also discussed.

## ACKNOWLEDGEMENTS

I would like to take a moment to express my gratitude to all of those who have contributed to this thesis in so many ways.

First I am deeply indebted to Miguel Molina, Brian Lins and Joyce Nukaya of ELE International for their generous funding and support through providing the equipment to make this research endeavor possible. Their decision to provide the equipment used in this study was the first step towards finishing this thesis. The learning opportunity they have helped provide is truly invaluable.

Second, I would like to thank my advisor, Dr. J. Antonio H. Carraro. His dedication and patience coupled with his drive for excellence have allowed me to develop myself intellectually as well as professionally. For his continued support thorough my master's program, I am extremely grateful. In addition, special thanks are also due to Dr. Charles D. Shackelford for instigating my love for geotechnical engineering. His extremely difficult coursework and lack of sugar coating have been influential in my career direction, drive to learn continuously and inspirational in the decision to attend graduate school. Additionally, I would like to extend many thanks to the Tailings and Mine Waste committee for affording me the opportunity to work on this project by providing the *MWR* research materials.

Lastly, but certainly not least, I would like to thank my loving family (well, most of them) for their undying love and support of me throughout my master's program. My

loving wife, Jo, has been a constant source of love, concern and, most of all, strength over the past several years, and, for that, I am enormously thankful. And finally, to my parents Ann and Ken, thank you for believing in me when I myself was ready to give up. Thank you for teaching me love, courage and dedication. You gave me life, support and love even when I gave you headaches. Your never-ending love and absolute confidence in me has given me the ability to achieve. To you three, I dedicate this thesis.

To my wife Jo, Mom and Dad:

## TABLE OF CONTENTS

ABSTRACT.....	ii
ACKNOWLEDGEMENTS.....	iv
LIST OF TABLES.....	viii
LIST OF FIGURES.....	xi
LIST OF SYMBOLS.....	xxi
LIST OF ACRONYMS.....	xxvii
CHAPTER 1: INTRODUCTION.....	1
1.1 Problem Statement.....	1
1.2 Research Objectives.....	3
1.3 Research Scope.....	4
1.4 Manuscript Organization.....	5
CHAPTER 2: MECHANICAL BEHAVIOR OF MINE WASTE ROCK (MWR).....	6
2.1 Background.....	6
2.2 Triaxial Testing.....	7
2.2.1 Scaling Techniques.....	10
2.2.2 Specimen Preparation.....	20
2.2.3 Dilatancy and Critical State.....	25
2.2.4 Particle Breakage.....	31
2.3 Summary of Literature Review.....	36
CHAPTER 3: CONCEPTUAL FRAMEWORK.....	39
3.1 Background.....	39
3.2 Critical State.....	41
3.3 Stress – Dilatancy Relationship.....	45
3.4 Particle Breakage.....	49
3.4.1 Fractal Dimension.....	55
3.4.2 Creep.....	56
CHAPTER 4: EXPERIMENTAL PROGRAM.....	59
4.1 Materials.....	59
4.2 Experimental Methods.....	61
4.2.1 Particle-Size Distribution.....	61
4.2.2 Parallel Gradation Technique.....	64
4.2.3 Atterberg Limits.....	67
4.2.4 Unified Soil Classification System.....	69
4.2.5 Specific Gravity of Solids.....	69
4.2.6 Scanning Electron Microscopy.....	70
4.2.7 X-Ray Diffraction.....	72
4.2.8 Limiting Void Ratios.....	74
4.2.9 Triaxial Testing.....	76
4.2.10 Particle Breakage and Fractal Dimension.....	97
CHAPTER 5: RESULTS.....	99
5.1 Isotropic Compression.....	99
5.2 Drained Monotonic Loading.....	102
5.3 Particle Breakage.....	109
5.4 Fractal Dimension.....	110

CHAPTER 6: ANALYSIS OF RESULTS .....	113
6.1 Limiting Void Ratios .....	113
6.2 Isotropic Compression .....	117
6.3 Drained Monotonic Axisymmetric Compression .....	124
6.3.1 Typical Stress-Strain-Volumetric Response .....	124
6.3.2 Critical State Friction Angle .....	127
6.3.3 Stress – Dilatancy Relationship .....	134
6.4 Particle Breakage .....	142
6.5 Fractal Dimension .....	142
6.6 Surface Energy .....	143
6.7 Comparison of Conventional and Large-scale Results .....	145
6.7.1 Isotropic Compression .....	146
6.7.2 Drained Monotonic Axisymmetric Compression .....	151
6.7.3 Particle Breakage .....	167
6.7.4 Fractal Dimension .....	169
6.7.5 Surface Energy .....	172
CHAPTER 7: CONCLUSIONS .....	174
7.1 Summary .....	174
7.2 Specimen Preparation and Uniformity .....	174
7.3 Isotropic Compression .....	175
7.4 Drained Monotonic Axisymmetric Compression .....	176
7.4.1 Typical Stress – Strain – Volumetric Response .....	176
7.4.2 Critical State Friction Angle .....	177
7.4.3 Stress – Dilatancy Relationship .....	177
7.5 Particle Breakage and Fractal Dimensions .....	178
7.6 Surface Energy .....	179
7.7 Parallel Gradation Technique .....	179
7.8 Suggestions for Future Work .....	180
LIST OF REFERENCES .....	182
APPENDIX A: X-RAY DIFFRACTION RESULTS .....	190
APPENDIX B: PARTICLE SIZE DISTRIBUTIONS .....	202
APPENDIX C: TRIAXIAL TEST RESULTS .....	212
APPENDIX D: FRACTAL DIMENSIONS .....	233
APPENDIX E: SCANNING ELECTRON MICROSCOPY IMAGES .....	244
APPENDIX F: CALIBRATIONS AND CALIBRATION VERIFICATIONS .....	263

## LIST OF TABLES

- Table 3.1: Range of values of measured surface free energy for certain materials.
- Table 3.2: Range of  $\beta_s$  and  $\beta_v$  values measured for certain geomaterials.
- Table 4.1: Sieve set used in the particle-size distribution analysis of the collected field samples.
- Table 4.2: Results of Atterberg Limit tests (ASTM D 4318).
- Table 4.3: Results of X-Ray diffraction testing.
- Table 4.4: USCS classification and parameters according to ASTM D 2487.
- Table 4.5: Calibration summary of transducers used in the present study.
- Table 4.6: Results of experimental program to verify  $D_R$  uniformity using the rigid, thin-walled tube reconstitution technique for “loose” weathered *MWR* specimens.
- Table 4.7: Results of experimental program to verify  $D_R$  uniformity using the rigid, thin-walled tube reconstitution technique for “dense” weathered *MWR* specimens.
- Table 4.8: Summary of  $D_R$ ,  $v$ ,  $i_F$ ,  $t_F$ , Flushing *PVs* and Final *B* values for unweathered *MWR* specimens.
- Table 4.9: Summary of  $D_R$ ,  $v$ ,  $i_F$ ,  $t_F$ , Flushing *PVs* and Final *B* values for weathered *MWR* specimens.
- Table 4.10: Results of elastic modulus testing for each membrane type used during triaxial testing.
- Table 5.1: Results of triaxial tests performed with unweathered *MWR* material.
- Table 5.2: Results of triaxial tests performed with weathered *MWR* material.
- Table 5.3: Values of  $D$  before and after testing for unweathered specimens.
- Table 5.4: Values of  $D$  before and after testing for weathered specimens.
- Table 6.1: Limiting void ratios, fines content and sample-size ratios from Fox (2011) and the present study
- Table 6.2: Critical state parameters  $\kappa$ ,  $v_{\kappa}$ ,  $\lambda$  and  $N$  determined during isotropic compression for unweathered and weathered *MWR* specimens.

Table 6.3: Extreme values of critical state parameters  $\kappa$ ,  $\nu_\kappa$ ,  $\lambda$  and  $N$  determined during isotropic compression for unweathered and weathered *MWR*.

Table 6.4: Tabulated values of  $(-\delta\varepsilon_p/\delta\varepsilon_a)_{max}$  during drained monotonic axisymmetric compression for unweathered and weathered *MWR* specimens.

Table 6.5: Tabulated values of intrinsic critical state parameters  $M$ ,  $\lambda_{cs}$  and  $\Gamma_{cs}$  determined for unweathered and weathered *MWR*.

Table 6.6: Comparison of measured and predicted values of  $\phi_p$  for the unweathered *MWR* material using Bolton's (1986) relationship and best fit values of  $Q$  and  $R$ .

Table 6.7: Comparison of measured and predicted values of  $\phi_p$  for the weathered *MWR* material using Bolton's (1986) relationship and best fit values of  $Q$  and  $R$ .

Table 6.8: Comparison of measured and predicted values of  $\phi_p$  for the unweathered *MWR* material using Bolton's (1986) relationship and best fit value of  $Q$  and  $R = 1$ .

Table 6.9: Comparison of measured and predicted values of  $\phi_p$  for the weathered *MWR* material using Bolton's (1986) relationship and best fit value of  $Q$  and  $R = 1$ .

Table 6.10: Values of  $\Gamma_{se}$  and  $dS$  determined for each triaxial test.

Table 6.11: Critical state parameters  $\kappa$  and  $\nu_\kappa$  determined after isotropic compression for unweathered and weathered *MWR LSTX* specimens (Modified after Fox 2011).

Table 6.12: Range of critical state parameters  $\kappa$ ,  $\nu_\kappa$ ,  $\lambda$  and  $N$  determined after isotropic compression for unweathered and weathered *MWR* in both conventional and large-scale triaxial tests.

Table 6.13: Tabulated values of  $(-\delta\varepsilon_p/\delta\varepsilon_a)_{max}$  during drained monotonic axisymmetric compression for unweathered and weathered *MWR LSTX* specimens.

Table 6.14: Tabulated values of  $M$ ,  $\phi_c$ ,  $\lambda_{cs}$ , and  $\Gamma_{cs}$  determined during drained monotonic axisymmetric compression for unweathered and weathered *MWR LSTX* specimens (Fox 2011).

Table 6.15: Comparison of final values of  $\phi_c$  determined during drained monotonic axisymmetric compression in conventional and large-scales (Fox 2011).

Table 6.16: Comparison of best fit values of  $Q$  and  $R$  between conventional and large-scale triaxial testing (Fox 2011).

Table 6.17: Comparison of measured and predicted values of  $\phi_p$  for the unweathered *MWR* material using Bolton's (1986) relationship and best fit values of  $Q$  and  $R$  for large-scale triaxial tests (calculated from data presented by Fox 2011).

Table 6.18: Comparison of measured and predicted values of  $\phi_p$  for the unweathered *MWR* material using Bolton's (1986) relationship and best fit values of  $Q$  and  $R$  for large-scale triaxial tests (calculated from data presented by Fox 2011).

Table 6.19: Comparison of measured and predicted values of  $\phi_p$  for the large-scale unweathered *MWR* material using Bolton's (1986) relationship and best fit values of  $Q$  and  $R$  for conventional scale triaxial tests (calculated from data presented by Fox 2011).

Table 6.20: Comparison of measured and predicted values of  $\phi_p$  for the large-scale weathered *MWR* material using Bolton's (1986) relationship and best fit values of  $Q$  and  $R$  for conventional scale triaxial tests (calculated from data presented by Fox 2011).

Table 6.21: Values of  $D_{final}$  and  $\Delta D$  determined for each *LSTX* test (Fox 2011).

Table 6.22: Values of  $\Gamma_{se}$  and  $dS$  determined for each *LSTX* test (Fox 2011).

Table A.1: Phases identified through *XRD* testing and their molecular formula (H & M Analytical report dated December 29, 2011).

Table F.1: Verification of calibration for pressure transducer PT14850.

Table F.2: Verification of calibration for pressure transducer PT14868.

Table F.3: Verification of calibration for pressure transducer PT14869.

Table F.4: Verification of calibration for pressure transducer PT14763.

Table F.5: Verification of calibration for pressure transducer PT14764.

Table F.6: Verification of calibration for pressure transducer PT14851.

Table F.7: Verification of calibration for volume change transducer VC27-1641.

Table F.8: Verification of calibration for volume change transducer VC27-1642.

Table F.9: Verification of calibration for load cell LC404303.

Table F.10: Verification of calibration for displacement transducer AD27-1617.

Table F.10: Determination of the Elastic Modulus for the 0.3-mm-thick membranes used during triaxial tests.

Table F.11: Determination of the Elastic Modulus for the 0.6-mm-thick membranes used during triaxial tests.

## LIST OF FIGURES

Figure 2.1: Normal strain and contact stress ( $\sigma_{max}$ ) for a pack of spheres subjected to an external stress ( $\sigma$ ) (Lowe 1964).

Figure 2.2: Gradations used in DEM analysis conducted by Sitharam et al. (2000).

Figure 2.3: Effects of maximum particle size on  $\phi_p$  in DEM analysis (Re-plotted from data presented by Sitharam et al. 2000).

Figure 2.4: Ranjit Sagar Dam field (prototype) and model gradations (Varadarajan et al. 2003).

Figure 2.5: Purulia Dam field (prototype) and model gradations (Varadarajan et al. 2003).

Figure 2.6: (a) Stress-strain and (b) volumetric strain results from the Ranjit Sagar Dam material (rounded/subrounded particles) (Varadarajan et al. 2003).

Figure 2.7: (a) Stress-strain and (b) volumetric strain results from the Purulia Dam material (angular particles) (Varadarajan et al. 2003).

Figure 3.1: Three dimensional view of the *CSL* and normal compression line (*NCL*) in  $p'$ - $q$ - $v$  space (After Muir-Wood 1990).

Figure 3.2: Two dimensional view of the isotropic *NCL* and *URL* in  $\ln(p')$ - $v$  space (Muir-Wood 1990).

Figure 4.1: Picture of the (a) unweathered and (b) weathered *MWR* parallel gradation materials tested in this study.

Figure 4.2: Particle-size distributions for the collected field samples of unweathered and weathered *MWR*.

Figure 4.3: Particle-size distributions for collected field samples and modeled gradations of unweathered *MWR* materials.

Figure 4.4: Particle-size distributions for collected field samples and modeled gradations of weathered *MWR* materials.

Figure 4.5: Microphotograph of unweathered *MWR* fines (particles passing the #200 sieve).

Figure 4.6: Microphotograph of weathered *MWR* fines (particles passing the #200 sieve).

Figure 4.7: Conventional-scale triaxial apparatus used in this study.

Figure 5.1: Isotropic compression data for unweathered *MWR* specimens.

Figure 5.2: Isotropic compression data for weathered *MWR* specimens.

Figure 5.3: Isotropic compression data for unweathered *MWR* specimens. An isotropic response line is also included to give an indication of the level of anisotropic volumetric response during isotropic loading.

Figure 5.4: Deviatoric stress versus axial strain for unweathered *MWR* specimens. The two plotted data points for each test represent peak and critical state stress states.

Figure 5.5: Volumetric strain versus axial strain for unweathered specimens. The two plotted data points for each test represent peak and critical state stress states.

Figure 5.6: Deviatoric stress versus axial strain for weathered *MWR* specimens. The two plotted data points for each test represent peak and critical state stress states.

Figure 5.7: Volumetric strain versus axial strain for weathered specimens. The two plotted data points for each test represent peak and critical state stress states.

Figure 5.8: Volumetric strain versus axial strain for unweathered specimens. The two plotted data points for each test represent peak and critical state stress states.

Figure 5.9: Volumetric strain versus axial strain for weathered specimens. The two plotted data points for each test represent peak and critical state stress states.

Figure 5.10: Upper bounds of post test gradations for the unweathered and weathered *MWR* material.

Figure 5.11: Evolution of the fractal dimension,  $D$ , for the unweathered and weathered *MWR* materials.

Figure 6.1: The effect of fines content on a silty sand containing fine Ottawa sand and non-plastic Loch Raven fines (Modified after Lade 2009).

Figure 6.2: Sphericity ( $S$ ) and roundness ( $R$ ) chart. Diagonal dotted lines correspond to constant particle regularity  $\rho=(R+S)/2$  (Cho et al. 2006).

Figure 6.3: Unloading-reloading lines for unweathered *MWR* specimens.

Figure 6.4: Unloading-reloading lines (solid) and normal compression lines (dashed) for weathered *MWR* specimens.

Figure 6.5: Deviatoric stress versus axial strain for unweathered and weathered *MWR* materials isotropically compressed to similar states at the same  $p'$ . The two plotted data points for each test represent peak and critical state stress states.

Figure 6.6: Volumetric strain versus axial strain for unweathered and weathered *MWR* materials isotropically compressed to similar states at the same  $p'$ . The two plotted data points for each test represent peak and critical state stress states.

Figure 6.7: *CSL* in  $p' - q$  space for unweathered and weathered *MWR* materials with a linear best fit value of  $M$  and the corresponding value of  $\phi_c$  (tests exhibiting shear bands during drained monotonic axisymmetric compression for the unweathered material were omitted).

Figure 6.8: *CSL* in  $\ln(p') - v$  space for unweathered and weathered *MWR* materials with a logarithmic best fit values of  $\lambda_{cs}$  and  $\Gamma_{cs}$  (tests exhibiting shear bands during drained monotonic axisymmetric compression for the unweathered material were omitted).

Figure 6.9: Shearing paths in  $\ln(p') - v$  space for unweathered *MWR* material.

Figure 6.10: Shearing paths in  $\ln(p') - v$  space for weathered *MWR* material.

Figure 6.11: Regression of the dilatancy response of unweathered and weathered *MWR* in accordance with the procedure outlined by Salgado et al. (2000).

Figure 6.12: Regression of the dilatancy response of unweathered and weathered *MWR* in accordance with the procedure outlined by Salgado et al. (2000) with the fitting parameter  $R = 1$ .

Figure 6.13: Unloading-reloading lines (solid) and normal compression lines (dashed) for unweathered *LSTX MWR* specimens (From data obtained by Fox 2011).

Figure 6.14: Unloading-reloading lines (solid) and normal compression lines (dashed) for weathered *LSTX MWR* specimens (From data obtained by Fox 2011).

Figure 6.15: Deviatoric stress versus axial strain for unweathered and weathered *MWR* materials isotropically compressed to similar states at the same  $p'$  for conventional and large-scale triaxial tests (Fox 2011) (the two data points shown correspond to measured values of peak and critical state strengths).

Figure 6.16: Volumetric strain versus axial strain for unweathered and weathered *MWR* materials isotropically compressed to similar states at the same  $p'$  for conventional and large-scale triaxial tests (Fox 2011) (the two data points shown correspond to measured values of peak and critical state strengths).

Figure 6.17: Shearing path in  $\ln(p') - v$  space for unweathered *MWR* material in conventional and large-scale triaxial tests (Fox 2011).

Figure 6.18: Shearing path in  $\ln(p') - v$  space for weathered *MWR* material in conventional and large-scale triaxial tests (Fox 2011).

Figure 6.19: *CSL* in  $p' - q$  space for unweathered and weathered *MWR* materials in large-scale triaxial testing with a linear best fit value of  $M$  and the corresponding value of  $\phi_c$  (Modified after Fox 2011) (tests exhibiting shear bands during drained monotonic axisymmetric compression were omitted).

Figure 6.20: *CSL* in  $\ln(p') - q$  space for unweathered *MWR* material in conventional and large-scale triaxial testing with a logarithmic best fit values of  $\lambda_{cs}$  and  $\Gamma_{cs}$  (Fox 2011) (tests exhibiting shear bands during drained monotonic axisymmetric compression were omitted).

Figure 6.21: *CSL* in  $\ln(p') - q$  space for weathered *MWR* material in conventional and large-scale triaxial testing with a logarithmic best fit values of  $\lambda_{cs}$  and  $\Gamma_{cs}$  (Fox 2011) (tests exhibiting shear bands during drained monotonic axisymmetric compression were omitted).

Figure 6.22: Regression of the dilatancy response of conventional and large-scale unweathered *MWR* in accordance with the procedure outlined by Salgado et al. (2000) (Fox 2011).

Figure 6.23: Regression of the dilatancy response of conventional and large-scale weathered *MWR* in accordance with the procedure outlined by Salgado et al. (2000) (Fox 2011).

Figure 6.24: Initial and post test gradations for conventional and large-scale triaxial tests on unweathered *MWR* specimens (Fox 2011).

Figure 6.25: Initial and post test gradations for conventional and large-scale triaxial tests on weathered *MWR* specimens (Fox 2011).

Figure 6.26: Evolution of the fractal dimension ( $D$ ) for the unweathered and weathered *MWR* materials in conventional and large-scale triaxial testing (From data obtained by Fox 2011).

Figure 6.27: Evolution of the fractal dimension ( $D$ ) for the unweathered and weathered *MWR* materials in conventional and large-scale triaxial testing normalized with respect to  $D_{Initial}$  (From data obtained by Fox 2011).

Figure A.1: Phase identification for the unweathered fine fraction sample (H & M Analytical report dated December 29, 2011).

Figure A.2: Exploded view showing the phase identification for the unweathered fine fraction sample (H & M Analytical report dated December 29, 2011).

Figure A.3: Exploded view showing the phase identification for the unweathered fine fraction sample (H & M Analytical report dated December 29, 2011).

Figure A.4: Exploded view showing the phase identification for the unweathered fine fraction sample (H & M Analytical report dated December 29, 2011).

Figure A.5: Exploded view showing the phase identification for the unweathered fine fraction sample (H & M Analytical report dated December 29, 2011).

Figure A.6: Phase identification for the unweathered coarse fraction sample (H & M Analytical report dated December 29, 2011).

Figure A.7: Exploded view showing the phase identification for the unweathered coarse fraction sample (H & M Analytical report dated December 29, 2011).

Figure A.8: Exploded view showing the phase identification for the unweathered coarse fraction sample (H & M Analytical report dated December 29, 2011).

Figure A.9: Exploded view showing the phase identification for the unweathered coarse fraction sample (H & M Analytical report dated December 29, 2011).

Figure A.10: Exploded view showing the phase identification for the unweathered coarse fraction sample (H & M Analytical report dated December 29, 2011).

Figure A.11 Phase identification for the weathered fine fraction sample (H & M Analytical report dated December 29, 2011).

Figure A.12: Exploded view showing the phase identification for the weathered fine fraction sample (H & M Analytical report dated December 29, 2011).

Figure A.13: Exploded view showing the phase identification for the weathered fine fraction sample (H & M Analytical report dated December 29, 2011).

Figure A.14: Exploded view showing the phase identification for the weathered fine fraction sample (H & M Analytical report dated December 29, 2011).

Figure A.15: Exploded view showing the phase identification for the weathered fine fraction sample (H & M Analytical report dated December 29, 2011).

Figure A.16: Phase identification for the weathered coarse fraction sample (H & M Analytical report dated December 29, 2011).

Figure A.17: Exploded view showing the phase identification for the weathered coarse fraction sample (H & M Analytical report dated December 29, 2011).

Figure A.18: Exploded view showing the phase identification for the weathered coarse fraction sample (H & M Analytical report dated December 29, 2011).

Figure A.19: Exploded view showing the phase identification for the weathered coarse fraction sample (H & M Analytical report dated December 29, 2011).

Figure A.20: Exploded view showing the phase identification for the weathered coarse fraction sample (H & M Analytical report dated December 29, 2011).

Figure B.1: Pre and post test particle size distribution for specimen U75-400.

Figure B.2: Pre and post test particle size distribution for specimen U77-200.

Figure B.3: Pre and post test particle size distribution for specimen U70-100.

Figure B.4: Pre and post test particle size distribution for specimen U68-400.

Figure B.5: Pre and post test particle size distribution for specimen U54-200.

Figure B.6: Pre and post test particle size distribution for specimen U50-100.

Figure B.7: Pre and post test particle size distribution for specimen U42-400.

Figure B.8: Pre and post test particle size distribution for specimen U40-200.

Figure B.9: Pre and post test particle size distribution for specimen U26-100.

Figure B.10: Pre and post test particle size distribution for specimen W92-400.

Figure B.11: Pre and post test particle size distribution for specimen W83-200.

Figure B.12: Pre and post test particle size distribution for specimen W78-100.

Figure B.13: Pre and post test particle size distribution for specimen W76-400.

Figure B.14: Pre and post test particle size distribution for specimen W72-200.

Figure B.15: Pre and post test particle size distribution for specimen W61-100.

Figure B.16: Pre and post test particle size distribution for specimen W55-400.

Figure B.17: Pre and post test particle size distribution for specimen W44-200.

Figure B.18: Pre and post test particle size distribution for specimen W34-100.

Figure C.1: Deviatoric stress and volumetric strain versus axial strain for specimen U75-400.

Figure C.2: Deviatoric stress and volumetric strain versus axial strain for specimen U77-200.

Figure C.3: Deviatoric stress and volumetric strain versus axial strain for specimen U70-100.

Figure C.4: Deviatoric stress and volumetric strain versus axial strain for specimen U68-400.

Figure C.5: Deviatoric stress and volumetric strain versus axial strain for specimen U54-200.

Figure C.6: Pre Deviatoric stress and volumetric strain versus axial strain for specimen U50-100.

Figure C.7: Deviatoric stress and volumetric strain versus axial strain for specimen U42-400.

Figure C.8: Deviatoric stress and volumetric strain versus axial strain for specimen U40-200.

Figure C.9: Deviatoric stress and volumetric strain versus axial strain for specimen U26-100.

Figure C.10: Deviatoric stress and volumetric strain versus axial strain for specimen W92-400.

Figure C.11: Deviatoric stress and volumetric strain versus axial strain for specimen W83-200.

Figure C.12: Deviatoric stress and volumetric strain versus axial strain for specimen W78-100.

Figure C.13: Deviatoric stress and volumetric strain versus axial strain for specimen W76-400.

Figure C.14: Deviatoric stress and volumetric strain versus axial strain for specimen W72-200.

Figure C.15: Deviatoric stress and volumetric strain versus axial strain for specimen W61-100.

Figure C.16: Deviatoric stress and volumetric strain versus axial strain for specimen W55-400.

Figure C.17: Deviatoric stress and volumetric strain versus axial strain for specimen W44-200.

Figure C.18: Deviatoric stress and volumetric strain versus axial strain for specimen W34-100.

Figure C.19: Back pressure saturation data for specimens U42-400, U40-200 and U26-100.

Figure C.20: Back pressure saturation data for specimens U68-400, U54-200 and U50-100.

Figure C.21: Back pressure saturation data for specimens U75-400, U77-200 and U70-100.

Figure C.22: Back pressure saturation data for specimens W55-400, W44-200 and W34-100.

Figure C.23: Back pressure saturation data for specimens W76-400, W72-200 and W61-100.

Figure C.24: Back pressure saturation data for specimens W92-400, W83-200 and W78-100.

Figure D.1: Initial regression of  $D$  for the unweathered material ( $D = 2.70$ ).

Figure D.2: Initial regression of  $D$  for the unweathered material ( $D = 2.97$ ).

Figure D.3: Post test regression of  $D$  for specimen U75-400.

Figure D.4: Post test regression of  $D$  for specimen U77-200.

Figure D.5: Post test regression of  $D$  for specimen U70-100.

Figure D.6: Post test regression of  $D$  for specimen U68-400.

Figure D.7: Post test regression of  $D$  for specimen U54-200.

Figure D.8: Post test regression of  $D$  for specimen U50-100.

Figure D.9: Post test regression of  $D$  for specimen U42-400.

Figure D.10: Post test regression of  $D$  for specimen U40-200.

Figure D.11: Post test regression of  $D$  for specimen U26-100.

Figure D.12: Post test regression of  $D$  for specimen W92-400.

Figure D.13: Post test regression of  $D$  for specimen W83-200.

Figure D.14: Post test regression of  $D$  for specimen W78-100.

Figure D.15: Post test regression of  $D$  for specimen W76-400.

Figure D.16: Post test regression of  $D$  for specimen W72-200.

Figure D.17: Post test regression of  $D$  for specimen W61-100.

Figure D.18: Post test regression of  $D$  for specimen W55-400.

Figure D.19: Post test regression of  $D$  for specimen W44-200.

Figure D.20: Post test regression of  $D$  for specimen W34-100.

Figure E.1: Photograph of the JEOL JSM-6500F Scanning Electron Microscope used to capture microphotographs of  $MWR$  fines used in the present study.

Figure E.2: Microphotograph of the unweathered fines at 100X magnification.

Figure E.3: Microphotograph of the unweathered fines at 100X magnification.

Figure E.4: Microphotograph of the unweathered fines at 200X magnification.

Figure E.5: Microphotograph of the unweathered fines at 200X magnification.

Figure E.6: Microphotograph of the unweathered fines at 400X magnification.

Figure E.7: Microphotograph of the unweathered fines at 400X magnification.

Figure E.8: Microphotograph of the unweathered fines at 500X magnification.

Figure E.9: Microphotograph of the unweathered fines at 500X magnification.

Figure E.10: Microphotograph of the unweathered fines at 1,000X magnification.

Figure E.11: Microphotograph of the unweathered fines at 1,000X magnification.

Figure E.12: Microphotograph of the unweathered fines at 1,500X magnification.

Figure E.13: Microphotograph of the unweathered fines at 2,000X magnification.

Figure E.14: Microphotograph of the unweathered fines at 2,000X magnification.

Figure E.15: Microphotograph of the unweathered fines at 4,000X magnification.

Figure E.16: Microphotograph of the unweathered fines at 4,000X magnification.

Figure E.17: Microphotograph of the unweathered fines at 5,000X magnification.

Figure E.18: Microphotograph of the unweathered fines at 6,000X magnification.

Figure E.19: Microphotograph of the weathered fines at 10,000X magnification.

Figure E.20: Microphotograph of the weathered fines at 100X magnification.

Figure E.21: Microphotograph of the weathered fines at 200X magnification.

Figure E.22: Microphotograph of the weathered fines at 400X magnification.

Figure E.23: Microphotograph of the weathered fines at 400X magnification.

Figure E.24: Microphotograph of the weathered fines at 500X magnification.

Figure E.25: Microphotograph of the weathered fines at 500X magnification.

Figure E.26: Microphotograph of the weathered fines at 1,000X magnification.

Figure E.27: Microphotograph of the weathered fines at 1,000X magnification.

Figure E.28: Microphotograph of the weathered fines at 1,500X magnification.

Figure E.29: Microphotograph of the weathered fines at 1,500X magnification.

Figure E.30: Microphotograph of the weathered fines at 2,000X magnification.

Figure E.31: Microphotograph of the weathered fines at 2,000X magnification.

Figure E.32: Microphotograph of the weathered fines at 4,000X magnification.

Figure E.33: Microphotograph of the weathered fines at 4,000X magnification.

Figure E.34: Microphotograph of the weathered fines at 6,000X magnification.

Figure E.35: Microphotograph of the weathered fines at 10,000X magnification.

## LIST OF SYMBOLS

$A$	–	Proportionality constant
$A_c$	–	Corrected cross sectional specimen area (m <sup>2</sup> )
$A_{ce}$	–	Cross sectional area of the specimen at the end of the test (m <sup>2</sup> )
$A_f$	–	Cross sectional area at failure (m <sup>2</sup> )
$A_o$	–	Cross sectional area at the end of isotropic compression (m <sup>2</sup> )
$B$	–	Skempton's (1954) pore pressure coefficient
$B_g$	–	Breakage factor (%)
$\beta_s$	–	Particle shape factor
$\beta_v$	–	Particle volume factor
$c'$	–	Apparent effective cohesion (kPa)
$C_u$	–	Coefficient of uniformity
$C_c$	–	Coefficient of curvature
$d$	–	Nominal particle diameter (mm)
$d_{im}$	–	Inner diameter of the triaxial membrane (mm)
$d_o$	–	Diameter of specimen at the end of isotropic compression (mm)
$d_a$	–	Perpendicular specimen axis measured in the major elliptical direction (mm)
$d_b$	–	Perpendicular specimen axis measured in the minor elliptical (mm)
$d_{max}$	–	Maximum particle size (mm)
$d_{sp}$	–	Triaxial specimen diameter (mm)
$dS$	–	Change in surface area (m <sup>2</sup> )
$dx$	–	Finite displacement in the direction of shearing in plain strain

$dy$	–	Finite displacement perpendicular to the plane of shearing in plain strain conditions
$D$	–	Fractal dimension
$d_{mi}$	–	Average diameter of the particle retained on sieve $d_i$
$d_{10}$	–	Particle size (mm) of which 10% of a material is finer
$d_{30}$	–	Particle size (mm) of which 30% of a material is finer
$d_{50}$	–	Mean particle size (mm)
$d_{60}$	–	Particle size (mm) of which 60% of a material is finer
$D_{Initial}$	–	Initial fractal dimension
$D_{Final}$	–	Final fractal dimension after test
$\Delta D$	–	Change in fractal dimension
$D_R$	–	Relative density (%)
$D_{R,Initial}$	–	Relative density after reconstitution (%)
$D_{R,AF}$	–	Relative density after flushing (%)
$D_{R,AS}$	–	Relative density after saturation (%)
$D_{R,AC}$	–	Relative density after isotropic compression (%)
$\delta_e$	–	axial strain due to movement along the shear plane (%)
$\delta\epsilon_q$	–	Triaxial shear strain
$\delta\epsilon_p$	–	Octahedral mean strain increment
$e$	–	Void ratio
$e_{min}$	–	Minimum void ratio
$e_{max}$	–	Maximum void ratio
$E_B$	–	Energy consumption due to particle breakage

$E$	–	Elastic modulus of the membrane (kPa)
$\varepsilon_1$	–	Major principal strain (%)
$\varepsilon_3$	–	Minor principal strain (%)
$\varepsilon_a$	–	Axial strain (%)
$\varepsilon_{ea}$	–	Axial strain at the end of the test (%)
$\varepsilon_{ap}$	–	Axial strain at peak deviator stress (%)
$\varepsilon_p$	–	Volumetric strain (%)
$\varepsilon_r$	–	Radial strain (%)
$h_p$	–	Height of the sample at the appearance of the shear band
$\Delta h_p$	–	Decrease in height of the sample after the appearance of the shear band
$i_F$	–	Gradient during flushing
$f$	–	Unit friction between the membrane and dummy (kPa)
$G_s$	–	Specific gravity of solids
$\Gamma$	–	Surface free energy (J/m <sup>2</sup> )
$\Gamma_{se}$	–	Surface energy (J/m <sup>2</sup> )
$\Gamma_{cs}$	–	Intercept of the critical state line at $p' = 1$ kPa in $\ln(p') - v$ space
$\phi$	–	Mobilized friction angle (deg.)
$\phi_c$	–	Critical state friction angle (deg.)
$\phi_{tb}$	–	Friction angle excluding dilatancy and including particle breakage (deg.)
$\phi_t$	–	Friction angle excluding dilatancy and particle breakage (deg.)
$\phi_p$	–	Peak friction angle (deg.)
$I_D$	–	Relative density index

$I_R$	–	Relative dilatancy index
$I_P$	–	Plasticity index (%)
$k$	–	Equals 1 for plain strain and 2 for axisymmetric conditions
$\kappa$	–	Slope of a <i>URL</i> in $\ln(p') - v$ space
$\lambda_{cs}$	–	Slope of the <i>CSL</i> in $\ln(p') - v$ space
$M$	–	Slope of the critical state line in $p' - q$ space
$M$	–	Dilatancy number
$M_i$	–	Mass retained on sieve $i$ (g)
$\mu$	–	Coefficient of frictional resistance
$N$	–	Intercept of the isotropic <i>NCL</i> at $p' = 1$ kPa in $\ln(p') - v$ space
$N_c$	–	Flow number (principal stress ratio) at critical state
$N(L > d)$	–	Number of particles of diameter $L$ greater than $d$
$n$	–	Porosity
$v$	–	Specific volume
$V_{Initial}$	–	Specific volume after reconstitution
$v_{AF}$	–	Specific volume after flushing
$v_{AS}$	–	Specific volume after saturation
$v_{AC}$	–	Specific volume after isotropic compression
$v_{\kappa}$	–	Specific volume along a <i>URL</i> at $p' = 1$ kPa in $\ln(p') - v$ space
$v_{\lambda}$	–	Specific volume along a <i>NCL</i> at $p' = 1$ kPa in $\ln(p') - v$ space
$v_{cs}$	–	Specific volume along the <i>CSL</i> at $p' = 1$ kPa in $\ln(p') - v$ space
$R_s$	–	Principal strain ratio
$\rho_s$	–	Dry density ( $\text{g}/\text{cm}^3$ )

$p'$	–	Mean effective stress (kPa)
$p'_{\text{yield}}$	–	Yield stress (kPa)
$p_A$	–	Reference stress (kPa)
$p_{om}$	–	Initial confining pressure caused by membrane (kPa)
$p'_{cs}$	–	Mean effective stress at the critical state (kPa)
$p'_p$	–	Peak mean effective stress (kPa)
$P$	–	Percentage by weight for a given nominal particle diameter ( $d$ ) for a quadratic grain size distribution
$q$	–	Deviatoric stress (kPa)
$q_{cs}$	–	Deviatoric stress at critical state (kPa)
$Q$	–	Bolton (1986) fitting parameter
$R$	–	Bolton (1986) fitting parameter
$S$	–	Surface area (m <sup>2</sup> )
$\sigma$	–	Normal stress (kPa)
$\sigma'$	–	Normal effective stress (kPa)
$\sigma'_1$	–	Major principal effective stress (kPa)
$\sigma'_3$	–	Minor principal effective stress (kPa)
$\sigma'_a$	–	Effective axial stress (kPa)
$\sigma'_c$	–	Effective confining stress (kPa)
$\sigma'_r$	–	Effective radial stress (kPa)
$t$	–	Time (hr)
$t_F$	–	Time to flush (d)
$T$	–	Shear force (kN)

$\tau$	–	Shear stress (kPa)
$V_T$	–	Total volume (m <sup>3</sup> )
$V_s$	–	Volume of solids (m <sup>3</sup> )
$w_L$	–	Liquid limit (%)
$w_P$	–	Plastic limit (%)
$\psi$	–	Dilatancy Angle (deg.)

## LIST OF ACRONYMS

<i>COV</i>	–	Coefficient of variation
<i>CSL</i>	–	Critical state line
<i>DEM</i>	–	Discrete element modeling
<i>LSTX</i>	–	Large-scale triaxial
<i>MSL</i>	–	Mean sea level
<i>MWR</i>	–	Mine waste rock
<i>NCL</i>	–	Normal compression line
<i>SSR</i>	–	Sample-size ratio
<i>URL</i>	–	Unloading-reloading line
<i>XRD</i>	–	X-Ray Diffraction

## CHAPTER 1: INTRODUCTION

### 1.1 Problem Statement

The period from 1911 to 2011 saw rockfill evolve into a frequently used construction material in a number of engineering applications. More specifically, rockfill materials excavated from mining operations, described herein as Mine Waste Rock (*MWR*), have been commonly used in the construction of embankment dams for mine tailings ponds. *MWR* is most commonly created by the excavation of overburden material during open pit mining operations of a variety of minerals and metals. Especially within this application, embankment dams constructed using *MWR* have become ever larger. This trend has resulted in greater requisite for ensuring long-term stability of the embankment dam and therefore this becomes a critical component of the design process for these and similar structures. Thus, a thorough understanding of the mechanical behavior of *MWR* is required.

Use of *MWR* as a construction material for embankment dams and tailings storage facilities requires a fundamental understanding and assessment of the physical properties and mechanical behavior of the material. Modeling *MWR* material to design an embankment dam requires an accurate estimation of the shear strength and durability of the material. No matter how complex and theoretically correct, the results of said model are useless without an accurate estimation of the material strength parameters and a rigorous conceptual framework in which to apply said properties. A thorough, full scale evaluation of *MWR* in a conventional soils laboratory is unusual due to the wide range of

particle sizes that are commonly present in *MWR*. With particle sizes ranging from meters to a few microns, a rigorous and systematic approach is required and must be followed to accurately characterize the mechanical behavior of *MWR* in the laboratory. Particle size has been shown both experimentally and theoretically to affect the mechanical behavior of soil/rock (Holtz & Gibbs 1956) and conventional geotechnical testing equipment such as triaxial compression, direct shear and direct simple shear are restricted in their use by the limiting maximum particle size ( $d_{max}$ ) associated with the sample size used. *MWR* frequently contains particles far greater than the  $d_{max}$  generally associated with conventional laboratory testing apparatus' and therefore a systematic method must be followed to account for the differences between the  $d_{max}$  in the field particle size distribution and the  $d_{max}$  in the laboratory particle size distribution.

In addition to particle size and effects related to scaling large-scale materials down to what can be tested in typical geotechnical laboratories, particle breakage during loading has been shown to affect the mechanical behavior of geomaterials (Marachi 1969, Marsal 1973). Geomaterials with large, angular or weak particles are especially prone to the phenomena of particle breakage (Marsal 1973). Due to the inherent challenges associated with the characterization of materials with large particle sizes, a rigorous description of the physical properties, and mechanical behavior of *MWR* requires an experimental framework that takes into account the intrinsic parameters of *MWR*, sample scaling for laboratory testing as well as the irrecoverable energy dissipated during loading due to particle breakage.

## 1.2 Research Objectives

The purpose of this research is to rigorously and systematically evaluate the intrinsic parameters of *MWR* as well as the effects of different state variables influencing the mechanical behavior of *MWR* in conventional scale drained monotonic axisymmetric compression. Intrinsic parameters were determined through a thorough laboratory testing program and the effect of state variables such as relative density ( $D_R$ ) and mean effective stress ( $p' = (\sigma'_1 + 2\sigma'_3)/3$ ) was observed and evaluated for two *MWR* geomaterials over a range of mean effective stresses, strains and densities. In addition to evaluating the parameters outlined above, the effect of particle size and sample scaling effects on the mechanical behavior of *MWR* was carried out by systematically comparing results for 70-mm triaxial specimens to the test results provided by Fox (2011) for 150-mm triaxial test specimens.

The specific objectives of the study were to:

1. Characterize the drained response of each material in conventional scale monotonic axisymmetric compression;
2. Determine the intrinsic parameters of two types of *MWR*;
3. Quantify the effect of particle size and sample scaling on the mechanical response and particle breakage of *MWR* using the intrinsic fractal dimension ( $D$ ); and
4. Quantify the effect of particle size and sample scaling on the measurement of intrinsic parameters of two types of *MWR*.

### 1.3 Research Scope

This research study focuses on the mechanical response of two different *MWR* materials. Both materials were removed from an open pit mine simultaneously from similar elevations with the main difference between the materials being the level of *in situ* weathering by different hydrogeologic conditions and particle size distributions. Bulk field samples were tested in a conventional triaxial apparatus using 70-mm diameter specimens. The bulk field samples contained particles far larger than the appropriate  $d_{max}$  of the triaxial device (ASTM D 4767) so the tested materials were scaled down to the recommended  $d_{max}$  using the parallel gradation technique (Lowe 1964, Marachi 1972, Sitharam et al. 2000). The parallel technique essentially is a method of sample scaling that maintains a constant proportionality ratio between the mean particle size ( $d_{50}$ ) and  $d_{max}$ . Other scaling techniques such as the scalping technique and quadratic grain size distributions have been proposed by others (Zeller 1957, Frost 1973), however, due to the limited amount of material dedicated to this research, only the parallel gradation technique was used to evaluate the mechanical behavior of *MWR*. Both materials were tested under saturated, drained, monotonic, axisymmetric compression at levels of  $p'$  equal to 100, 200 or 400 kPa. Particle size distributions of the initial and final specimen states were determined for all specimens to quantify particle breakage during loading. A more specific description and discussion of the experimental testing program is presented in Chapter 4. The tests were carried out under similar initial  $D_R$  and  $p'$  to those completed by Fox (2011) to provide a total of 36 triaxial test results of both large and conventional scale for analysis.

## 1.4 Manuscript Organization

Organization of this thesis includes six additional chapters that cover several aspects relating to the mechanical behavior of *MWR*. Chapter 2 is a comprehensive literature review of previous investigations involving similar geomaterials and testing procedures. Chapter 3 presents the theoretical framework applied in this study. Chapter 4 is a discussion on and description of the experimental testing program used in the course of the research. Chapter 5 presents the results from the experimental testing program. Chapter 6 is an analysis and discussion of the results presented in Chapter 5. Chapter 7 is a summary of the main conclusions discovered during the research program.

## CHAPTER 2: MECHANICAL BEHAVIOR OF MINE WASTE ROCK (MWR)

### 2.1 Background

A thorough characterization of the mechanical behavior of *MWR* comes with extreme difficulties, most of which are derived from the wide range of particle sizes generally associated with *MWR* geomaterials which often include very large particles. While triaxial testing is widely used to evaluate the shear strength and mechanical behavior of geomaterials, limitations arise from the size of the triaxial apparatus and the maximum particle size ( $d_{max}$ ) of the geomaterials to be tested. Conventional triaxial devices are commonly suited to carry out tests on specimens ranging from 30 - 100 mm in diameter with corresponding appropriate maximum particle sizes of 5 - 17 mm based on a diameter to maximum particle size ratio of 6.

Testing geomaterials such as *MWR* in conventional triaxial testing devices requires a systematic approach to scale down the specimen  $d_{max}$  to the appropriate size as dictated by the specimen to be tested. By scaling specimens to include testable ranges of particle sizes in a way that is representative of the field scale material, an accurate estimation of the mechanical response of full-scale *MWR* can be made. This chapter provides a summary of the literature focusing on investigations on geomaterials scaled down to facilitate triaxial compression testing, specimen preparation techniques, conceptual frameworks used to analyze triaxial testing results, and particle breakage during testing.

## 2.2 Triaxial Testing

Triaxial testing has been a widely used tool to evaluate the shear strength and mechanical behavior of geomaterials since the mid 1900's. However, testing constraints relating to the maximum particle size suitable to the size of the testing apparatus has introduced new challenges in testing rockfill geomaterials such as *MWR*. Numerous research studies have attempted to increase the maximum particle size for the specimens tested by increasing the size of the testing apparatus (Holtz & Gibbs 1956, Lowe 1964, Marachi 1969, 1972, Marsal 1973) in order to more accurately model field scale mechanical behavior of rockfill geomaterials. The larger scale testing apparatuses were designed to test specimens with a diameter of up to 1.4 m and a maximum particle size of up to 150 mm (Marachi 1972). Conventionally, triaxial devices are designed to test specimens ranging from 30 - 100 mm in diameter with maximum particle sizes up to 17 mm. Large-scale triaxial testing often requires specialized equipment and far more testing materials than what is commonly used for triaxial shear strength testing. However, the maximum particle size for even the largest triaxial apparatus is far less than common particle sizes associated with *MWR* and scaling is still required.

Triaxial testing is commonly associated with what is described as the sample-size ratio (*SSR*), which is the ratio of the specimen diameter to the maximum particle size of the specimen,  $d_{max}$  (Vallerga et al. 1957, Marachi 1969). Numerous research studies have shown that particle-size effects can be avoided if the specimen size is sufficiently larger than the maximum particle size of the specimen (Holtz & Gibbs 1956, Leslie 1969). Typically, values of *SSR* less than five have been shown to have pronounced effects on

the measured strength during testing due to interference from the larger particles (Leslie 1969, Marsal 1969). Provided no more than about 30 percent (%) of the material is retained on the maximum sieve size in a set of sieves used for determining the specimen particle-size distribution, a *SSR* equal to 6 is sufficient to prevent particle-size effects during triaxial shear strength testing (Marachi 1969). The American Society for Testing and Materials (ASTM) also suggest that a *SSR* of 6 be used for testing granular materials in triaxial compression (ASTM D 4767). A *SSR* equal to 6 yields a maximum nominal particle size of 11.7 mm for a conventional 70-mm triaxial specimen. Because geomaterials such a *MWR* comprise of particles with nominal diameters far larger than 11.7 mm, scaling gradations requires assumptions be made as to the intrinsic mechanical properties of the particles within a given gradation being constant for all particle sizes and introduces limitations with respect to conventional-scale triaxial testing. The assumptions regarding the intrinsic mechanical properties of individual particles will be discussed further in section 2.2.1.

Holtz and Gibbs (1956) addressed the issue of maximum particle size and its effect on triaxial shear strength testing through a testing program that included 183 large-scale triaxial tests conducted over a range of relative densities ( $D_R$ ) and mean effective stresses,  $p' = (\sigma'_1 + 2\sigma'_3)/3$ , where  $\sigma'_1$  and  $\sigma'_3$  are the effective major and minor principal stresses, respectively. Results of the study showed an increase in shearing resistance for more well-graded materials containing up to 50-60 percent gravel at similar initial  $D_R$  over a range of  $p'$ . As the material became more poorly-graded after crossing the before mentioned threshold, shearing resistance does not increase and may decrease.

Recommended  $SSRs$  presented in the study ranged from 3 to 7.3 depending on the specimen size and the relative amount of coarse particles present in the specimen. Particle shape was also concluded to significantly affect the frictional characteristics of the material. Specimens with particles with high angularity showed an increase in shear resistance with increasing  $D_R$  significantly increasing the magnitude of shearing resistance.

Marachi (1969, 1972) conducted an investigation that encompassed mechanical behavior and particle-size effects in plane strain and axisymmetric compression. Marachi et al. (1972) conducted drained axisymmetric compression tests on three rockfill materials of different mineralogical composition with a minimum of four tests conducted with specimen sizes of 70 mm, 300 mm, and 900 mm at initial levels of  $p'$  equal to 207 kPa, 965 kPa, 2896 kPa, and 4482 kPa. The specimens tested were reconstituted using the parallel gradation technique proposed by Lowe (1964), which will be discussed further in section 2.2.1. In all cases, results show that the peak internal friction angle ( $\phi_p$ ) was overestimated by as much as 3 - 4° for specimen sizes of 70 mm compared to the actual values measured for 900-mm specimens, regardless of  $p'$ . However, the discrepancy was more pronounced for tests conducted at the lowest  $p'$  of 207 kPa. Conversely, the smaller specimen size reduced the compressibility of the material during testing, regardless of specimen mineralogy. Conclusions of the study propose that  $\phi_p$  decreases with increasing particle size and increasing  $p'$  whereas compressibility increases with increasing particle size and  $p'$ . An important consideration here is that the research focused primarily on the effect of specimen size and particle size on  $\phi_p$ . No emphasis was given to the mechanical

behavior of the different specimen sizes at large strains where a strong trend is observed in which the principal stress ratio,  $\sigma'_1/\sigma'_3$ , approaches unity for all specimen sizes. This observation leads to the possible hypothesis that only  $\phi_p$  is affected by sample-size effects and, at large strains, materials exhibiting parallel gradations to actual field gradations may be representative when quantifying the mechanical behavior of the material in terms of the critical state friction angle,  $\phi_c$ , provided all other material characteristics (mineralogy, particle shape, etc) are kept constant.

### 2.2.1 Scaling Techniques

Several scaling techniques have been developed to address the challenge associated with laboratory testing of granular geomaterials with large particle sizes. Scaling is defined as the process in which materials with large particle sizes are modified such that the maximum particle size is reduced to facilitate laboratory testing. Scaling techniques include the scalping technique (Zeller & Wulliman 1957), the quadratic grain size distributions (Fumagalli 1969), and the parallel gradation technique (Lowe 1964). Fumagalli (1969) proposed that a laboratory gradation scaled from the field gradation, referred hereon as model gradation, should have similar grain size curves, void ratios and particle shape as the field gradation. Assuming that particle strength is constant throughout all particle size fractions, model gradations can be developed to simulate the mechanical behavior of rockfill geomaterials under realistic laboratory testing conditions.

### 2.2.1.1 Scalping Technique

The most common technique adopted in most conventional laboratories is the scalping technique (Zuller & Wulliman 1957), in which all particles greater than the  $d_{max}$  suitable for the testing apparatus are removed. The finer fractions with particle sizes less than  $d_{max}$  are scaled-up by a constant factor. The scalping technique does not allow for similitude between field scale gradations because the shape of the grain size distribution curve is not retained. Therefore laboratory test specimen gradations and may cause specimens to contain an excessive portion of fines relative to the field gradation. Neves (1990) proposed that scalping from both the top and bottom of the gradation curve may be necessary to limit the amount of fines during testing and allow the specimen to be free draining. However, ensuring perfectly drained conditions in laboratory triaxial testing is not just a measure of fines content, but also depends on the rate of axial displacement during the test.

### 2.2.1.2 Quadratic Grain Size Distribution Technique

Fumagalli (1969) proposed a scaling technique by use of quadratic grain size distribution curves. The curves were constructed using following equation:

$$P = 100 \sqrt{\frac{d}{d_{max}}} \quad (2.1)$$

where:  $P$  is the percentage, by weight, for a given nominal particle diameter ( $d$ ), and  $d_{max}$  is the maximum particle size that will be tested. Equation 2.1 represents a scaling technique that assumes that grain size distributions are parabolic in nature and are mathematically defined in quadratic form. This gross assumption of the shape of the

grain size distribution curve limits the applicability of Equation 2.1 to well-graded geomaterials that exhibit parabolic grain size distribution curves.

#### 2.2.1.3 Parallel Gradation Technique

A more realistic way to scale field gradations is known as the parallel gradation technique developed by Lowe (1964). Research conducted by Lowe consisted of modeling field scale materials to be used in the construction of the Shihmen Dam in Taiwan to be tested under triaxial compression using 150-mm diameter specimens. Since field scale materials consisted of particles with a nominal diameter of 300 mm, model gradations were constructed such that each particle was exactly one eighth the size of the corresponding field scale particle size. In essence, the field scale gradation curve was shifted by a factor of one eighth and the corresponding model gradation was exactly parallel to the field gradation. A factor of one eighth lead to a *SSR* equal to 4, under the minimum value of 6 typically adopted for triaxial testing (ASTM D 4767) and under the recommended minimum value of 5 proposed by Leslie (1969) and Marsal (1969). This leads to the assumption that a factor of one eighth was used for convenience and sufficient knowledge of the material allowed for a smaller *SSR* to be used. Extra effort was taken by Lowe to duplicate the particle shape and mineralogical composition of the field scale particles. An assumption was made that the particles passing the #200 sieve (with nominal diameter of 0.075 mm) were similar in plasticity and shear characteristics to those particles passing the #30 sieve (nominal diameter of 0.6 mm, which is exactly eight times the nominal diameter of the fraction passing the #200 sieve). With this assumption, modeling the field scale gradation was considered feasible because the

modeled gradations would share similar grain size distribution curves and shear characteristics. Lowe describes the basis for the parallel gradation technique as the formula presented on Figure 2.1, which shows that, for a packing of spheres, the strain and maximum contact stresses are independent of maximum particle size and dependent solely upon the applied stress and the intrinsic mechanical properties of the material (spheres) being loaded. This idealization allows the parallel gradation technique to conform to the constraints presented by Fumagalli (1969) but also assumes constant mechanical properties, such as modulus of elasticity, particle surface roughness, particle shape, particle strength and plasticity, throughout the material (Marachi 1969).

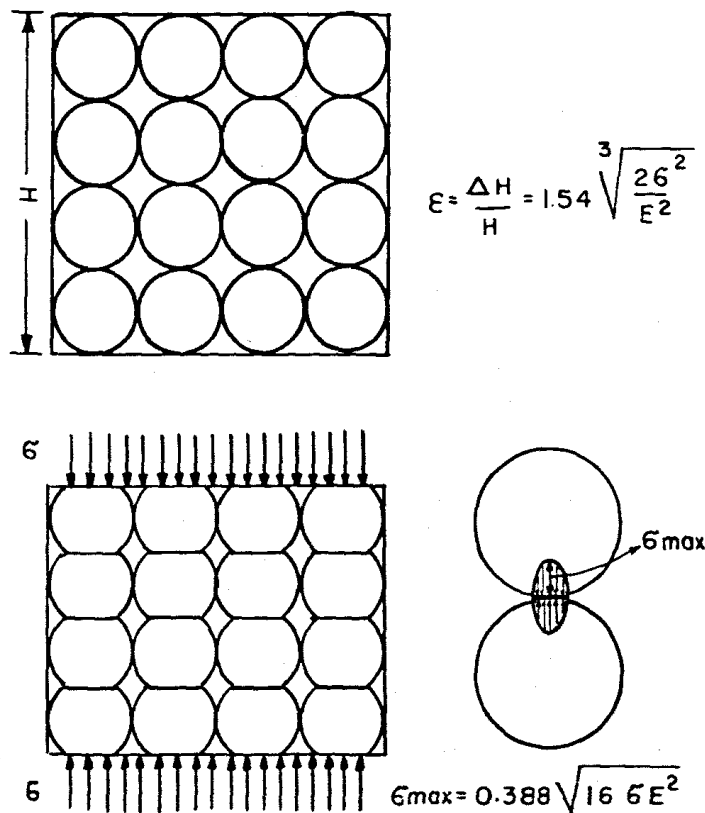


Figure 2.1: Normal strain and contact stress ( $\sigma_{max}$ ) for a pack of spheres subjected to an external stress ( $\sigma$ ) (Lowe 1964).

#### 2.2.1.4 Comparison of Scaling Techniques

Further research was conducted by Sitharam et al. (2000) in an attempt to observe the effects of modeling laboratory gradations by way of the widely used scalping technique versus the exactly parallel gradation technique. The effects of maximum particle size, particle gradation, particle sorting and soil fabric were investigated by use of Discrete Element Modeling (DEM). Grain size distribution curves for the two models are presented on Figure 2.2. Particles were modeled as round discs in their study and state parameters  $p'$  and  $D_R$  were held constant for each simulated grain size distribution. Results from their study indicate that parallel gradations (gradations a, c, d and e on Figure 2.2) have the same or very similar fabric, which makes them behave similarly under identical boundary conditions provided several other parameters are kept constant (e.g. particle shape, stiffness, plasticity, etc.). Only a minor increase in  $\phi_p$  was observed for parallel gradations as the maximum particle size increases. This was attributed to increasing contact area between individual grains with increasing particle size. On the contrary, model gradations (created by the scalping technique) that exhibit the same minimum grain size (presented on Figure 2.2 as gradations b, e, f and g) have a different initial gradation, and correspondingly, a different initial fabric which causes model gradations to behave differently under identical boundary conditions. A substantial decrease in  $\phi_p$  was observed for the model gradations with the same minimum particle size as maximum particle size increases. The reduction in  $\phi_p$  was attributed to the initial arrangement and uniformity of grains and induced anisotropy development in contact forces. McDowell et al. (1996) defines the coordination number as the number of inter-particle contacts subjected on a particle within a soil matrix. For perfectly parallel

gradations, the initial contact number was the same the equilibrated coordination number was found to also be equal. In the case of the scalped grain size distributions, the initial coordination number was found to vary as well as throughout the DEM simulations. An error in the analysis presented by Sitharam et al. (2000) was found during analysis of the publication where gradation b in Figure 2.2 was said to be parallel to gradations a, c and d. As previously stated and presented in Figure 2.2, gradation e is parallel to gradation a, c and d. Re-plotting the data presented by Sitharam et al. (2000) correctly, effects of maximum particle size for both scaling techniques from the study are presented on Figure 2.3.

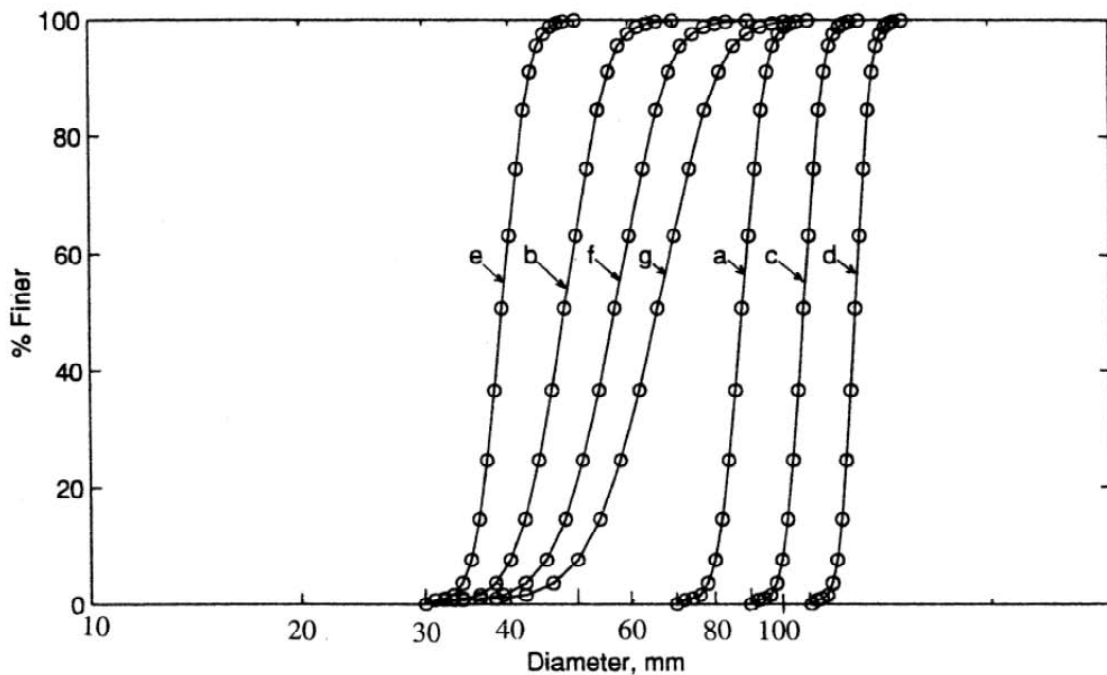


Figure 2.2: Gradations used in DEM analysis conducted by Sitharam et al. (2000).

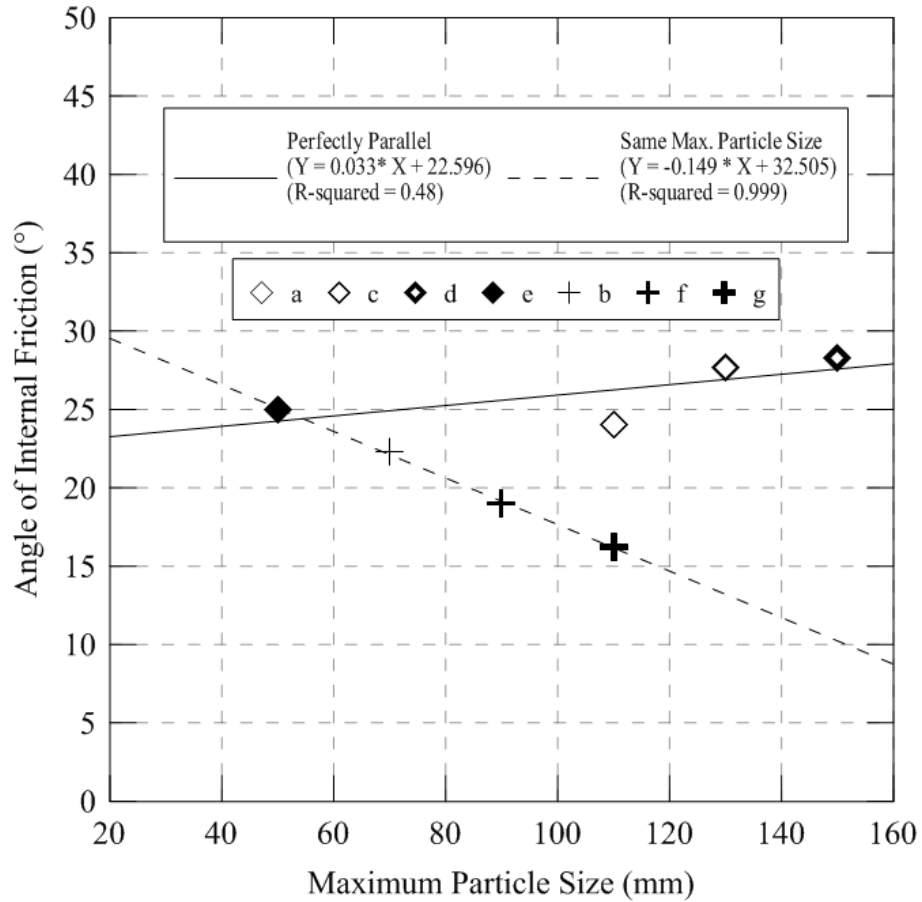


Figure 2.3: Effects of maximum particle size on  $\phi_p$  in DEM analysis (Re-plotted from data presented by Sitharam et al. 2000).

Varadarajan et al. (2003) conducted an experimental program to observe the effects of particle shape on the mechanical response of rockfill geomaterials. Two materials were tested using the parallel gradation technique as proposed by Lowe (1964). The first sample was a rockfill material from the Ranjit Sagar Dam in India, which consisted of alluvial material with rounded/subrounded particles. The second sample was a rockfill material from the Purulia Dam in India, which consisted of angular and subangular particles obtained by blasting. Grain size distribution curves for the field and modeled gradations are presented on Figures 2.4 and 2.5 for the Ranjit Sagar Dam and Purulia Dam, respectively. An interesting note to consider is the fact that the Ranjit Sagar

material had fines in the field gradation, which, upon translation to finer particle sizes, increases from ~2% passing the #200 sieve to ~17% passing the #200 sieve. The Purulia Dam material was obtained by blasting and most likely underwent prescreening or a selective process in picking particle sizes such that no particles were finer than ~6 mm (far coarser than 0.075 mm). Research by Salgado et al. (2000) on non-plastic silty sands demonstrated experimentally that  $\phi_p$  increases as much as  $10^\circ$ , depending on the level of  $p'$  at a constant  $D_R$ , and  $\phi_c$  increases by as much as  $4^\circ$  with increasing fines content from 0 – 20%. Data describing the plasticity of the fines in the Ranjit Sagar Dam material was not presented by Varadarajan et al. (2003). The lithology/mineralogy of the Ranjit Sagar Dam material was said to contain a conglomerate of sandstone, quartzite, shale, claystone and other materials which suggest the fines did exhibit some plasticity. Although plasticity data was omitted from the analysis, the results from testing the Ranjit Sagar Dam material conditionally support observations made by Salgado et al. (2000) with regard to increasing  $\phi_p$  with increasing fines content from ~ 2 – 17%. The lack of fines in the Purulia Dam material may have had some effect in the decreasing friction angle measured for increasing particle sizes. Results of the study are also in partial agreement, with respect to the Ranjit Sagar Dam material, with Sitharam et al. (2000), who modeled gradations as round disks. Results from the Ranjit Sagar Dam material showed an increase in the internal angle of friction of about  $9^\circ$  with increasing particle size from 25 - 320mm. The rounded, alluvial particles comprising the Ranjit Sagar Dam material behave similarly as to what was predicted by DEM. The more angular particles associated with the Purulia Dam material had the inverse effect on  $\phi_p$  as particle size increased from 25 – 1200 mm, where the friction angle was decreased by about  $6^\circ$ . Due

to the lack of fines in the Purulia Dam material, and therefore no uncertainty associated with the plasticity of the fines, the results suggest that particle shape plays a significant role in scaling techniques and is most likely the reason for the observed changes in  $\phi_p$ . For rounded particles,  $\phi_p$  increases with increasing particle size. Angular particles, conversely, showed a decrease in  $\phi_p$  with increasing particle size.

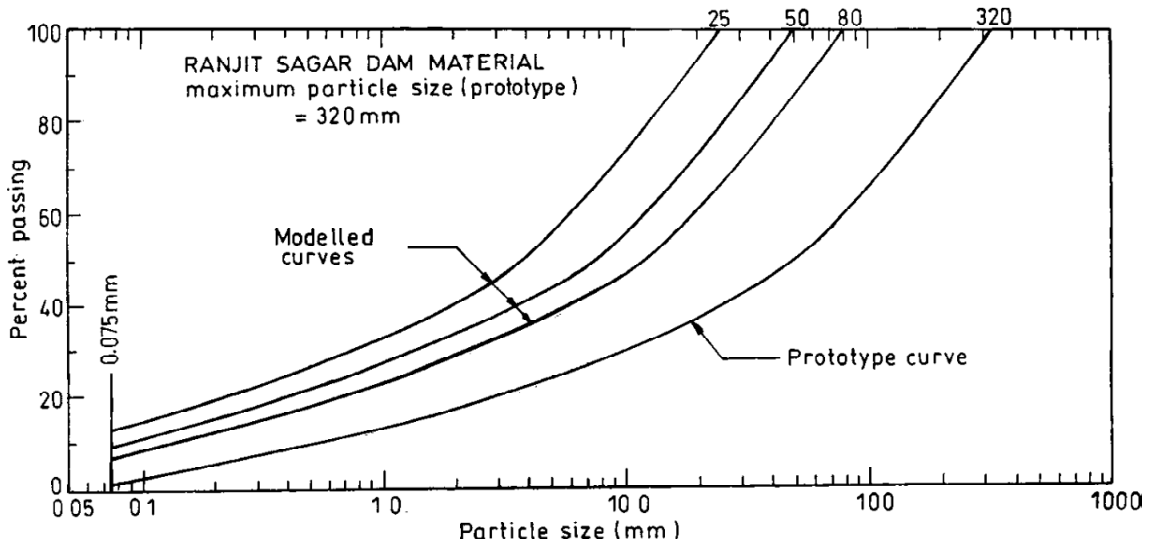


Figure 2.4: Ranjit Sagar Dam field (prototype) and model gradations (Varadarajan et al. 2003).

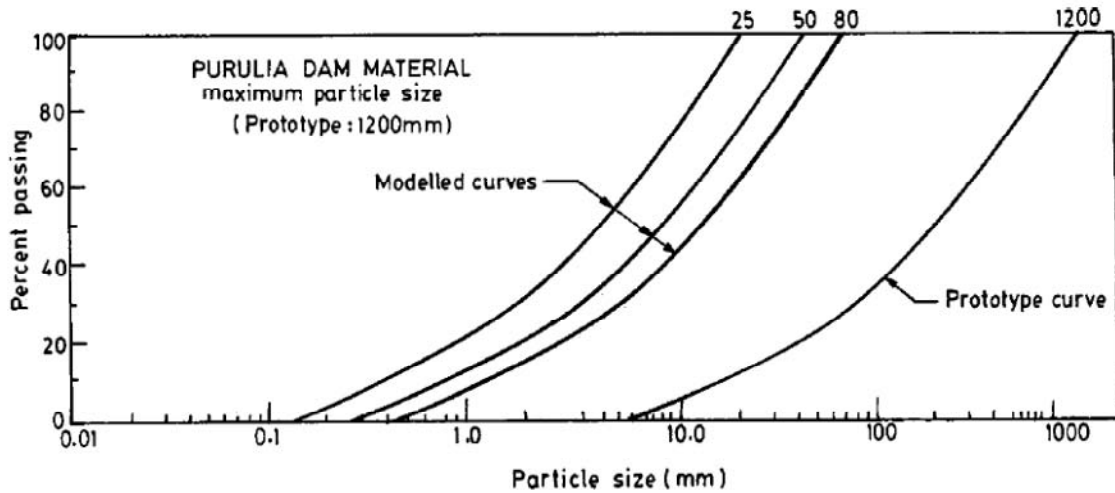


Figure 2.5: Purulia Dam field (prototype) and model gradations (Varadarajan et al. 2003).

Research presented by Lowe (1964), Marachi (1969) and Varadarajan et al. (2003) indicate that a common base for the minimum sieve size for modeling field gradations based on the parallel gradation technique is the #200 sieve (0.075-mm nominal particle diameter). The smallest sieve is more than likely based upon feasibility of dry-sieving fine material over very fine sieves (smaller than the #200 sieve). The assumptions made by Marachi (1969) as to the consistency of shape, mineralogical composition and strength of particles throughout the range of particle sizes is critical to the applicability of the parallel gradation technique but also raises questions as far as the effect of increasing fines content with decreasing maximum particle size of model gradations. As in the case of the material studied by Varadarajan et al (2003), the modeled gradation for the Ranjit Sagar Dam with the smallest maximum particle size increased in fines content by about 15%. Further research is needed on the effect of modeling gradations using the parallel gradation technique when the resulting gradation is associated with a significant increase in fines content as compared to the original field gradation.

Based on the literature presented above, the parallel gradation technique appears to be the most accurate method for the creation of model gradations for laboratory testing. Following the principles of similitude presented by Fumagalli (1970) and placing much emphasis on matching the particle shape, mineralogy and grain size distribution for all scaled fractions might ensure the most accurate and repeatable laboratory test results when characterizing the mechanical behavior of rockfill geomaterials. Other research studies have included the use of the parallel gradation technique such as the investigation by Sevi (2008) where the physical modeling of railway ballast under the cyclical triaxial

framework was used. As suggested by Sevi (2008), the present study focuses on the use of the parallel gradation technique to model gradations for testing in a slightly smaller (70-mm diameter) triaxial apparatus.

### 2.2.2 Specimen Preparation

Soil fabric is defined by Lambe and Whitman (1969) as the arrangement of particles and voids within a soil element. Mitchell and Soga (2005) further describe soil fabric as the arrangement of particles, particle groups, and pore spaces in soil. Previous research has shown that soil fabric significantly affects the mechanical response of soils in shear strength testing (Oda 1972, Vaid et al. 1999, Salgado et al. 2000, Yimsiri and Soga 2010). The fabric of a soil element has been shown, through experimental evidence, to be a function of the specimen preparation technique. The literature references several techniques, including a combination of techniques, for fully disturbed reconstitution of granular geomaterials in the laboratory. As presented by Frost (2003), reconstitution techniques are categorized according to: (1) water content of the soil (dry, moist, wet), (2) medium through which the soil is placed (air or water) and (3) method of placement (pouring, funneling, etc.). The water content of the soil to be reconstituted generally is determined by the method of placement in the field. After placement of the material, the required density of the material can be obtained through a variety of means including tamping, tapping, kneading and vibrating. Use of any of the above mentioned techniques, or a combination thereof, should replicate, as near and uniformly as possible, the fabric of the material in the field.

Previous research (Oda 1972, Ladd 1978, Chang et al. 2011) has shown that specimen reconstitution can lead to fabric anisotropy within a soil specimen. These heterogeneities can significantly affect the mechanical behavior and compressibility of test specimens (Yamamuro et al. 2008, Yimsiri et al 2010). Particularly in the case of well-graded materials and/or soil mixtures, water pluviation leads to large amounts of segregation of particle sizes and lack of  $D_R$  and fabric uniformities in specimen reconstitution (Ladd 1978). This observation is expected with application of Stoke's Law to calculate the settling time of a given particle size. In turn, particle segregation can lead to preferential shear bands and/or unrealistic observations of mechanical behavior for a given material. Especially in the case of granular materials containing fines (a.k.a. soil mixtures and/or transitional soils), particle segregation causes changes in mechanical behavior particularly through fabric effects. Salgado et al. (2000) describes soil fabric as either floating or non-floating in regard to the orientation and location of fines throughout the specimen. A floating fabric is a fabric in which coarser particles are predominantly separated by the fines present in the specimen, whereas a non-floating fabric represents a soil element with fines where the coarse particles are, in essence, in contact with each other with the fines filling all or part of the remaining voids (Carraro 2004). In specimens containing large amounts of fines (typically more than 25 – 30%), a floating fabric is expected. On the contrary, specimens containing less than 25 – 30% fines generally have a non-floating fabric (Carraro 2004). Wood et al. (2008) used five different reconstitution techniques on silty sand to analyze their effect on particle segregation. The five methods were tapped funnel deposition, water sedimentation, slurry deposition, mixed dry deposition and air pluviation. Out of the five methods,

mixed dry deposition resulted in the most homogeneous specimens. Mixed dry deposition is performed by placing material in a tube, thoroughly mixing the tube by slowly inverting the specimen (for about 1 hour), placing the tube in a split mold and carefully removing the tube. The fabric effects greatly influence the micromechanical shear characteristics of soils, and if reconstituted fabrics vary significantly between the field and the laboratory, unrealistic mechanical behaviors will be observed (Wood et al. 2008).

Other research studies (Oda 1972, Yamamuro et al. 2008) attempted to study the effect of various reconstitution techniques on soil fabric by injecting resin into specimens prepared by different techniques. Oda (1972) prepared specimens by pouring oven dried soil into a mold and subsequently compacting the soil by tapping the side of the reconstitution mold or kneading (plunging a rod into the soil repetitiously). Injecting resin into the reconstituted specimen allowed for the examination of the soil fabric created by each reconstitution technique. Mechanical behavioral characteristics were then observed by performing drained triaxial compression tests on samples reconstituted with each technique. Yamamuro et al. (2008) prepared specimens using water pluviation and dry funnel deposition. Both studies focused on not only the particle orientation (defined as the orientation of the longest and shortest axis for non-spherical particles) but also the inter-particle contact orientation. Oda (1972) proposed that a homogenous fabric should, conceptually speaking, comprise of similar particle orientations and particle coordination throughout. Results of Oda's study reveal that particle shape, specifically spherical versus nonspherical shapes, drastically affects the level of fabric anisotropy through both

the tapping and kneading methods. Specimens with spherical particles were shown to exhibit an isotropic fabric when using the tapping method, whereas the fabric became anisotropic in the case of kneading. Nonspherical particles exhibited anisotropic fabric due to nonuniform particle orientation throughout the specimen. Yamamuro et al. (2008) showed that stability of the soil fabric depends on the soil contacts and defined a stable contact as contact between two large particles with smaller (non plastic silt) particles filling the voids. Non-stable contacts are defined as contacts between large and small particles or voids, such that two large particles separated by a smaller particle, is unstable. During undrained triaxial shear, unstable fabrics caused temporary phase transformation (liquefaction) of the soil until a stable fabric is formed. Stable fabrics did not liquefy. Analyzing the effect of specimen preparation using water pluviation and dry funnel deposition revealed that water pluviation resulted in a more stable fabric where dry funnel deposition yielded a less stable fabric. In some cases, liquefaction occurred during undrained loading of the dry funnel deposition specimens. These results suggest particle segregation is occurring during water pluviation causing a nonuniform distribution of small silt sized particles and allowing for the larger sand sized particles to congregate and create a more stable fabric with an increased number of large particle – large particle contacts than that of dry funnel deposition where the fines are more uniformly distributed throughout the specimen.

In the case of wet, dry or moist tamping in lifts, density anisotropy can occur such that the lower portion of the specimen is denser than the upper portion because the compaction of each overlying layer resulted in further densification of the underlying

layer(s). Ladd (1978) proposed the under-compaction technique to yield specimens with a more uniform density profile throughout the specimen. Generally, specimen homogeneity as far as grain size distribution and density can be achieved at higher levels of accuracy, with respect to sample density, by reconstituting specimens in lifts. Typically, the number of required lifts will increase as the required dry unit weight increases. The maximum layer thickness should not exceed 25 mm for specimens with a maximum particle size smaller than 102 mm. The recommended lift thickness is 12 mm (Ladd 1978).

Another issue that arises with specimen preparation is the method of placement. As a resource regarding specimen preparation and homogeneity, ASTM D 4254 has several methods pertaining to the minimum index density and the maximum void ratio,  $e_{max}$ , which can be used qualitatively for sample reconstitution. Reconstitution of soil specimens should be performed without bias in the following areas: the location of placement, the potential energy associated with placement, and the material to be placed. Location of placement refers to the point of deposition and should be evenly varied around the cross-sectional area of the specimen. Deposition in one location, such as the center or a specific side should be avoided. Potential energy of placement refers to, for example, the height of deposition during funnel pluviation. A constant height should be maintained between the funnel and the sample throughout the deposition process such that the funnel is raised while the specimen is deposited within a mold. The material to be placed should be thoroughly mixed and homogeneous as possible without preferential placement of either coarse or fine particles. When placement of material is manual and

incremental, such as Method A in ASTM D 4254, care should be taken to avoid placement in a concentrated location within the specimen and to maintain a constant height at which the material is deposited. Method “B”, a more repeatable method similar to the dry funnel deposition method used by Wood et al. (2000) and Yamamuro et al. (2008), calls for the use of a rigid, thin-walled tube that is filled with soil in a manner that is unbiased in reference to grain size distribution throughout. The tube is filled and subsequently lifted promptly, allowing the material to be deposited in a uniform, random manor. The thin-walled tube deposition technique is believed to provide the most uniform particle arrangement based on the data presented by Wood et al. (2000) and Yamamuro et al. (2008).

### 2.2.3 Dilatancy and Critical State

Since the 18<sup>th</sup> century, the Mohr-Coulomb framework has been widely used to describe the shear characteristics of soil by way of two experimental parameters,  $c$  and  $\phi$ , which represent the apparent cohesion and the internal angle of friction, respectively. The Mohr-Coulomb framework assumes a homogeneous mass with constant mechanical properties and is helpful in regard to earth pressure theory, but the framework lacks the fundamental integration of the inter-particle mechanics that truly govern soil behavior. A more rigorous approach in modeling geomaterials includes taking particle interaction into account by introducing the phenomenon of dilatancy. The concept of dilatancy was first proposed by Reynolds (1885) who observed the effect of density on the volumetric response of sands during shear. Under the Mohr-Coulomb framework, the measured shear strength,  $\tau$ , is purely attributed to certain mechanical properties within a

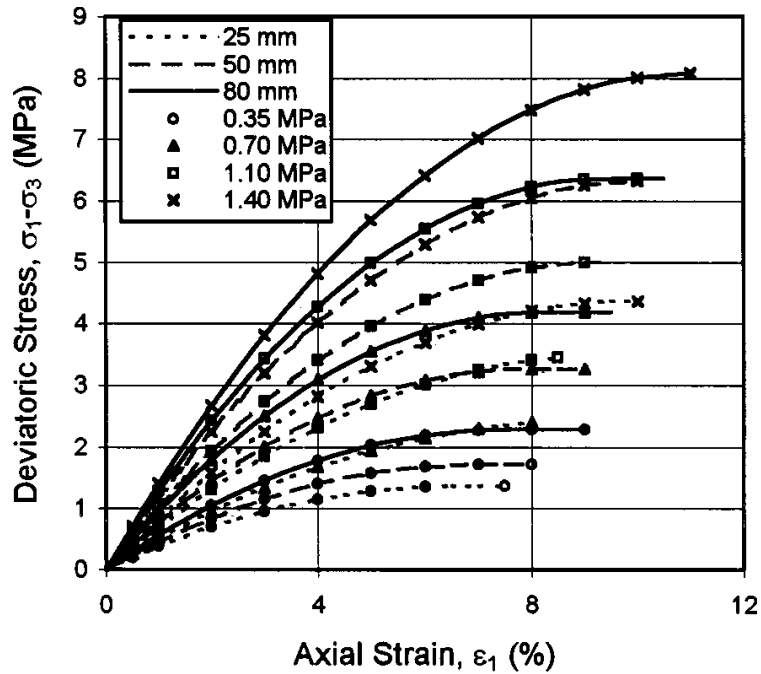
geomaterial, which is assumed as a homogeneous mass, neglecting the effects of inter-particle interactions. The introduction of dilatancy reveals that the Mohr-Coulomb framework is fundamentally incorrect for particulate geomaterials and shear strength is strongly related to inter-particle interactions. Schofield and Wroth (1968) describe a critical state at which geomaterials subjected to shear will develop constant shear stress at constant volume and constant mean effective stress and fabric upon further loading. Constant volume is only achieved once dilatancy has ceased to exist so that the mobilized shear stresses are purely due to friction. Following this approach, loose sands will contract during drained shear until critical state is reached. Conversely, dense sands will dilate during drained shear to reach critical state. Dilation during shearing complements the frictional components of the shearing resistance and results in mobilization of a peak shear stress before critical state is reached. As such, the soil state, with respect to density (hereon referred to as relative density,  $D_R$ ) and mean effective stress,  $p' = (\sigma'_1 + 2\sigma'_3)/3$ , are the primary factors affecting dilation and are the main factors contributing to the curvature of the failure envelope when plotted in normal versus shear stress space.

Numerous research studies have attempted to observe and model the mechanical behavior of rockfill geomaterials (Holtz & Gibbs 1956, Marachi 1969, Marsal 1973, Lee 1992, Bolton et al. 1993, Indraratna et al. 1998, and others). Only during the latter half of the 20<sup>th</sup> century have researchers acknowledged the significant effect of soil state on said mechanical behavior (Marachi 1969, Leps 1970, Marsal 1973, Lee 1992, Indraratna et al. 1998, Indraratna 2002). Leps (1970) provided an extensive literature review of shear strength testing for rockfill geomaterials, predominantly in large-scale triaxial

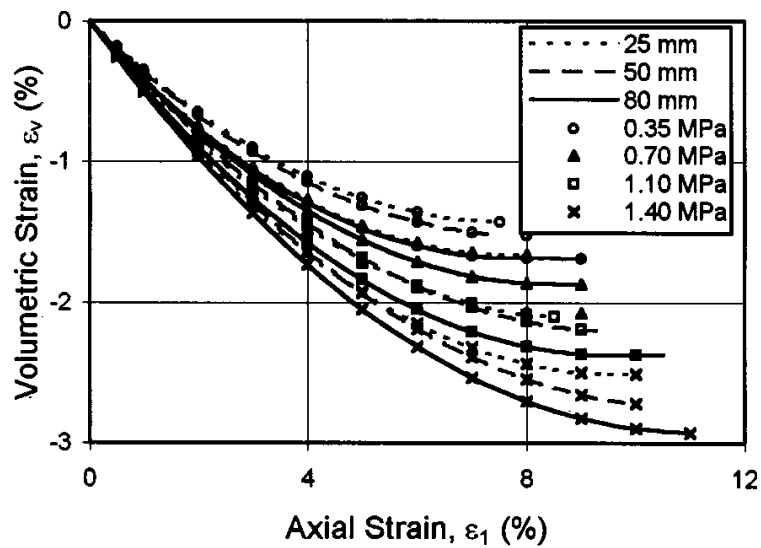
compression with specimens with maximum particle sizes ranging from 150 – 1130 mm and 38 – 203 mm, respectively. Although a vast amount of data was compiled, Leps acknowledged shortcomings of the research relating to  $D_R$ , particle strength and shape, and effective normal stress,  $\sigma'_{N}$ , on the shear plane at failure was presented. Attempting to show the effect of  $\sigma'_{N}$ , Leps proposed a linear dependence of  $\phi_p$  with respect to the logarithm of  $\sigma'_{N}$ , such that  $\phi_p$  decreases as  $\sigma'_{N}$  increases. An upper and lower bound was presented for the compilation of data relating to “strong” and “weak” rockfill geomaterials corresponding to the sensitivity  $\phi_p$  to  $p'$ .

A more rigorous approach to define the shear characteristics of granular materials was presented by Bolton (1986) in which a delineation between the peak friction angle,  $\phi_p$ , and the critical state friction angle,  $\phi_c$ , by the taking into account the angle of dilation,  $\psi$ , such that  $\phi_c = \phi_p - \psi$ .  $\phi_c$  is supposedly an intrinsic (unchanging) parameter for any geomaterial with strong grains and will be discussed further in the next paragraph. Fundamentally,  $\phi_p$  is related to the peak mean effective stress,  $p'_p$ , due to the dependence on the mobilized  $\psi$  with respect to  $p'_p$ . The higher  $p'_p$ , the more dilatancy is suppressed and the measured  $\phi_p$  approaches the value of  $\phi_c$  with increasing  $p'$ . Density is also an influential factor and application of upper and lower bounds with respect to  $D_R$  can be made (the upper bound relating to a  $D_R = 100\%$  and the lower bound relating to  $D_R = 0\%$ ). Fundamental understanding of the inter-particle relationships and the effects of soil state for geomaterials is crucial to understanding their mechanical behavior.

Similar to the discussion in section 2.2.1.4, particle shape can play a significant role in achieving critical state in laboratory tests. Research conducted by Varadarajan et al. (2003) on material from the Ranjit Sagar Dam and Purulia Dam, discussed previously, indicate that critical state is achieved at smaller axial strains for rounded particles and larger axial strains for angular particles. Based on the definition of critical state presented by Schofield and Wroth (1968), that is constant stress and constant volume upon further deformation or triaxial shear strain of the material, stress-strain behavior of the material can be analyzed to determine if critical state has been achieved. Figures 2.6 and 2.7 show the stress-strain and corresponding volumetric strain response for the Ranjit Sagar Dam material and Purulia Dam material, respectively. The results show the rounded particles of the Ranjit Sagar Dam material approaching constant deviatoric stress at a constant volume at axial strains of about 8-11%. Conversely, the angular particles of the Purulia Dam material show the material approaching a “constant” stress but constant volume is far from being reached due to the highly dilative material. Although a more definitive analysis could be performed if data presented by Varadarajan et al. (2003) was extended further, the results of the present study agree with the results published by Varadarajan et al. (2003) indicating angular particles (such as the *MWR* tested in the present study) require axial strains far greater than 10% to reach critical state.

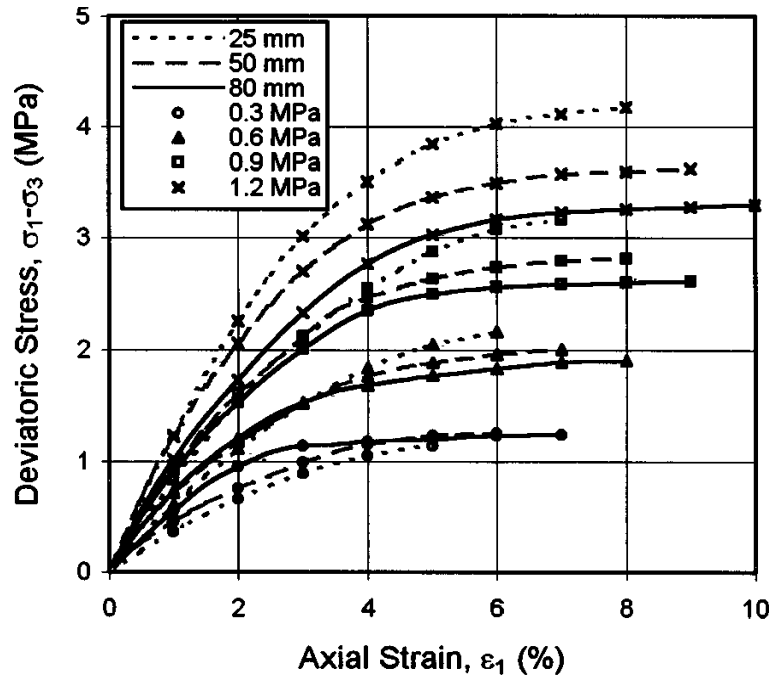


(a) Stress-Strain Behavior

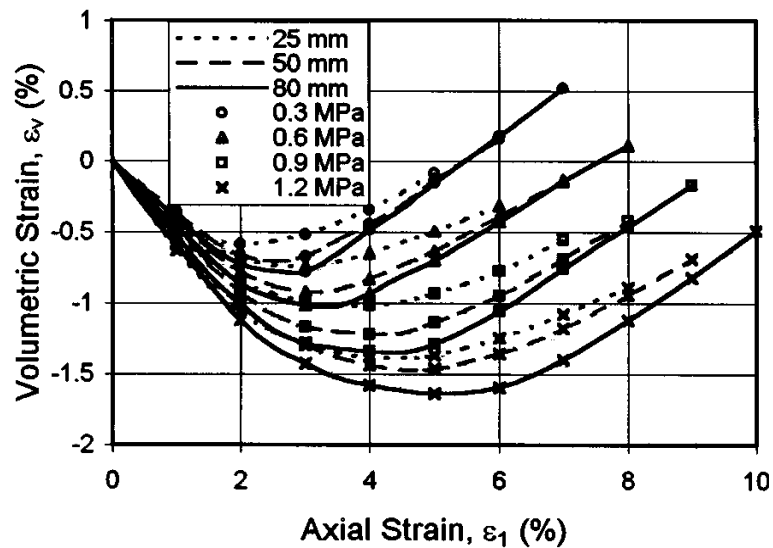


(b) Volume Change Behavior

Figure 2.6: (a) Stress-strain and (b) volumetric strain results from the Ranjit Sagar Dam material (rounded/subrounded particles) (Varadarajan et al. 2003).



**(a) Stress-Strain Behavior**



**(b) Volume Change Behavior**

Figure 2.7: (a) Stress-strain and (b) volumetric strain results from the Purulia Dam material (angular particles) (Varadarajan et al. 2003).

The critical state of geomaterials is considered intrinsic and is related to the natural characteristics of the geomaterial. Provided that these natural characteristics remain unchanged, critical state parameters will remain constant for the life of the geomaterials

or the structure constructed of said geomaterials. Schofield and Wroth (1968) describe characteristics influencing the critical state of geomaterials as grain size distribution, mineralogy, and particle shape. A thorough and detailed discussion on critical state soil mechanics can be found in Schofield and Wroth (1968) and Muir-Wood (1990).

#### 2.2.4 Particle Breakage

The shear strength of geomaterials has been attributed to inter-particle friction and interlocking changes (dilation) required for shearing to occur. Taylor (1948) proposed that shearing resistance is a function of work dissipation caused by inter-particle friction and volumetric changes within a soil element sheared under plane strain conditions:

$$Tdx - Ndy = \mu Ndx \quad (2.2)$$

where:  $dx$  and  $dy$  are displacements in plane strain conditions and  $T$  and  $N$  are shear and normal forces, respectively. Rowe (1962) broadened the work by Taylor by developing a stress-dilatancy relationship which relates inter-particle friction and volumetric changes to  $\phi_c$  and dilatancy in triaxial conditions:

$$\frac{\sigma_1'}{\sigma_3'} = \tan^2 \left( 45 + \frac{\phi_c}{2} \right) \left( 1 - \frac{d\varepsilon_p}{d\varepsilon_1} \right) \quad (2.3)$$

where:  $\varepsilon_p$  and  $\varepsilon_1$  are the volumetric and major principal strains, respectively. At a certain stress level, Rowe's stress-dilatancy relationship becomes invalid if particle breakage takes place (Tarantino and Hyde 2005). Due to the irrecoverable energy dissipation caused by particle breakage, particle breakage may also play a significant role in the mechanical shearing response of geomaterials containing crushable grains and should be

rigorously evaluated in order to thoroughly characterize the mechanical response of such materials during shear.

Methods of analyzing particle breakage in the literature are typically of two types: (1) quantification of particle breakage, and (2) incorporation of particle breakage into a conceptual framework. To quantify particle breakage, Marsal (1972) presented a term known as the breakage factor,  $\beta_g$ . The breakage factor represents the percentage of particles, by weight, that has undergone particle breakage and is defined as the sum of the increased weight retained on a given sieve size. Further investigation by Marsal suggests that particle breakage increases with increasing effective stress, increasing particle uniformity, increasing particle angularity, decreasing initial density, and decreasing particle strength.

Hardin (1985) quantified particle breakage in terms of total breakage. In an attempt to quantify particle breakage, total breakage is defined as the area between grain size distribution curves before and after shear. This incorporates the total change in grain size distribution relative to the initial grain size distribution curve instead of summing several differences at specific grain size distributions as the Marsal approach suggests. The investigation by Hardin consisted of analyzing data from 31 different geomaterials with varying particle shape, void ratios and particle breakage. The results of the study indicate increasing total particle breakage with: increasing particle size, increasing initial void ratio, decreasing particle strength, more uniform particle-size distributions.

Another approach to quantifying particle breakage is presented by Miura and O-Hara (1979) where breakage is defined in terms of a change in specific surface area, defined as the surface area per unit volume of soil solids. Assuming the particles are spherical in shape, the surface area can be estimated by the nominal diameter of each sieve size. In the case where particles are not spheres, an underestimate of the actual surface area will result, but because the main objective is to obtain *changes* in specific surface area, errors associated with the spherical particle assumption will not have significant effects (Ueng and Chen 2000). Ueng and Chen developed Rowe's stress-dilatancy equation to separate  $\phi_p$  into three components: (1) friction, (2) dilatancy, and (3) particle breakage. By neglecting the effect of dilatancy and particle breakage, the basic or critical state friction angle,  $\phi_c$ , is calculated. Including the effect of particle breakage but still neglecting dilation,  $\phi_{fb}$  can be calculated. The difference between  $\phi_c$  and  $\phi_{fb}$  (i.e.,  $\phi_c - \phi_{fb}$ ) allows the effect of particle breakage on the measured angle of friction to be expressed as a portion of the total measured friction angle. Ueng and Chen tested three different materials, Fulung sand, Tamsui river sand, and a dense decomposed granite. The two sand materials were tested at  $D_R$  values of 50% and 75%, whereas the granite was tested at an unknown relative density. Results indicate that particle breakage effects increase with increasing  $p'$  and decreasing particle strength.

Following a similar approach to Ueng and Chen (2000), Indraratna and Salim (2002) used the difference between  $\phi_f$  and  $\phi_{fb}$  to quantify particle breakage effects. However, their study used the approach developed by Marsal (1972) of accounting for particle breakage using a breakage factor,  $B_g$ . Through an intensive triaxial testing program in

which particle breakage was measured at various levels of axial strain,  $\varepsilon_a$  ( $\varepsilon_a = \varepsilon_1$  in triaxial compression testing), and  $p'$  at a constant  $D_R$ . With  $E_B$  representing the energy consumption due to particle breakage, a power relationship between the rate of energy consumption due to particle breakage,  $(dE_B/d\varepsilon_1)_f$ , and the rate of particle breakage,  $(dB_g/d\varepsilon_1)_f$ , was developed with empirical constants  $a$  and  $b$ :

$$\left(\frac{dE_B}{d\varepsilon_1}\right)_f = a \left[\left(\frac{dB_g}{d\varepsilon_1}\right)_f\right]^b \quad (2.4)$$

Results of the study demonstrate that particle breakage increases with increasing axial strain and increasing effective confining stress while the rate of particle breakage decreases with axial strain but increases with effective confining stress.

#### 2.2.4.1 Fractal Dimension

McDowell et al. (1996) described particle breakage statistically with the main factors affecting particle breakage identified as: applied macroscopic (specimen scale) stress, particle size and coordination number (the number of inter-particle contacts for a given particle). Increasing macroscopic stress increases the likelihood of particle breakage due to finite particle strength. Likelihood of particle breakage increases with increasing particle size due to the higher probability of weak planes or micro-fractures existing within a given particle. Microscopic stress distribution is defined as the stress distribution over a given particle. Microscopic stress is a function of applied macroscopic stress and coordination number of the particle. As the coordination number increases for a given particle, the microscopic stress distribution increases (becomes less concentrated), thus decreasing the likelihood of particle breakage.

Turcotte (1986) proposed an equal likelihood of particle breakage in a given matrix once self-similarity is achieved within the matrix. Self-similar media represent materials that have a similar shape or distribution as a whole compared to the parts that make up the material. Self-similar geometries are known as fractal geometries (Mandelbrot 1982). Following the work from Turcotte (1986), the particle-size distribution of a granular media was characterized by the fractal dimension,  $D$ . A fractal is a power law relationship between the number and size of geometries and the fractal dimension represents the fragility, or the susceptibility to fracture, of a given material (Turcotte 1986). The power law relationship between number and size of particles is represented by:

$$N(L > d) = A \cdot d^{-D} \quad (2.5)$$

where:  $N(L > d)$  represents the number of particles of size  $L$  greater than  $d$ ,  $A$  is a constant of proportionality and  $D$  is the fractal dimension. Assuming particle breakage evolves a grain size distribution into a fractal geometry, McDowell et al. (1996) modified the Granta Gravel work equation from Schofield and Wroth (1968) to incorporate the irrecoverable energy dissipation due to particle breakage:

$$q \delta \varepsilon_q^p + p' \delta \varepsilon_p^p = M p' \delta \varepsilon_q^p + \frac{\Gamma dS}{V_s (1 + e)} \quad (2.6)$$

where:  $q$  is the deviator stress,  $p'$  is the mean effective stress,  $\delta \varepsilon_q^p$  is the irrecoverable plastic triaxial shear strain ( $\delta \varepsilon_q = \varepsilon_a - \frac{\varepsilon_p}{3}$ ),  $\delta \varepsilon_p^p$  is the irrecoverable plastic volumetric strain,  $M$  is the slope of the critical state failure envelope in  $p'$ - $q$  space,  $\Gamma$  is the surface free energy of the material,  $dS$  is the change in surface area in the volume of solids,  $V_s$ ,

and  $e$  is the void ratio of the soil. Experimental data from Tarantino and Hyde (2005) corroborates the modified work equation presented by McDowell et al. (1996) by direct shear testing on crushable carbonaceous Dog's Bay sand. Results show that particle crushing evolves the initial grain size distribution into a constant fractal geometry defined by the fractal dimension  $D$  at high vertical effective stresses ( $\sigma'_v > 1000$  kPa). Tarantino and Hyde (2005) also show that the "apparent" critical state friction angle measured at constant volume is comprised of both frictional and elastic components (the energy associated with particle breakage) where the true critical state friction angle is comprised of purely frictional components. Using the modified work equation, the true critical state friction angle can be calculated provided that the rate of particle crushing, normalized with respect to the normal force on the shear plane, approaches zero. In order to measure the normalized rate of particle breakage tests must be terminated at specific strain levels and requires the use of multiple tests for just one combination of  $p'$  and  $D_R$ . However, the stress normalized rate of particle crushing approaches zero at a constant, or stable, fractal dimension. The stable fractal dimension is considered an intrinsic soil parameter and, once achieved, the true critical state friction angle has been mobilized and can be calculated assuming that the stress normalized rate of particle breakage is zero.

### 2.3 Summary of Literature Review

A summary of the thorough literature review presented in this chapter on Triaxial Testing is as follows:

Scaling Techniques:

- (1) Similarity between field scale materials and materials scaled down for laboratory testing purposes is of primary concern for accurate estimations of mechanical response in field scale applications.
- (2) The parallel gradation technique has been shown to be the most accurate specimen size reduction technique available.

#### Specimen Preparation:

- (1) Specimen reconstitution techniques have shown to affect initial soil fabric, a state variable shown to significantly affect the mechanical response of geomaterials during laboratory testing.
- (2) A method of reconstitution that is repeatable and mimics, as closely as possible, the field placing technique is of utmost importance.
- (3) A method of reconstitution using a thin-walled, rigid tube to deposit the test material is the most applicable method of reconstitution for triaxial test specimens scaled-down from larger collected field samples.

#### Dilatancy and Critical State:

- (1) Separating the effects of dilatancy and friction in data analysis provides a more rigorous and systematic approach in describing the mechanical behavior of geomaterials at any specimen state.

#### Particle Breakage and Fractal Dimension:

- (1) Particle breakage dissipates irrecoverable energy during loading that was not previously accounted for in the original work equation presented by Taylor (1948) and subsequently Rowe's stress-dilatancy relationship (1962).

- (2) Particle breakage is affected by soil state ( $p'$  and  $D_R$ ), particle shape, particle strength, particle size and uniformity of particle-size distribution.
- (3) Dilatancy can be significantly affected by particle breakage, which suppresses dilatancy at high levels of  $p'$  and low levels of  $D_R$ .
- (4) McDowell et al. (1996) introduced an additional term to the work equation presented by Taylor (1948) to account for energy dissipation due to particle breakage.

## CHAPTER 3: CONCEPTUAL FRAMEWORK

As discussed in the introductory chapter, the main focus of this investigation is to systematically study the effect of particle size and scaling techniques on the mechanical behavior of *MWR* in the laboratory. Critical state soil mechanics was used as a basis in this study to characterize the mechanical response of two types of *MWR* (weathered and unweathered) under monotonic axisymmetric compression. Factors affecting the mechanical behavior can be fundamentally separated into state and intrinsic variables, which are discussed in this chapter. Intrinsic parameters, such as  $\phi_c$ ,  $Q$ ,  $R$  and  $D$  are uniquely defined for a given material and form the beginning of any study of a material's mechanical behavior. State parameters, such as  $p'$ ,  $D_R$  and fabric, are factors that are not uniquely defined but still affect the mechanical response of the material to a great extent.

### 3.1 Background

The academic field of soil mechanics has evolved greatly between the 18<sup>th</sup> and 21<sup>st</sup> centuries. However, the contrary can be said about how industry and standards of practice have evolved to implement “new” concepts and frameworks related to soil mechanics. This section provides a background to critical state soil mechanics in contrast to the widely used and generally accepted Mohr-Coulomb framework. Most practicing geotechnical engineers in the United States have been accustomed to using the Mohr-Coulomb framework for analysis and design purposes. Although extensively used since its development, the Mohr-Coulomb framework was hypothesized by assuming a soil conglomerate to be a homogeneous mass. Failure analysis included the addition of a

shear plane upon which the mass would deform. This analysis only took into account the mechanisms of shear on the shear plane and lacked fundamental integration of the inter-particle mechanics throughout the entire soil mass that truly govern the behavior of the soil mass.

The widely used Mohr-Coulomb framework describes the shear strength of soil through the expression:

$$\tau = c' + \sigma' \tan(\phi') \quad (3.1)$$

where:  $\tau$  = mobilized shear strength of the soil,  $c'$  = apparent effective cohesion,  $\sigma'$  = effective normal stress on the shearing plane and  $\phi'$  = effective internal friction angle.

The apparent effective cohesion is a misinterpretation of dilatancy in noncemented soils. Dilatancy causes curvature of the failure envelope for soil elements subjected to relatively low confining stresses and in the case of dilative noncemented soils, such as *MWR*,  $c' = 0$ . Therefore, Equation 3.1 reduces to:  $c'$

$$\tau = \sigma' \tan(\phi') \quad (3.2)$$

Often internal angles of friction are delineated between total and effective stress friction angles by the use of “ ’ “ such that the effective stress internal angle of friction would be denoted as  $\phi'$ . However, since the mechanical response soil, and subsequently rockfill, is governed by effect stresses, all further discussion regarding friction angles is strictly in terms of effective stress friction angle and the “ ’ “ has been purposely neglected. For axisymmetric and plain strain testing conditions,  $\phi$  can be expressed in terms of the principal effective stresses as:

$$\sin(\phi) = \frac{\frac{\sigma'_1}{\sigma'_3} - 1}{\frac{\sigma'_1}{\sigma'_3} + 1} \quad (3.3)$$

where  $\sigma'_1$  and  $\sigma'_3$  are the major and minor principal effective stresses, respectively and  $\sigma'_1/\sigma'_3$  is known as the principal effective stress ratio or the flow number,  $N$  ( $N = \sigma'_1/\sigma'_3$ ). When  $\phi$  is determined at the maximum value of  $N$ , the calculated value is known as the peak friction angle ( $\phi_p$ ). Following the mobilization of  $\phi_p$ , depending on the state of the specimen (parameters  $p'$ ,  $D_R$  and fabric) and typically at large strains typically on the order of 20 – 30%, the value of  $\phi_p$  may reduce to what has been described in the past as the residual effective internal angle of friction ( $\phi_r$ ) (Das 2006). Additional research has shown that  $\phi_r$  actually decreases further at extremely large strains, sometimes on the order of 11,000%, especially for materials that contain crushable grains (Coop et al. 2004).

### 3.2 Critical State

In an attempt to introduce the mechanics of inter-particle interactions into a conceptual framework by which to analyze soil mechanics, Schofield and Wroth (1968) developed critical state soil mechanics. Critical state soil mechanics characterizes the mechanical behavior of geomaterials in terms of the intrinsic (unchanging) parameter, the critical state friction angle  $\phi_c$ . In terms of the mechanical response to loading, loose soil will contract until a critical state is reached such that there is no further change in shear stress, volume and mean effective stress. On the other hand, dense soil will generally contract initially and subsequently dilate as it approaches critical state. The initial contraction and

subsequent dilation causes a peak shear stress to be mobilized at the maximum dilation rate. Upon further loading, the shear stress will drop until critical state is reached (Salgado et al. 2000). Although  $\phi_c$  is an intrinsic soil parameter, dilation is highly dependent on state parameters  $p'$ ,  $D_R$  and fabric.

For practicality, a reduction of the principal effective stresses into a simpler form such that the deviatoric stress during shear is represented by:

$$q = \sigma_1' - \sigma_3' \quad (3.4)$$

and the mean effective stress is represented by:

$$p' = \frac{\sigma_1' + \sigma_2' + \sigma_3'}{3} \quad (3.5)$$

In triaxial testing the intermediate principal stress  $\sigma_2' = \sigma_3' = \sigma_r'$ : radial stress, and  $\sigma_1' = \sigma_a'$ : axial stress, such that Equation 3.5 reduces to:

$$p' = \frac{\sigma_1' + 2\sigma_3'}{3} \quad (3.6)$$

Another fundamental parameter describing the soil state is the specific volume,  $v$ .

$$v = \frac{V_T}{V_s} \quad (3.7)$$

where:  $V_T$  = total sample volume and  $V_s$  = volume of solids within the sample. From the work of Schofield and Wroth (1968), a unique graphical representation of the critical state line (*CSL*) can be depicted in  $p'$ - $q$ - $v$  space. The basis of the *CSL* is the idea that all soils have a unique failure envelope that governs the soil's behavior at sufficiently large strains such that the effect of initial soil state no longer exists. The *CSL* can also be

depicted in two dimensions in  $p'$ - $v$  and  $p'$ - $q$  space. Following this approach, the following relationships are derived:

$$q_{cs} = M \cdot p'_{cs} \quad (3.8)$$

and

$$v_{cs} = -\lambda_{cs} \cdot \ln(p'_{cs}) + \Gamma_{cs} \quad (3.9)$$

where:  $M$  = critical state parameter representing the slope of the  $CSL$  in  $p'$ - $q$  space,  $v_{cs}$  = specific volume at critical state,  $p'_{cs}$  = mean effective stress at critical state,  $\lambda_{cs}$  = critical state parameter representing the slope of the  $CSL$  in  $p'$ - $v$  space and  $\Gamma_{cs}$  = critical state parameter representing the value of  $v_{cs}$  at  $p' = 1\text{kPa}$  (Muir-Wood 1990). Because soils no longer behave as a solid at zero effective stress and for simplicity, the value of 1 was chosen as a reference stress for determining  $\Gamma_{cs}$ .  $\Gamma_{cs}$  depends on the reference units and since this study uses kPa for units of stress,  $\Gamma_{cs} = v_{cs}$  at  $p' = 1\text{kPa}$ . Equations 3.8 and 3.9 mathematically describe the  $CSL$ . Figure 3.1 is a graphical representation of the  $CSL$  in  $p'$ - $q$ - $v$  space. Projections of the  $CSL$  onto 2-d  $p'$ - $q$  space and  $\ln(p')$ - $v$  space are described mathematically by Equations 3.8 and 3.9, respectively. The slope of the  $CSL$  in  $p'$ - $q$  space is mathematically related to  $\phi_c$  by the following:

$$\sin(\phi_c) = \frac{3M}{6 + M} \quad (3.10)$$

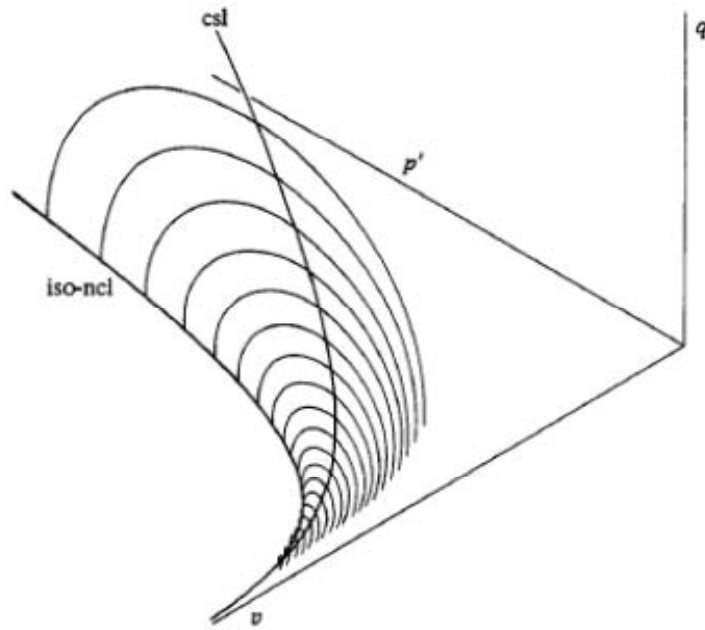


Figure 3.1: Three dimensional view of the *CSL* and normal compression line (*NCL*) in  $p'$ - $q$ - $v$  space (Muir-Wood 1990).

Under isotropic compression, normally consolidated soils follow a linear line in  $\ln(p') - v$  space, similar to the linear line in  $e - \log(p')$  space typically observed in 1-D axisymmetric compression in an oedometer consolidation test. This line is known as the isotropic normal compression line (*NCL*). Similar to the *CSL*, the *NCL* can be described mathematically by:

$$v = -\lambda \cdot \ln(p') + N \quad (3.11)$$

where:  $\lambda$  = critical state parameter representing the slope of the *NCL* in  $p'$ - $v$  space and  $N$  = critical state parameter representing the value of  $v$  at  $p' = 1 \text{ kPa}$  (Muir-Wood 1990).

At levels of  $p'$  not sufficiently elevated to make a soil element yield (i.e. values of  $p'$  less than the yield stress,  $p'_{yield}$ ) approach a unique *NCL* soil elements follow the unloading-reloading line (*URL*). Similar to the *NCL*, the *URL* can be described mathematically by:

$$v = -\kappa \cdot \ln(p') + v_{\kappa} \quad (3.12)$$

where:  $\kappa$  = critical state parameter representing the slope of the *URL* in  $\ln(p')$  -  $v$  space and  $N$  = the critical state parameter representing the value of  $v$  at  $p' = 1$  kPa (Muir-Wood 1990). The *NCL* and *URL* are depicted graphically in  $\ln(p')$ - $v$  space on Figure 3.2.

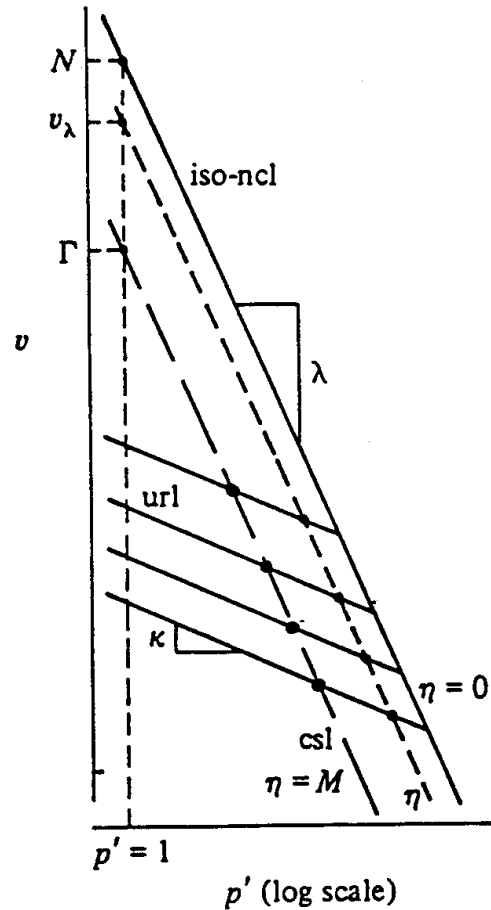


Figure 3.2: Two dimensional view of the isotropic *NCL* and *URL* in  $\ln(p')$ - $v$  space (Muir-Wood 1990).

### 3.3 Stress – Dilatancy Relationship

Rowe (1962) developed a relationship between stress and dilatancy by modifying Taylor's (1948) work equation in terms of  $\phi_c$  and a new parameter, the dilatancy angle,  $\psi$ . At critical state, the sample is at constant volume during shear (i.e. the dilatancy rate is

effectively zero) leading to the following relationship between the mobilized friction angle  $\phi$ ,  $\phi_c$  and  $\psi$ .

$$\phi = \phi_c + \psi \quad (3.13)$$

Substituting Equation 3.13 into Equation 3.2 results in the following expression for the mobilized shear strength:

$$\tau = \sigma' \tan(\phi_c + \psi) \quad (3.14)$$

Rowe's (1962) stress-dilatancy relationship is based on the hypothesis that a minimum energy ratio is achieved at failure. The work done by Rowe (1962) was validated by De Josselin de Jong (1976). The resulting stress-dilatancy theory can be expressed as:

$$N = M \cdot N_c \quad (3.15)$$

where:  $N_c$  = flow number (principal stress ratio) at critical state and  $M$  = dilatancy number =  $1 - d\varepsilon_p/d\varepsilon_1$ , where  $d\varepsilon_p$  = volumetric strain increment and  $d\varepsilon_1$  = major principal strain increment (axial strain increment in triaxial tests).  $N$ ,  $N_c$  and  $M$  can be expressed in terms of  $\phi$ ,  $\phi_c$  and  $\psi$  by:

$$N = \frac{1 + \sin \phi}{1 - \sin \phi} = \tan^2 \left( 45 + \frac{\phi}{2} \right) \quad (3.16)$$

$$N_c = \frac{1 + \sin \phi_c}{1 - \sin \phi_c} = \tan^2 \left( 45 + \frac{\phi_c}{2} \right) \quad (3.17)$$

$$M = \frac{1 + \sin \psi}{1 - \sin \psi} = \tan^2 \left( 45 + \frac{\psi}{2} \right) \quad (3.18)$$

The dilatancy angle,  $\psi$ , approaches a maximum in non crushable aggregates at the maximum rate of dilatancy (Schofield and Wroth 1968) and can be expressed as:

$$\sin \psi = -\frac{\frac{d\varepsilon_1}{kd\varepsilon_3} + 1}{\frac{d\varepsilon_1}{kd\varepsilon_3} - 1} \quad (3.19)$$

where:  $d\varepsilon_1$  and  $d\varepsilon_3$  = major and minor principal strain increments and  $k = 1$  for plane strain conditions or 2 for axisymmetric (triaxial) conditions.

Bolton (1986) observed the stress-dilatancy characteristics of 17 different sands under both plain strain and axisymmetric conditions. Comparing Equation 3.13 to Rowe's plain strain stress-dilatancy relationship,

$$\frac{\sigma'_1}{\sigma'_3} = \left[ \frac{\sigma'_1}{\sigma'_3} \right]_c \left( 1 - \frac{d\varepsilon_p}{d\varepsilon_1} \right) \quad (3.20)$$

where:  $(\sigma'_1/\sigma'_3)_c$  is the principal stress ratio at critical state. Bolton (1986) found that Equation 3.13 over estimates  $\phi$  by about 20% and thus, the following relationship can be formed:

$$\phi = \phi_c + 0.8\psi \quad (3.21)$$

Bolton (1986) expanded on the stress-dilatancy relationship to relate  $\phi_p$  to  $\phi_c$  by introducing a term known as the relative dilatancy index,  $I_R$ , such that:

$$\phi_p = \phi_c + A \cdot I_R \quad (3.22)$$

where:  $A = 3$  for axisymmetric conditions and 5 for plain strain conditions, respectively and  $I_R$  can be defined for both axisymmetric and plain strain conditions by:

$$I_R = -\frac{10}{3} \left( \frac{d\varepsilon_p}{d\varepsilon_1} \right)_{\max} \quad (3.23)$$

$I_R$  can also be defined by relative density,  $D_R$ , and mean effective stress,  $p'_p$ , by:

$$I_R = \left[ \frac{D_R}{100} \left( Q - \ln \left( \frac{100 p'_p}{p_A} \right) \right) - R \right] \quad (3.24)$$

where:  $p_A$  = reference stress (100 kPa for  $p'_p$  in units of kPa), and  $Q$  and  $R$  are fitting parameters and are considered intrinsic soil parameters that can be determined for any geomaterial. Previous research has determined  $Q$  and  $R$  for various geomaterials such as clean sands (Bolton 1986), non-plastic silty sands (Salgado et al. 2000) and transitional soils with plastic and non-plastic fines (Carraro et al. 2009).

In order to determine the dilatancy index at a given  $D_R$  and  $p'$ , Bolton proposed the following relationship for  $I_R$ :

$$I_R = \frac{D_R}{100} [Q - \ln(p')] - R \quad (3.25)$$

Because critical state is determined to be where a sample is observed to have a constant shear stress with a constant volume, the dilatancy index,  $I_R$ , equals zero. Thus at critical state,  $p' = p'_c$  and  $I_R = 0$ . By testing samples at various levels of  $D_R$  and  $p'$ , the intrinsic fitting parameters  $Q$  and  $R$  can be estimated by

$$\ln(p'_c) = Q - \frac{R}{D_R/100} \quad (3.26)$$

For clean quartz sand, Bolton (1986) found  $Q = 10$  and  $R = 1$ . Bolton (1986) also proposed the use of the above relationships, more specifically Equation 3.21, to determine upper and lower bounds of the failure envelope relating to  $\phi_p$ . The upper bound is calculated when  $D_R = 100\%$  while the lower bound (equal to  $\phi_c$ ) is calculated when  $D_R = 0\%$ .

### 3.4 Particle Breakage

Particle breakage plays a significant role in the mechanical behavior of crushable aggregates and especially coarse grained crushable aggregates such as *MWR*. With the dilatancy component of the shearing resistance decreasing with increasing  $p'$ , particle breakage also tends to suppress, if not eliminate, dilatancy during shearing of crushable geomaterials (Coop et al. 2004 and Bolton 1986). Dissipation of irrecoverable energy invalidates the classic Cam-Clay and subsequently Granta-Gravel work equations presented by Schofield and Wroth (1968). The Cam-Clay work equation is expressed as:

$$q\delta\varepsilon_q^p + p'\delta\varepsilon_p^p = Mp'\delta\varepsilon_q^p \quad (3.27)$$

The difference between the Granta-Gravel and the Cam-Clay work equations is that the Granta-Gravel work equation ignores elastic strains in the material and the Cam-Clay work equation incorporates these elastic strains. Ignoring elastic strains the Cam-Clay work equation reduces to the Granta-Gravel work equation:

$$q\delta\varepsilon_q + p'\delta\varepsilon_p = Mp'\delta\varepsilon_q \quad (3.28)$$

where:  $q$  is the deviator stress,  $p'$  is the mean effective stress,  $\delta\varepsilon_q$  is the irrecoverable plastic triaxial shear strain increment ( $\varepsilon_q = \varepsilon_a - \frac{\varepsilon_p}{3}$ ),  $\delta\varepsilon_p$  is the irrecoverable plastic volumetric strain increment, and  $M$  is the slope of the critical state failure envelope in  $p'$ - $q$  space. The left hand side of Equation 3.28 represents the plastic work done per unit volume by  $q$  and  $p'$ . The right hand side represents the work dissipated by internal friction. There is no term in Equation 3.28 to take into account the irrecoverable energy dissipation caused by particle breakage. McDowell and Bolton (1998) proposed that an

additional term be added to the right hand side to account for particle breakage. The new work equation can be presented as:

$$q\delta\varepsilon_q^p + p'\delta\varepsilon_p^p = Mp'\delta\varepsilon_q^p + \frac{\Gamma_{se}dS}{V_s(1+e)} \quad (3.29)$$

where:  $\Gamma_{se}$  is the surface free energy of the material,  $dS$  is the incremental change in surface area in the volume of solids,  $V_s$ , and  $e$  is the void ratio of the soil.

Equation 3.29 is difficult to evaluate due to the requirement of a reliable estimate of the material surface energy,  $\Gamma_{se}$ . Traditionally, the surface energy of a material has been considered a material constant (Ashby and Jones 1986). Determining the surface energy of liquids is relatively easy through a relationship between surface energy and contact angle. However, measuring the surface energy of solids does not have a satisfactory solution and generally can only be measured at a given state of the solid surface at the interface between liquid and solid phases (Shaevich 2007). This generally involves heating a material to extreme temperatures and results may not be valid at other surface states. To this day, no rigorous or systematic approach has been developed to measure the surface energy of solids at any surface state. Ashby and Jones (1986) suggested a surface energy equal to 10 J/m<sup>2</sup> for calcite and 25 J/m<sup>2</sup> for rocks. Tarantino and Hyde (2005) back calculated  $\Gamma$  from Equation 3.27 and data obtained from direct shear tests on Dogs Bay sand and found  $\Gamma$  to be equal to 19 J/m<sup>2</sup>. Their results from Tarantino and Hyde (2005) correlate well with the suggested values presented by Ashby and Jones (1986) and are of the same order of magnitude. The results are well explained when describing the strength of the materials in question such that calcite is weaker than the

carbonaceous Dogs Bay sand, which is known to be a crushable material weaker than most “rocks”. Forootan-Rad and Moavenzadeh (1968) and Friedman et al. (1972) found values of  $\Gamma$  for granite, marble and quartzite (hard metamorphic rocks) ranging from 40 – 62 J/m<sup>2</sup>. Limestone, sandstone and firebrick (material generally used to line high temperature furnaces) have values of  $\Gamma$  ranging from 9 – 49 J/m<sup>2</sup>. Measured values of  $\Gamma$  for single crystals of calcite and quartzite range from 0.23 – 1.03 J/m<sup>2</sup> (Gilman 1960, Santhanan and Gupta 1968, Brace and Walsh 1962). The lower values of measured  $\Gamma$  are attributed to boundary conditions within the material being tested, with single crystals lacking confinement along fractures and reducing the value of  $\Gamma$ . *MWR* materials tested in this study are most closely related to materials such as “rocks” (Ashby and Jones 1986), limestone and sandstone (Nakayama 1965, Perkins Bartlett 1963, Perkins and Krech 1966, Friedman et al. 1972), and sand (Tarantino and Hyde 2005). Selected published values of surface energy are presented in Table 3.1. Based on the range of data presented in Table 3.1, the range of 9 – 38 J/m<sup>2</sup> seems appropriate for use in evaluation of Equation 3.27.

Table 3.1: Range of values of measured surface free energy for certain materials.

Material	$\Gamma$ (J/m <sup>2</sup> )	Source
Calcite Crystal (Single Crystal)	0.23	Gilman (1960)
Quartz Crystal (Single Crystal)	0.41-1.03	Brace and Walsh (1962)
Carthage Limestone	38	Perkins and Bartlett (1963)
Lueders Limestone	19	Perkins and Bartlett (1963)
Indiana Limestone	42	Perkins and Bartlett (1963)
Chamotte Firebrick	30	Nakayama (1965)
High-Alumina Firebrick	49	Nakayama (1965)
Basic Firebrick	42	Nakayama (1965)
Silica Firebrick	30	Nakayama (1965)
Carthage Limestone	17	Perkins and Krech (1966)
Lueders Limestone	35	Perkins and Krech (1966)
Calcite Crystal (Single Crystal)	0.35	Santhanan and Gupta (1968)
Chelmsford Granite	45-55	Forootan-Rad and Moavenzadeh (1968)
Danby Marble	40-60	Forootan-Rad and Moavenzadeh (1968)
Lueders Limestone	9-12	Friedman et al. (1972)
Indiana Limestone	16-22	Friedman et al. (1972)
Coconino Sandstone	22-26	Friedman et al. (1972)
Tennessee Sandstone	38	Friedman et al. (1972)
Chilhowie Quartzite	49-62	Friedman et al. (1972)
Calcite	10	Ashby and Jones (1986)
Rocks	25	Ashby and Jones (1986)
Dogs Bay Sand (Carbonaceous Sand)	19	Tarantino and Hyde (2005)

A second difficulty arises when evaluating Equation 3.29 in terms of calculating the surface area, and correspondingly the incremental change in surface area of the material. Typically, the surface area is calculated by assuming perfectly spherical particles in a porous media such that the surface area can be calculated for a given particle using the average nominal particle diameter between two conjoining sieves. Due to the fact that the particles associated with *MWR* are generally non-spherical, the assumption of spherical particles is fundamentally flawed. McDowell and Bolton (1998) presented surface and volume shape factors to determine the surface area of a material with non-spherical particles.

$$S(d) = \beta_s \cdot d^2 \quad (3.30)$$

and

$$V(d) = \beta_v \cdot d^3 \quad (3.31)$$

where  $S(d)$  = surface area of particle with average diameter  $d$ ,  $\beta_s$  = surface shape factor,  $V(d)$  = volume of particle with diameter  $d$ , and  $\beta_v$  = volume shape factor. Substituting the surface area and volume of a sphere in Equations 3.30 and 3.31, one can determine  $\beta_s$  and  $\beta_v$  values for spheres as 3.14 and 0.52, respectively. The average nominal particle diameter for a specific particle size is defined as the average of the apertures of the sieve through which the particles pass and the sieve on which the particles are retained. Using Equation 3.28 and 3.29, the total surface area,  $S_i$ , of the particles retained on a sieve with aperture  $d_i$  with an average nominal particle diameter  $d_{mi}$  can be expressed as:

$$S_i = \frac{M_i}{\rho_s \cdot \beta_v \cdot d_{mi}^3} \cdot \beta_s \cdot d_{mi}^2 = \frac{\beta_{si}}{\beta_{vi}} \left( \frac{M_i}{\rho_s \cdot d_{mi}} \right) = \frac{\beta_{si}}{\beta_{vi}} S_i^* \quad (3.32)$$

where:  $M_i$  = mass retained on sieve  $i$ ,  $\rho_s$  = particle dry density,  $d_{mi}$  = average diameter of the particle retained on sieve  $d_i$  ( $d_{mi} = (d_i + d_{i-1})/2$ ), and  $S_i^*$  = is the surface area reduced by the factor  $\frac{\beta_{si}}{\beta_{vi}}$  (Tarantino and Hyde 2005). If  $\beta_s$  and  $\beta_v$  are assumed constant for all  $d_i$ ,

the total surface area of the specimen is expressed as:

$$S = \sum \frac{\beta_{si}}{\beta_{vi}} S_i^* = \frac{\beta_s}{\beta_v} \sum S_i^* \quad (3.33)$$

Tarantino and Hyde (2005) reported  $\beta_s = 5.6$  and  $\beta_v = 0.2$  for Dogs Bay sand (crushable carbonaceous sand with angular and flakey particles) with reasonable results of surface energy evaluated from Equation 3.29 (i.e. 19 J/m<sup>2</sup>, which is in the range of 9 – 38 J/m<sup>2</sup>). Marsal (1973) proposed a similar approach to quantify particle breakage by defining a particle breakage parameter,  $\beta_g$ , which represented the volume of broken/fractured

particles per unit total volume of material. Similar to the shape factors presented by McDowell and Bolton (1998), Marsal (1973) presented a shape factor to relate particle volume to the average nominal particle diameter between two adjoining sieves. Marsal (1973) also conducted a study in which angular rockfill particles retained on a range of sieves (12 – 76 mm) were tested for their surface area and volume such that a representative shape factor could be calculated. Using the data presented by Marsal (1973), the shape factors presented by McDowell and Bolton (1998) can be calculated. Average values of shape factors,  $\beta_s$  and  $\beta_v$ , calculated from Marsal’s (1973) data are 3.74 and 0.44, respectively. Although a limited sieve range was used, the  $\beta_s$  and  $\beta_v$  values used in this study are assumed to be equal to the average values of  $\beta_s$  and  $\beta_v$  calculated from data reported by Marsal (1973). This assumption has a relatively small impact on the final values of  $S$  due to the fact that Equation 3.29 is dealing with the change in surface area, not the exact surface area (Ueng and Chen 2000). Selected values of  $\beta_s$  and  $\beta_v$  are presented in Table 3.2.

Table 3.2: Range of  $\beta_s$  and  $\beta_v$  values measured for certain geomaterials.

Material	$\beta_s$	$\beta_v$	$\beta_s/\beta_v$	Reference
Angular Rockfill	3.98	0.41	9.7	Marsal 1973
Angular Rockfill	3.44	0.43	8.0	Marsal 1973
Angular Rockfill	3.60	0.44	8.1	Marsal 1973
Angular Rockfill	3.56	0.41	8.7	Marsal 1973
Angular Rockfill	3.39	0.47	7.2	Marsal 1973
Angular Rockfill	4.47	0.51	8.8	Marsal 1973
Crushed Quartz	--	--	14 - 18	Harr 1977
Dogs Bay Sand	5.60	0.20	28.0	Tarantino and Hyde 2005

### 3.4.1 Fractal Dimension

Particle breakage has long been known to affect the mechanical behavior of granular media such as rockfill and *MWR*. However, quantification of particle breakage and its effect on energy dissipation during loading has been a source of speculation (Marsal 1973, McDowell and Bolton 1998, Ueng and Chen 2000, Indraratna et al. 2002, Varadarajan et al. 2003). One portion of the particle breakage concept, however, is constant through all research studies available in the literature related to particle breakage: the crushing of particles in a granular material must be related to changes in the particle size distribution of the material (Marsal 1973, Hardin 1985, McDowell and Bolton 1998, Indraratna et al. 2002, Varadarajan et al. 2003). Incorporating a term known as the fractal dimension,  $D$ , McDowell et al. (1996) used the concept of fractals to describe particle breakage in crushable aggregates. Fractals have long been known to be a means of quantifying a variety of scale-invariant processes in nature (Mandelbrot 1982). Using a simple power-law relationship between number and size in a particle size distribution, a fractal dimension can be expressed as:

$$N(L > d) = A \cdot d^{-D} \quad (3.34)$$

where:  $N(L > d)$  = number of particles with characteristic length (diameter, etc.)  $L$  greater than  $d$ ,  $A$  = constant of proportionality and  $D$  is the fractal dimension. The dimension  $d$  is analogous to the aperture of each sieve used in pre and post particle-size analyses. Thus, for each sieve used in the particle-size analysis, the number of particles with characteristic length  $L$  greater than  $d$  (i.e.  $N(L > d)$ ) can be calculated for each sieve size and plotted with the corresponding sieve aperture ( $d$ ) on a log-log scale. The value of  $D$  is then computed by fitting a power trendline to the plotted data.

Fractal crushing of particles is a probabilistic approach in describing particle breakage such that the probability of any one particle fracturing is related to the applied macroscopic stress, size of the particle, tensile strength of the particle and the coordination number (number of inter-particle contacts) for the given particle (McDowell et al. 1996). Determination of the fractal dimension requires evaluation of the particle size distribution and reliable estimate of the shape factors presented by McDowell and Bolton (1998). By calculating the volume of material retained on a given sieve using the mass and specific gravity of solids for the material and assuming that particle shape remains relatively constant through the crushing process (i.e. constant shape factors  $\beta_s$  and  $\beta_v$ ), the fractal dimension of a material can be calculated. Research by Tarantino and Hyde (2005) has shown that a material's initial fractal dimension will evolve into a constant, or stable, fractal dimension through particle crushing/breakage. The value of  $D$  approaches a constant as the rate of particle crushing approaches zero. With the rate of particle breakage equal to zero, a true critical state friction angle is mobilized and can be calculated. Once the stable fractal dimension is obtained, evaluation of the energy dissipation due to dilatancy, particle breakage and friction can be independently evaluated. This study will evaluate particle breakage of *MWR* by measuring changes in the fractal dimension,  $D$ , during drained axisymmetric loading by evaluating  $D$  before and after each triaxial test.

### 3.4.2 Creep

Creep is defined as time-dependent volumetric strain at a constant effective stress, i.e. after all excess pore-water pressures have been dissipated (Kuhn et al. 1993). Creep in

granular materials with has been described in many research studies (Lade 1994, McDowell and Khan 2003, McDowell 2003, Karimpour and Lade 2010, Kuhn 2010). Typically, volumetric strain due to creep is proportional to the logarithm of time (McDowell and Khan 2003). Because mechanical behavior of material undergoing shear is directly related to the state of the material before shear, creep in granular materials has a direct effect on the mechanical behavior of the material. Following the procedure outlined by Fox (2011), creep was systematically taken into account by allowing the rate of volumetric strain ( $\delta\varepsilon_p/\delta t$ ) to reach a specified value of 0.05%/h before the next stage of testing was continued.

One explanation for creep in brittle granular materials is particle crushing (Karimpour and Lade 2010). Time dependent crushing of particles is attributed to particle fatigue under constant load (Karimpour and Lade 2010). Measuring particle breakage during isotropic consolidation phases would require multiple specimens for each test. After each consolidation phase, the test would be terminated to measure the amount of particle breakage that has occurred in the specimen. Then, a new but identical specimen would be reconstituted and isotropically consolidated to the next stage and the test terminated at the next level of  $p'$  to measure particle breakage. Particle breakage for shearing would be measured using another identical specimen that was isotropically consolidated to each of the previous stages, and subsequently sheared. Due to a limited amount of material, measuring particle breakage during each stage of isotropic consolidation and shearing would require the reuse of material. To ensure the quality of results, only virgin material was used during the experimental testing program of the present study and thus particle

breakage during isotropic consolidation phases of each test was not monitored. Although creep in granular geomaterials is generally attributed to particle breakage (Lade 1994, McDowell and Khan 2003, McDowell 2003, Karimpour and Lade 2010), other mechanisms may play a role in creep behavior of granular geomaterials. These mechanisms may include but are not limited to fabric anisotropy and reorientation of particles under constant stress due to localized friction failures between particles. Additional mechanisms of creep behavior in granular materials were not included in the scope of this study.

## CHAPTER 4: EXPERIMENTAL PROGRAM

A comprehensive and systematic experimental program was conducted to: (1) characterize several aspects of the mechanical behavior of the two types of *MWR* tested in this study, (2) determine the intrinsic parameters associated with the two materials and, (3) compare results of conventional-scale triaxial tests to large-scale triaxial tests. Index properties of the *MWR* were measured at this stage and conducted in the same manner for both materials. The following sections describe, in detail, the index properties measured and the experimental methods used to determine the index properties and intrinsic parameters of the *MWR* materials studied.

### 4.1 Materials

The two types of *MWR* tested in this study originate from the Goldstrike gold mine, which is located approximately 60 km northwest of Elko, Nevada. The materials were blasted from the Ordovician Vinini formation within the mine site. The Ordovician era represents the time period within the Paleozoic era approximately 488 to 444 million years ago. The Ordovician Vinini formation is primarily comprised of black and gray cherty mudstone and siltstone with planar to wavy bands with alternating dark gray siltstone beds with 1 to 5-mm-thick light gray dolomitic limestone interbeds. The thickness of the formation varies drastically due to structural thickening along low angle faults in the area (Jory 1999).

The *MWR* materials tested in this study were obtained by blasting at two different locations within the mine site at an elevation of approximately 1585 m above mean sea level. The primary difference between the two materials is the level of *in situ* weathering due to varying hydrogeologic conditions in the area and, thus, the materials will be discussed here on as weathered or unweathered. Pictures of the weathered and unweathered *MWR* tested in this study are presented on Figure 4.1. The weathered *MWR* was removed from the formation approximately 18.3 m below the original ground surface. The unweathered *MWR* was removed from the formation approximately 24.4 m below the original ground surface. The *MWR* removed from the formation is primarily used in the construction of embankment dams for tailings storage facilities associated with the Goldstrike gold mine and as pit backfill. Further information regarding the removal of the *MWR* and the locations in which the *MWR* was obtained is discussed by Fox (2011).



Figure 4.1: Picture of the (a) unweathered and (b) weathered *MWR* parallel gradation materials tested in this study.

## 4.2 Experimental Methods

Several experimental methods were used to study two types of *MWR* tested (weathered and unweathered) in this study. All methods were performed in accordance with ASTM standards, when available. A detailed description of each experimental method is presented in the following sub-sections.

### 4.2.1 Particle-Size Distribution

Field samples of both the weathered and unweathered *MWR* material were collected by Fox (2011) on March 15, 2010. Field sampling was performed by hand and shovel from rock piles placed by large earth movers at the mine site. Much care was taken to obtain a sample representative of the total volume by obtaining material from various locations within and around the rock pile. Although this method of field sampling is analogous to the scalping technique for scaling down particle sizes of collected samples, the chosen method of collection was limited to unavailability of large earth movers and the method of transport to the testing facility at Colorado State University in Fort Collins, Colorado. Subsequent analyses and testing of the collected field samples using the parallel gradation technique is intended to show the suitability of the parallel gradation technique. Results of this study will show that the techniques implemented in this study can be easily applied to actual field conditions. A more rigorous and systematic sampling program is recommended when following the experimental program and experimental techniques described here on such that the described techniques reference the actual field conditions.

Typically, the particle-size distribution of a material is determined by splitting the entire sample into a smaller sub-sample that is representative of the entire sample (ASTM D 421). However, the process of sub-sampling is associated with uncertainties and may lead to errors in analysis. The fines content (*FC*) is measured through wet washing the material over the #200 sieve (0.075-mm nominal diameter) and subsequently oven drying the material. Once dried, the material is dry-sieved over a range of sieve sizes ranging in size from gravel sizes to fine sand sizes. Further analysis on the particle-size distribution of the fines (particles passing the #200 sieve) is accomplished by performing a hydrometer analysis (ASTM D 422).

The parallel gradation technique requires the material to be sorted into its respective particle sizes retained on specified sieves such that model gradations can be built for subsequent testing. Sorting the entire collected field samples allowed for the particle-size distribution of each sample to be determined at the time of sorting. This method of determining the particle-size distribution was performed in partial accordance with ASTM D 6913, Method B. ASTM D 6913, Method B requires that the maximum particle size of the sample tested be less than or equal to 4.75 mm. The maximum particle size of the collected field samples contained particles as large as 87.5-mm nominal diameter. Although the maximum particle sizes of the *MWR* are far larger than the recommended maximum particle size as presented in ASTM D 6913, Method B, the standard was considered appropriate to determine the particle-size distribution of the materials based on the necessity to sort the material into respective particle sizes retained on specific sieves for the testing program. Modifying the method outlined in ASTM D

6913, Method B also allowed for the entire collected field sample to be used in evaluating the particle-size distribution and retention of the entire sample which would not be possible when using the methods outlined in ASTM D 421 and ASTM D 422. A hydrometer analysis (ASTM D 422) was not performed on the *MWR* material and, therefore, the limiting sieve used in the analysis was the #200 sieve (0.075-mm nominal particle diameter). The sieve set used for the particle-size analysis in this study and the study by Fox (2011) is presented in Table 4.1. The results of the particle-size distribution analyses for both *MWR* materials are presented on Figure 4.2.

Table 4.1: Sieve set used in the particle-size distribution analysis of the collected field samples.

Sieve	Aperture (mm)
3 1/2"	87.5
3"	75
2 1/2"	62.5
2"	50
1 3/4"	43.75
1 1/2"	37.5
1 1/4"	31.25
1"	25
3/4"	19
1/2"	12.5
7/16"	11.2
3/8"	9.5
1/4"	6.3
(#4)	4.75
(#8)	2.36
(#16)	1.18
(#30)	0.6
(#40)	0.425
(#50)	0.3
(#100)	0.15
(#200)	0.075
Pan	--

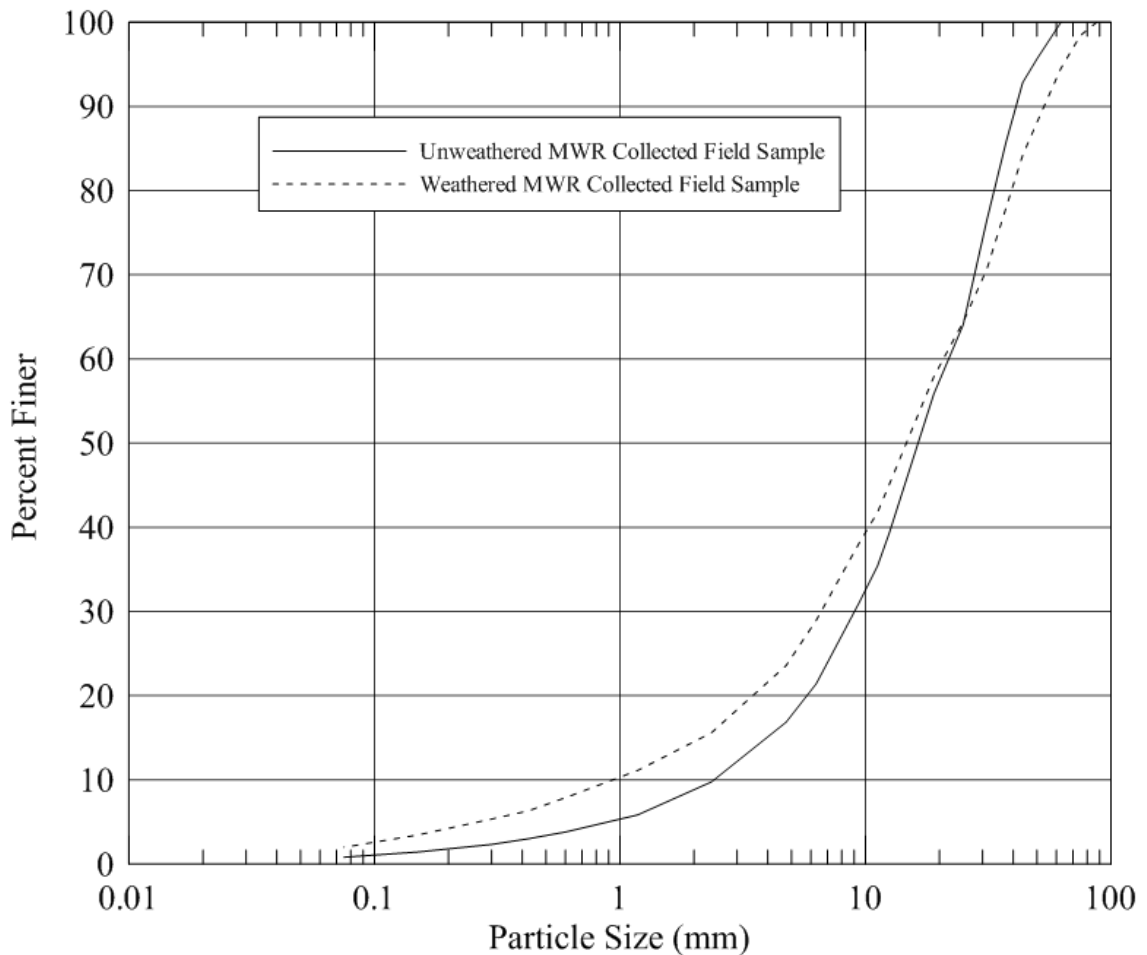


Figure 4.2: Particle-size distributions for the collected field samples of weathered and unweathered *MWR*.

#### 4.2.2 Parallel Gradation Technique

As discussed in sections 2.2.1.3 and 2.2.1.4, the parallel gradation technique was used in this study to scale-down the collected field sample into specimens with maximum particle sizes appropriate for the testing apparatus used. This study characterizes the mechanical behavior of *MWR* in drained monotonic, axisymmetric compression in a conventional-scale triaxial apparatus with a specimen diameter of 70 mm. The corresponding maximum particle size for the 70-mm triaxial apparatus is 11.7 mm in order to maintain a sample-size ratio of 6 (ASTM D 4767). Because standard sieve apertures nearest to

11.7-mm are 11.2-mm and 12.5-mm, the 11.2-mm sieve was chosen as the limiting sieve for the coarse fraction of the modeled gradation using the parallel gradation technique presented by Lowe (1964). This results in a *SSR* of 6.25 which is slightly greater than the required sample-size ratio of 6 as required by ASTM D 4767 and greater than the recommended sample-size ratio as presented by Marachi (1969). The maximum particle sizes for the weathered and unweathered *MWR* are 87.5-mm and 62.5-mm, respectively. Scaling the sample down into specimens testable in the 70-mm-diameter triaxial apparatus yields an 87.2-% and 82.1-% reduction in maximum particle size for the weathered and unweathered *MWR*, respectively. Large-scale triaxial testing was performed by Fox (2011) with a 152.4-mm diameter triaxial apparatus and corresponding maximum particle size of 25.4 mm. Using the parallel gradation technique, Fox (2011) modeled triaxial specimen gradations with a maximum particle size of 25 mm which yields a 71.4-% and 60.0-% reduction in maximum particle size for the weathered and unweathered *MWR* material, respectively. Particle-size distributions of the modeled gradations used in conventional-scale triaxial testing (present study), large-scale triaxial testing (Fox 2011) and the corresponding collected field gradations for unweathered and weathered *MWR* are presented on Figures 4.3 and 4.4, respectively.

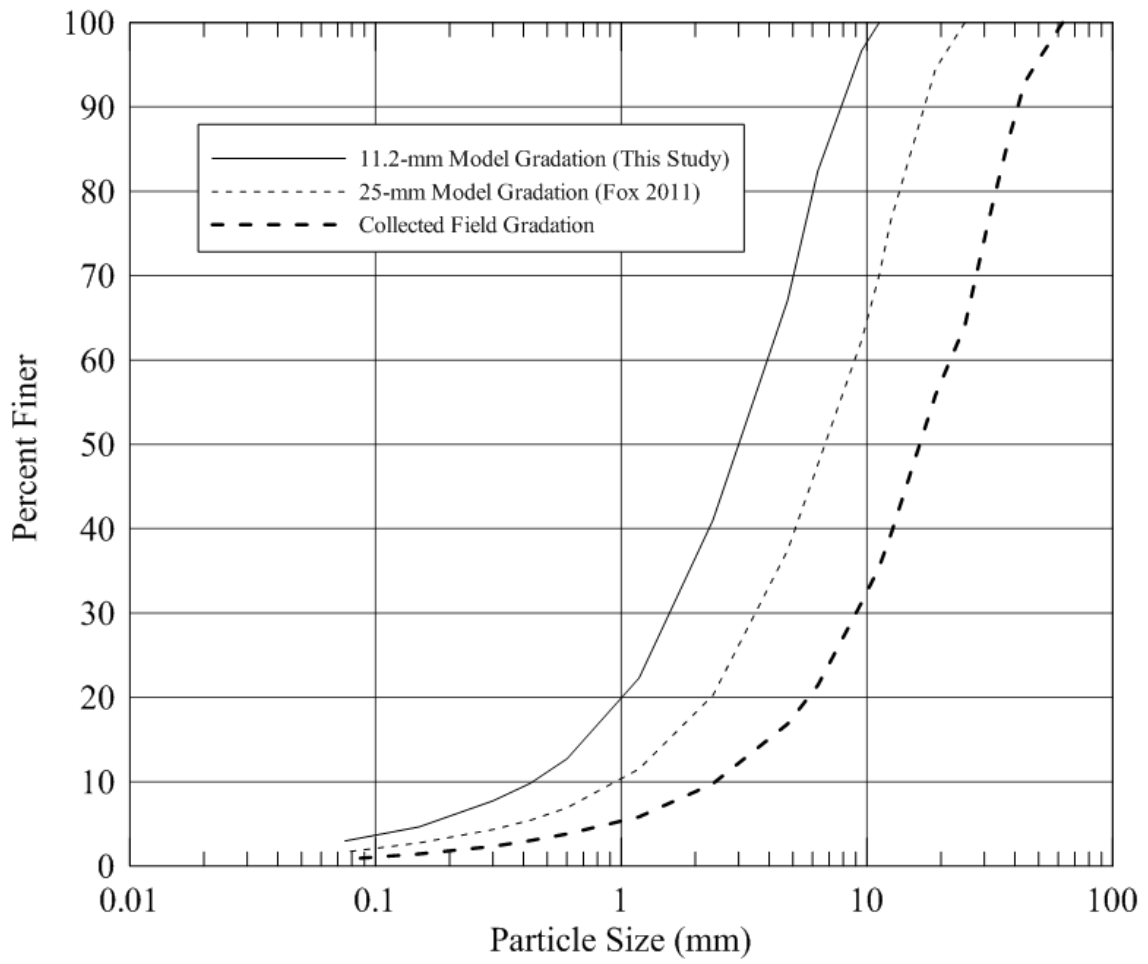


Figure 4.3: Particle-size distributions for collected field samples and modeled gradations of unweathered *MWR* materials.

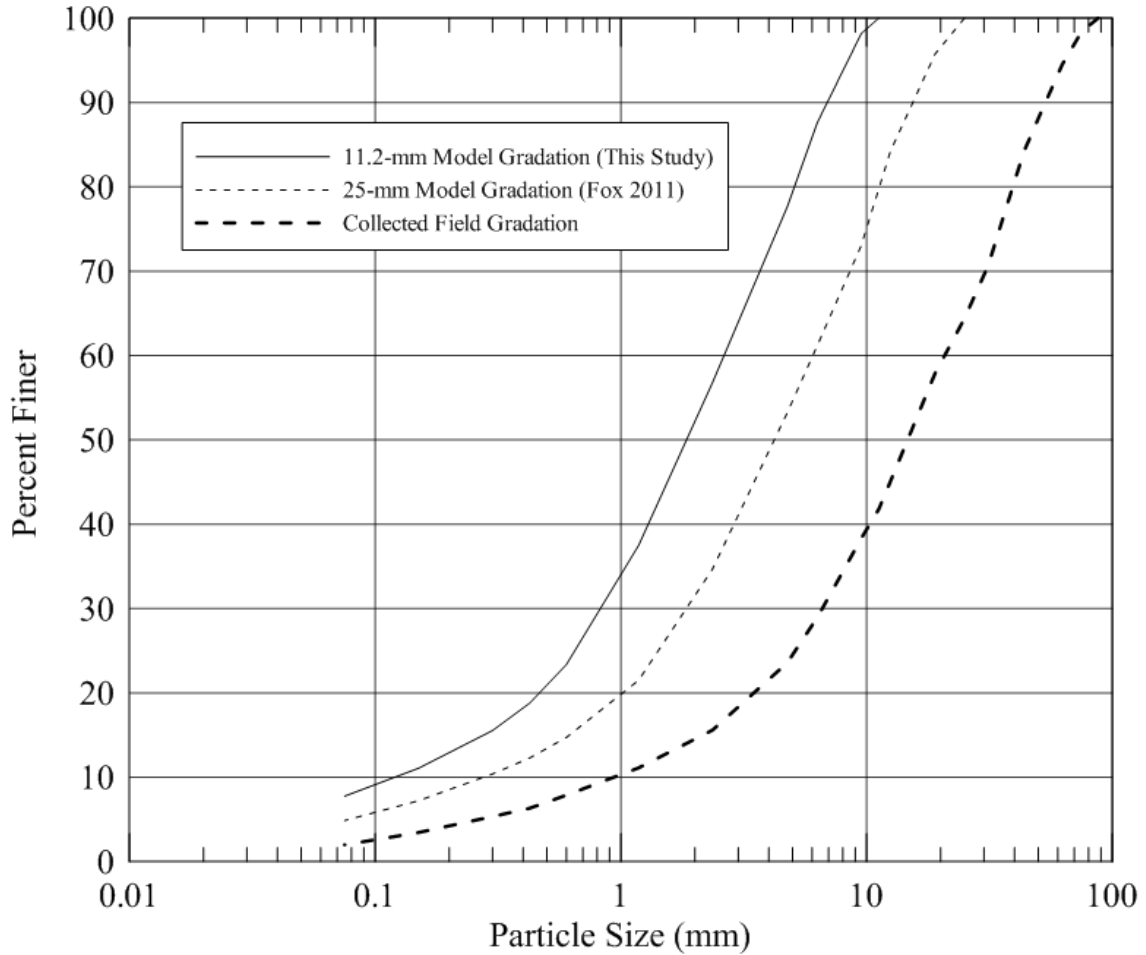


Figure 4.4: Particle-size distributions for collected field samples and modeled gradations of weathered *MWR* materials.

#### 4.2.3 Atterberg Limits

As presented in the particle-size distribution curves on Figures 4.3 and 4.4, due to sample scaling effects, the *FC* for both *MWR* materials tested in this study increases from 2.0% to 7.8% and 0.8% to 3.0% for the weathered and unweathered *MWR*, respectively. To classify the material according to the Unified Soil Classification System (*USCS*), quantification of the plasticity properties of the fines for each material through Atterberg Limits was determined in accordance with ASTM D 4318. Unlike the particle-size

analysis, the Atterberg Limit samples had to be sub-sampled from the collected field gradation. Specimen preparation in accordance with ASTM D 4318 requires the sample to be passed over the #40 sieve (0.425-mm) and particle aggregates broken up with a mortar and pestle. Due to the dry sieving process of the particle-size analysis, aggregated particles were broken up during the sieving process and breaking up particle aggregates with a mortar and pestle was not necessary. A model gradation of both *MWR* materials was created after the particle-size distribution for each material was determined. The model gradations for the Atterberg Limit samples were created such that the shape of the particle-size distribution curve passing the #40 sieve was identical to that of the collected field samples. Results of Atterberg Limit tests for each *MWR* material is presented in Table 4.2.

Table 4.2: Results of Atterberg Limit tests (ASTM D 4318).

	$w_L$	$w_P$	$I_P (=w_L - w_P)$
Weathered <i>MWR</i>	26.9%	16.4%	10.5%
Unweathered <i>MWR</i>	Non plastic		

Results from the Atterberg Limit tests may be related to the amount of alteration that has taken place within the weathered *MWR* as compared to the unweathered *MWR*. Research has shown an increase in soil plasticity due to changes in soil mineralogy due to hydrogeologic weathering and oxidation (Bozzano et al. 2006). For example, oxidation and/or dissolution of iron bearing clay minerals, calcite and other mica-like minerals with a comparable increase in iron-hydroxides instigate chemical and mineralogical changes during hydrogeologic weathering. The chemical and mineralogical changes within the material cause an increase in the plasticity from the unweathered to the weathered

material state. Bozzano et al. (2006) explains the weathering process as a cyclical pattern in which meteoric water seeps, dissolves and subsequently migrates dissolved chemical constituents and changes the chemical and mineralogical composition of the parent (unweathered) material. The research presented by Bozzano et al. (2006) provides a possible explanation for the increase in soil plasticity for the weathered *MWR* material compared to that of the unweathered *MWR* material. Further discussion on hydrogeologic weathering of can be found in the study presented by Bozzano et al. (2006).

#### 4.2.4 Unified Soil Classification System

Results of the particle-size distribution analyses and Atterberg Limit analyses for the field and modeled gradations were analyzed in accordance with the *USCS* (ASTM D 2487). The particle-size diameters  $d_{10}$ ,  $d_{30}$ ,  $d_{50}$  and  $d_{60}$  corresponding to 10%, 30%, 50% and 60% passing the cumulative particle-size distribution curve were determined. The coefficient of uniformity ( $C_u$ ) and coefficient of curvature ( $C_c$ ) were subsequently calculated with knowledge of  $d_{10}$ ,  $d_{30}$ , and  $d_{60}$ . Results of the analysis in accordance to the *USCS* are presented in Table 4.4.

#### 4.2.5 Specific Gravity of Solids

The specific gravity of solids ( $G_s$ ) was measured for both *MWR* materials in accordance to ASTM D 854 for materials passing the #4 sieve (4.75-mm) and ASTM C 127 for materials retained on the #4 (4.75-mm) sieve. The  $G_s$  for each specimen was calculated by a weighted average of the amount passing and retained on the #4 (4.75-mm) sieve.

Results of the specific gravity tests from Fox (2011) and the present study are presented in Table 4.4. Results of the specific gravity tests show increases from the field gradations to the modeled gradations of 2.63 to 2.71 and 2.60 to 2.67 for the weathered and unweathered *MWR*, respectively. The increase of specific gravity from the field gradations to the model gradations can be attributed to the increase in *FC* for the two modeled gradations of the two *MWR* materials. Greater *FC* in the weathered *MWR* material, along with mineralogical differences between the weathered and unweathered *MWR* materials are probable explanations for the weathered material having a greater specific gravity as compared to the unweathered *MWR* material for all gradations considered in this study.

#### 4.2.6 Scanning Electron Microscopy

Particle shape is easily observable for particles on the order of 0.15-mm nominal diameter and above, generally with a magnifying glass for particles between 0.15 mm and 0.6 mm. However, to characterize the shape of particles finer than 0.15-mm nominal diameter, a slightly greater effort is required. In order to characterize the relative impact of fines on the mechanical behavior of the *MWR* materials tested in this study, scanning electron microscopy (*SEM*) was used to take microphotographs of the particles passing the #200 sieve. *SEM* analysis of the materials was conducted within Colorado State University's chemistry department using a JEOL JSM-6500F Scanning Electron Microscope. Microphotographs were taken at a range of different magnifications ranging from 100X to 10,000X. The weathered *MWR* fines are primarily comprised of plate-like particles with some prismatic particles with rounded edges. Unlike the weathered *MWR*

fines, the unweathered *MWR* fines are primarily comprised of prismatic particles with sharp and slightly rounded edges. Although some plate-like particles were observed in the unweathered *MWR* material, the amount of plate-like particles as compared to the weathered *MWR* material is far less. Figures 4.5 and 4.6 show a microphotograph of the fines for the unweathered and weathered *MWR*, respectively. Additional microphotographs from *SEM* analysis and details of equipment and procedures used are presented in Appendix E.

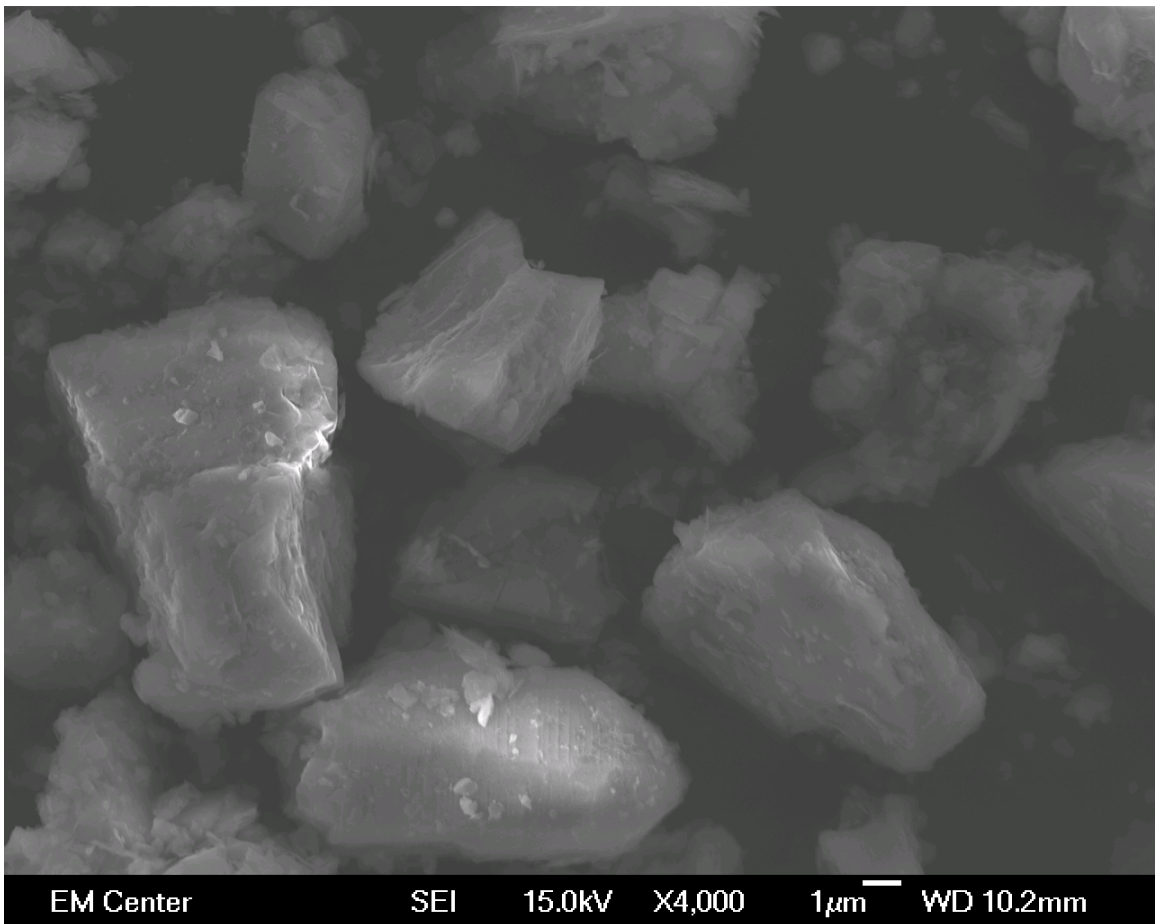


Figure 4.5: Microphotograph of unweathered *MWR* fines (particles passing the #200 sieve) at 4,000 times magnification.

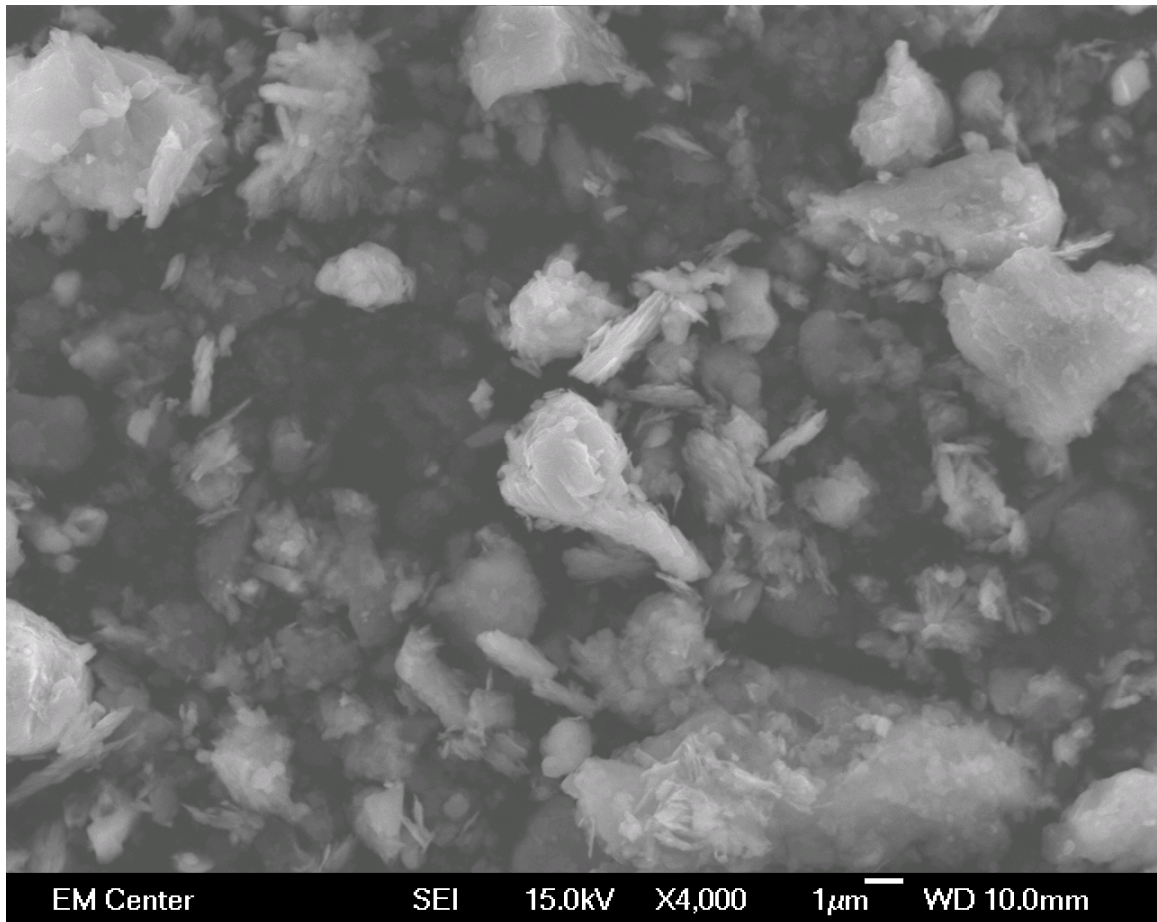


Figure 4.6: Microphotograph of weathered *MWR* fines (particles passing the #200 sieve) at 4,000 times magnification.

#### 4.2.7 X-Ray Diffraction

In order to quantify the difference between the mineralogical compositions of the unweathered and weathered *MWR*, X-Ray diffraction (*XRD*) testing was completed by H & M Analytical, Inc. based in Allentown, NJ. Given the results of Atterberg limit testing, four specimens were prepared in order to determine the mineralogical composition of the finer fraction (material passing the #200 sieve) and coarse fraction (material retained on the #200 sieve). Specimens of the coarse fraction were modeled using similar ratios between the maximum particle sizes evaluated in the present study (11.2 mm and 25.0

mm (Fox 2011)) and the collected field gradation. The finer fraction was effectively scaled from the coarse grained sample and a separate sample exclusively of fines was created. The coarse grained fraction was processed by H & M Analytical, Inc. using a crusher to pass the particles over the #200 sieve. Because specimen size for *XRD* is so small (on the order of tens of grams), a rigorous evaluation of the mineralogy of the two types of *MWR* tested in the present study is not possible. Therefore, the presented results are only intended for illustrative purposes relating to the differences in material mineralogy only. Further systematic testing must be completed in order to definitively characterize the mineralogical composition of the two materials and the variation in mineralogy throughout the collected field sample. The analysis did, however, provide results of the mineralogical composition in percentages by weight of both *MWR* materials that clearly reveal stark contrasts between the two *MWR* materials. Both the fine and coarse fraction of each material were shown to be primarily comprised of quartz. However, the unweathered material was comprised of more than 20% dolomite in both the fine and coarse fractions whereas the weathered material lacked the mineral altogether. Instead, about 5% of the coarse fraction and about 10% of the fine fraction comprising the weathered material was kaolinite, a low plasticity clay, which explains the increase in plasticity. An indication of weathering in the weathered material is the elevated level of goethite, which is a common iron hydroxide found in strongly weathered geomaterials (Bohn et al. 2001). Results of the mineralogical analysis for the unweathered and weathered *MWR* materials are tabulated in Table 4.3. For more detailed *XRD* results, the complete results submitted by H & M Analytical, Inc. can be found in Appendix A.

Table 4.3: Results of X-Ray diffraction testing.

	Quantitative Phase Analysis (% by weight)			
	Unweathered Fine Fraction (Passing #200 sieve)	Unweathered Coarse Fraction (Retained on #200 sieve)	Weathered Fine Fraction (Passing #200 sieve)	Weathered Coarse Fraction (Retained on #200 sieve)
Quartz	58.7	58.9	47	56.1
Pyrite	1.2	1.0	0.9	0.8
Gypsum	1.5	1.5	0.8	0.2
Rutile	0.1	0.1	0.3	0.2
Anatase	0.1	0.1	0.5	0.5
Siderite	0.2	0.1	5.0	4.5
Muscovite	0.8	2.0	12.6	13.2
Kaolinite	0.6	0.3	10.0	5.1
Magnetite	0.3	0.3	2.6	1.2
Geothite	0.2	0.2	8.1	7.9
Phengite	4.1	2.8	12.3	10.2
Calcite	8.8	10.2	--	--
Dolomite	22.3	21.2	--	--
Barite	1.1	1.3	--	--

Note: "--" indicates the mineral was not present.

#### 4.2.8 Limiting Void Ratios

The limiting void ratios,  $e_{min}$  and  $e_{max}$ , were determined for the model gradations tested in this study in accordance with ASTM D 4253, Method 1A and ASTM D 4254, Method A, respectively. Specimens were prepared using the parallel gradation technique to a total weight of 11 kg, as recommended by the two corresponding ASTM standards. A standard mold with a volume of  $0.1 \text{ ft}^3$  was used for both limiting void ratio tests ( $SSR = 13.7$ ). ASTM D 4253, Method 1A was used for determining  $e_{min}$ . The material was carefully placed within the standard mold with a hand scoop and placed on an electromagnetic, vertically vibrating table with a 14-kPa surcharge to the top of the specimen. Testing to determine  $e_{max}$  according to ASTM D 4254 would be normally be completed according to Method B (appropriate for material passing the 3/4-in sieve),

however, Method A was chosen to be consistent with the method used by Fox (2011) for measuring  $e_{min}$  for the large-scale specimens. The material was carefully placed with a hand scoop into the mold to measure the minimum index density of the two *MWR* materials. The two key differences in the limiting void ratio tests conducted in the present study compared to the study conducted by Fox (2011) are mold size and the corresponding *SSR*. The mold volume used by Fox (2011) was equal to 0.5 ft<sup>3</sup> with a value of *SSR* equal to 11.2. Results of the limiting void ratio tests completed by Fox (2011) and during the course of this study are summarized in Table 4.4. A detailed analysis of the results of the limiting void ratio tests can be found in Chapter 5, section 5.1.

Table 4.4: *USCS* classification and parameters according to ASTM D 2487.

	$d_{10}$ (mm)	$d_{30}$ (mm)	$d_{50}$ (mm)	$d_{60}$ (mm)	$C_u$	$C_c$	<i>USCS</i> *	<i>FC</i> (%)	$G_s$	$e_{min}$	$e_{max}$
Unweathered MWR Field	2.4	9.1	16.7	22.0	9.0	1.5	GW <sup>1</sup>	0.8	2.60	--	--
Unweathered MWR Model (Fox 2011)	1.0	3.7	6.8	9.0	9.1	1.6	GW <sup>1</sup>	1.7	2.63	0.360	0.753
Unweathered MWR Model (This study)	0.4	1.6	3.2	4.1	10.4	1.7	SW <sup>2</sup>	3.0	2.67	0.403	0.739
Weathered MWR Field	1.0	6.7	15.0	20.9	21.4	2.2	GW <sup>1</sup>	2.0	2.63	--	--
Weathered MWR Model (Fox 2011)	0.3	1.9	4.3	6.1	21.7	2.2	SW <sup>2</sup>	4.9	2.67	0.420	0.803
Weathered MWR Model (This study)	0.1	0.9	1.9	2.7	21.7	2.2	SW-SC <sup>3</sup>	7.8	2.71	0.416	0.848

<sup>1</sup>GW – Well graded gravel with sand

<sup>2</sup>SW – Well graded sand with gravel

<sup>3</sup>SW-SC – Well graded sand with silty clay and gravel

#### 4.2.9 Triaxial Testing

In an effort to make tests comparable to those completed by Fox (2011), a total of eighteen triaxial tests were performed as a part of this study. Specimens were reconstituted to initial levels relative densities ( $D_R$ ) representing “loose”, “medium” and “dense” specimens, similar to the approach used in a previous study for large-scale triaxial tests (Fox 2011). Specimens were isotropically compressed to levels of  $p'$  of 100, 200 or 400 kPa before being sheared in drained, monotonic, axisymmetric compression. To systematically compare the results of this study and to the large-scale test results presented by Fox (2011), test designations were given to each specific test to represent (1) the type of *MWR* material used, (2) the actual  $D_R$  achieved at the end of isotropic compression and (3) the nominal level of  $p'$  at the end of isotropic compression. For example, a weathered *MWR* specimen isotropically compressed to  $p' = 400$  kPa with  $D_R = 92\%$  will be referred to W92-400.

##### 4.2.9.1 Triaxial Test Equipment

The equipment used in this study was manufactured by ELE International, Loveland, CO. The triaxial apparatus was capable of testing triaxial specimens with diameters as large as 70 mm with applied confining pressures up to 1,700 kPa. A height to diameter ratio of two was used for all specimens, as prescribed by ASTM D 4767, yielding a specimen height of 140 mm. The control panel boards used in this study were an ELE Tri-Flex 2 Master Control Panel and an ELE Tri-Flex 2 Auxiliary Control Panel capable of delivering pressures up to 1,034 kPa. Back pressure and cell pressure was applied via manual air pressure regulators installed on the master and auxiliary control panel boards.

Pressure was applied to the cell water and pore-water through burettes mounted to the master and auxiliary control panel boards. The burettes function as an air-water interface between the applied air pressure and the cell/pore-water during the test. The load frame used in this study was an ELE Digital Tritest 50 Load Frame capable of delivering a maximum axial load of 50 kN with programmable displacement rates between 0.00001 and 9.99999 mm/min. A strain rate of 0.3 mm/min was used for all tests resulting in an axial strain of 0.21 %/min. This strain rate was conservatively determined using the procedure outlined by Head (1986) in which volumetric strains or excess pore-water pressures are plotted against the logarithm or square root of time in minutes. Due to the material properties, the excess pore-water pressures measured within the specimens under undrained loading conditions dissipated in less than 30 seconds. This fast rate of excess pore-water pressure dissipation allowed for strain rates as high as 5 mm/min as determined by the approach outlined by Head (1986). In an attempt to obtain a relatively large amount of data and to be conservative as to not incorporate strain rate effects in triaxial testing, the strain rate of 0.3 mm/min was chosen.

Because two identical triaxial cells were used in this study, a total of six pressure transducers and two volume change transducers were used. By shearing only one specimen at a time, the displacement transducer and the force transducer were shared between the two cells. The pressure transducers used in this study were ELE pressure transducers with a capacity of 1,700 kPa. The load on the specimen was measured with an ELE 9,000-N capacity force transducer. Axial strain was measured by an ELE LVDT (linear variable differential transformer) axial strain transducer with a range of 50 mm.

Data acquisition was used for pressure, volumetric, load and displacement measurements throughout each test. The data acquisition device used was the ELE Autonomous Data Acquisition Unit (ADU) capable of taking up to 100 readings per second from the entire range of different transducers at the same time. Combining the transducers and the ADU system, a relatively continuous data set was obtained for each test. A summary of the calibration information for each transducer used in this study is presented in Table 4.5. A photograph of the triaxial apparatus used in this study is presented on Figure 4.7.

Table 4.5: Calibration summary of transducers used in the present study.

	Unit	Resolution (unit)	Capacity (unit)	Accuracy (%)
Displacement Transducer AD27-1617	mm	0.01	50	0.09
Force Transducer LC404303	N	1	9000	0.08
Volume Change Transducer VC27-1641	mL	0.01	80	0.19
Volume Change Transducer VC27-1642	mL	0.01	80	0.13
Pore Pressure Transducer PT14850	kPa	0.1	1700	0.17
Pore Pressure Transducer PT14868	kPa	0.1	1700	0.35
Back Pressure Transducer PT14869	kPa	0.1	1700	0.53
Back Pressure Transducer PT14763	kPa	0.1	1700	0.28
Cell Pressure Transducer PT14764	kPa	0.1	1700	0.18
Cell Pressure Transducer PT14851	kPa	0.1	1700	0.16



Figure 4.7: Conventional-scale triaxial apparatus used in this study.

Due to the absence of an ASTM standard for isotropically compressed, drained triaxial tests, well-established techniques presented by Head (1986) for testing of clean sands in drained axisymmetric compression) were used. Procedures used during the preparation, reconstitution and intermediate test phases (such as isotropic compression) followed ASTM standards, whenever available.

#### 4.2.9.2 Specimen Preparation

In order to create the modeled gradations for each triaxial test performed, the collected field sample had to be sorted into buckets with each bucket corresponding to mass retained upon a specific sieve size. In an effort to eliminate bias in creation of each

modeled gradation, the entire sample was sorted all at once. Sorting the entire sample before triaxial testing began also removed the risk of sample-splitting errors in the particle-size distribution analysis by allowing for a particle-size distribution analysis of the entire field collected sample at the time of sorting. Sorting the collected field gradations of the *MWR* materials comprised of dry-sieving the materials over specified sieves in accordance with ASTM D 6913, Method B with the only deviation from the standard being the recommended maximum particle size for the analysis.

As discussed in Chapter 2, Section 2.2.2, specimen fabric and uniformity can have a pronounced effect on the mechanical behavior of soils. Specimens should be reconstituted in a manner that (1) is repeatable, (2) yields a fabric representative of the fabric in the field (Wood et al. 2008) and (3) yields uniform density (in terms of  $D_R$ ) throughout the specimen (Ladd 1978). To accomplish this, a slight modification to ASTM D 4254 (minimum index density), Method B was used as the reconstitution technique of a triaxial specimen for this present study. The technique is similar to the mixed dry deposition technique presented by Wood et al. (2008). Using this technique, triaxial specimen preparation over a wide range of initial relative densities (i.e.  $17\% < D_R < 71\%$ ) was possible.

ASTM D 4254 Method B calls for the use of a rigid, thin-walled tube with a volume 1.25 to 1.30 times the volume of the mold in which the specimen is to be placed. The inner diameter of the tube shall be about 0.7 times the inner diameter of the mold. Using a 70-mm-diameter triaxial apparatus and reconstituting specimens to a height of

approximately 140 mm, the rigid, thin-walled tube used in the present study was 270-mm-tall with an inner diameter of 50.8 mm. To ensure a relatively uniform  $D_R$  throughout the specimen, specimen reconstitution was performed through placement of two identical lifts created using the parallel gradation technique. The rigid, thin-walled tube was centered in a 70-mm-diameter vacuum split mold lined with a latex membrane. The contents of the first lift were carefully funneled into the tube and, as prescribed in Method B of ASTM D 4254, the tube was removed quickly allowing the material to be deposited evenly within the vacuum split mold. The second lift was placed upon the first lift using the same procedure. The top cap was then installed on the specimen and an initial effective stress of 30 kPa was applied with a vacuum pump. The cell was then assembled and filled, while maintaining the 30-kPa-vacuum. To create denser specimens, a 39-N surcharge was placed on each lift and vibration was applied in evenly timed increments to the top of the lift and the sides of the split mold using a hand-held vibrator. For dense specimens, an initial target  $D_R$  was set for each specimen ranging from 20% to 90%. Each lift was then compacted to a previously determined height within the vacuum split mold or until no further densification was observed under repeated vibratory compaction efforts. A summary of  $D_R$  values obtained after reconstitution can be found in Tables 4.6 and 4.7 for the weathered and unweathered *MWR* materials, respectively.

#### 4.2.9.3 Specimen Uniformity

Before any triaxial compression tests were completed, an experimental testing program was conducted to verify the  $D_R$  uniformity throughout the specimen using the rigid, thin-

walled tube technique and the weathered *MWR* material. The program consisted of testing the  $D_R$  for the first lift before and after the application of the second lift for the densest and loosest states. An average  $D_R$  for the specimen was then calculated using the final states for both lifts. Results of this program were analyzed in terms of average values and the corresponding coefficients of variation (*COV*) and are presented in Tables 4.4 and 4.5. Similar to the results presented by Fox (2011), the “dense” specimens were more repeatable and uniform than the “loose” specimens. Large-scale specimens (Fox 2011) had an average *COV* of 15.3% and 8.0% for “loose” and “dense” specimens, respectively. Conventional scale specimens in the present study have an average *COV* of 4.1% and 2.5% for “loose” and “dense” specimens, respectively, suggesting that the smaller conventional scale specimens are more repeatable and uniform than large-scale specimens.

Table 4.6: Results of experimental program to verify  $D_R$  uniformity using the rigid, thin-walled tube reconstitution technique for “loose” weathered *MWR* specimens.

Trial	$D_R$ (%)				<i>COV</i>
	Lift 1	Lift 1 After Placement of Lift 2	Lift 2	Average	
1	16	17	18	17	5.5
2	17	17	18	18	4.0
3	15	17	17	17	2.8

Table 4.7: Results of experimental program to verify  $D_R$  uniformity using the rigid, thin-walled tube reconstitution technique for “dense” weathered *MWR* specimens.

Trial	$D_R$ (%)				<i>COV</i>
	Lift 1	Lift 1 After Placement of Lift 2	Lift 2	Average	
1	69	70	71	71	1.3
2	67	69	72	71	3.7

#### 4.2.9.4 Flushing

Each specimen was thoroughly flushed with fresh de-aired water after reconstitution according to the procedure outlined in section 4.2.8.2. The cell was pressurized slowly from 0 kPa to 30 kPa while decreasing the vacuum at the same rate from 30 kPa to 0 kPa thus maintaining a constant 30-kPa initial mean effective stress throughout the sample. Flushing commenced by opening the top drainage line to the atmosphere and slowly flushing water from the bottom of the specimen to the top. Due to the larger  $FC$  of the weathered specimens compared to the unweathered specimens (7.8% compared to 3.0%), a larger hydraulic gradient was required to facilitate flushing in the weathered specimens. A hydraulic gradient during flushing  $i_F$ , equal to 3.4 and 0.9 was used to facilitate flushing for the weathered and unweathered specimens respectively. The hydraulic gradient equal to 3.4 for the weathered specimens was obtained by applying an air pressure of approximately 5.4 kPa to the air-water interface in the control panel board to the bottom drainage lines. The hydraulic gradient equal to 0.9 for the unweathered specimens was obtained by changing in elevation head only. To ensure migration of fines did not occur during the flushing stage under the before mentioned hydraulic gradients, fines content was visually monitored throughout the sample before, during and after each test when the triaxial apparatus was dismantled. No migration of fines was observed in any test, likely to the well graded nature of both  $MWR$  materials. The minimum effective stress in each specimen during the flushing stage was equal to 24.6 kPa and was achieved at the bottom of the specimen where the  $PWP$  was equal to 5.4 kPa. The maximum effective stress during the flushing stage was equal to 30 kPa in each specimen and was observed at the top of the sample which was vented to the atmosphere with  $PWP$  equal to

0 kPa. Liquefaction of the material during flushing under the before mentioned hydraulic gradients was not observed due to the fact that the specimen was loaded with an all around total stress (cell pressure) of 30 kPa with a minimum  $p'$  equal to 27.3 kPa  $((24.6 \text{ kPa} + 30 \text{ kPa})/2 = 27.3 \text{ kPa})$ . The total volume of water flushed through each specimen ranged from 9 – 24 pore-volumes ( $PVs$ ) and was terminated when entrapped air bubbles ceased to exit the top of the specimen and corresponding drainage lines were free of air bubbles. The duration of the flushing stage,  $t_F$ , took a minimum of 1 day and a maximum of 3 days for both  $MWR$  materials, depending on reconstituted  $D_R$  and final  $p'$  for each test. A summary of  $D_R$  after flushing,  $D_{R, AF}$ ,  $v$  after flushing,  $v_{AF}$ ,  $t_F$  and flushing  $PVs$  for each test can be found in Tables 4.7 and 4.8 for the weathered and unweathered  $MWR$  materials, respectively.

#### 4.2.9.5 Back Pressure Saturation

After the flushing stage outlined in the previous section, specimens were back pressure saturated according to the procedure prescribed by Head (1986). Back pressure increments of 30 kPa were used with an initial  $p'$  also equal to 30 kPa. Specimen saturation was verified using the pore-pressure parameter  $B$  ( $B = \Delta u / \Delta \sigma_r$  where  $\Delta u =$  change in pore-water pressure and  $\Delta \sigma_r =$  changed in applied total radial stress, also known as cell pressure) (Skempton 1954). Specimens were back pressure saturated until the  $B$  value was equal to or greater than 0.98. Back pressures between 300 kPa and 580 kPa were required to reach a  $B$  value of 0.98 or greater. The back pressure saturation stage of each test was proportional to the final  $p'$  and initial  $D_R$  of each specimen. Typically as the final  $p'$  and initial  $D_R$  increase, the time required for back pressure

saturation increased. For loose samples isotropically compressed to a final  $p'$  equal to 100 kPa, the back pressure saturation stage lasted approximately 24 h. For dense samples isotropically compressed to a final  $p'$  equal to 400 kPa, the back pressure saturation stage lasted approximately 72 h.

As described by Head (1986), required back pressure levels depend on the initial saturation of the specimens, which is directly related to the amount of  $PVs$  flushed during the flushing stage, among other factors such as specimen stiffness,  $\Delta\sigma_r$ , used, and density. Once air pockets in the voids become discontinuous, the advective transport process that effectively pushes the air out of the specimen ceases due to a discontinuity in the phase continuum (Corey 1994). After this point, the saturation process is dominated by diffusion of air pockets into the de-aired water surrounding the air pocket (Head 1986). Diffusion is a concentration and time dependent process and during the back pressure saturation stage, the air concentration within the pore-water is effectively zero (freshly de-aired water) and time becomes the limiting factor. Although  $PWPs$  equalized in specimens in less than 1 m for each back pressure increment, diffusion is a time dependent process and thus back pressure saturation stages were conducted with a minimum of 1 h between stages and a maximum of 16 h between stages.

Because of the initial unsaturated state, some volume change (compression) does occur during the flushing and back pressure saturation stage. To accurately define the specimen state before isotropic compression and shearing stages, the actual volume of the specimen must be known. Following the procedure outlined by Fox (2011), the  $\varepsilon_a$  of each

specimen was measured before and after the flushing and back pressure saturation stage. The measured  $\varepsilon_a$  was used to estimate the  $\varepsilon_p$  during those two stages. The approximation assumes that the major principal strain ratio ( $R_s$ ) during both stages is equal to the  $R_s$  measured during isotropic compression (outlined in section 4.2.8.6). For isotropic compression, the major principal strain ratio is defined as:

$$R_s = \frac{\varepsilon_3}{\varepsilon_1} \quad (4.1)$$

where:  $\varepsilon_3$  and  $\varepsilon_1$  are the minor and major principal strains, respectively. A summary of  $D_R$  after saturation,  $D_{R,AS}$ ,  $v$  after flushing,  $v_{AS}$ , and final  $B$  values obtained for each specimen can be found in Tables 4.7 and 4.8, respectively.

#### 4.2.9.6 Isotropic Compression

At the conclusion of the back pressure saturation stage, triaxial specimens were at a  $p'$  equal to 30 kPa. Additional incremental increases of  $p'$  were applied to each specimen to obtain a final  $p'$  equal to 100, 200 or 400 kPa, after isotropic compression. For the triaxial specimens isotropically compressed to 100 kPa, the intermediate stages of  $p'$  were 30, 50 and 100 kPa. For triaxial specimens isotropically compressed to 200 kPa, the intermediate stages of  $p'$  were 30, 50, 100 and 200 kPa. The final set of triaxial specimens isotropically compressed to 400 kPa had intermediate stages of  $p'$  equal to 30, 100, 200 and 400 kPa. Volumetric strains were measured throughout the isotropic compression stage with an ELE Volume Change Unit (*VCU*). Axial strains ( $\varepsilon_a$ ) were measured by measuring the displacement of the triaxial apparatus actuator and a hand help digital caliper before and after each compression increment. The specimen was

subjected to double drainage (drainage from the top cap and base pedestal) during isotropic compression. Due to the nature of both *MWR* materials, side drains were deemed not necessary and were not used during the triaxial testing program. A summary of  $D_R$  after isotropic compression,  $D_{R,AC}$ , and  $v_{AC}$  obtained for each specimen can be found in Tables 4.8 and 4.9 for the unweathered and weathered *MWR* materials.

Table 4.8: Summary of  $D_R$ ,  $v$ ,  $i_F$ ,  $t_F$ , Flushing *PVs* and Final *B* values for unweathered *MWR* specimens.

	U26-100	U50-100	U70-100	U40-200	U54-200	U77-200	U42-400	U68-400	U75-400
$D_{R, Initial}$ (%)	16	43	64	22	43	68	20	51	64
$D_{R, AF}$ (%)	19	44	65	24	44	69	23	52	64
$D_{R, AS}$ (%)	20	46	67	29	45	71	25	55	65
$D_{R, AC}$ (%)	26	50	70	40	54	77	42	68	75
$v_{Initial}$	1.68	1.60	1.52	1.67	1.59	1.51	1.67	1.57	1.53
$v_{AF}$	1.67	1.59	1.52	1.66	1.59	1.51	1.66	1.56	1.52
$v_{AS}$	1.67	1.59	1.51	1.64	1.59	1.50	1.65	1.55	1.52
$v_{AC}$	1.65	1.57	1.51	1.61	1.56	1.48	1.60	1.51	1.49
$i_F$	0.9	0.9	0.9	0.9	0.9	0.9	0.9	0.9	0.9
$t_F$ (d)	1.0	1.0	1.0	1.0	1.0	1.0	1.0	1.0	1.0
Flushing <i>PVs</i>	9.3	17.9	15.0	11.9	23.3	16.8	12.6	13.9	24.0
Final <i>B</i> Value (%)	98	100	98	98	99	98	98	98	98

Table 4.9: Summary of  $D_R$ ,  $v$ ,  $i_F$ ,  $t_F$ , Flushing  $PVs$  and Final  $B$  values for weathered  $MWR$  specimens.

	W34-100	W61-100	W78-100	W44-200	W72-200	W83-200	W55-400	W76-400	W92-400
$D_{R, Initial}$ (%)	17	52	71	19	56	71	16	49	71
$D_{R, AF}$ (%)	21	55	73	23	57	72	20	53	72
$D_{R, AS}$ (%)	24	55	74	24	58	73	23	53	73
$D_{R, AC}$ (%)	34	61	78	44	72	83	55	76	92
$v_{Initial}$	1.77	1.62	1.54	1.77	1.61	1.54	1.78	1.64	1.54
$v_{AF}$	1.76	1.61	1.53	1.75	1.60	1.54	1.76	1.62	1.54
$v_{AS}$	1.74	1.61	1.53	1.74	1.60	1.53	1.75	1.62	1.53
$v_{AC}$	1.70	1.58	1.51	1.66	1.54	1.49	1.61	1.52	1.45
$i_F$	3.4	3.4	3.4	3.4	3.4	3.4	3.4	3.4	3.4
$t_F$ (d)	2.0	2.5	2.5	2.0	2.5	2.5	2.0	2.5	3.0
Flushing $PVs$	9.3	17.9	15.0	11.9	23.3	16.8	12.6	13.9	24.0
Final $B$ Value (%)	98	100	98	98	99	98	98	98	98

#### 4.2.9.7 Creep

Creep is defined as additional  $\varepsilon_p$  after full dissipation of excess  $PWPs$  (Kuhn et al. 1993). Creep was observed in all tests conducted and ranged from 0.1 – 0.5% for the unweathered material and 0.2 – 1.2% for the weathered material. The amount of creep highly depends on the  $D_R$ ,  $p'$ , boundary conditions, stress induced anisotropy, specimen anisotropy and material type. Time effects relating to additional  $\varepsilon_p$  after full dissipation of excess pore-water pressures in granular geomaterials has been associated with particle breakage (Lade and Karimpour 2010). Although some particle breakage may have occurred during the isotropic compression phase of testing, the extent of particle breakage during isotropic compression was not quantified in the present study. However

triaxial specimens were allowed to reach a constant soil state (constant  $p'$  and  $D_R$ ) before additional compression stages (isotropic or drained, monotonic) were applied to the specimen. Following Fox (2011), a constant soil state was assumed to be achieved once the rate of volumetric strain was less than or equal to 0.05%/h. Typically, the time required to dissipate all excess pore water pressures at various consolidation stages of testing was less than about 1 min. The time required for the rate of creep to fall below 0.05%/h was on the order of 2 to 4 h.

#### 4.2.9.8 Drained Monotonic Axisymmetric Compression

Following the critical state framework, the intrinsic parameters  $\phi_c$ ,  $Q$  and  $R$  were determined through a systematic triaxial testing program in which specimens were subjected to drained monotonic axisymmetric compression. The compression stage of testing was terminated at an axial strain greater than or equal to 30%. For loose specimens (e.g. initial  $D_R = 16\%$ ) at high initial effective stress (e.g.  $p' = 400$  kPa) tests were terminated closer to 30% axial strain due to a fixed actuator length on the triaxial apparatus. The looser specimens isotropically compressed to a higher  $p'$  had a higher axial strain during isotropic compression and thus the height of the specimen before shear was less for dense specimens isotropically compressed to a lower  $p'$  before shear. For dense specimens (e.g. initial  $D_R = 64\%$ ) at low initial effective stress (e.g.  $p' = 100$  kPa) tests were able to be continued to an axial strain as high as 33.3%. All tests were performed under strain controlled conditions. In an effort to remove strain rate effects during analysis of results, all tests were conducted at an axial strain rate of 0.21%/min. The appropriate axial strain rate was determined after the first test using the approach

outlined by Head (1986). The axial strain rate used during testing was reduced from the value determined through Head's (1986) approach such that the chosen strain rate would be conservative for all future tests for both weathered and unweathered *MWR* materials. During axisymmetric compression, the specimen was subjected to double drainage.

#### 4.2.9.8.1 Area Corrections for Triaxial Results

During compression, the cross-sectional area, and subsequently the area of the shear plane(s) during shear, of triaxial test specimens does not remain constant. Numerous frameworks have been proposed to correct measured deviator stresses for this phenomenon (Henkel and Gilbert 1952, Head 1986, La Rochelle et al. 1988, ASTM D 4767, Baxter 2000). Out of the available frameworks to correct for changes in cross-sectional area, La Rochelle et al. (1988) was determined to be the most rigorous in regard to correcting triaxial test data based on the comprehensive analysis and systematic procedure that takes into account the volumetric response due to axial deformation as well as the specific failure mechanism observed during the triaxial test. Results presented in Chapter 5 were corrected according to the framework outlined by La Rochelle et al. (1988).

The framework proposed by La Rochelle et al. (1988) takes into account three failure mechanisms; (1) bulging failure (2) shear plane failure and (3) bulging and shear plane failure. Bulging failures, also known as barreling failures (Head 1986), are corrected according to La Rochelle et al (1988) using the assumption that the specimen deforms as a right cylinder. Specimens reconstituted to the loosest levels of  $D_R$  and isotropically

compressed to the highest levels of  $p'$  and sheared under drained conditions typically exhibit this type of failure. The corrected area,  $A_c$ , for bulging failure is calculated according to:

$$A_c = A_o \left( \frac{1 - \varepsilon_p}{1 - \varepsilon_a} \right) \quad (4.2)$$

where:  $A_c$  = corrected cross-sectional area of the deformed specimen,  $A_o$  = cross-sectional area of the specimen after isotropic compression,  $\varepsilon_a$  = axial strain during monotonic axisymmetric compression and  $\varepsilon_p$  = volumetric strain during monotonic axisymmetric compression.

Shear plane failures can be described as a failure of a right cylinder in which the only deformation of the sample takes place along a single shear plane. The top and bottom portions of the specimens act as rigid blocks and retain the facade of a right cylinder. For shear plane failures, the change in cross-sectional area is a function of the movement and the angle of inclination of the shear plane (La Rochelle et al. 1988). Typically, cemented soils, very stiff clays and clay shales exhibit a shear plane failure. The  $A_c$  for a shear plane failure can be calculated with the following:

$$A_c = \frac{d_o^2}{4} \left( \frac{\pi\theta}{180} - \sin(\theta) \right) \quad (4.3)$$

and

$$\theta = 2 \arccos \left( \frac{2\delta_e}{\tan(\alpha)} \right) \quad (4.4)$$

and

$$\delta_e = \frac{-\Delta h_p}{h_p} \quad (4.5)$$

where:  $d_o$  = initial specimen diameter,  $\alpha$  = angle of the shear plane with respect to the horizontal,  $h_p$  = height of the sample at the appearance of the shear plane should be taken at peak  $q$  as shear planes are only visible after peak  $q$  and  $\Delta h_p$  = decrease of height after shear plane appears.

More often than not, when a shear plane develops, the specimen being tested actually exhibits a combination of bulging and shear plane failures (with the possible exception of cemented soils and highly over consolidated shales). Typically, the specimen forms an elliptical shape where the shear plane extends the specimen further in one direction relative to the other. In this case, the shear plane develops at the peak of the stress-strain curve (La Rochelle et al. 1988) and Equation 4.2 is used for area correction until peak deviator stress occurs. Following peak deviator stress, the corrected area is calculated by the following:

$$A_c = A_p + (A_{ce} - A_f) \left( \frac{\varepsilon_a - \varepsilon_{ap}}{\varepsilon_{ea} - \varepsilon_{ap}} \right) \quad (4.6)$$

where:  $A_p$  = cross-sectional area at peak deviator stress,  $\varepsilon_a$  = axial strain,  $\varepsilon_{ap}$  = axial strain at peak deviator stress,  $\varepsilon_{ea}$  = axial strain at the end of the test and  $A_{ce}$  = cross-sectional area at the end of the test and is defined by:

$$A_{ce} = \frac{\pi}{4} d_a \cdot d_b \quad (4.7)$$

where:  $d_a$  and  $d_b$  are perpendicular specimen axes measured in the major and minor elliptical directions, respectively. In the case of shear plane failures, La Rochelle et al.

(1988) recommends that, at the end of the test, the actuator and backpressure be held constant (undrained conditions) while the cell is relieved of cell pressure and drained. Then, the cell can be dismantled and the final dimensions of the sample can be measured. The final specimen dimensions of the *MWR* specimens tested in this study were estimated from pictures of the samples at the end of the test.

Three specimens in this study exhibited a combination of a bulging and shear plane failures (U50-100, U70-100 and U75-400). The estimation of the final specimen dimensions through the aforementioned process introduces uncertainty in the results for a combination of bulging and shear plane failures if it is not done in a systematic and careful way. Thus, the critical state friction angle ( $\phi_c$ ) for each *MWR* material tested was systematically evaluated by excluding the tests exhibiting combined bulging and shear plane failures.

#### 4.2.9.8.2 Membrane Corrections for Triaxial Results

Similar to the area correction, the framework outlined by La Rochelle et al. (1988) was used to apply a correction for the effect of membrane restraint upon the sample. The first step in correcting for membrane restraint is to correct the specimen for the increase in initial confining pressure. The increase in initial confining pressure is a function of the elastic modulus and the initial diameters of the membrane and specimen (La Rochelle et al. 1998). Following the framework outlined by La Rochelle et al. (1988), the initial confining pressure applied to the specimen by the membrane can be calculated as follows:

$$p_{om} = 2E \left( \frac{d_o - d_{im}}{d_o \cdot d_{im}} \right) \quad (4.8)$$

where:  $p_{om}$  = initial confining pressure applied to the specimen by the membrane,  $E$  = elastic modulus (kN/m) of the membrane,  $d_o$  = diameter of specimen at the end of isotropic compression and  $d_{im}$  = initial diameter of the membrane. Due to the relative thinness of the membranes used in this study, the value of  $p_{om}$  was calculated as approximately 0.0002 kPa for each specimen. This value is below the resolution of the triaxial apparatus and data collection system used in this study and therefore was taken as zero for the membrane correction analyses.

The deformed shape of the membrane during isotropic compression and drained monotonic compression stages also affects where correction is applied, i.e. if the correction is applied to the effective axial stress,  $\sigma'_a$ , or the effective radial stress,  $\sigma'_r$ . If the membrane is held firmly against the membrane, the membrane acts as a reinforcing compression cell and is applied to the  $\sigma'_a$ . When the membrane buckles due to specimen deformation, the membrane acts as a reinforcing belt and the applied  $\sigma'_r$  is increased progressively throughout the test due to hoop stresses induced by the membrane (La Rochelle et al. 1988). Contrary to the large-scale triaxial tests performed by Fox (2011), all tests of both *MWR* materials were observed to have no lateral buckling of the membranes. In tests exhibiting only a bulging failure, the membrane was assumed to act as a reinforcing compression cell around the specimen. Based on the “compression theory”,  $\sigma'_a$  was reduced by the following:

$$\Delta\sigma'_a = \frac{\pi \cdot d_o \cdot E \cdot \varepsilon_a}{A_c} \quad (4.9)$$

where:  $\Delta\sigma'_a$  = decrease in effective axial stress due to membrane reinforcement,  $d_o$  = specimen diameter at the end of isotropic compression (m),  $E$  = elastic modulus of the membrane (kN/m),  $\varepsilon_a$  = axial strain (%) and  $A_c$  = corrected cross-sectional area of the deformed specimen (m<sup>2</sup>).

For the three tests exhibiting a combination of a bulging and shear plane failure, the effect of membrane restraint was applied to  $\sigma'_1$  by Equation 4.9 until peak strength was mobilized. Once peak strength, also known as the peak deviator stress,  $q = \sigma'_1 - \sigma'_3$ , the value of  $q$  was corrected for membrane straining along the direction of the shear plane (La Rochelle et al. 1988). The correction was calculated by the following:

$$\Delta(\sigma'_a - \sigma'_r)A_c = 1.5 \cdot \pi \cdot d_o \sqrt{E \cdot f \cdot d_o \cdot \delta} \quad (4.10)$$

where:  $\sigma'_a$  and  $\sigma'_r$  are the major and minor principal stresses (kPa), respectively,  $A_c$  = corrected cross-sectional area of the deformed specimen (m<sup>2</sup>),  $d_o$  = specimen diameter at the end of isotropic compression (m),  $E$  = elastic modulus of the membrane (kN/m),  $f$  = unit friction between the membrane and specimen and  $\delta$  = axial strain due to the movement along the shear plane. The variables  $f$  and  $\delta$  can be calculated by the following (La Rochelle et al. 1988):

$$f = \sigma'_3 \cdot \tan(\phi') \quad (4.11)$$

and

$$\delta = \delta_e \left( \frac{\varepsilon_a - \varepsilon_f}{\varepsilon_{ae} - \varepsilon_f} \right) \quad (4.12)$$

Due to the nature of the material's highly angular particles, multiple membranes were required to prevent puncture during testing. The elastic modulus of each membrane was determined for the two membranes used in the triaxial tests of this study according to the procedure outlined by ASTM D 4767, Section 10.4.3.2. The two types of membranes used were 0.3-mm and 0.6-mm thick. The tests on the weathered specimens were conducted using three of the 0.3-mm membranes while the unweathered specimens were tested using one 0.3-mm thick membrane and a 0.6-mm membrane. Tests were conducted by taking a 15-mm thick circumferential strip of membrane on a thin dowel and hanging premeasured weights to the end of the strip. A total of three weights were added to each membrane strip and the elastic modulus calculated for each weight addition. This procedure was carried out four times with four different membrane strips for both the 0.3-mm and 0.6-mm membranes. The values of the elastic moduli used in this study were taken as the combined average of the calculated values from the four sets of tests (a total of 12 values for each type of membrane). Results of the elastic modulus testing are presented in Table 4.10 and a complete set of calibration data is presented in Appendix F.

Table 4.10: Results of elastic modulus testing for each membrane type used during triaxial testing.

Thickness	0.3	0.6
$E$ (kN/m)	0.2	0.6
$E$ (kPa)	819	918

#### 4.2.10 Particle Breakage and Fractal Dimension

As discussed in Section 2.2.4, particle breakage consumes irrecoverable energy that was not previously accounted for in the original work equation presented by Taylor (1948) and subsequently Rowe's stress-dilatancy relationship (1962). Although there have been numerous attempts to quantify particle breakage (Marsal 1973, Miura and O-Hara 1979, Hardin 1985), quantification of particle breakage does not necessarily address the irrecoverable energy dissipation during axisymmetric compression. Not until McDowell et al. (1996) introduced an additional term to the Granta Gravel work equation, originally presented by Schofield and Wroth (1968), was it possible to take this irrecoverable energy dissipation into account. This study follows the approach outlined by McDowell et al. (1996) and Tarantino and Hyde (2005) to calculate the amount of irrecoverable energy dissipation during axisymmetric compression.

Particle breakage yields an increase in surface area within a specimen. As discussed in Section 3.3, the surface area and volume of each nominal particle size was determined by using the shape factors  $\beta_s$  and  $\beta_v$  presented by McDowell and Bolton (1998) in equations 3.27 and 3.28. Average values of  $\beta_s$  and  $\beta_v$  were calculated from the data presented by Marsal (1972) yielding values of  $\beta_s$  and  $\beta_v$  equal to 3.74 and 0.44, respectively.

Using the calculated surface area of each specimen, the fractal dimension,  $D$ , was determined for each specimen according to equation 3.30. Although some particle breakage occurred during the isotropic compression phases of each test, only the total particle breakage for both the isotropic compression phases and axisymmetric

compression stages combined was determined in this study. By reconstituting each sample using the parallel gradation technique, the initial gradations for either the weathered or unweathered *MWR* specimens were kept constant with  $D$  equal to 2.97 and 2.70, respectively. Immediately after each test was terminated, the specimens were oven dried and an after-test gradation was performed, surface area calculated and the new  $D$  determined for each specimen. Following the work presented by Tarantino and Hyde (2005), once a constant fractal dimension is achieved, the modified work equation (Equation 3.26) presented by McDowell et al. (1996) can be evaluated.

## CHAPTER 5: RESULTS

Throughout this chapter, results of the laboratory testing program for this study are presented. As mentioned previously in Chapter 4, Section 4.2.8 Triaxial Testing, specific test designations were given to each test to represent (1) the type of *MWR* material used, (2) the actual  $D_R$  achieved at the end of isotropic compression and (3) the nominal level of  $p'$  at the end of isotropic compression. For example, a weathered *MWR* specimen isotropically compressed to  $p' = 400$  kPa with  $D_R = 92\%$  will be referred to W92-400.

### 5.1 Isotropic Compression

Following back pressure saturation, specimens were isotropically compressed to  $p'$  values equal to 100, 200, or 400 kPa. Isotropic consolidation steps of  $p'$  equal to 30, 50, 100 kPa were used for specimens isotropically compressed to  $p'$  equal to 100 kPa. Isotropic consolidation steps of  $p'$  equal to 30, 50, 100, 200 kPa were used for specimens isotropically compressed to  $p'$  equal to 200 kPa. Isotropic consolidation steps of  $p'$  equal to 30, 100, 200, 400 kPa were used for specimens isotropically compressed to  $p'$  equal to 400 kPa. Results of isotropic compression are presented for the unweathered and weathered *MWR* specimens in specific volume,  $v$ , versus the natural logarithm of  $p'$  space on Figures 5.1 and 5.2, respectively.

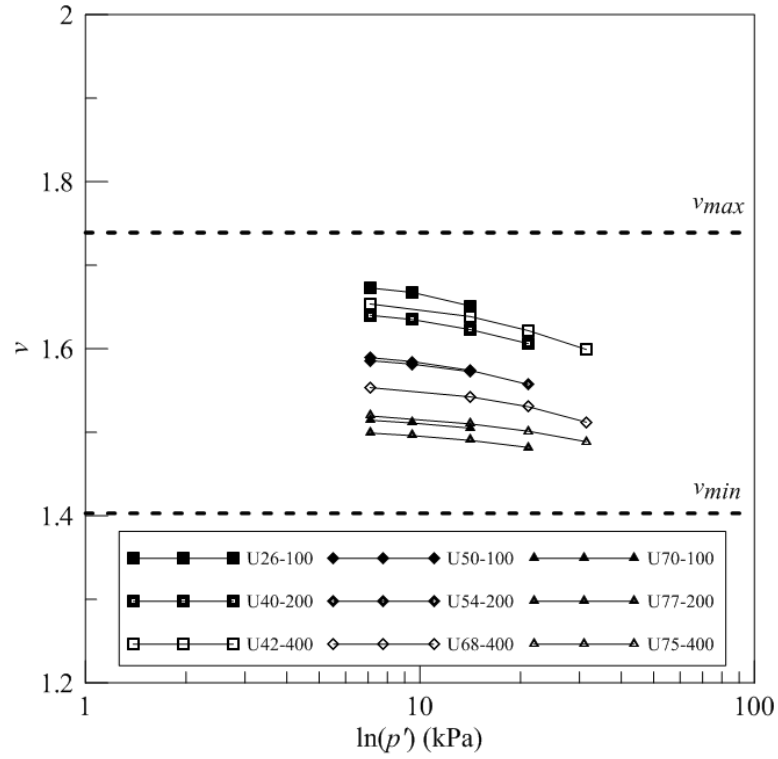


Figure 5.1: Isotropic compression data for unweathered MWR specimens.

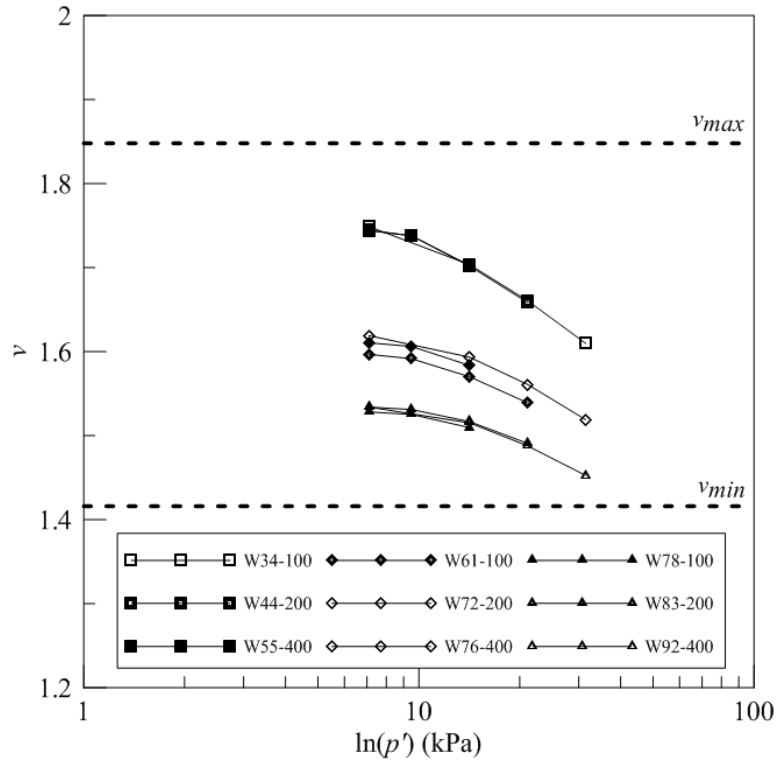


Figure 5.2: Isotropic compression data for weathered MWR specimens.

As previously mentioned in Chapter 4, Section 4.2.8.5 Back Pressure Saturation, due to the unavailability of radial strain transducers, specimen volume changes during flushing and back pressure saturation were estimated by assuming  $R_s$  is constant for a given material during the flushing, back pressure and isotropic compression stages of each test. The  $R_s$  for each material was determined using a linear best fit regression of isotropic compression data from each test. Regression of this data yields an R-squared value of 0.964 and 0.938 for the weathered and unweathered *MWR* materials, respectively. The data and best fit linear regression is presented on Figure 5.3.

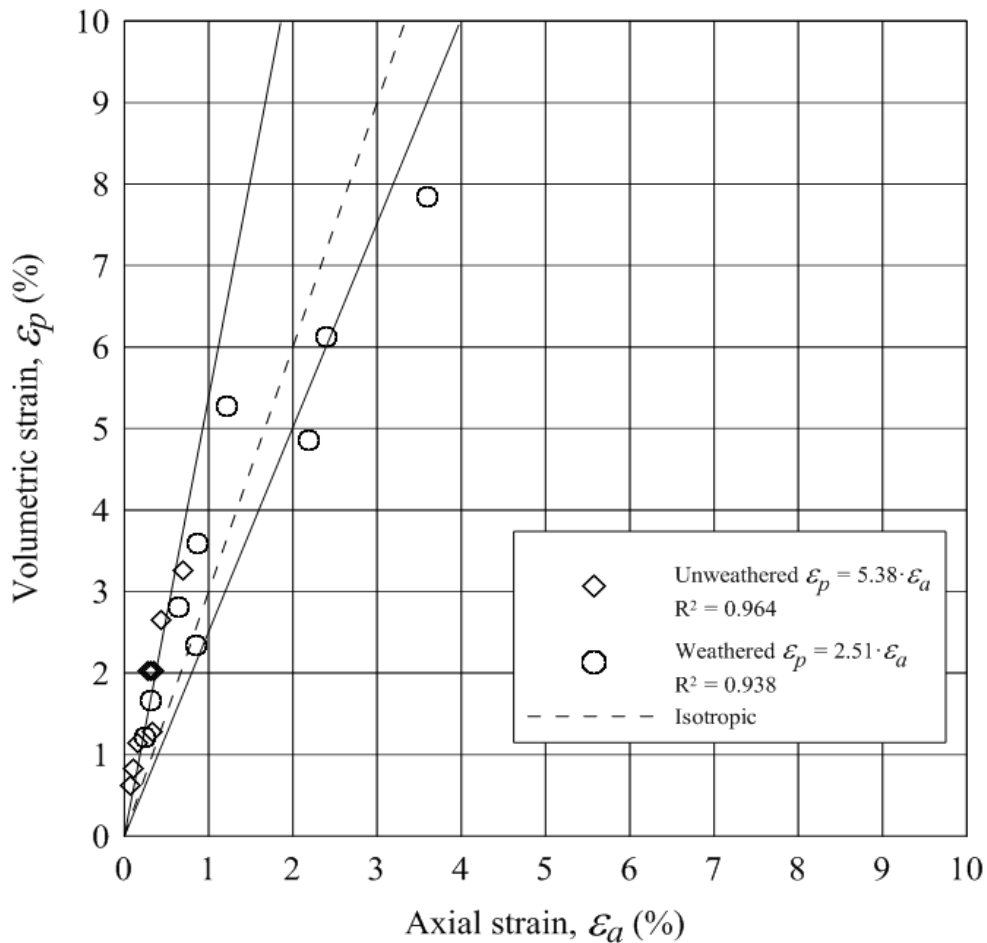


Figure 5.3: Isotropic compression data for unweathered MWR specimens. An isotropic response line is also included to give an indication of the level of anisotropic volumetric response during isotropic loading.

## 5.2 Drained Monotonic Loading

Drained monotonic axisymmetric compression tests were performed on the isotropically compressed specimens with  $p'$  equal to 100, 200 and 400 kPa and  $D_R$  values between 34 and 92 % and between 26 and 77 % and unweathered *MWR* materials, respectively. The displacement rate was held constant at 0.3 mm/min for each test corresponding to an axial strain rate of 0.21 %/min. As mentioned in Chapter 4, Section 4.2.8.8, this axial strain rate was determined after the first test using the approach outlined by Head (1986).

Plots of the variation of the deviatoric stress invariant  $q$  versus  $\epsilon_a$  and variation in  $\epsilon_p$  versus  $\epsilon_a$  are presented on Figures 5.4 and 5.5 for the unweathered *MWR* specimens, respectively. As previously mentioned in Chapter 4, Sections 4.2.8.8.1 and 4.2.8.8.2, the formation of a shear band leads to uncertainty in the area and membrane corrections due to the lack of post test specimen diameter measurements. Thus, tests which exhibited shear bands (U75-400, U70-100, and U50-100) are plotted in Figure 5.4 with dashed lines after peak deviator stress to indicate the uncertainty due to area and membrane corrections. Similar to the tests on the weathered *MWR* material, critical state was defined as the final data point at maximum axial strain.

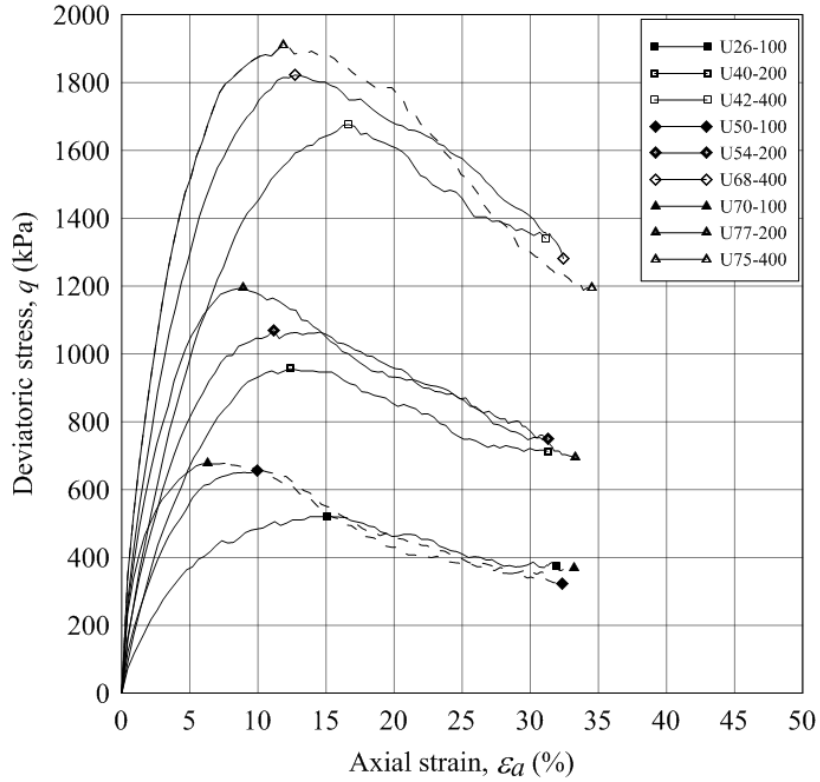


Figure 5.4: Deviatoric stress versus axial strain for unweathered *MWR* specimens. The two plotted data points for each test represent peak and critical state stress states.

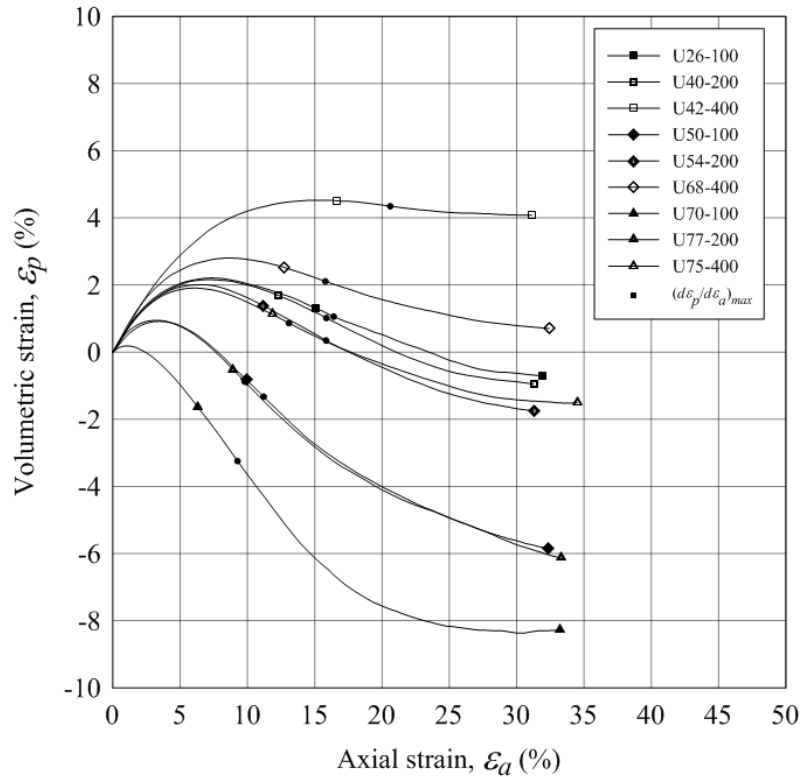


Figure 5.5: Volumetric strain versus axial strain for unweathered specimens. The two plotted data points for each test represent peak and critical state stress states.

Plots of the variation of the deviatoric stress invariant  $q$  versus  $\epsilon_a$  and variation in  $\epsilon_p$  versus  $\epsilon_a$  are presented on Figures 5.6 and 5.7 for the weathered *MWR* specimens, respectively. For all tests, critical state was defined as the final data point at maximum axial strain. The final data point represents the best estimate of the critical state condition of the specimen in each test as they approach a constant state of stress. A constant state of stress is defined as constant  $p'$ ,  $q$ , and  $v$  with continued axial strain.

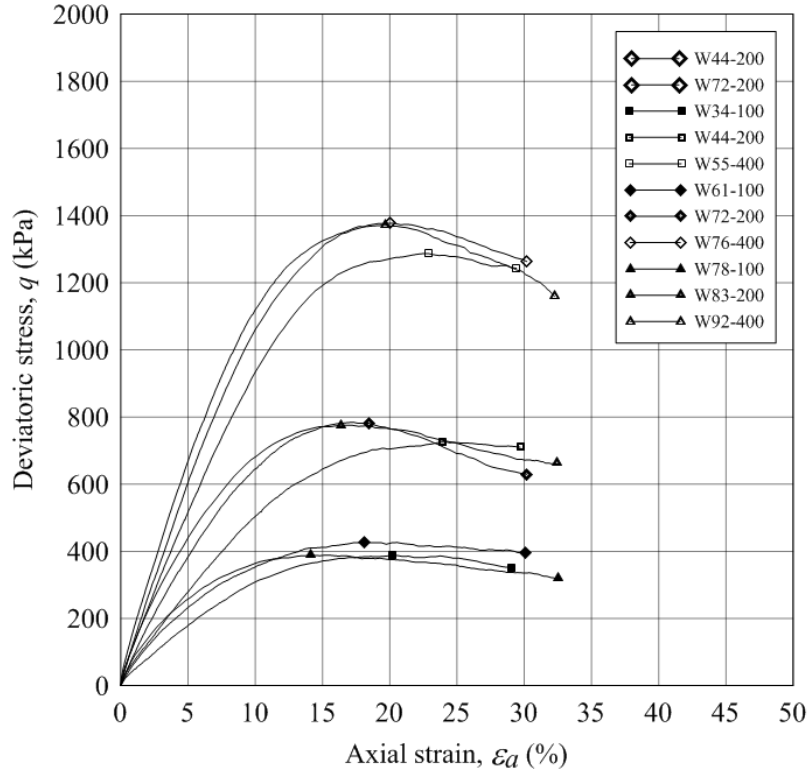


Figure 5.6: Deviatoric stress versus axial strain for weathered *MWR* specimens. The two plotted data points for each test represent peak and critical state stress states.

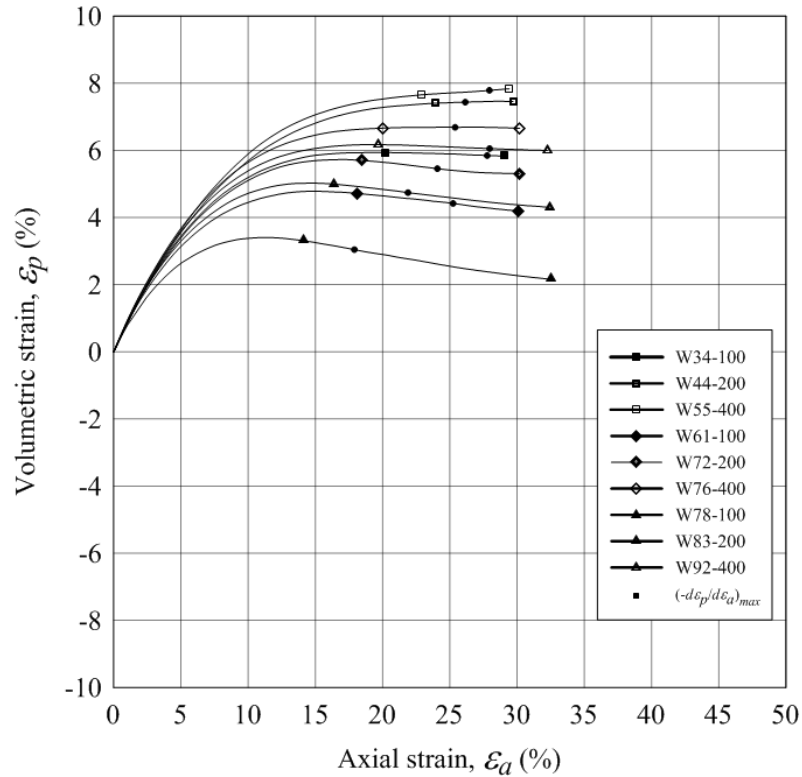


Figure 5.7: Volumetric strain versus axial strain for weathered specimens. The two plotted data points for each test represent peak and critical state stress states.

Effective stress paths in terms of stress invariants  $p'$  and  $q$  are presented on Figures 5.8 and 5.9 for the unweathered and weathered *MWR* specimens, respectively.

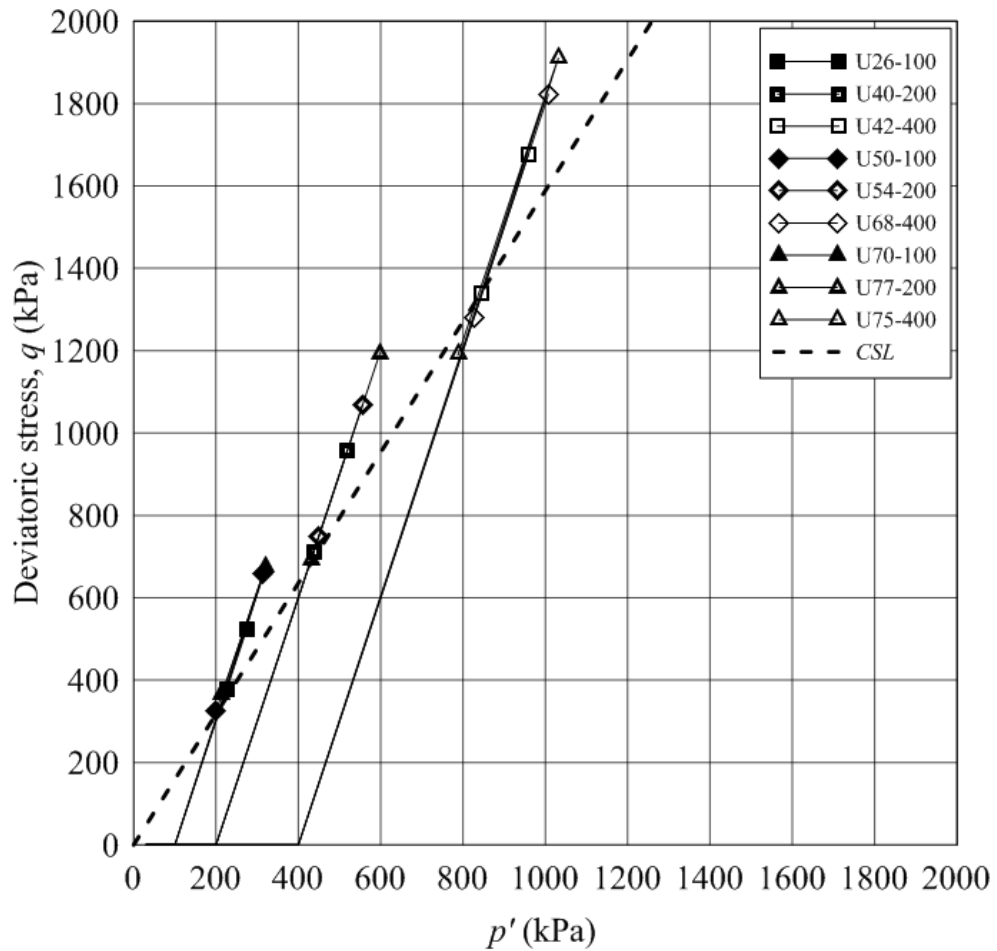


Figure 5.8: Volumetric strain versus axial strain for unweathered specimens. The two plotted data points for each test represent peak and critical state stress states.

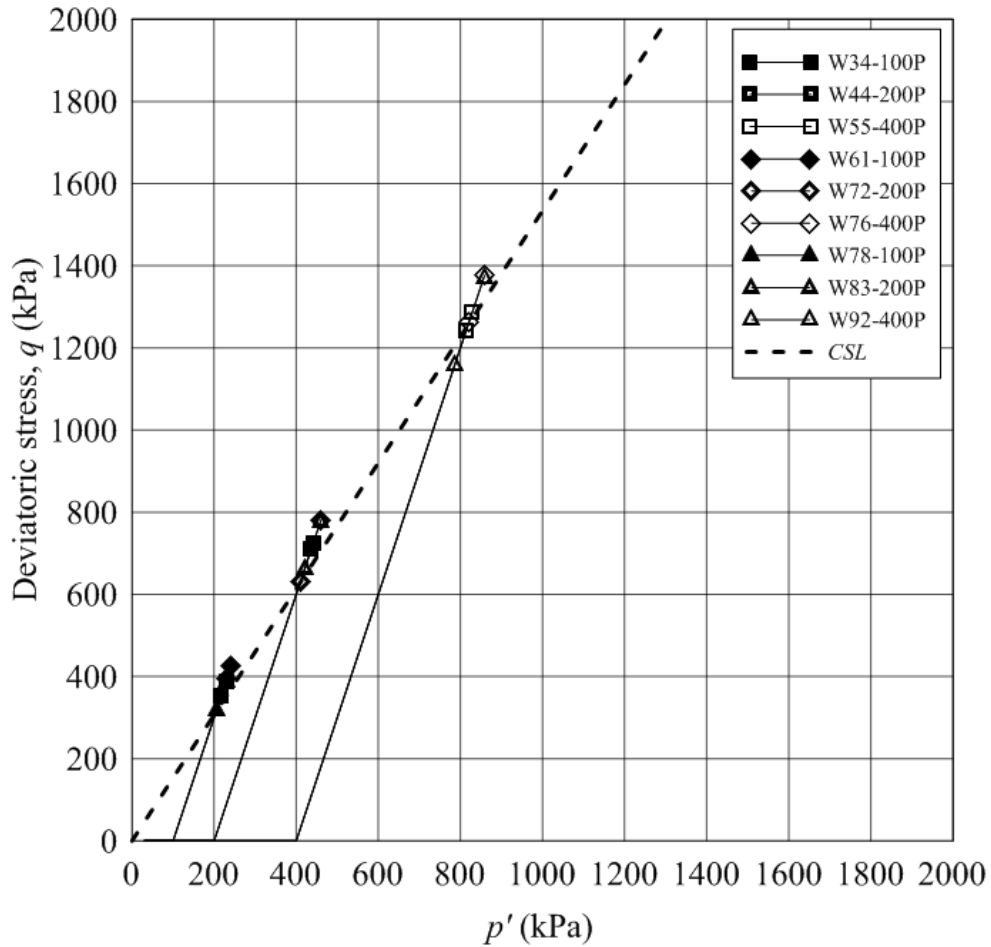


Figure 5.9: Volumetric strain versus axial strain for weathered specimens. The two plotted data points for each test represent peak and critical state stress states.

Results are tabulated for each test performed for the unweathered and weathered *MWR* specimens in Tables 5.1 and 5.2, respectively. Values of mobilized peak and critical state friction angles ( $\phi_p$  and  $\phi_c$ ) are presented along with their corresponding states in terms of  $p'$  and  $D_R$  after initial specimen set up (e.g.  $D_{R, Initial}$ ), after flushing and back pressure saturation stages (e.g.  $D_{R, AS}$ ) as well as after isotropic compression before the start of drained monotonic axisymmetric compression (e.g.  $D_{R, AC}$ ). The average value of  $\phi_c$  presented in Tables 5.1 and 5.2 are calculated using only  $\phi_c$  values that were measured without the formation of a shear band during the monotonic axisymmetric compression.

Specimens exhibiting a purely bulging failure are denoted by “B” under the “Failure Type” where specimens exhibiting bulging and shear bands during monotonic axisymmetric compression are denoted by “B-S”. Critical state values of  $p'$ ,  $q$  and  $v$  are also tabulated for each test in Tables 5.1 and 5.2 and are designated  $p'_{cs}$ ,  $q_{cs}$  and  $v_{cs}$ . The maximum dilatancy rate observed during each test,  $(-\delta\varepsilon_p/\delta\varepsilon_a)_{max}$ , is also tabulated.

Table 5.1: Results of triaxial tests performed with unweathered *MWR* material.

Test	U26-100	U50-100	U70-100	U40-200	U54-200	U77-200	U42-400	U68-400	U75-400	Avg.
$p'$ (kPa)	100	100	100	200	200	200	400	400	400	--
$D_{R, initial}$ (%)	16	43	64	22	43	68	20	51	64	--
$D_{R, AS}$ (%)	20	46	67	29	45	71	25	55	65	--
$D_{R, AC}$ (%)	26	50	70	40	54	77	42	68	75	--
$\phi_p$ (deg)	46	50	50	45	47	49	43	44	45	--
$\phi_c$ (deg)	41	40	38	40	41	39	39	38	37	39.6
$v_{cs}$	1.66	1.66	1.63	1.62	1.58	1.57	1.53	1.50	1.51	--
$p'_{cs}$ (kPa)	225	200	214	437	450	431	847	827	789	--
$q_{cs}$ (kPa)	376	324	367	712	749	694	1340	1281	1194	--
$(-\delta\varepsilon_p/\delta\varepsilon_a)_{max}$	0.182	0.390	0.544	0.196	0.218	0.410	0.052	0.132	0.203	--
Failure Type	B	B-S	B-S	B	B	B	B	B	B-S	--
$B$	1.00	1.00	0.98	1.00	0.98	1.00	0.98	0.98	0.98	--

Table 5.2: Results of triaxial tests performed with weathered *MWR* material.

Test	W34-100	W61-100	W78-100	W44-200	W72-200	W83-200	W55-400	W76-400	W92-400	Avg.
$p'$ (kPa)	100	100	100	200	200	200	400	400	400	--
$D_{R, Initial}$ (%)	17	52	71	19	56	71	16	49	71	--
$D_{R, AS}$ (%)	24	55	74	24	58	73	23	53	73	--
$D_{R, AC}$ (%)	34	61	78	44	72	83	55	76	92	--
$\phi_p$ (deg)	41	43	41	40	41	41	38	39	39	--
$\phi_c$ (deg)	40	42	38	40	38	39	38	38	36	38.7
$v_{cs}$	1.60	1.52	1.48	1.53	1.46	1.43	1.48	1.42	1.37	--
$p'_{cs}$ (kPa)	217	232	206	437	410	421	814	821	786	--
$q_{cs}$ (kPa)	351	395	318	710	629	662	1243	1263	1159	--
$(-\delta\varepsilon_p/\delta\varepsilon_a)_{max}$	0.013	0.043	0.070	-0.007	0.042	0.047	-0.017	0.007	0.013	--
Failure Type	B	B	B	B	B	B	B	B	B	--
$B$	0.98	1.00	0.98	0.98	0.99	0.98	0.98	0.98	0.98	--

### 5.3 Particle Breakage

Through the course of this study, particle breakage was quantified by performing a particle size distribution analysis on each specimen after each triaxial test was completed according to ASTM D 6913, Method B. The upper bound for which all post test gradations fall beneath is presented graphically on Figure 5.10 for each material. Results for pre and post gradations for each triaxial test are presented in Appendix B.

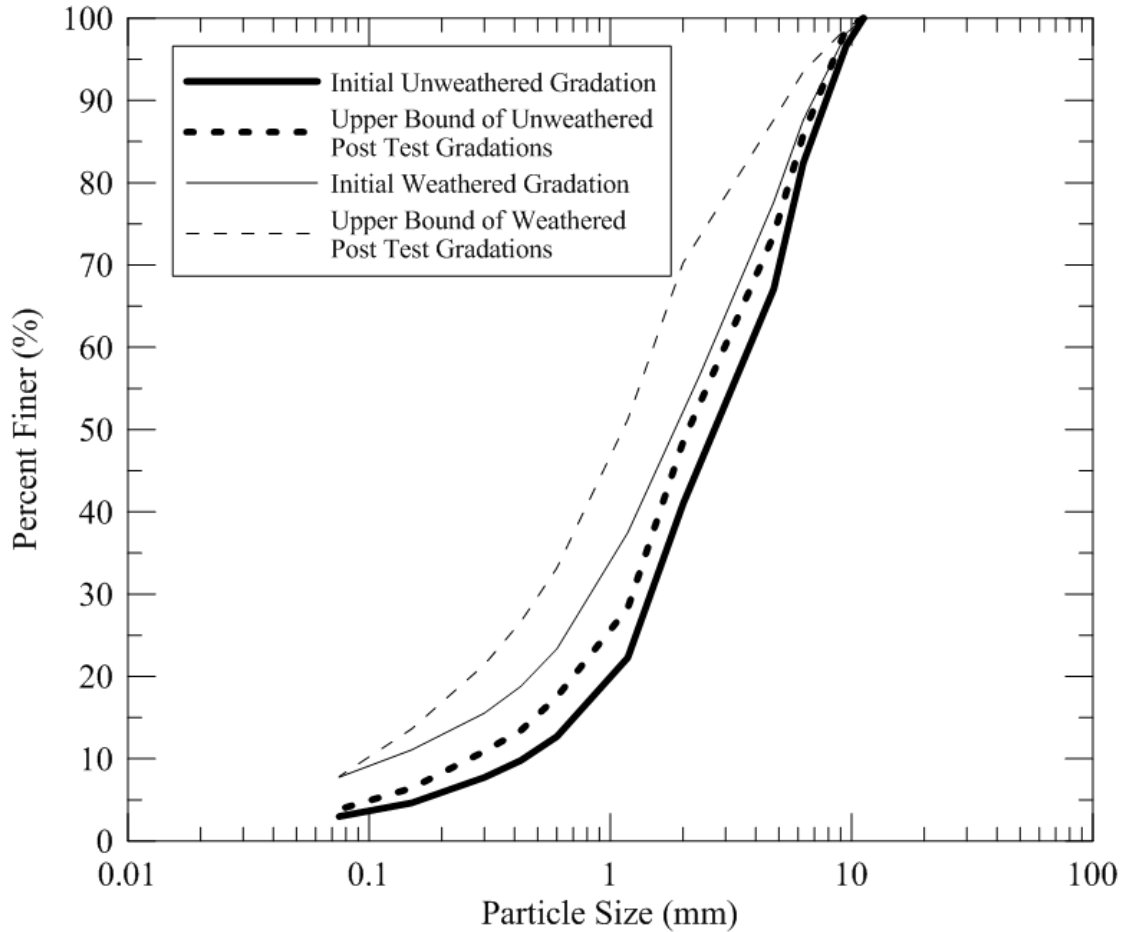


Figure 5.10: Upper bounds of post test gradations for the unweathered and weathered *MWR* material.

#### 5.4 Fractal Dimension

The fractal dimension,  $D$ , was determined for each specimen following each test. As discussed in Chapter 4, Section 4.2.9, once a constant  $D$  is achieved, the modified work equation (Equation 3.26) presented by McDowell et al. (1996) can be evaluated. The initial  $D$ ,  $D_{Initial}$ , for each material was determined for each materials respective model gradation that was scaled down from the collected field gradation using the parallel gradation technique. The  $D_{Initial}$  for the weathered *MWR* material was equal to 2.97

where the  $D_{Initial}$  for the unweathered *MWR* material was 2.70. Tables 5.3 and 5.4 demonstrate the advancement from  $D_{Initial}$  to the final  $D$ ,  $D_{Final}$ , after testing at various levels of  $p'$  and  $D_R$ . The cumulative change in  $D$ ,  $\Delta D$ , represents the change in  $D$  due to the combined effects of isotropic and drained monotonic axisymmetric compression. Results the evolution of  $D$  are plotted on Figure 5.11 for the unweathered and weathered *MWR* materials. The dashed lines on Figure 5.11 represents the average path which  $D$  evolves for each material and was determined by plotting the line through the average  $D$  for each specific value of  $p'$  (i.e. 100, 200, and 400 kPa). The average value of  $D$  at  $p' = 400$  kPa was taken as the  $D_{Final}$  for each material and is plotted as a solid line on Figure 5.11. This  $D_{Final}$  value is the best estimate for the constant fractal dimension as defined by Tarantino and Hyde (2005).

Table 5.3: Values of  $D$  before and after testing for unweathered specimens.

Test	$D_{Initial}$	$D_{Final}$	$\Delta D$
U26-100	2.70	2.76	0.06
U50-100	2.70	2.76	0.06
U70-100	2.70	2.77	0.07
U40-200	2.70	2.80	0.10
U54-200	2.70	2.78	0.09
U77-200	2.70	2.78	0.09
U42-400	2.70	2.88	0.18
U68-400	2.70	2.83	0.13
U75-400	2.70	2.85	0.15

Table 5.4: Values of  $D$  before and after testing for weathered specimens.

Test	$D_{Initial}$	$D_{Final}$	$\Delta D$
W34-100	2.97	3.10	0.14
W61-100	2.97	3.12	0.15
W78-100	2.97	3.13	0.17
W44-200	2.97	3.16	0.19
W72-200	2.97	3.13	0.17
W83-200	2.97	3.14	0.18
W55-400	2.97	3.16	0.20
W76-400	2.97	3.16	0.19
W92-400	2.97	3.17	0.20

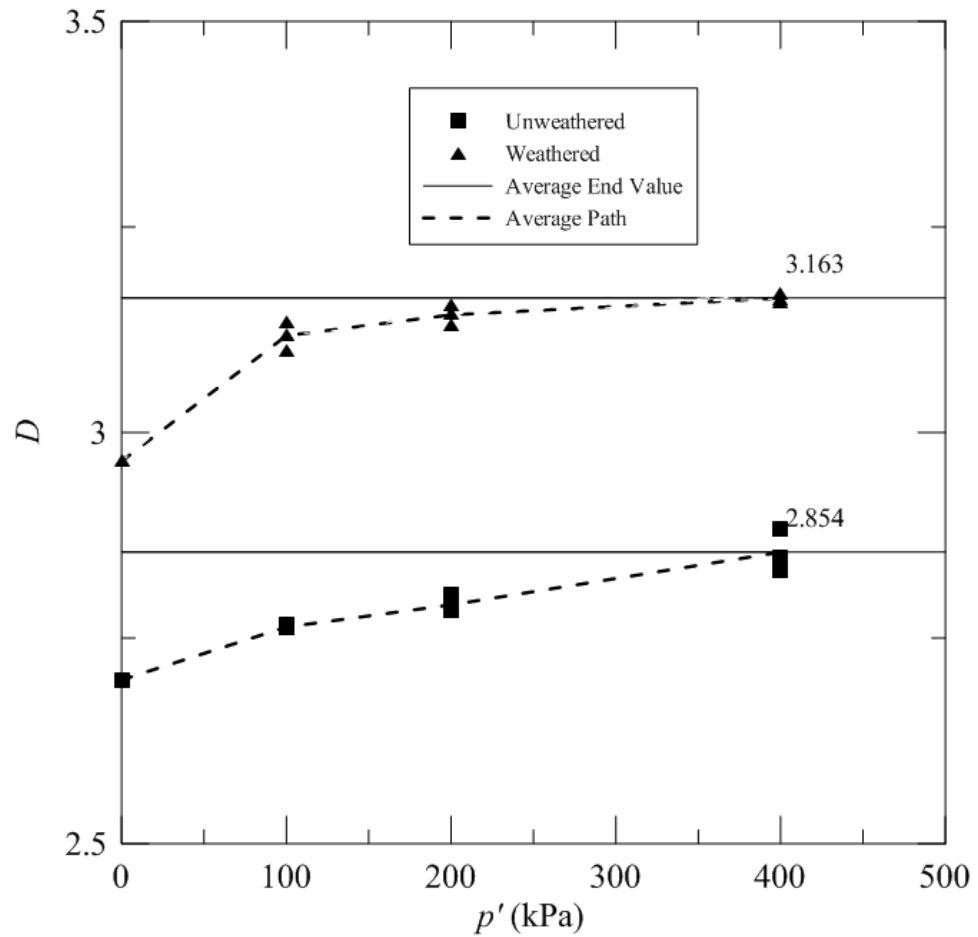


Figure 5.11: Evolution of the fractal dimension,  $D$ , for the unweathered and weathered *MWR* materials.

## CHAPTER 6: ANALYSIS OF RESULTS

As previously discussed, this study was designed to systematically evaluate the intrinsic parameters of the weathered and unweathered *MWR* in conventional scale (70-mm diameter) drained monotonic axisymmetric compression as well as the effect of state variables on their mechanical behavior. In addition to these objectives, particle size and sample scaling effects were evaluated by systematically comparing results for 70-mm-diameter triaxial specimens to the test results presented by Fox (2011) for 150-mm-diameter triaxial specimens.

Although the weathered and unweathered *MWR* materials tested in this study were obtained from the same site and yielded similar particle size distributions, the mechanical response of the two materials exhibit remarkably different characteristics in index testing as well as mechanical behavior. This chapter will discuss some of the observed differences in the mechanical response of the two materials as well as systematically compare results obtained as part of this study to results of the study conducted by Fox (2011).

### 6.1 Limiting Void Ratios

The limiting void ratios measured in the course of this study present interesting results when compared to the limiting void ratios in the study conducted by Fox (2011). Results of limiting void ratio tests are tabulated for both the present study and the study carried out by Fox (2011) in Table 6.1.

Table 6.1: Limiting void ratios, fines content and sample-size ratios from Fox (2011) and the present study

	$e_{min}$	$e_{max}$	$FC$ (%)	$d_{50}$ (mm)	$d_{max}$ (mm)	$SSR$
Unweathered MWR (Fox 2011)	0.360	0.753	1.7	6.8	25	11.2
Unweathered MWR (This study)	0.403	0.739	3.0	3.2	11.2	13.7
Weathered MWR (Fox 2011)	0.420	0.803	4.9	4.3	25	11.2
Weathered MWR (This study)	0.416	0.848	7.8	1.9	11.2	13.7

The  $e_{min}$  and  $e_{max}$  decreased for the unweathered *MWR* material whereas a slight decrease in  $e_{min}$  and increase in  $e_{max}$  was observed for the weathered *MWR* material with decreasing maximum particle size. These results are not directly comparable due to the slight differences in testing methods (i.e. mold size and *SSR*) and differences in *FC*. A number of explanations can be postulated to explain the discrepancy in the results presented above for both *MWR* materials including, but not limited to: fines content, fines plasticity, mineralogy, and particle shape.

Research has shown that *FC* plays a significant role in a materials maximum and minimum void ratio (Townsend 1973, Pitmen et al 1994, Lade et al. 1998, Carraro 2004, Cho et al. 2006, Lade et al. 2009). Figure 6.1 schematically illustrates this point with results from Lade et al. (2009) showing the effect of *FC* on silty Ottawa sand with non plastic Loch Raven Fines. It should be noted that Figure 6.1 is presented here for illustration purposes only. Analysis of the effects of *FC* on the index properties of *MWR* is not in the scope of this study and therefore additional limiting void ratio tests with

varying amounts of fines were not conducted. Therefore a systematic comparison of the results presented by Lade et al. (2009) and the results of the present study would be merely speculation.

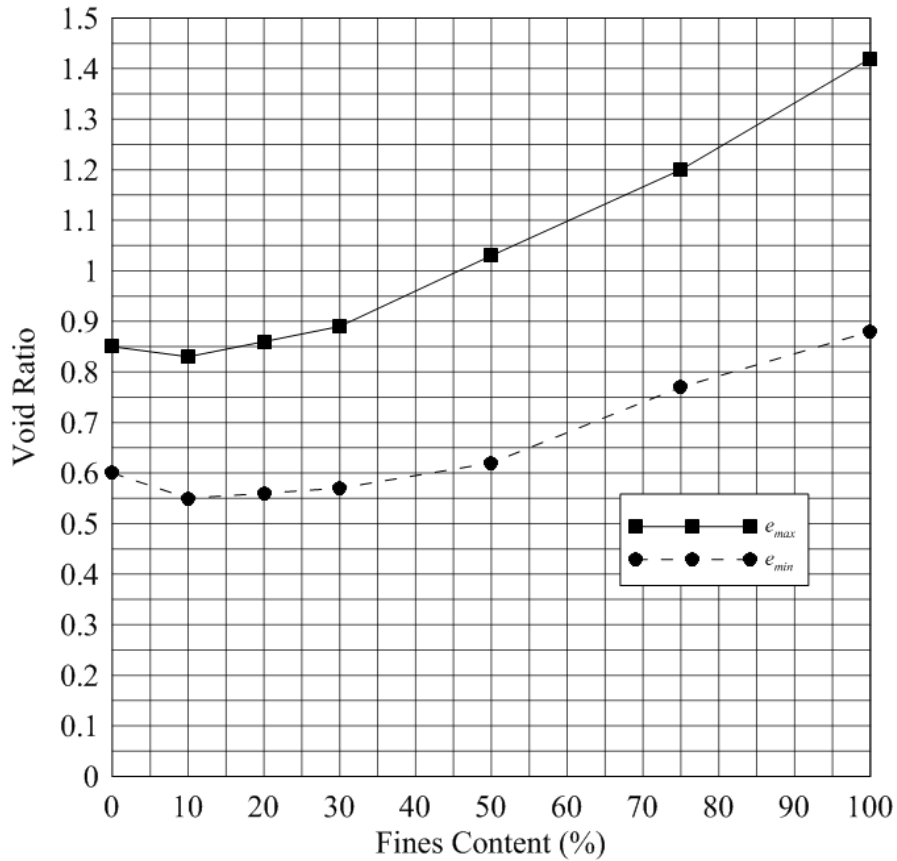


Figure 6.1: The effect of fines content on a silty sand containing fine Ottawa sand and non-plastic Loch Raven fines (Modified after Lade 2009).

The intrinsic characteristics of the fines such as mineralogy and plasticity also affect the limiting void ratios of a material (Townsend 1973, Pitman et al. 1994, Carraro 2004). While the fines in the unweathered material exhibited no plasticity, the fines in the weathered *MWR* material yielded a plasticity index,  $I_p$ , of 10%. Increased plasticity and *XRD* results indicate an evolution in material mineralogy during *in-situ* hydrogeologic weathering.

Finally, particle shape has shown to play a pivotal role in the limiting void ratios of a given material (Cho et al. 2006). Cho et al. (2006) defined three variables to illustrate the effect of particle shape on the limiting void ratios of a material: roundness (R), sphericity (S) and particle regularity ( $\rho$ ). Each variable is measured on a scale of 0 to 1. Roundness is defined as 1 for a perfect sphere and 0 for a highly angular, plate-like particle. Sphericity is defined as the ratio of the maximum interior radius,  $r_{max-in}$ , to the minimum radius in which the particle will be fully encapsulated by a circle,  $r_{min-cir}$ . A perfect sphere would yield a sphericity value of 1 where a rectangular plate like particle will yield a sphericity value of 0. Figure 6.2 illustrates the relationship between particle shape and sphericity in terms of  $r_{max-in}$  and  $r_{min-cir}$ . Particle regularity is computed as the average between roundness and sphericity. Each variable is determined by comparing two dimensional photographs to the chart presented on Figure 6.2. Limiting void ratios increase as  $\rho$  decreases, corresponding to an increase in either particle angularity and/or eccentricity (Cho et al. 2006). It should be noted that two dimensional photographs of each material were not taken during the course of this study and the parameters presented by Cho et al. (2006) were not calculated. Therefore Figure 6.2 is presented for illustration purposes only and further research into the role that particle shape plays in the limiting void ratios of *MWR* is suggested.

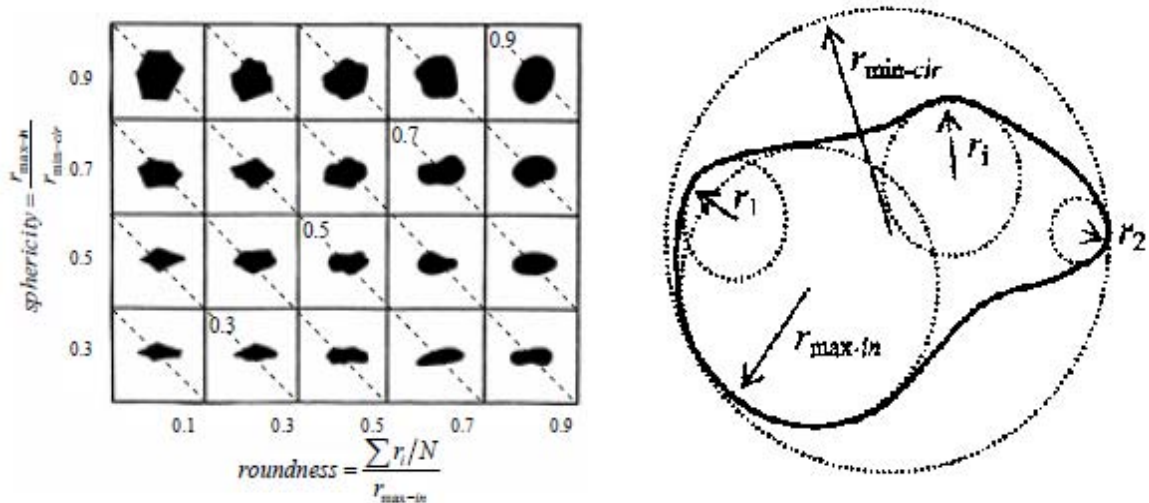


Figure 6.2: Sphericity ( $S$ ) and roundness ( $R$ ) chart. Diagonal dotted lines correspond to constant particle regularity  $\rho=(R+S)/2$  (Cho et al. 2006).

Summarizing analyses for the limiting void ratio results, a combination of effects related to the methods used, increase in  $FC$ , plasticity of the fines, mineralogical evolution, and particle shape. Other factors may have played a role in the values of the limiting void ratios measured for each material and are beyond the scope of this study.

## 6.2 Isotropic Compression

As discussed previously in Section 4.2.8 (Triaxial Testing), specific test designations were given to each test to represent (1) the type of  $MWR$  material used, (2) the actual  $D_R$  achieved at the end of isotropic compression and (3) the nominal level of  $p'$  at the end of isotropic compression. For example, a weathered  $MWR$  specimen isotropically compressed to  $p' = 400$  kPa with  $D_R = 92\%$  will be referred to W92-400. In the next section, results of drained monotonic axisymmetric compression will be analyzed in terms of the  $D_R$  achieved after isotropic compression (i.e. the specimen state at the beginning of axisymmetric compression) at constant  $p'$ . However, in the case of isotropic

compression, an important factor to consider is the state of the specimen at the beginning of isotropic compression, not the beginning of shear.

Both *MWR* materials were subjected to various isotropic compression increments to final levels of  $p'$  equal to 100, 200 or 400 kPa. All specimens were initially reconstituted to a value of  $p'$  equal to 30 kPa. Intermediate stages of  $p'$  were 50 and/or 100 and 200 kPa depending on the final level of  $p'$  for each specimen. For all unweathered triaxial specimens, the levels of  $p'$  were not sufficiently high enough to achieve a unique normal compression line (*NCL*). As such, specimens were observed to follow an unloading-reloading line (*URL*) in  $\ln(p') - v$  space during isotropic compression depending upon the state of the specimen prior to isotropic compression. The slope of the *URL* ( $\kappa$ ) in  $\ln(p') - v$  space and the value of  $v$  at  $p' = 1\text{kPa}$  ( $v_\kappa$ ) depend on  $D_{R, Initial}$  for each specimen (McDowell et al. 2002, Been and Jefferies 2000, Muir-Wood 1990). For the weathered triaxial specimens, seven specimens exhibited yielding behavior and a *NCL* was achieved and irrecoverable plastic strains occurred. Specimens that exhibited yielding behavior during isotropic compression were observed to initially follow an *URL* and, once yielding occurred, specimens followed a unique *NCL* in  $\ln(p') - v$  space defined by  $\lambda$  and  $N$  where  $\lambda$  is the slope of the *NCL* and  $N$  is the value  $v$  at  $p' = 1\text{kPa}$ . The unique *NCL* for each specimen depended on the state of the specimen prior to isotropic compression. While the *NCL* is considered intrinsic to a given geomaterial, subtle changes in fabric and uniformity between specimens as well as particle breakage during isotropic compression may change the shape of the *NCL* for each specimen tested. Isotropic compression data for all unweathered and weathered *MWR* specimens are presented on Figures 5.1 and 5.2,

respectively. Building off of Figures 5.1 and 5.2, isotropic compression data plotted with the corresponding *URL* and *NCL* (for applicable weathered specimens) for each test is presented on Figures 6.3 and 6.4 for unweathered and weathered *MWR* tests, respectively. Critical state parameters  $\kappa$ ,  $v_\kappa$ ,  $\lambda$  and  $N$  were determined by logarithmic regression for each test, where applicable, for both *MWR* materials and are tabulated in Table 6.2. Values of  $\kappa$  and  $v_\kappa$  were determined by logarithmic regression of data points with  $p' < p'_{\text{yield}}$  where values of  $\lambda$  and  $N$  were determined by logarithmic regression of data points with  $p' > p'_{\text{yield}}$ .

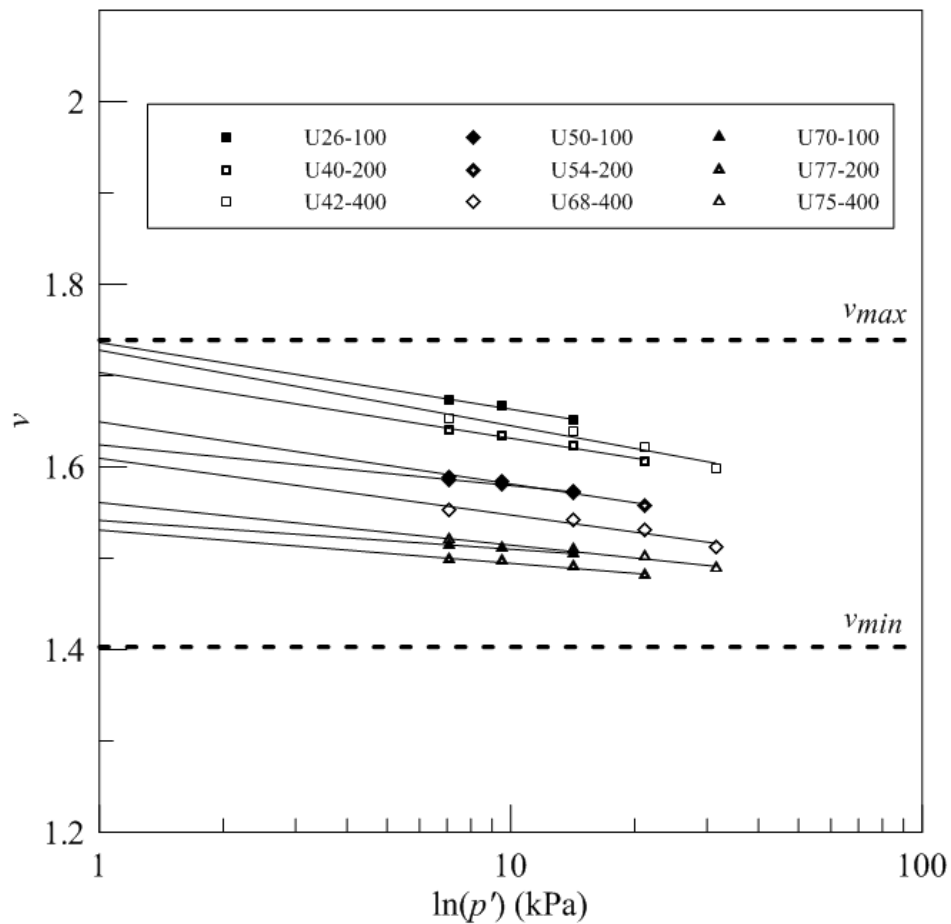


Figure 6.3: Unloading-reloading lines for unweathered *MWR* specimens.

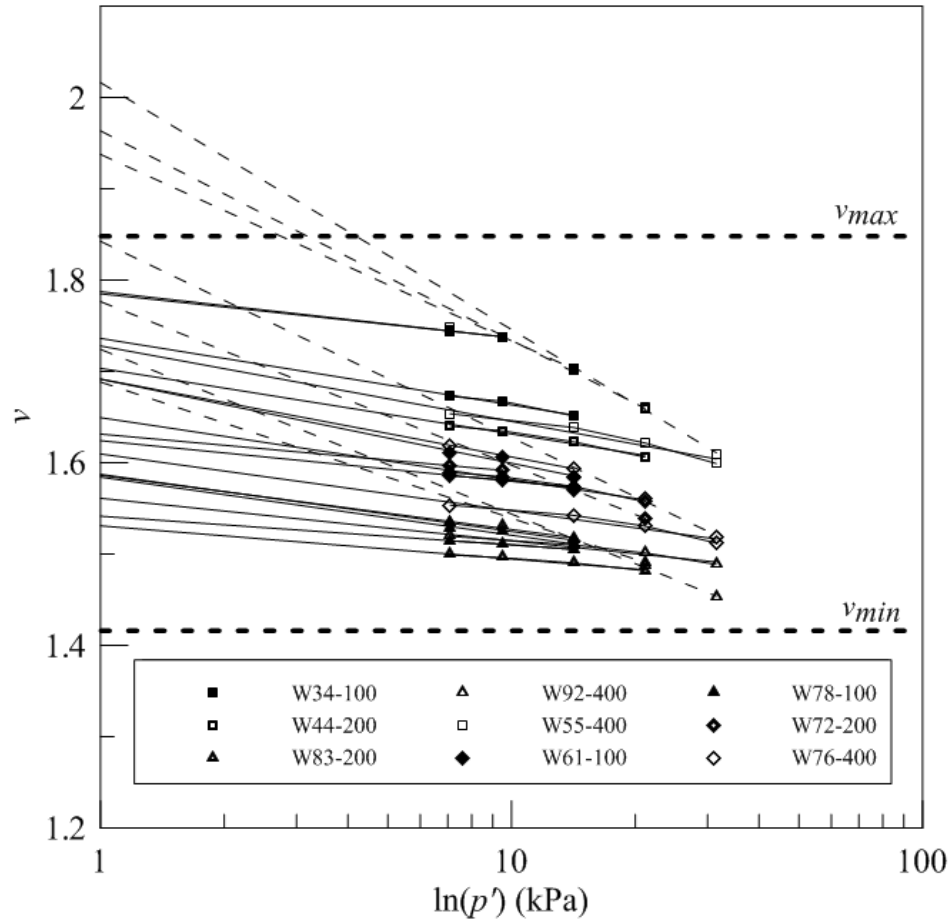


Figure 6.4: Unloading-reloading lines (solid) and normal compression lines (dashed) for weathered *MWR* specimens.

Table 6.2: Critical state parameters  $\kappa$ ,  $\nu_\kappa$ ,  $\lambda$  and  $N$  determined after isotropic compression for unweathered and weathered *MWR* specimens.

Test	$D_{R, Initial}$ (%)	$\kappa$	$\nu_\kappa$	$R^{2(1)}$	$\lambda^{(2)}$	$N^{(2)}$	$R^{2(1)}$
U26-100	16	0.018	1.74	0.96	--	--	--
U50-100	43	0.011	1.62	0.99	--	--	--
U70-100	64	0.008	1.54	0.99	--	--	--
U40-200	22	0.018	1.70	0.97	--	--	--
U54-200	43	0.017	1.65	0.97	--	--	--
U77-200	68	0.009	1.53	0.98	--	--	--
U42-400	20	0.021	1.73	0.95	--	--	--
U68-400	51	0.016	1.61	0.94	--	--	--
U75-400	64	0.012	1.56	0.96	--	--	--
W34-100	17	0.012	1.79	--	0.051	1.94	--
W61-100	52	0.023	1.69	0.92	--	--	--
W78-100	71	0.016	1.58	0.92	--	--	--
W44-200	19	0.013	1.79	--	0.057	1.96	1.00
W72-200	56	0.010	1.63	--	0.045	1.78	--
W83-200	71	0.015	1.59	0.93	0.037	1.69	--
W55-400	16	--	--	--	0.068	2.02	1.00
W76-400	49	0.021	1.69	--	0.054	1.84	0.99
W92-400	71	0.016	1.59	--	0.045	1.72	0.99

<sup>1</sup> Coefficient of determination values were not calculated for data sets with less than three data points

<sup>2</sup> Value determination was not applicable to results observed for the specific test indicated by "--"

The range of  $\kappa$  values determined for the unweathered and weathered *MWR* materials was 0.008 – 0.021 and 0.010 – 0.023, respectively. The range  $\nu_\kappa$  values determined for the unweathered and weathered *MWR* materials were 1.53 – 1.74 and 1.58 – 1.79, respectively. In both cases, the values of measured critical state parameters during isotropic compression for unweathered material were consistently less than those measured for the weathered material. Similarly, the variability of the measured  $\kappa$  and  $\nu_\kappa$  values indicate a lower variability in the unweathered *MWR* material compared to that of the weathered *MWR* material indicated by the magnitude of the range of values measured. The increased values of the critical state parameters  $\kappa$  and  $\nu_\kappa$  for the weathered *MWR* material indicates higher compressibility in the weathered *MWR* material for the same  $p'$

range used. Also  $\kappa$  and  $\nu_\kappa$  were found to increase with decreasing  $D_R$  and increasing  $p'$  for both materials. As the critical state parameters  $\kappa$  and  $\nu_\kappa$  are directly related to the compressibility of the material and compressibility of geomaterials increases with decreasing  $D_R$  and increasing  $p'$  the afore mentioned results are to be expected. Table 6.3 provides a comparison of the extreme values of  $\kappa$  and  $\nu_\kappa$  for each material.

The higher compressibility in the weathered material compared to that of the unweathered is caused by a combination of several factors including but not limited to: increased  $FC$ , increased plasticity, reduced particle strength (Fox 2011), and differences in the fabric of the material. Due to this increased compressibility, the  $p'_{\text{yield}}$  for the weathered material is less than that of the unweathered material. Therefore determination of the critical state parameters  $\lambda$  and  $N$  (mathematically describing the  $NCL$  in  $\ln(p') - v$  space) is possible. Extreme values of the critical state parameters  $\lambda$  and  $N$  are presented in Table 6.3. Comparison of these values against the unweathered material is not possible due to the apparent fact that significantly higher values of  $p'$  are required to achieve plastic yielding in the unweathered material compared to the weathered material.

Table 6.3: Extreme values of critical state parameters  $\kappa$ ,  $\nu_\kappa$ ,  $\lambda$  and  $N$  determined after isotropic compression for unweathered and weathered *MWR*

Material	Unweathered <i>MWR</i>	Weathered <i>MWR</i>
Maximum $D_R$ (%)	77	92
Minimum $D_R$ (%)	26	34
Maximum $\kappa$	0.021	0.023
Minimum $\kappa$	0.008	0.010
Maximum $\nu_\kappa$	1.74	1.79
Minimum $\nu_\kappa$	1.53	1.58
Maximum $\lambda$ <sup>1</sup>	--	0.068
Minimum $\lambda$ <sup>1</sup>	--	0.037
Maximum $N$ <sup>1</sup>	--	2.02
Minimum $N$ <sup>1</sup>	--	1.69

<sup>1</sup> Value determination was not applicable to results observed for the specific test indicated by "--"

While the *URL* is directly related to the  $D_{R, Initial}$  to which the specimens were reconstituted (McDowell et al. 2002, Been and Jefferies 2000, Muir-Wood 1990), the *NCL* is considered an intrinsic property of a given geomaterial (Muir-Wood 1990). While the effect of *FC* and specimen fabric was not evaluated in the course of this study, the effect of particle strength on compressibility can be evaluated. As previously discussed, particle breakage may occur during isotropic compression. Been and Jefferies (2000) propose that particle breakage during isotropic compression of sands has a direct impact on the shape of not only the *URL* but also the *NCL*. Point load test results presented by Fox (2011) indicate that the unweathered material is approximately 10 times stronger than the weathered material which would suggest that more particle breakage may occur during isotropic compression in the weathered material compared the unweathered material. Thus, an increase in material compressibility due to particle breakage may be expected in the weathered *MWR* material. Because particle breakage

was not measured just for the isotropic compression stage of triaxial testing, particle breakage possibly affecting the shape of the *URL* and *NCL* for the two *MWR* materials is only suggested as one of the plausible explanations of the results presented above. Other factors such as increased *FC*, increased plasticity, and differences in the fabric of the material may also play a role. Further systematic research into the role that particle breakage plays on the shape of the *URL* and *NCL* during isotropic compression is recommended.

### 6.3 Drained Monotonic Axisymmetric Compression

While results for all triaxial tests are presented in Chapter 5 and Appendix C, this section will focus on selected tests performed on each material in order to compare the mechanical response of the two materials. During triaxial testing, several specimens from each material were isotropically compressed to similar levels of  $D_R$  and  $p'$ . Similar levels of  $D_R$  at the same  $p'$  allows for a systematic comparison of the mechanical response of the two *MWR* materials.

#### 6.3.1 Typical Stress-Strain-Volumetric Response

Observed mechanical responses of the two *MWR* materials at similar states (i.e. same/similar  $D_R$  at the same  $p'$ ) are noticeably different before peak strength is mobilized. Figures 6.5 and 6.6 show the stress-strain and volumetric-axial strain response of unweathered and weathered *MWR* material specimens with similar states. Data presented on Figures 6.5 and 6.6 are plotted as lines due to the large number of data points used to generate the plot. In general, the unweathered *MWR* material exhibited strain softening

behavior after peak strength is mobilized where strain hardening behavior was observed for the weathered *MWR* material. Volumetric responses indicate the stronger tendency for dilation in the unweathered material versus the weathered material. In all cases, the weathered material exhibited a net contractive volumetric response where only two specimens (U42-400 and U68-400) exhibited a net contractive volumetric response. Although the weathered material exhibited net contraction during drained monotonic loading, a slight dilative response occurred at strains greater than 12% for most tests. Two weathered tests (W44-200 and W55-400) did not ever dilate during loading and exhibited purely contractive behavior towards critical state. These results are expected due to the relatively low  $D_R$  at higher levels of  $p'$ . As in the case for non crushable geomaterials, the point of peak strength and  $(-\delta\varepsilon_p/\delta\varepsilon_a)_{max}$  should occur at the same  $\varepsilon_a$ . For geomaterials comprised of crushable grains, as is the case with both *MWR* materials tested in this study, the peak strength is mobilized before  $(-\delta\varepsilon_p/\delta\varepsilon_a)_{max}$  occurs due to the irrecoverable energy dissipation associated with particle breakage (McDowell and Bolton 1996). Peak dilatancy rates,  $(-\delta\varepsilon_p/\delta\varepsilon_a)_{max}$ , observed in the unweathered material were generally an order of magnitude higher than the weathered material indicating an increased tendency for particle breakage in the weathered material (Coop et al. 2004). An increase in *FC* and fines plasticity may also play a role in the reduced magnitudes of  $(-\delta\varepsilon_p/\delta\varepsilon_a)_{max}$ . Average values of  $(-\delta\varepsilon_p/\delta\varepsilon_a)_{max}$  were determined to be 0.259 and 0.025 for the unweathered and weathered *MWR*, respectively. Tabulated values of  $(-\delta\varepsilon_p/\delta\varepsilon_a)_{max}$  are presented in Table 6.4 for each triaxial test.

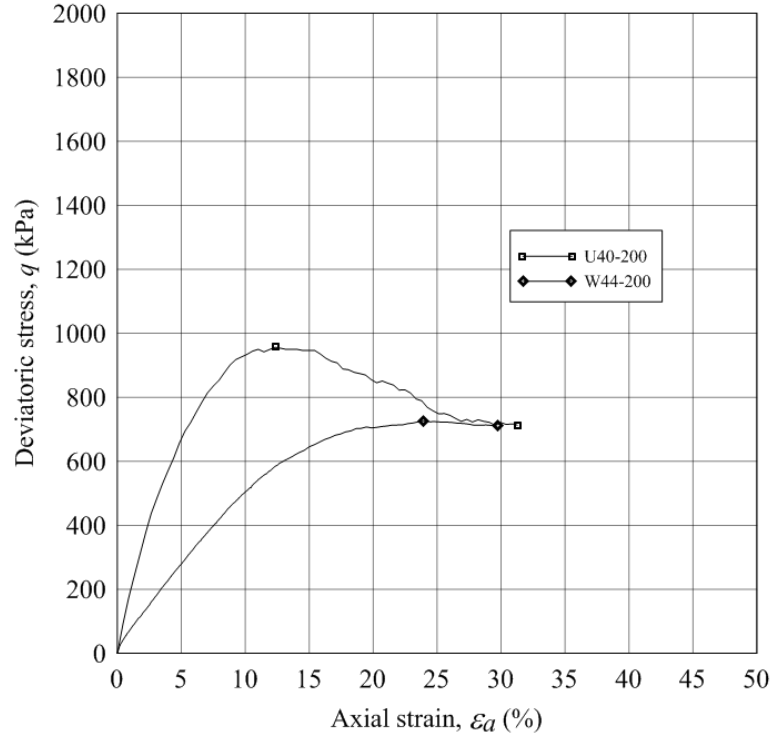


Figure 6.5: Deviatoric stress versus axial strain for unweathered and weathered *MWR* materials isotropically compressed to similar states at the same  $p'$ . The two plotted data points for each test represent peak and critical state stress states.

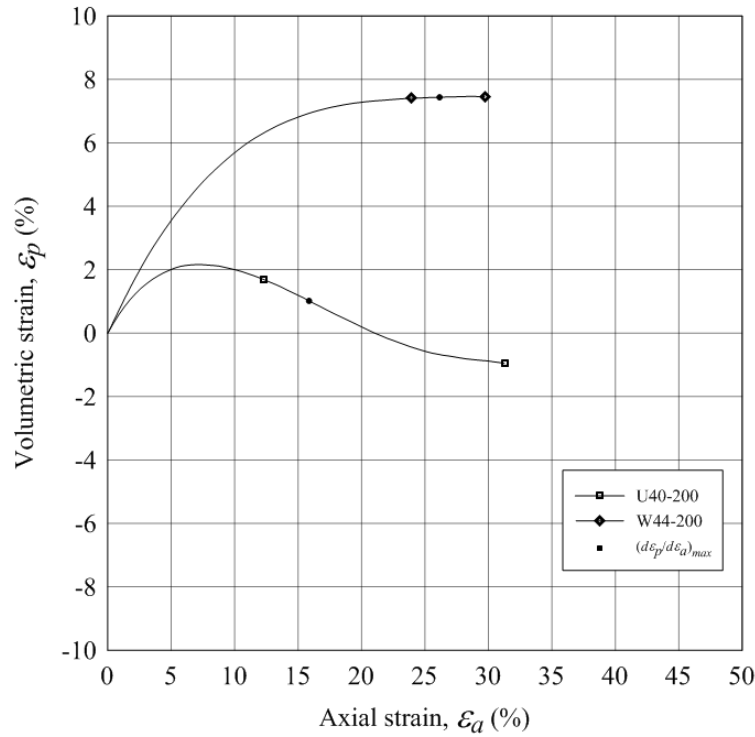


Figure 6.6: Volumetric strain versus axial strain for unweathered and weathered *MWR* materials isotropically compressed to similar states at the same  $p'$ . The two plotted data points for each test represent peak and critical state stress states.

Table 6.4: Tabulated values of  $(-\delta\varepsilon_p/\delta\varepsilon_a)_{max}$  during drained monotonic axisymmetric compression for unweathered and weathered *MWR* specimens

Test	$(-\delta\varepsilon_p/\delta\varepsilon_a)_{max}$	Average
U26-100	0.182	0.259
U50-100	0.390	
U70-100	0.544	
U40-200	0.196	
U54-200	0.218	
U77-200	0.410	
U42-400	0.052	
U68-400	0.132	
U75-400	0.203	
W34-100	0.013	
W61-100	0.043	
W78-100	0.070	
W44-200	-0.007	
W72-200	0.042	
W83-200	0.047	
W55-400	-0.017	
W76-400	0.007	
W92-400	0.013	

### 6.3.2 Critical State Friction Angle

As discussed previously, critical state was defined as the point of maximum axial strain for each test. Two specific methods were employed to determine the critical state friction angle: the first, based on the location of the critical state line in  $p' - q$  space, and the second, from specific test results on specimens reconstituted to the loosest levels of  $D_R$  and highest levels of  $p'$ . Regression of the *CSL* in  $p' - q$  space, Figure 6.7, yields values of  $M$  equal to 1.59 and 1.55 for the unweathered and weathered *MWR* materials, respectively. Test results from specimens exhibiting shear bands during monotonic axisymmetric compression were omitted from the regression due to the uncertainty with membrane and area corrections. Three specific tests from the unweathered material

exhibited shear bands (U50-100, U75-400 and U70-100) while the weathered material did not exhibit visual shear bands during shear during any test. Using Equation 3.10, the value of  $\phi_c$  can be determined. Using the location of the *CSL* in  $p' - q$  space to calculate  $\phi_c$  yielded values of  $40.1^\circ$  and  $38.1^\circ$  for the unweathered and weathered *MWR* materials, respectively. Coefficient of determinations ( $R^2$ ) for both materials yielded values of 0.999. For the unweathered *MWR* material,  $M$  and  $\phi_c$  were determined by omitting the tests where specimens exhibited shear bands during monotonic axisymmetric compression. Tabulated values of  $M$  are presented in Table 6.5.

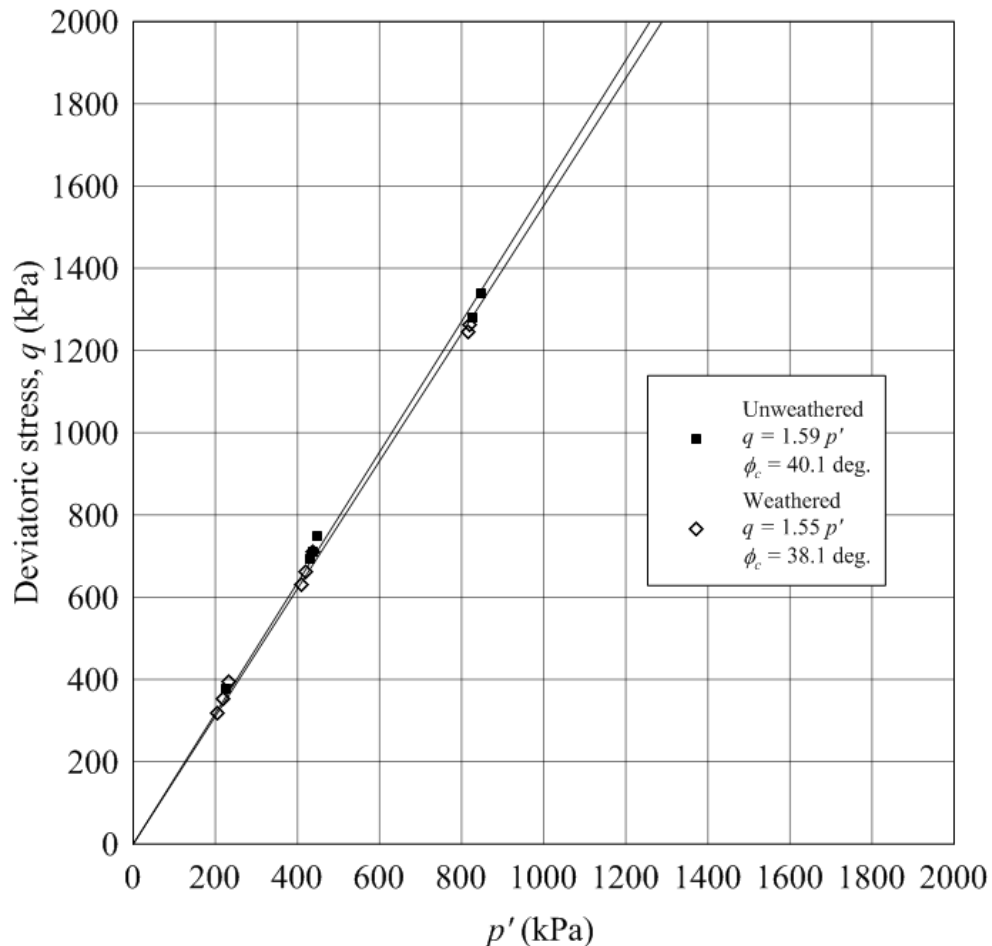


Figure 6.7: *CSL* in  $p' - q$  space for unweathered and weathered *MWR* materials with a linear best fit value of  $M$  and the corresponding value of  $\phi_c$  (tests exhibiting shear bands during drained monotonic axisymmetric compression for the unweathered material were omitted).

Plotting the location of the *CSL* in  $\ln(p')$  -  $\nu$  space, Figure 6.8, allows the determination of the intrinsic critical state parameters  $\lambda_{cs}$  and  $\Gamma_{cs}$  (Muir-Wood 1990). Values of  $\lambda_{cs}$  and  $\Gamma_{cs}$  determined by regression of the *CSL* in  $\ln(p')$  -  $\nu$  space are tabulated in Table 6.5. Regression of the *CSL* in  $\ln(p')$  -  $\nu$  space for the unweathered and weathered *MWR* yielded  $R^2$  values of 0.885 and 0.431, respectively. While the  $R^2$  value for the unweathered *MWR* material shows relatively good correlation between the presented data, the weathered material indicates highly variable critical state values, as is evident on Figure 6.8. The highly variable results of critical state when plotted in  $\ln(p')$  -  $\nu$  space may be attributed to factors such as: the individual particle strength, increased *FC* and increased fines plasticity.

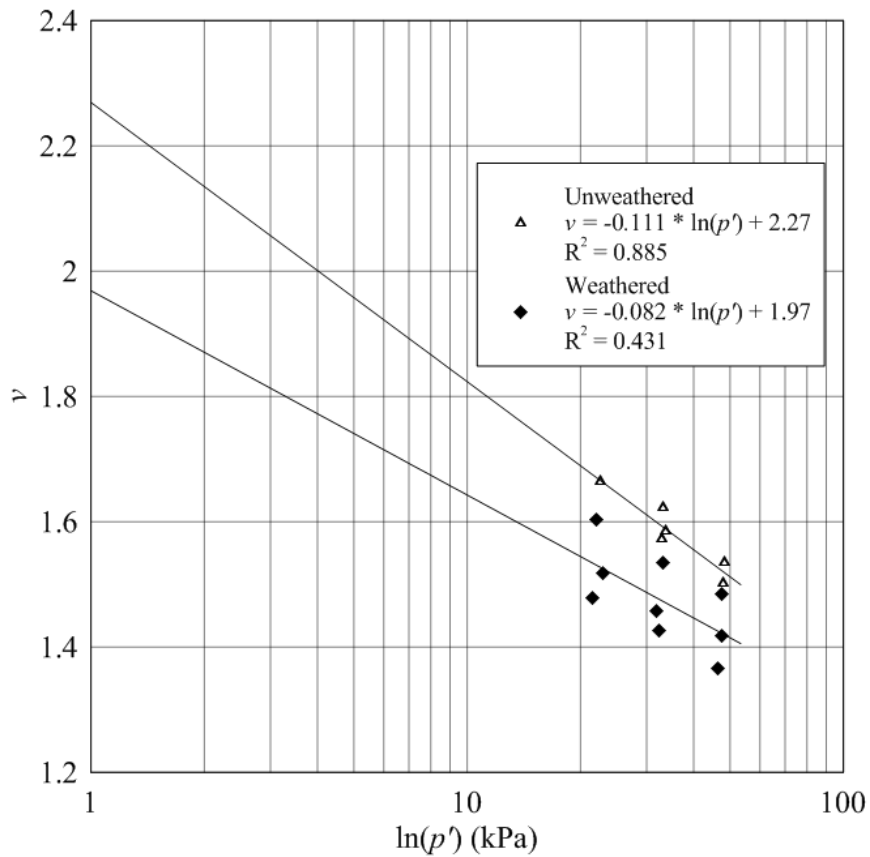


Figure 6.8: *CSL* in  $\ln(p')$  -  $\nu$  space for unweathered and weathered *MWR* materials with a logarithmic best fit values of  $\lambda_{cs}$  and  $\Gamma_{cs}$  (tests exhibiting shear bands during drained monotonic axisymmetric compression for the unweathered material were omitted).

Table 6.5: Tabulated values of intrinsic critical state parameters  $M$ ,  $\lambda_{cs}$  and  $\Gamma_{cs}$  determined for unweathered and weathered  $MWR$

	$M$	$\lambda_{cs}$	$\Gamma_{cs}$
Unweathered	1.59	0.111	2.27
Weathered	1.55	0.082	1.97

As previously discussed, data presented by Fox (2011) indicates the particle strength of the unweathered material is approximately 10 times greater than that of the weathered material. Weaker particle strength goes hand in hand with increased particle breakage during shear. Particle breakage during shear is accompanied by additional volumetric compression such that a state of constant stress and, most importantly, constant volume is even more difficult to achieve over the range of strains experienced in traditional triaxial tests (Coop et al. 2004). Other factors such as increased  $FC$  and increased fines plasticity may also increase difficulty in achieving constant volume of the weathered material. Figures 6.9 and 6.10 show the paths taken by each specimen at the beginning of shear to the point of maximum axial strain in  $\ln(p') - v$  space for the unweathered and weathered material, respectively. Data presented on Figures 6.9 and 6.10 show the strong tendency for the unweathered material towards dilation and volumetric expansion. Conversely, the weathered material tends almost exclusively towards volumetric contraction. Data presented by Coop et al. (2004) on friable Dog's Bay sand indicates it may take extremely large strains (up to 11,000%) to reach a constant grading in crushable geomaterials. However, data suggests that the mobilized angle of shearing resistance at conventional levels of axial strain is not significantly different than that of the "true"  $\phi_c$  mobilized at enormously large strains. Therefore, for the course of this study, the value of  $\phi_c$  measured for the weathered  $MWR$  material at the points of maximum axial strain was deemed appropriate. Nevertheless, the assumption of critical state at the point of

maximum axial strain (about 30%) for the weathered material yields poor correlation between the data and a low  $R^2$  when regressing the  $CSL$  in  $\ln(p') - v$  space. Variations in fabric and amounts of particle breakage may influence the poor correlation as these factors influence the formation of a certain “critical packing” of grains at which continuous flow is possible at constant  $p'$ .

While the unweathered material did not exhibit plastic yielding behavior during isotropic compression, the weathered material did in several tests. Comparison of values of  $\lambda_{cs}$  and  $\lambda$  for the weathered material show an increase in the value of  $\lambda$  during shear from an average value of 0.051 to 0.082. While the value of  $\lambda$  should remain constant for a given material with non crushable grains (Schofield and Wroth 1968, Muir-Wood 1990), the slight increase may be attributed to particle breakage during shear. Because the value of  $\lambda$  is related to the compressibility of the material and particle breakage during shear increases a specimen's compressibility (Coop et al. 2004). The value of  $\Gamma_{cs}$  measured for the weathered material shows a very good correlation with the value of  $N$  for specimens isotropically compressed to the loosest levels of  $D_R$ . The increased value of  $\Gamma_{cs}$  compared to the average value of  $N$  determined for the weathered material may be attributed to the increased compressibility of the material and correspondingly the increased value of  $\lambda$ . As Figure 6.10 shows, the weathered material was primarily on the “wet” side of the  $CSL$  and primarily exhibited contractive behavior during shear (Schofield and Wroth 1968).

Because the unweathered material did not exhibit yielding during isotropic compression, the differences in values of  $\lambda$  and  $N$  cannot be compared to those of  $\lambda_{cs}$  and  $\Gamma_{cs}$ . However,

the relatively good coefficient of determination determined through regression of the *CSL* in  $\ln(p')$  -  $v$  space suggests the material is less compressible than the weathered material (supported by isotropic compression data as well) and tends towards relatively constant values of  $\lambda_{cs}$  and  $\Gamma_{cs}$ . The unweathered material exhibited behavior indicating it is on the “dry” side of the *CSL* (Figure 6.9) and the tendency to dilate during shear is expected (Schofield and Wroth 1968).

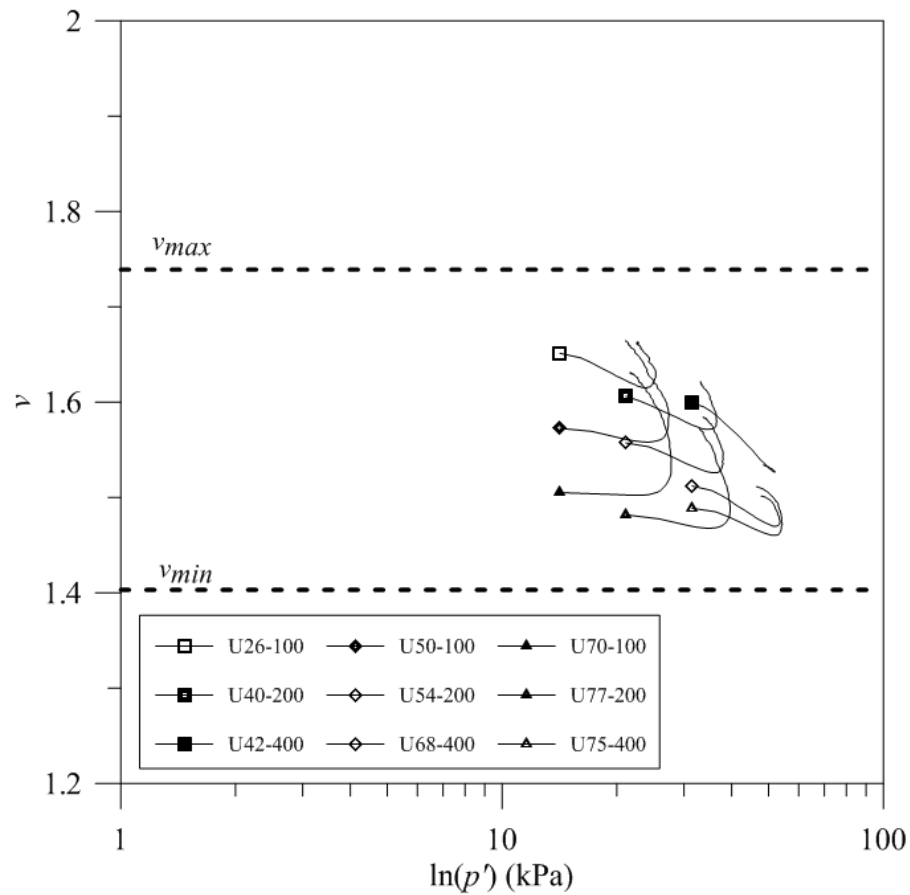


Figure 6.9: Shearing paths in  $\ln(p')$  -  $v$  space for unweathered *MWR* material.

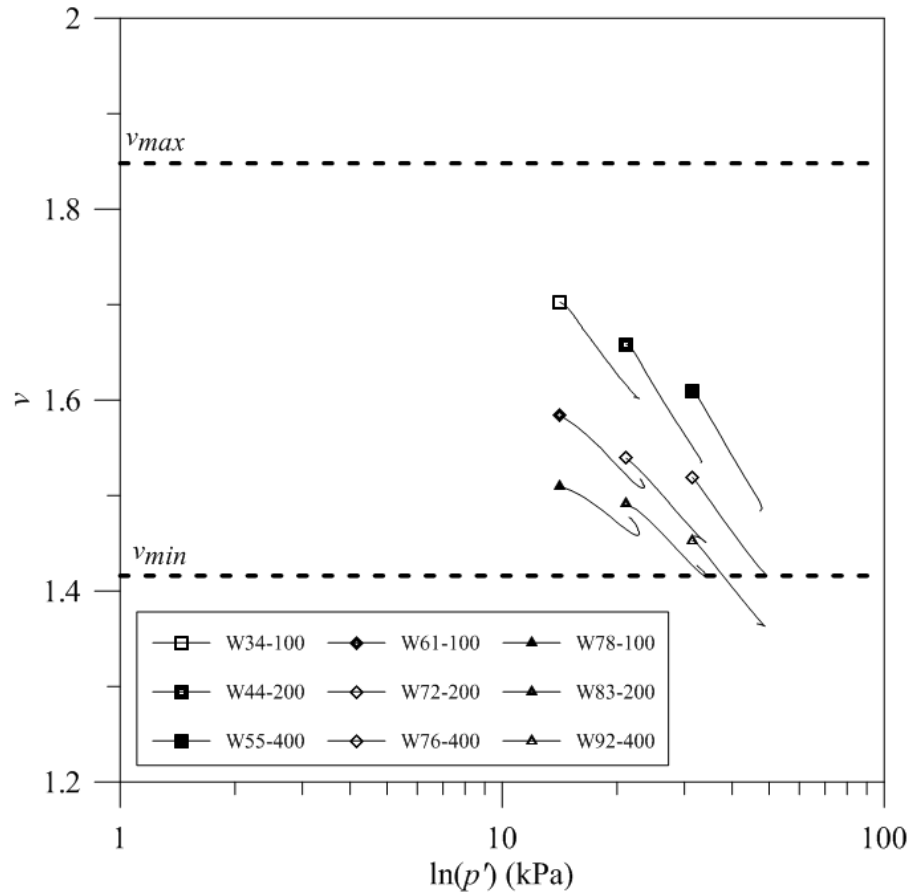


Figure 6.10: Shearing paths in  $\ln(p')$  -  $v$  space for weathered *MWR* material.

Because the point of maximum axial strain for each test may not truly represent critical state due to combined effects of particle breakage, dilatancy, *FC*, plasticity, etc., the final value of  $\phi_c$  for the unweathered and weathered *MWR* material was determined by selecting tests that most nearly exhibited critical state behavior. Tests reconstituted to relatively low  $D_R$  at the highest levels of  $p'$  generally exhibited mechanical behavior that most nearly meets the critical state criteria ( $\delta v/\delta \epsilon_q = \delta p'/\delta \epsilon_q = \delta q/\delta \epsilon_q = 0$ ). Additionally, the final value of the fractal dimension ( $D$ ), was found to level off only in tests isotropically compressed to the highest level of  $p'$  (400 kPa). Data presented by Tarantino and Hyde (2005) suggest that a constant  $D$  indicates that particle breakage within the specimen is tending towards a constant value and the mobilized angle of

shearing resistance most accurately represents the intrinsic frictional characteristics of the geomaterial, or  $\phi_c$ . Figure 5.11 illustrates the final values of  $D$  measured at  $p' = 400$  kPa which most accurately represents the stable value of the  $D$  for each material. Tests U42-400 and W76-400 were found to most accurately meet the conditions described above and were used to determine the final value of  $\phi_c$  for each material. Values of  $\phi_c$  were determined to be  $39^\circ$  and  $38^\circ$  for the unweathered and weathered *MWR* materials, respectively. These values of  $\phi_c$  compare fairly well with values of  $\phi_c$  based on  $M$ , relying on a larger number of tests.

### 6.3.3 Stress – Dilatancy Relationship

Using Equations 3.22 and 3.24, Bolton's (1986) stress – dilatancy relationship originally established for clean sands can be combined into the following:

$$I_R = \frac{\phi_p - \phi_c}{3} = I_D \left( Q - \ln \left( \frac{100p'_p}{p_A} \right) \right) - R \quad (6.1)$$

where:  $I_D = D_R$  (%)/100. The remaining variables have already been defined in Chapter 3. Using Equation 6.1, the relative dilatancy index,  $I_R$ , is related to the mobilized  $\phi_p$  through the state variables  $p'$  and  $D_R$  and the intrinsic variables. By knowing or estimating  $\phi_c$ , geotechnical engineers may estimate the value of  $\phi_p$  for a given material at a certain  $p'$  and  $D_R$  through an iterative procedure outlined by Salgado (2008) as long as  $Q$  and  $R$  are known. Following the work of Salgado et al. (2000),  $Q$  and  $R$  may be determined from the slope and intercept of the best fit lines through data plotted in  $I_R + I_D \ln(100p'_p/p_A)$  versus  $I_D$  space. Figure 6.11 illustrates the use of the procedure outlined by Salgado et al. (2000) to determine  $Q$  and  $R$  by regression.

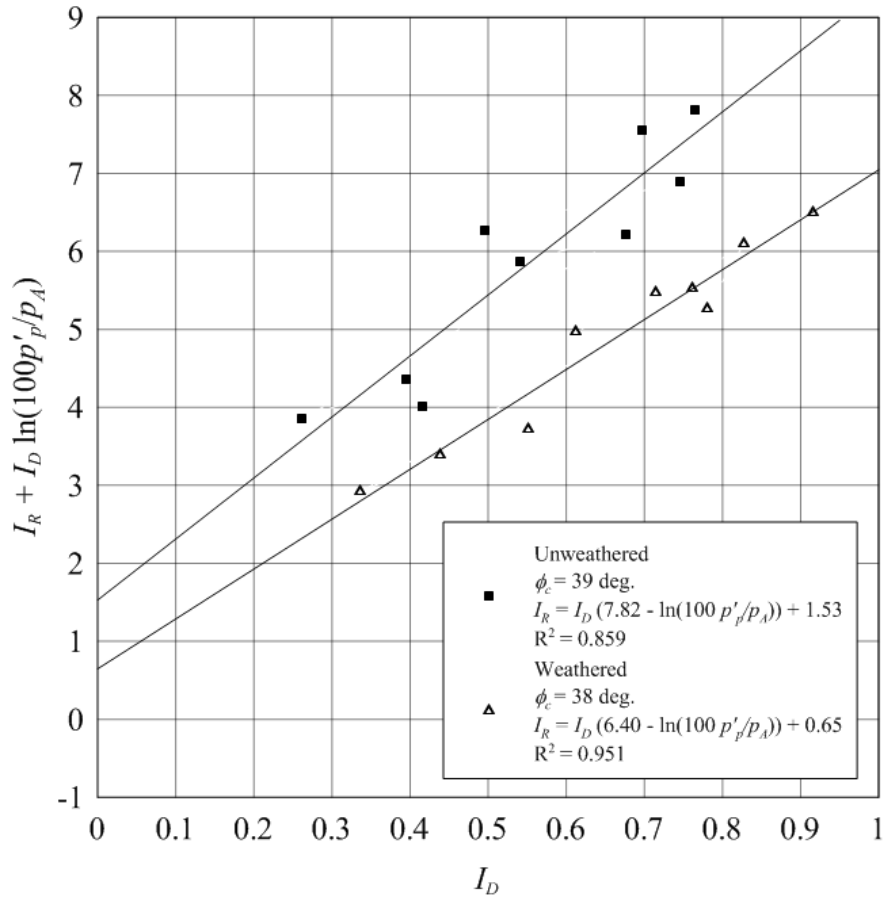


Figure 6.11: Regression of the dilatancy response of unweathered and weathered *MWR* in accordance with the procedure outlined by Salgado et al. (2000).

Bolton (1986) relates  $Q$  to the strength of individual soil grains in a geomaterial such that geomaterials with weaker grains will have a reduced  $Q$  in Equation 6.1. The fitting parameter  $R$  is generally described as an intrinsic fitting parameter for a given geomaterial. Using the best fit procedure outlined by Salgado et al (2000) yields values of  $Q$  and  $R$  equal to 7.82 and -1.53 for the unweathered *MWR* and 6.40 and -0.65 for the weathered *MWR*, respectively. The higher value of  $Q$  for the unweathered material indicates stronger grains exist compared to that of the weathered material. This is consistent with particle strength testing presented by Fox (2011). The fitting parameter  $R$  was found to be negative for both materials when applying linear best fit regression

analysis. This is consistent with results published by Carraro et al. (2004) for silty Ottawa sands containing 5 – 10% non plastic fines with  $D_R$  values between 14.0% and 80.3% with  $p'$  between 100 and 400 kPa.

Tabulated values of measured and predicted values of  $\phi_p$  for the unweathered and weathered *MWR* materials are presented in Tables 6.6 and 6.7, respectively. On average, the absolute difference ( $\Delta \phi_p = \phi_{p,measured} - \phi_{p,predicted}$ ) from the measured to the predicted values of  $\phi_p$  is about  $1.5^\circ$  for the unweathered material and about  $1.6^\circ$  for the weathered material.

Table 6.6: Comparison of measured and predicted values of  $\phi_p$  for the unweathered *MWR* material using Bolton's (1986) relationship and best fit values of  $Q$  and  $R$

	$\phi_c$ (deg.)	$Q$	$R$	
	39	7.82	-1.53	
	$I_D$	Predicted $\phi_p$ (deg.)	Measured $\phi_p$ (deg.)	$\Delta \phi_p$ (deg.)
U26-100	0.26	45.3	46.3	1.0
U50-100	0.50	46.8	49.9	3.1
U70-100	0.70	48.1	50.5	2.4
U40-200	0.40	45.4	44.8	-0.6
U54-200	0.54	46.1	46.7	0.6
U77-200	0.77	47.0	48.5	1.5
U42-400	0.42	44.7	42.6	-2.1
U68-400	0.68	45.3	44.0	-1.3
U75-400	0.75	45.5	44.8	-0.7
			Average Difference	1.5

Table 6.7: Comparison of measured and predicted values of  $\phi_p$  for the weathered MWR material using Bolton's (1986) relationship and best fit values of  $Q$  and  $R$

	$\phi_c$ (deg.)	$Q$	$R$	
	38	6.40	-0.65	
	$I_D$	Predicted $\phi_p$ (deg.)	Measured $\phi_p$ (deg.)	$\Delta \phi_p$ (deg.)
W34-100	0.34	40.9	38.1	-2.8
W61-100	0.61	41.7	40.1	-1.6
W78-100	0.78	42.1	41.3	-0.8
W44-200	0.44	40.3	39.2	-1.1
W72-200	0.72	40.6	41.5	0.9
W83-200	0.83	40.7	42.9	2.2
W55-400	0.55	39.4	39.2	-0.2
W76-400	0.76	39.1	41.3	2.2
W92-400	0.92	39.0	41.3	2.3
			Average Difference	1.6

For quartz and feldspar clean sands, Bolton found that a good correlation with  $Q = 10$  and  $R = 1$ . For purpose of comparison with data presented by Bolton (1986), the procedure outlined by Salgado et al. (2000) was repeated by forcing the fitting parameter  $R$  to equal 1. Figure 6.12 illustrates use of procedure outlined by Salgado et al. (2000) to determine  $Q$  with  $R = 1$  by regression.

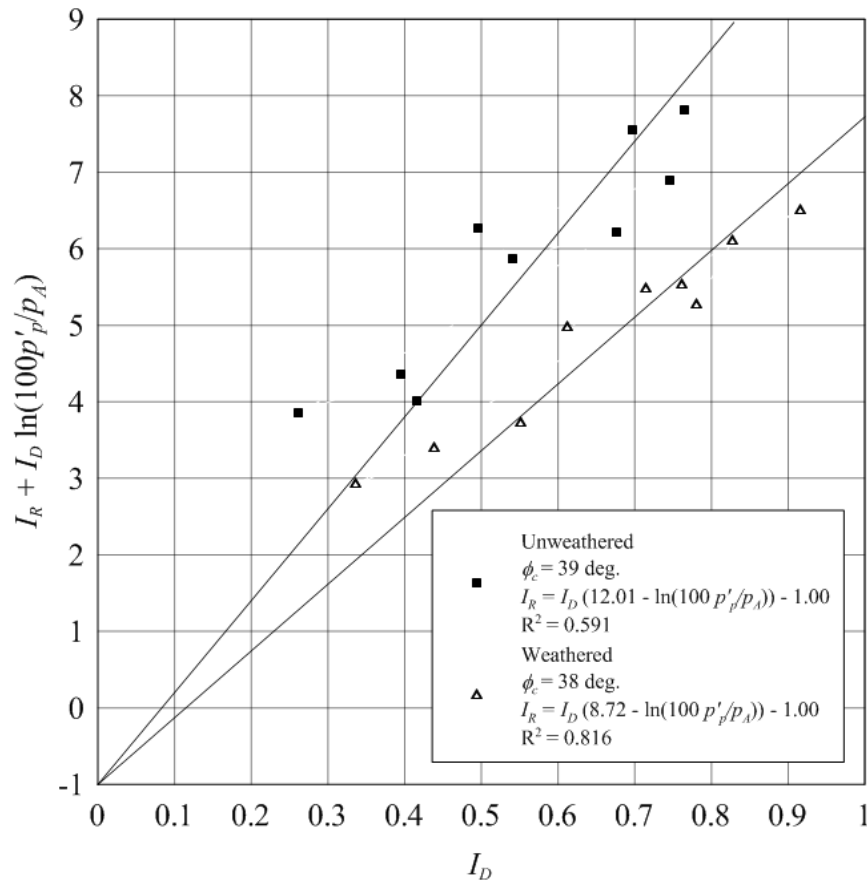


Figure 6.12: Regression of the dilatancy response of unweathered and weathered *MWR* in accordance with the procedure outlined by Salgado et al. (2000) with the fitting parameter  $R = 1$ .

Implementing Bolton's (1986) fitting parameter for quartz and feldspar sands ( $R = 1$ ) and  $\phi_c$  determined for each material, values of  $Q$  were determined to be 12.01 and 8.72 for the unweathered and weathered *MWR* materials, respectively. Again, the larger value of  $Q$  determined for the unweathered material compared to the weathered material is consistent with the higher particle strength of the unweathered material. The measured  $\phi_p$  was again compared to that estimated through Equation 6.1. Tables 6.8 and 6.9 summarize the results of the comparison of the measured and predicted  $\phi_p$  using values of  $Q$  determined through regression analysis and  $R = 1$  for the unweathered and weathered

*MWR* materials, respectively. On average, the average absolute difference from the measured to the predicted was about  $2.1^\circ$  for the unweathered material and about  $1.0^\circ$  for the weathered material. It should be noted that forcing  $R$  equal to 1 is for illustrative purposes only. The data in Tables 6.8 and 6.9 may not have a physical meaning because  $R = 1$  does not represent the materials tested properly.

Table 6.8: Comparison of measured and predicted values of  $\phi_p$  for the unweathered *MWR* material using Bolton's (1986) relationship and best fit value of  $Q$  and  $R = 1$ .

	$\phi_c$ (deg.)	$Q$	$R$	
	39	12.01	1	
	$I_D$	Predicted $\phi_p$ (deg.)	Measured $\phi_p$ (deg.)	$\Delta \phi_p$ (deg.)
U26-100	0.26	41.2	46.3	5.1
U50-100	0.50	45.6	49.9	4.3
U70-100	0.70	49.1	50.5	1.4
U40-200	0.40	42.9	44.8	1.9
U54-200	0.54	45.3	46.7	1.4
U77-200	0.77	48.9	48.5	-0.4
U42-400	0.42	42.4	42.6	0.2
U68-400	0.68	46.2	44.0	-2.2
U75-400	0.75	47.1	44.8	-2.3
			Average Difference	2.1

Table 6.9: Comparison of measured and predicted values of  $\phi_p$  for the weathered *MWR* material using Bolton's (1986) relationship and best fit value of  $Q$  and  $R = 1$ .

	$\phi_c$ (deg.)	$Q$	$R$	
	38	8.72	1.00	
	$I_D$	Predicted $\phi_p$ (deg.)	Measured $\phi_p$ (deg.)	$\Delta \phi_p$ (deg.)
W34-100	0.34	38.4	38.1	-0.3
W61-100	0.61	41.0	40.1	-0.9
W78-100	0.78	42.6	41.3	-1.3
W44-200	0.44	38.5	39.2	0.7
W72-200	0.72	40.6	41.5	0.9
W83-200	0.83	41.4	42.9	1.5
W55-400	0.55	38.3	39.2	0.9
W76-400	0.76	39.5	41.3	1.8
W92-400	0.92	40.3	41.3	1.0
			Average Difference	1.0

The results presented in Tables 6.6 through 6.9 bring up an interesting discussion topic with regard to using the best fit parameters determined through the procedure outlined by Salgado et al. (2000) and forcing the fitting parameter  $R$  to equal 1. For the unweathered material, Equation 6.1 most accurately estimates the value of  $\phi_p$  with the best fit parameters (Table 6.6 compared to Table 6.8). However, for the weathered material, forcing  $R$  equal to 1 provides more accurate measurements of  $\phi_p$  (Table 6.7 compared to Table 6.9) although there is no physical meaning to support the approach.

The most plausible explanation for these results may be the difference in particle strength and the amount of particle breakage that occurs during each test. Because the relationship proposed by Bolton (1986) in Equation 6.1 only takes stress and dilatancy explicitly into account, not the irrecoverable energy dissipation associated with particle breakage, the relationship is only ideal for materials lacking crushable grains. Also,

Bolton's relationship makes a direct correlation between  $\phi_p - \phi_c$  and  $(-\delta\varepsilon_p/\delta\varepsilon_a)_{max}$ . In geomaterials that contain crushable grains,  $\phi_p$  may not only be related to  $(-\delta\varepsilon_p/\delta\varepsilon_a)_{max}$  but also to the strength of the individual grains comprising the crushable media (McDowell and Bolton 1996). For geomaterials with crushable grains, as particle strength increases the tendency towards dilation also increases whereas decreases in particle strength inhibits dilation through the phenomena of particle breakage (Coop et al. 2004). With the weathered material having individual particle strengths approximately 10 times less than those of the unweathered material, the tendency for the weathered material to dilate may have been inhibited by the increased particle breakage and other factors such as  $FC$  and fines plasticity (see Figures 5.5, 5.7, 5.10, 6.9, and 6.10). Additionally, the decrease in particle strength and increase in the amount of particle breakage leads to the development of a stable  $D$  at lower confining stresses, i.e. 200 kPa (see Figures 5.11 and 5.12), which indicates a greater tendency for particle breakage within the weathered material. Using Equation 6.1, dilatancy increases as  $Q$  increases and decreases with increasing  $R$  (Bolton 1986, Salgado et al. 2000). Due to the highly contractive nature of the weathered  $MWR$  material, likely due low particle strength and increased particle breakage (Coop et al. 2004), increasing the value of  $R$  from the best fit value of -0.65 to 1.00 lowers the influence of dilatancy in Bolton's relationship and provides a more accurate prediction of  $\phi_p$ . For the unweathered material, the mechanical response was found to be highly dilative and therefore increasing the value of the fitting parameter  $R$  from -1.53 to 1.00 reduces the influence of dilatancy and causes the use of Equation 6.1 to become more inaccurate. However, again it must be stated that forcing the  $R$  to equal 1 (or any value for that matter) is an artificial approach with not physical meaning. The preceding

discussion was presented for illustrative purposes only in regard to the mathematical relationship proposed by Bolton (1986).

The results and discussion presented above supports the theory that measured strength is comprised of frictional and clastic components with the clastic components not only being comprised of dilatancy effects but also the effects of particle breakage (McDowell and Bolton 1996, Tarantino and Hyde 2000). Therefore use of Bolton's relationship in its original form may be limited to those materials that are not comprised of crushable grains.

#### 6.4 Particle Breakage

Particle breakage was measured by conducting post test particle-size analyses on each triaxial test specimen. The upper bound for each material corresponding to the test that experienced the largest amount of particle breakage is plotted on Figure 5.10. As expected, the stronger unweathered material experienced less total change in the gradation over the course of the triaxial test than that of the weathered material. As previously discussed, particle breakage likely plays a role in the mechanical response of both materials during shear (Figures 6.9 and 6.10). Post test particle-size distributions for each triaxial test are presented in Appendix B.

#### 6.5 Fractal Dimension

The fractal dimension ( $D$ ) is a simple power-law relationship between number and size in a particle size distribution (Equation 3.34). The initial  $D$  for all unweathered and

weathered *MWR* tests was equal to 2.699 and 2.965, respectively. Figure 5.11 shows the evolution of  $D$  after testing at various levels of  $p'$  for both materials. The initial values of  $D$ , plotted on Figures 5.11 and 5.12 at  $p' = 0$  kPa, correspond to the fractal dimension of the model gradation used to reconstitute each specimen. In general, the change in fractal dimension ( $\Delta D$ ) measured for each test was found to increase with increasing  $p'$ .  $\Delta D$  was found to be consistently greater in the weathered material than for the unweathered material (Tables 5.3 and 5.4), which indicates a larger tendency towards particle breakage during triaxial testing in the weathered material, as supported by Figure 5.10. Due to this tendency of the weathered material, the value of  $D$  began to level off at levels of  $p'$  equal to 200 kPa at a value of 3.163 where the unweathered material was not considered stable until levels of  $p'$  equal to 400 kPa at a value of 2.854. Ideally, testing at levels of  $p'$  past 400 kPa should have been used to support the claim of a stable  $D$  at  $p'$  equal to 400 kPa for the unweathered material but equipment limitations prevented such tests. Furthermore, the final value of  $D$  determined for each test was found to be independent of  $D_R$  and highly dependent on the level of  $p'$  (Figures 5.11 and 5.12) for both materials. Plots of  $N(L>d)$  versus  $d$  and the corresponding  $D$  determined by regression are presented in Appendix D.

## 6.6 Surface Energy

The surface energy ( $\Gamma_{se}$ ) was determined for each material following the approach outlined by Fox (2011). By integrating the modified Granta-Gravel work equation presented by McDowell and Bolton (1996), Equation 3.29, over the range of  $\varepsilon_q$  and  $\varepsilon_p$  obtained during drained monotonic axisymmetric compression, it is possible to solve for

$\Gamma_{se}$  and  $dS$ . The value of  $dS$  was estimated using calculated values of  $S$  determined from pre and post test gradations and the shape factors  $\beta_s$  and  $\beta_v$  presented by McDowell and Bolton (1998) (Equations 3.30 and 3.31). Using the data presented by Marsal (1973) on angular rockfill, average values of shape factors presented by McDowell and Bolton (1998) were calculated for  $\beta_s$  and  $\beta_v$  as 3.74 and 0.44, respectively. These values of  $\beta_s$  and  $\beta_v$  were assumed to be constant and applicable for use considering the nature of the two *MWR* materials. Table 6.10 presents values of  $\Gamma_{se}$  and  $dS$  calculated for each triaxial test for both the unweathered and weathered *MWR* materials. Values of  $\Gamma_{se}$  were determined to be within 7.2 and 23.7 J/m<sup>2</sup> for the unweathered material and 3.7 and 6.8 J/m<sup>2</sup> for the weathered material. Smaller values of  $\Gamma_{se}$  determined for the weathered material are expected due to the lower particle strength of its individual grains. These values are similar to values presented in the literature (see Table 3.1) for various rock types (Gilman 1960, Brace and Walsh 1962, Perkins and Bartlett 1963, Nakayama 1965, Perkins and Krech 1966, Santhanan and Gupta 1968, Forootan-Rad and Moavenzadeh 1968, Friedman et al. 1972, Ashby and Jones 1986, Tarantino and Hyde 2005 and Fox 2011). It was generally observed that  $dS$  increases with increasing  $p'$  and  $D_R$  which is expected as particle breakage generally increases with increasing  $p'$  and  $D_R$  and  $dS$  increases with the phenomena of particle breakage. Values of calculated  $\Gamma_{se}$  did not seem to follow any specific trend by way of  $p'$  and  $D_R$ . However, it should be noted that these results may be limited in accuracy due to the assumption of constant shape factors  $\beta_s$  and  $\beta_v$ .

Table 6.10: Values of  $\Gamma_{se}$  and  $dS$  determined for each triaxial test.

Test	$\Gamma_{se}$ (J/m <sup>2</sup> )	$dS$ (m <sup>2</sup> )
U26-100	17.4	0.4
U50-100	10.4	0.7
U70-100	12.4	0.9
U40-200	10.2	0.7
U54-200	17.0	0.8
U77-200	7.2	1.1
U42-400	23.7	0.8
U68-400	16.5	1.2
U75-400	11.0	1.5
W34-100	5.4	0.8
W61-100	6.7	0.8
W78-100	3.7	0.7
W44-200	5.2	1.1
W72-200	6.1	1.1
W83-200	6.8	1.1
W55-400	5.1	1.2
W76-400	5.7	1.3
W92-400	4.6	1.5

### 6.7 Comparison of Conventional and Large-scale Results

As previously mentioned, the scope of this study was not only to examine the mechanical behavior of two types of *MWR* in conventional scale triaxial testing but also to compare the results to those obtained through large-scale triaxial (*LSTX*) testing. Fox (2011) presented *LSTX* results for the same unweathered and weathered *MWR* materials used in the present study that will be referenced for comparison in this current section. *LSTX* triaxial tests conducted by Fox (2011) were completed in the same manner as those in the present study, the only difference being the scale of the specimens, which makes the comparison of the results ideal. The *SSR* used by Fox (2011) was 6 compared to a value of 6.25 used in the present study. Several of the data sets presented by Fox (2011) were

presented as average values for a range of  $D_R$ . For these data sets, raw data from the triaxial test conducted by Fox (2011) was replotted to provide a quantitative comparison to triaxial test results presented in the present study. For the sake of comparison, *LSTX* tests are designated using the same technique as the triaxial test results presented in this study with the addition of “LS”. For example, a weathered *LSTX MWR* specimen isotropically compressed to  $p' = 400$  kPa with  $D_R = 96\%$  will be referred to W96-400 LS.

### 6.7.1 Isotropic Compression

Isotropic compression data obtained by Fox (2011) in *LSTX* testing is presented on Figures 6.13 and 6.14 for the unweathered and weathered *MWR* material, respectively. Critical state parameters  $\kappa$  and  $\nu_\kappa$  determined during isotropic compression for unweathered and weathered *MWR* materials in *LSTX* testing are tabulated in Table 6.11. Minimum, maximum and average values of critical state parameters  $\kappa$  and  $\nu_\kappa$  are tabulated for both *MWR* materials during conventional and large-scale triaxial testing in Table 6.12. The lowest and highest values of  $\kappa$  and  $\nu_\kappa$  were found to correlate well between large and small scale. The range of  $\kappa$  values determined during *LSTX* testing for the unweathered and weathered material was 0.006 – 0.017 and 0.001 – 0.013, compared to 0.008 – 0.021 and 0.010 – 0.023 determined for the conventional scale tests. The range of  $\nu_\kappa$  values determined during *LSTX* testing for the unweathered and weathered material was 1.48 – 1.69 and 1.44 – 1.66, respectively, compared to 1.53 – 1.74 and 1.58 – 1.79 determined for the conventional scale tests.

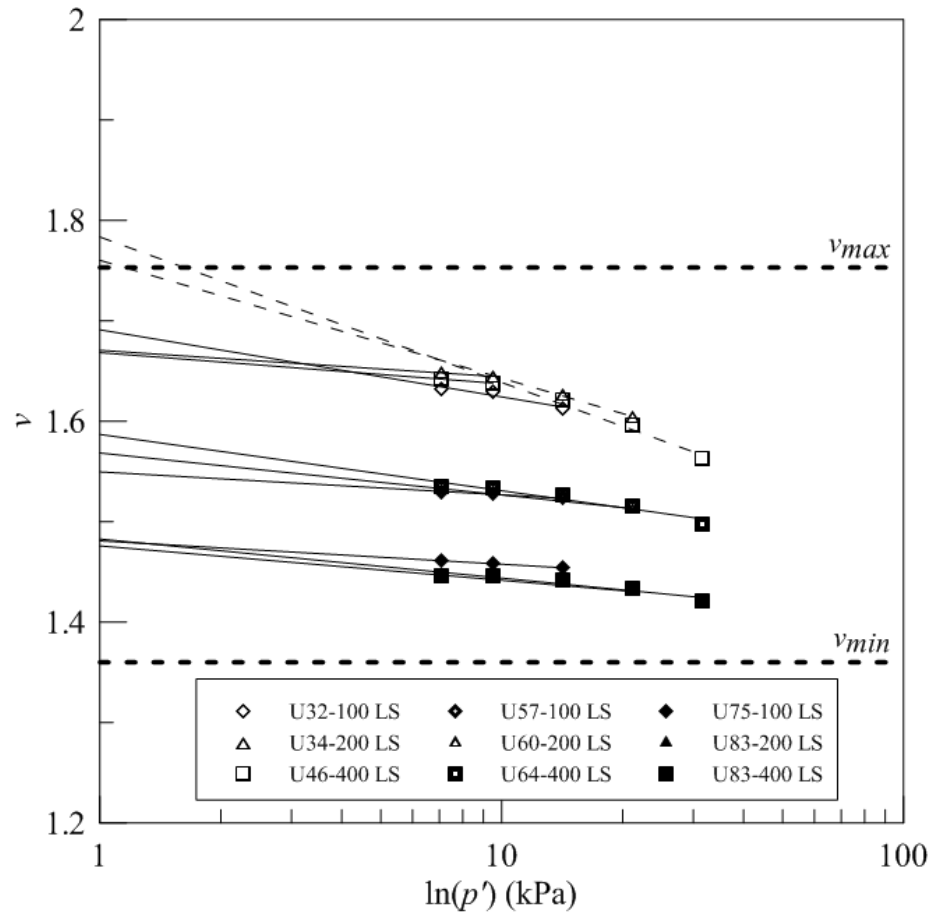


Figure 6.13: Unloading-reloading lines (solid) and normal compression lines (dashed) for unweathered *LSTX MWR* specimens (From data obtained by Fox 2011).

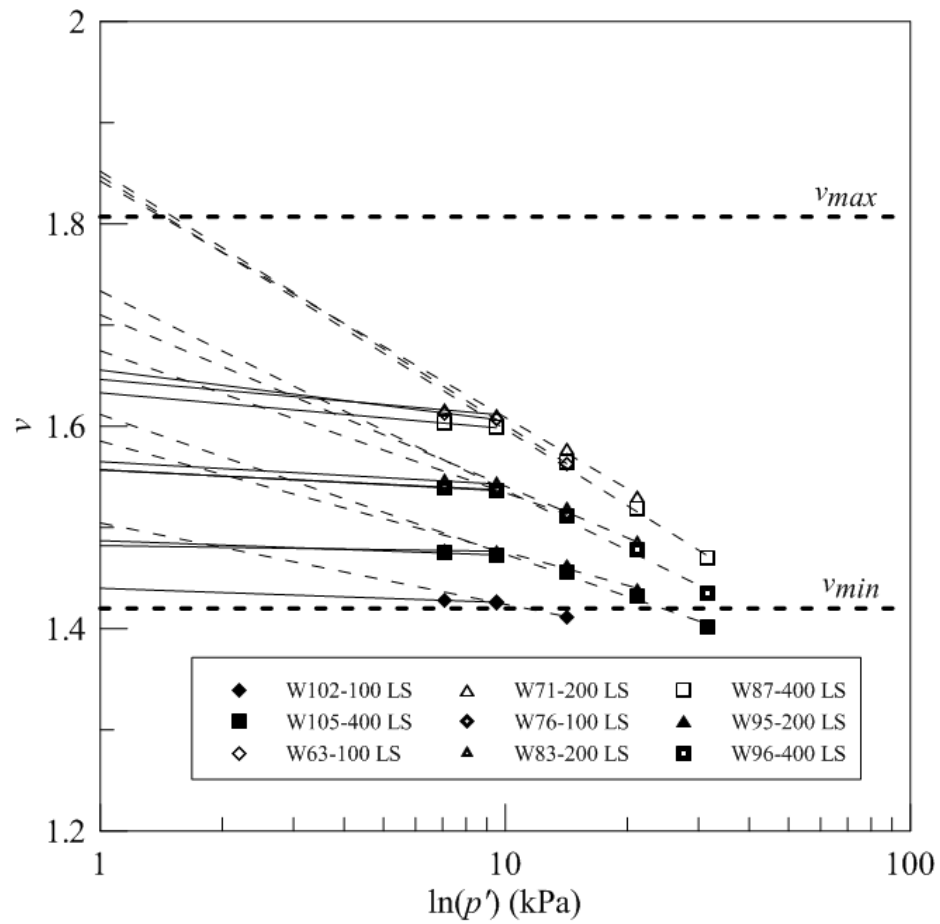


Figure 6.14: Unloading-reloading lines (solid) and normal compression lines (dashed) for weathered LSTX MWR specimens (From data obtained by Fox 2011).

Table 6.11: Critical state parameters  $\kappa$ ,  $\nu_\kappa$ ,  $\lambda$  and  $N$  determined after isotropic compression for unweathered and weathered *MWR LSTX* specimens (From data obtained by Fox 2011)

Test	$D_{R, Initial}$	$\kappa$	$\nu_\kappa$	$R^{2(1)}$	$\lambda^{(2)}$	$N^{(2)}$	$R^{2(1)}$
U32-100 LS	28	0.017	1.69	0.94	--	--	--
U57-100 LS	55	0.006	1.55	0.99	--	--	--
U75-100 LS	73	0.006	1.48	0.95	--	--	--
U34-200 LS	28	0.007	1.67	--	0.029	1.76	0.99
U60-200 LS	54	0.010	1.57	0.91	--	--	--
U83-200 LS	77	0.009	1.48	0.92	--	--	--
U46-400 LS	26	0.008	1.67	--	0.036	1.78	0.98
U64-400 LS	55	0.014	1.57	0.92	--	--	--
U83-400 LS	75	0.010	1.48	0.90	--	--	--
W63-100 LS	42	0.013	1.66	--	0.063	1.85	--
W76-100 LS	66	0.005	1.56	--	0.035	1.67	--
W102-100 LS	98	0.004	1.44	--	0.020	1.50	1.00
W71-200 LS	41	0.009	1.65	--	0.058	1.84	0.99
W83-200 LS	69	0.006	1.57	--	0.042	1.71	0.99
W95-200 LS	85	0.001	1.48	--	0.027	1.59	0.98
W87-400 LS	44	0.009	1.63	--	0.063	1.85	0.99
W96-400 LS	65	0.005	1.56	--	0.049	1.73	0.99
W105-400 LS	85	0.004	1.49	--	0.035	1.61	0.98

<sup>1</sup> Coefficient of determination values were not calculated for data sets with less than three data points

<sup>2</sup> Value determination was not applicable to results observed for the specific test indicated by "--"

Table 6.12: Range of critical state parameters  $\kappa$ ,  $\nu_\kappa$ ,  $\lambda$  and  $N$  determined after isotropic compression for unweathered and weathered *MWR* in both conventional and large-scale triaxial tests (From data obtained by Fox 2011).

Material	Unweathered	Unweathered	Weathered	Weathered LS
Highest $D_{R, Initial}$ (%)	68	77	71	98
Lowest $D_{R, Initial}$ (%)	16	26	16	41
Highest $\kappa$	0.021	0.017	0.023	0.013
Lowest $\kappa$	0.008	0.006	0.010	0.001
Highest $\nu_\kappa$	1.74	1.69	1.79	1.66
Lowest $\nu_\kappa$	1.53	1.48	1.58	1.44
Highest $\lambda$ <sup>1</sup>	--	0.036	0.068	0.063
Lowest $\lambda$ <sup>1</sup>	--	0.029	0.037	0.020
Highest $N$ <sup>1</sup>	--	1.78	2.02	1.85
Lowest $N$ <sup>1</sup>	--	1.76	1.69	1.50

<sup>1</sup> Value determination was not applicable to results observed for the specific test indicated by "--"

Critical state parameters  $\kappa$ ,  $\nu_\kappa$ ,  $\lambda$  and  $N$  determined during isotropic compression are similar for both conventional and large-scale tests on both *MWR* materials. The range of  $\kappa$  and  $\nu_\kappa$  values are very close for the unweathered material when comparing conventional and large-scale results. The range of  $\kappa$  and  $\nu_\kappa$  values determined for the weathered material, however, indicate slightly higher compressibility in conventional scale specimens. The higher compressibility in conventional scale specimens may be caused by a number of factors including, but not limited to: increased *FC*, increased fines plasticity, the amount of particle breakage during isotropic compression and the range of  $D_{R, Initial}$  to which specimens were originally reconstituted. This point is also supported in comparing  $\lambda$  values between conventional and large-scale test results from the weathered material. Although the highest values of  $\lambda$  measured are very similar, the lowest values measured during large-scale tests fall out of the range measured for the conventional specimens. It should be noted that large-scale tests that have a value of  $\lambda$  that falls significantly beneath the lower bound of conventional tests have values of  $D_{R, Initial}$  far greater than the highest value  $D_{R, Initial}$  for the conventional scale triaxial specimens and a decrease in compressibility is expected. The similarities between measured  $\kappa$ ,  $\nu_\kappa$ ,  $\lambda$  and  $N$  values suggests that use of the parallel gradation technique proposed by Lowe (1964) can be used in isotropic compression to reconstitute scaled specimens that reasonably emulate the fabric of their larger predecessor provided that the range of  $D_{R, Initial}$  is similar between scales. The similarities also suggest that the individual material properties of the grains comprising the large and conventional scale gradations are reasonably similar. Because particle breakage has been shown to increase compressibility of geomaterials (Coop et al. 2004), the above data may suggest the hypothesis that particle breakage during isotropic

compression does not vary significantly between conventional and large-scale specimens. This hypothesis is supported by the range of  $D_R$  tested in the present study compared to the study presented by (Fox 2011). Similar values of  $\kappa$  and  $\nu_\kappa$  measured for the ranges of  $D_R$  presented in Table 6.12 indicate similar levels of compressibility in both sizes of triaxial tests during isotropic compression. This hypothesis, however, cannot be supported fully due to the lack of measurement of particle breakage during isotropic compression during the present study or the study presented by Fox (2011).

## 6.7.2 Drained Monotonic Axisymmetric Compression

### 6.7.2.1 Typical Stress – Strain – Volumetric Response

Similar mechanical responses were observed for the unweathered and weathered *MWR* materials during drained monotonic axisymmetric compression of both conventional and *LSTX* specimens. Stress-strain and stress-volumetric responses of conventional and large-scale specimens with similar states are presented on Figures 6.15 and 6.16 for the unweathered and weathered *MWR* materials, respectively. As discussed in Chapter 5, the dashed line in Figure 6.15 represented the formation of a shear band during monotonic loading and uncertainty is associated with the data after peak strength. As it was observed in the present study, *LSTX* testing typically showed strain softening behavior with a propensity towards dilation and volumetric expansion for the unweathered *MWR* material where the weathered material exhibited strain hardening behavior and had a strong tendency towards volumetric compression during drained monotonic axisymmetric contraction. Similar to the conventional scale tests in the present study, peak dilatancy rates,  $(-\delta\varepsilon_p/\delta\varepsilon_a)_{max}$ , observed in the unweathered material were generally an order of

magnitude higher than the weathered material during *LSTX* testing. For large-scale specimens, average values of  $(-\delta\varepsilon_p/\delta\varepsilon_a)_{max}$  were determined to be 0.125 and 0.033 for the unweathered and weathered *MWR*, respectively. Tabulated values of  $(-\delta\varepsilon_p/\delta\varepsilon_a)_{max}$  are presented in Table 6.13 for each *LSTX* test.

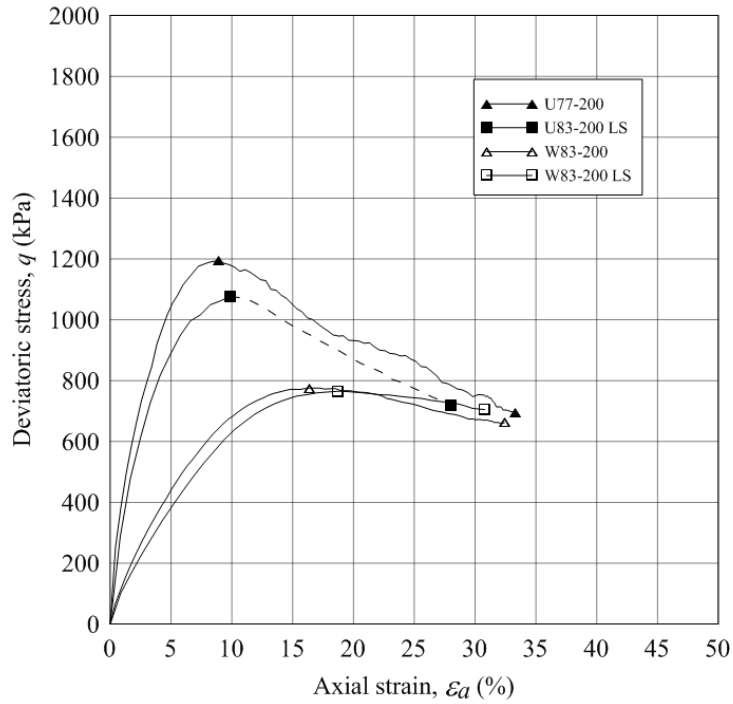


Figure 6.15: Deviatoric stress versus axial strain for unweathered and weathered *MWR* materials isotropically compressed to similar states at the same  $p'$  for conventional and large-scale triaxial tests (Fox 2011) (the two data points shown correspond to measured values of peak and critical state strengths).

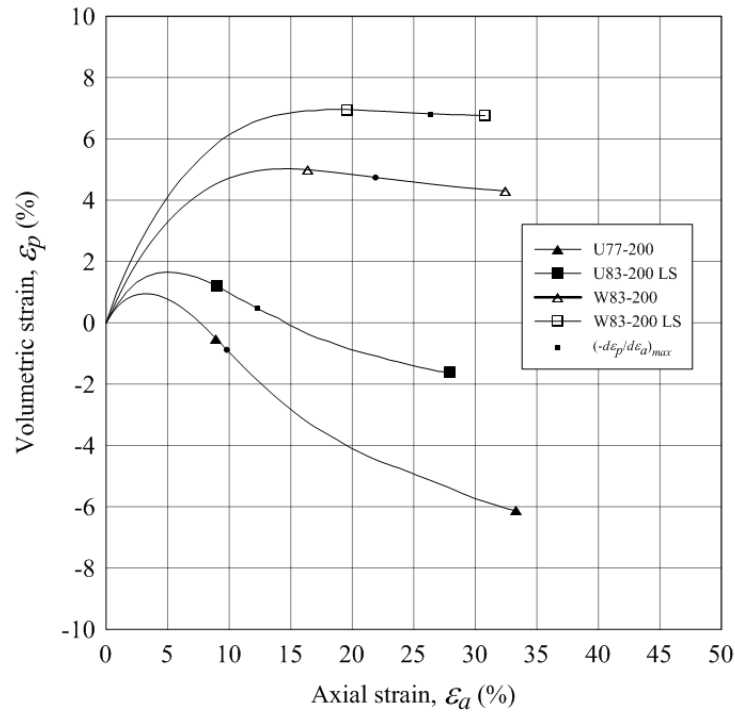


Figure 6.16: Volumetric strain versus axial strain for unweathered and weathered *MWR* materials isotropically compressed to similar states at the same  $p'$  for conventional and large-scale triaxial tests (Fox 2011) (the two data points shown correspond to measured values of peak and critical state strengths).

Table 6.13: Tabulated values of  $(-\delta\varepsilon_p/\delta\varepsilon_a)_{max}$  during drained monotonic axisymmetric compression for unweathered and weathered *MWR LSTX* specimens (From data obtained by Fox 2011).

Test	$(-\delta\varepsilon_p/\delta\varepsilon_a)_{max}$	Average
U32-100 LS	0.067	0.122
U57-100 LS	0.212	
U75-100 LS	0.336	
U34-200 LS	0.035	
U60-200 LS	0.136	
U83-200 LS	0.221	
U46-400 LS	-0.030	
U64-400 LS	0.023	
U83-400 LS	0.099	
W63-100 LS	-0.037	
W76-100 LS	0.059	
W102-100 LS	0.113	
W71-200 LS	-0.008	
W83-200 LS	0.021	
W95-200 LS	0.057	
W87-400 LS	-0.020	
W96-400 LS	0.006	
W105-400 LS	0.047	

Values of  $(-\delta\varepsilon_p/\delta\varepsilon_a)_{max}$  observed in *LSTX* testing during monotonic loading was found to be approximately half of that measured during conventional scale tests giving suggesting that particle breakage may increase with increasing particle size. These results corroborate the data presented by Varadarajan et al. (2003) indicating that dilatancy generally increases with decreasing particle size as well as data presented by Hardin (1985) indicating that particle breakage increases with increasing particle size. Similar values of the average  $(-\delta\varepsilon_p/\delta\varepsilon_a)_{max}$  were observed for the weathered *MWR* material in both conventional and large-scale testing contradicting published data (Salgado et al. 2000, Varadarajan 2003). These results are attributed to individual particle strength and varying material properties over the range of particle sizes tested in conventional and

large-scale. With decreasing particle strength in the finer fraction of the large-scale specimens (corresponding to the full fraction of the conventional scale test), increasing particle breakage is expected in the conventional scale tests, thus reducing the dilative response. Analysis of the differences in  $FC$  and fines plasticity may also play a role in the results presented above. Published data by Salgado et al. (2000) and Carraro (2004) suggest that dilatancy decreases with increasing  $FC$  (with both plastic and non plastic fines) which is contradictory to the results presented above. While the  $FC$  for the unweathered material increased from about 1.7% to 3.0% between large and conventional scale tests, the fines were found to be non plastic and SEM of the fines showed less plate like particles (more angular and sub angular, see Figures 4.5 and 4.6) than that of the weathered fines which had increased plasticity. The weathered material increased in  $FC$  from about 4.9% to 7.8% from large to conventional tests. Although literature suggests the increase in  $FC$  for both materials would generate less dilative behavior, the nature of the non plastic unweathered fines may increase dilatancy in conventional scale specimens relative to that of the large-scale specimens because of the fines particle shape. The similar average values of  $(-\delta\varepsilon_p/\delta\varepsilon_a)_{max}$  for the conventional and large-scale triaxial tests with the weathered  $MWR$  specimens suggest that while the increased  $FC$  of the material may be inhibiting dilative behavior in conventional scale tests, particle breakage in the large-scale tests may be inhibiting dilative behavior as well. The relative magnitude of the effects of  $FC$  and particle breakage in conventional and large-scale would be difficult to determine and further systematic research into these effects at different scales is suggested. Figures 6.17 and 6.18 show the mechanical response of each material in  $LSTX$

testing in  $\ln(p')$  -  $v$  space compared to that of conventional scale triaxial tests during drained monotonic axisymmetric compression.

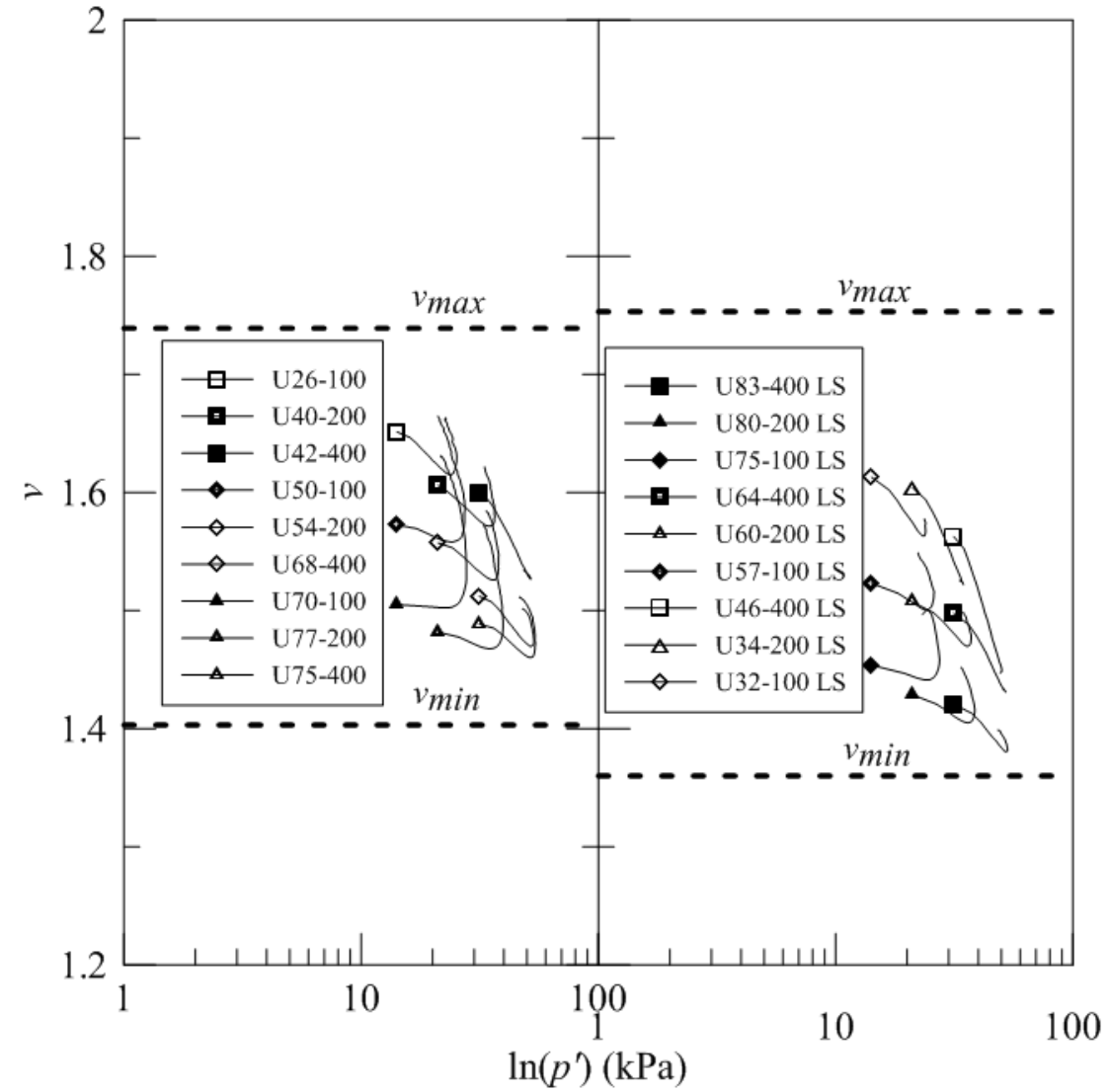


Figure 6.17: Shearing path in  $\ln(p')$  -  $v$  space for unweathered *MWR* material in conventional and large-scale triaxial tests (Fox 2011).

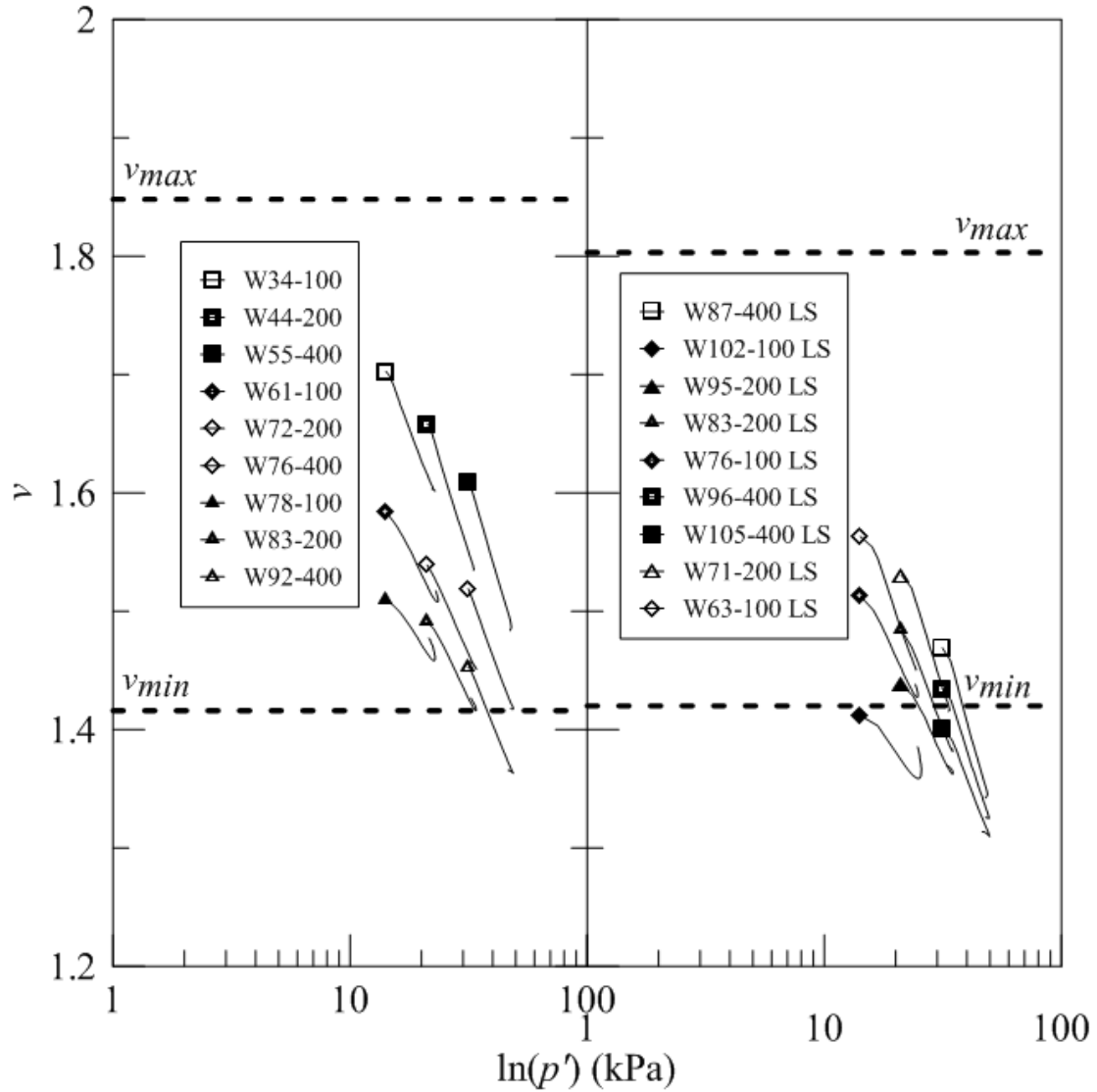


Figure 6.18: Shearing path in  $\ln(p')$  -  $v$  space for weathered *MWR* material in conventional and large-scale triaxial tests (Fox 2011).

Similar to the conventional scale specimens, the large-scale specimens indicate the material is on the “dry” side of the *CSL* for the unweathered material and the “wet” side for the weathered material. Figure 6.17 shows the much more dilative response from the unweathered material during monotonic loading in the conventional scale tests compared to the large-scale tests. The weathered material exhibited similar responses in  $\ln(p')$  -  $v$  space for both scales.

### 6.7.2.2 Critical State Friction Angle

For comparison, the *CSL* determined from large-scale triaxial testing is plotted in  $p' - q$  space in Figure 6.19. In the same way as the  $p' - q$  plot on Figure 6.7, tests exhibiting a shear band during monotonic loading were omitted. Additionally, the *CSL* is plotted in  $\ln(p') - v$  space in Figures 6.20 and 6.21 for conventional and large-scale unweathered and weathered *MWR* materials, respectively. Values of  $M$ ,  $\phi_c$ ,  $\lambda_{cs}$ , and  $\Gamma_{cs}$  determined by regression of the *CSL* in  $p' - q$  and  $\ln(p') - q$  space are tabulated in Table 6.14.

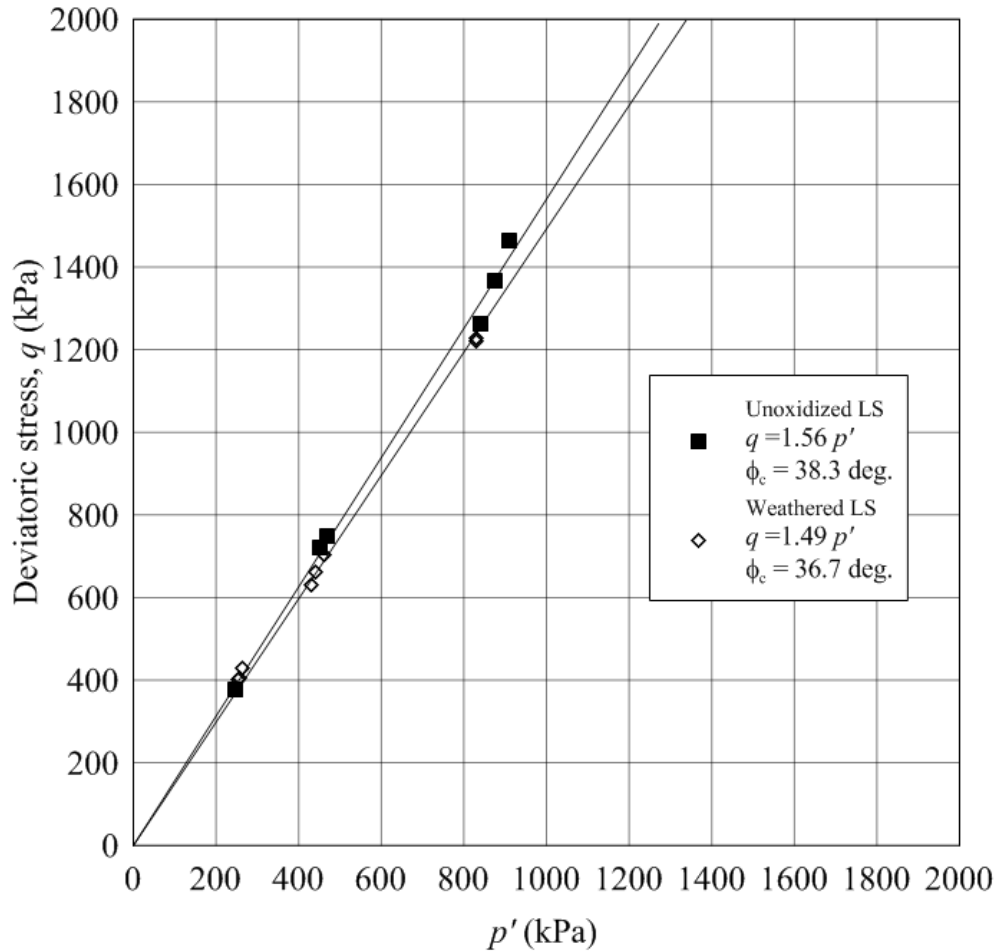


Figure 6.19: *CSL* in  $p' - q$  space for unweathered and weathered *MWR* materials in large-scale triaxial testing with a linear best fit value of  $M$  and the corresponding value of  $\phi_c$  (Modified after Fox 2011) (tests exhibiting shear bands during drained monotonic axisymmetric compression were omitted).

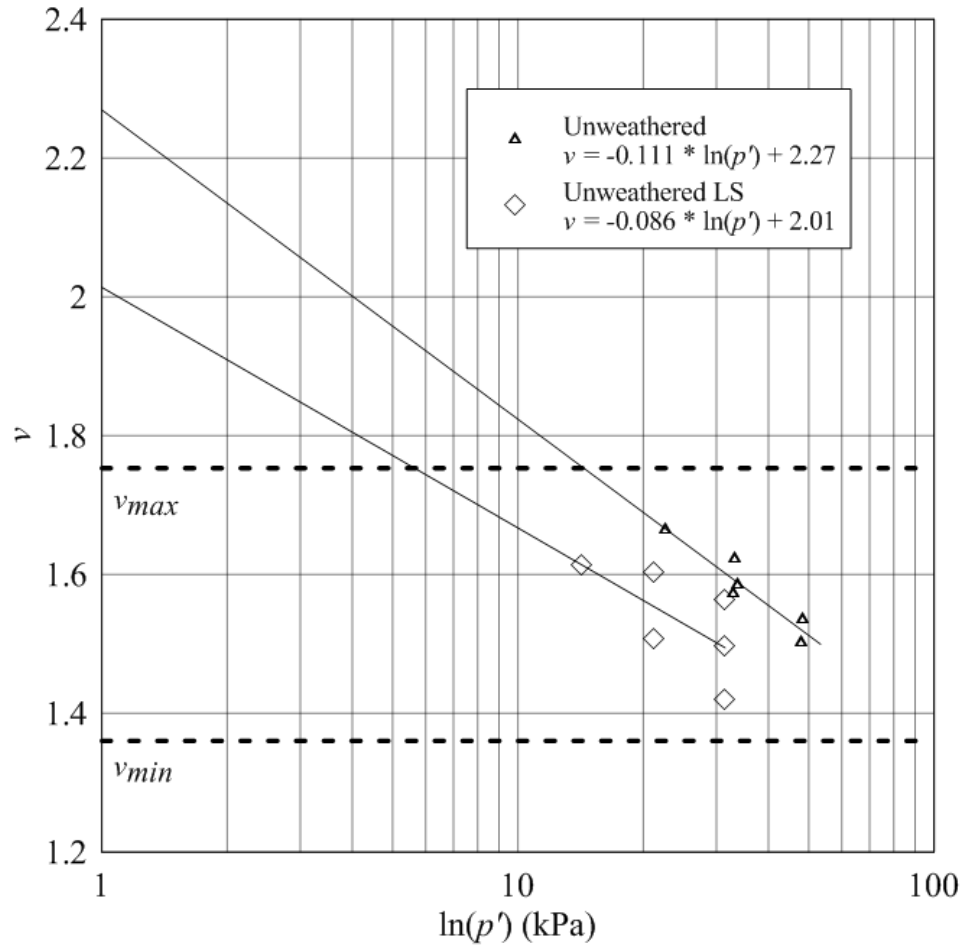


Figure 6.20: CSL in  $\ln(p')$  -  $q$  space for unweathered *MWR* material in conventional and large-scale triaxial testing with a logarithmic best fit values of  $\lambda_{cs}$  and  $\Gamma_{cs}$  (Fox 2011) (tests exhibiting shear bands during drained monotonic axisymmetric compression were omitted).

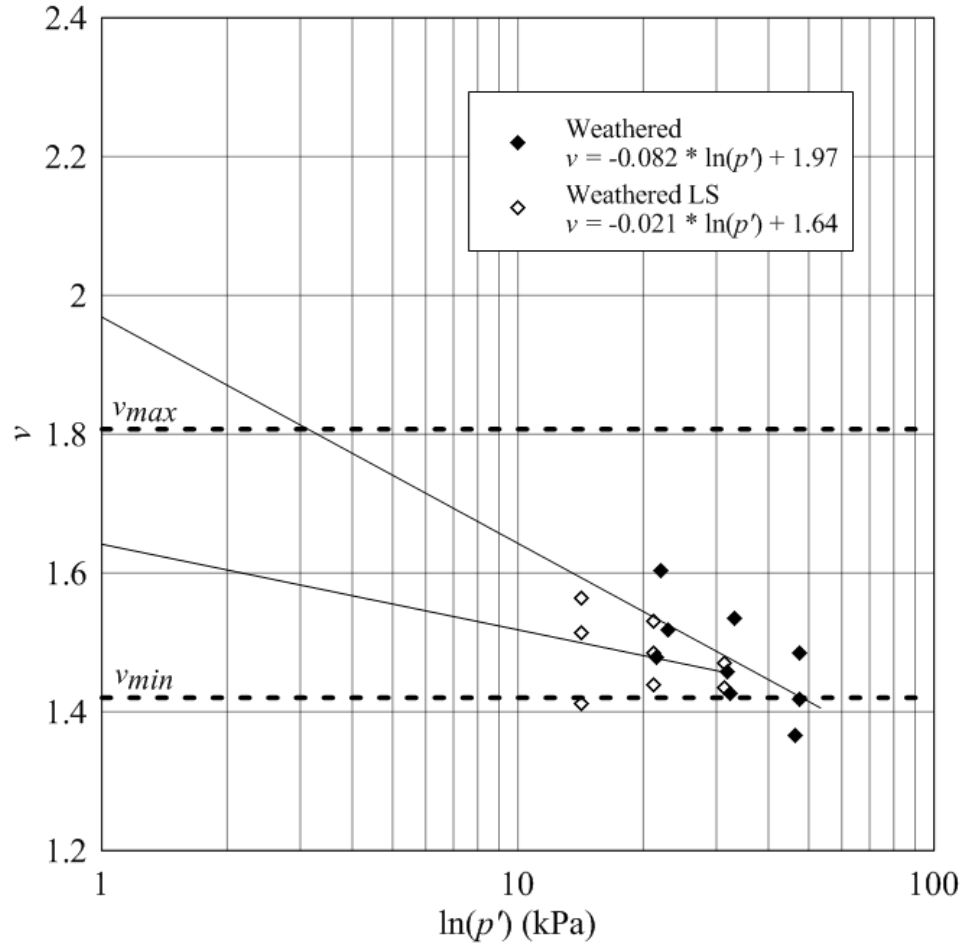


Figure 6.21: *CSL* in  $\ln(p')$  -  $q$  space for weathered *MWR* material in conventional and large-scale triaxial testing with a logarithmic best fit values of  $\lambda_{cs}$  and  $\Gamma_{cs}$  (Fox 2011) (tests exhibiting shear bands during drained monotonic axisymmetric compression were omitted).

Table 6.14: Tabulated values of  $M$ ,  $\phi_c$ ,  $\lambda_{cs}$ , and  $\Gamma_{cs}$  determined during drained monotonic axisymmetric compression for unweathered and weathered *MWR LSTX* specimens (Fox 2011).

Material	$M$	$\phi_c$ (deg.)	$\lambda_{cs}$	$\Gamma_{cs}$
Unweathered	1.59	40.1	0.111	2.27
Unweathered LS	1.56	38.3	0.086	2.01
Weathered	1.55	38.1	0.082	1.97
Weathered LS	1.49	36.7	0.021	1.64

In both cases, the critical state parameters  $M$ ,  $\phi_c$ ,  $\lambda_{cs}$ , and  $\Gamma_{cs}$  were found to decrease with increasing particle size indicating compressibility and frictional characteristics during

monotonic loading increase with decreasing particle size. Decreasing  $M$  and correspondingly  $\phi_c$  compliment the data presented by Varadarajan et al. (2003) for angular rockfill (Purulia Dam Material). The larger decrease in  $\lambda_{cs}$ , and  $\Gamma_{cs}$  observed in the weathered material is attributed to increased particle breakage during monotonic loading, increased  $FC$  and increased fines plasticity. Other factors may play a role as well and are beyond the scope of this study.

Fox (2011) also determined the final value of  $\phi_c$  by analyzing tests reconstituted to relatively low levels of  $D_R$  at the highest levels of  $p'$  which generally exhibited mechanical behavior that most nearly meets the critical state criteria ( $\delta v/\delta \varepsilon_q = \delta p'/\delta \varepsilon_q = \delta q/\delta \varepsilon_q = 0$ ). Fox (2011) selected tests U47-400 LS and W87-400 LS and came up with final values of  $\phi_c$  equal to  $38^\circ$  and  $36^\circ$  for the unweathered and weathered material, respectively. The conventional scale final value of  $\phi_c$  was  $1^\circ$  greater for the unweathered material and  $2^\circ$  greater for the weathered material. Again, these results are consistent with those presented by Varadarajan et al. (2003). Tabulated values of the final value of  $\phi_c$  determined for each material for conventional and large-scale triaxial tests are presented in Table 6.15 for comparison.

Table 6.15: Comparison of final values of  $\phi_c$  determined during drained monotonic axisymmetric compression in conventional and large-scale triaxial tests (Fox 2011).

Material	$\phi_c$ (deg.)
Unweathered	39
Unweathered LS	38
Weathered	38
Weathered LS	36

### 6.7.2.3 Stress – Dilatancy Relationship

Similar to Section 6.3.3 presented above, Fox (2011) determined the values of parameters  $Q$  and  $R$  by following the procedure outlined by Salgado et al. (2000). Regression of the *LSTX* data presented by Fox (2011) compared to conventional scale data is presented on Figures 6.22 and 6.23 for the unweathered and weathered material, respectively. Best fit values of  $Q$  equal to 10.8 and 8.5 were determined for the unweathered and weathered materials, respectively, and best fit values of  $R$  equal to 1.17 and 0.73 were determined for the unweathered and weathered materials, respectively. These values compare well to the conventional scale data presented in the present study in that the unweathered  $Q$  is higher than that of the weathered, indicating higher particle strength in the unweathered material. Comparing best fit values of  $Q$  and  $R$  for conventional and large-scale testing reveals that  $Q$  and  $R$  increase with increasing particle size. Values of  $R$  decreased by different rates in both materials, but as  $R$  is purely a fitting parameter, the rate of change of the parameter for different materials is erroneous due to the fact that  $R$  is purely a fitting parameter and is not associated with a specific material property. Values of  $Q$  and  $R$  for both conventional scale and large-scale triaxial tests are tabulated in Table 6.16 for comparison.

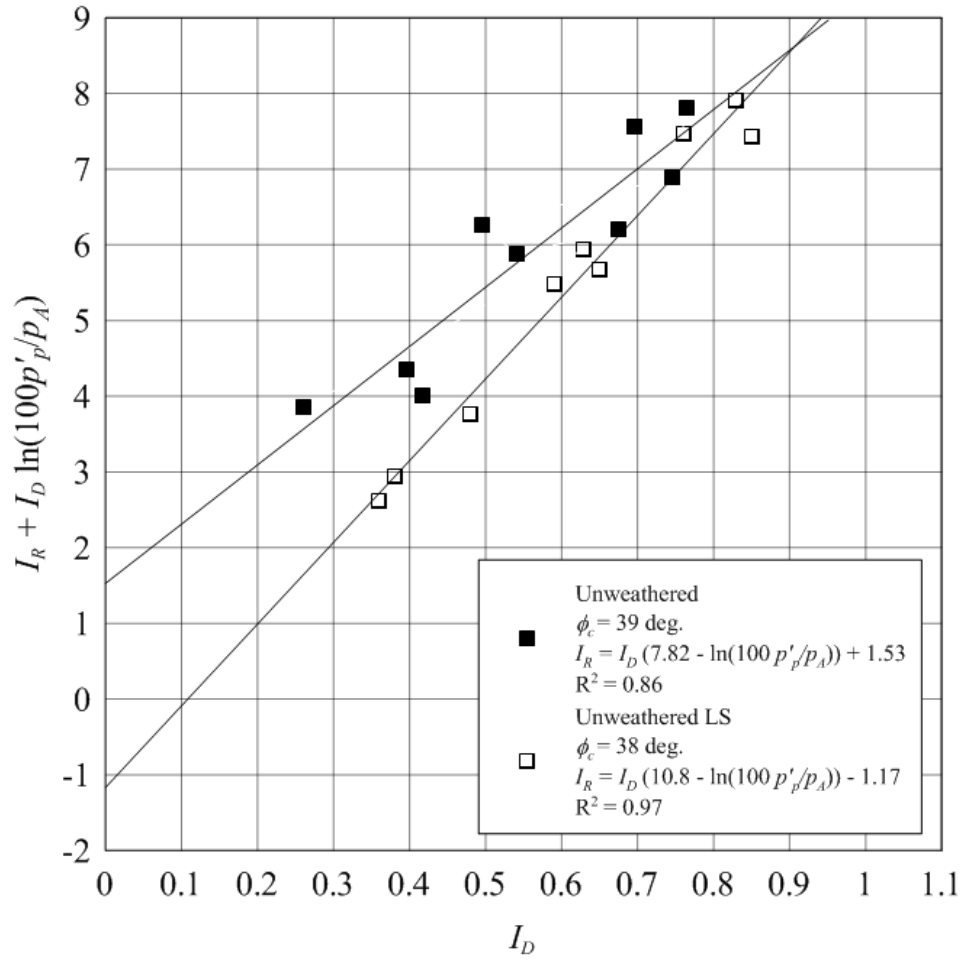


Figure 6.22: Regression of the dilatancy response of conventional and large-scale unweathered *MWR* in accordance with the procedure outlined by Salgado et al. (2000) (Fox 2011).

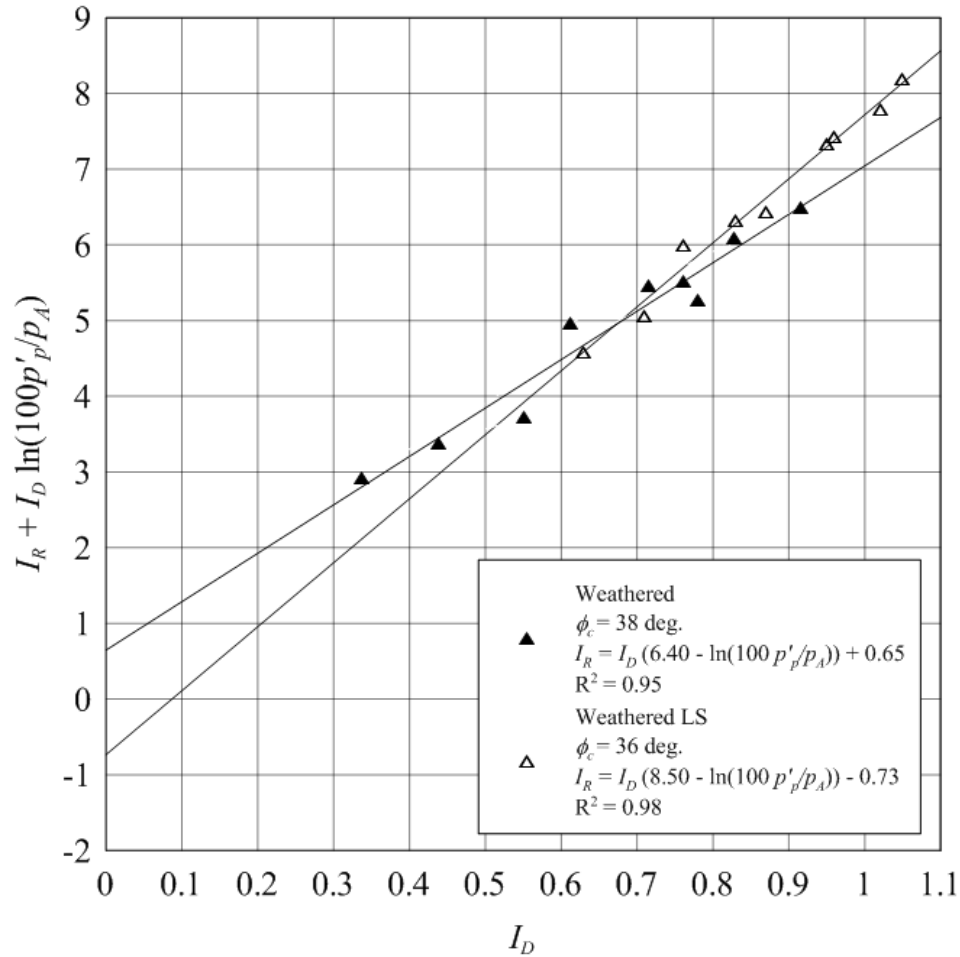


Figure 6.23: Regression of the dilatancy response of conventional and large-scale weathered  $MWR$  in accordance with the procedure outlined by Salgado et al. (2000) (Fox 2011).

Table 6.16: Comparison of best fit values of  $Q$  and  $R$  between conventional and large-scale triaxial testing (Fox 2011).

Material	$Q$	$R$
Unweathered	7.82	-1.53
Unweathered LS	10.8	1.17
Weathered	6.40	-0.65
Weathered LS	8.50	0.73

For comparison purposes, Bolton's (1986) stress – dilatancy relationship was implemented using values of  $\phi_c$ ,  $Q$ , and  $R$  determined by Fox (2011) according to the iterative procedure outlined by Salgado (2008). Using large-scale triaxial testing results

provided much more accurate predictions of  $\phi_p$  compared to those of conventional scale tests. Average differences were  $0.7^\circ$  and  $0.5^\circ$  for the unweathered and weathered *MWR* materials, respectively. Results of  $\phi_p$  predictions using Bolton's relationship are presented in Tables 6.17 and 6.18 for large-scale triaxial tests. Additionally, the values of  $\phi_c$ ,  $Q$  and  $R$  determined in conventional scale triaxial testing were used to predict  $\phi_p$  for the large-scale triaxial specimens. In both *MWR* materials, the prediction of  $\phi_p$  was unconservative with a more unconservative difference for the unweathered material (an average of  $3.4^\circ$  higher than measured values). The weathered material predicted  $\phi_p$  values  $1.1^\circ$  higher than measured values, on average. In the case of both *MWR* materials, more accurate predictions of  $\phi_p$  were obtained for specimens isotropically compressed to higher levels of  $D_R$ . Predictions of  $\phi_p$  for large-scale triaxial tests using Bolton's (1986) relationship and values of  $\phi_c$ ,  $Q$  and  $R$  determined in conventional scale triaxial testing are presented in Tables 6.19 and 6.20.

Table 6.17: Comparison of measured and predicted values of  $\phi_p$  for the unweathered *MWR* material using Bolton's (1986) relationship and best fit values of  $Q$  and  $R$  for large-scale triaxial tests (calculated from data presented by Fox 2011).

	$\phi_c$ (deg.)	$Q$	$R$	
	38	10.80	1.17	
	$I_D$	Predicted $\phi_p$ (deg.)	Measured $\phi_p$ (deg.)	$\Delta \phi_p$ (deg.)
U32-100 LS	0.32	39.7	40	0.2
U57-100 LS	0.57	43.5	44	0.9
U75-100 LS	0.75	46.2	47	1.1
U34-200 LS	0.34	39.3	40	0.5
U60-200 LS	0.6	42.8	44	1.1
U83-200 LS	0.83	45.7	46	0.2
U46-400 LS	0.46	40	39	-0.5
U64-400 LS	0.64	42.1	42	-0.5
U83-400 LS	0.83	44.2	43	-1.5
			Average Difference	0.7

Table 6.18: Comparison of measured and predicted values of  $\phi_p$  for the unweathered *MWR* material using Bolton's (1986) relationship and best fit values of  $Q$  and  $R$  for large-scale triaxial tests (calculated from data presented by Fox 2011).

	$\phi_c$ (deg.)	$Q$	$R$	
	36	8.50	0.73	
	$I_D$	Predicted $\phi_p$ (deg.)	Measured $\phi_p$ (deg.)	$\Delta \phi_p$ (deg.)
W63-100 LS	0.63	39.7	39	-0.4
W76-100 LS	0.76	40.8	41	0.5
W102-100 LS	1.02	43.0	42	-0.9
W71-200 LS	0.71	39.0	38	-0.8
W83-200 LS	0.83	39.8	40	-0.2
W95-200 LS	0.95	40.6	40	-0.2
W87-400 LS	0.87	38.4	38	-0.7
W96-400 LS	0.96	38.9	39	-0.1
W105-400 LS	1.05	39.3	39	-0.1
			Average Difference	0.5

Table 6.19: Comparison of measured and predicted values of  $\phi_p$  for the large-scale unweathered *MWR* material using Bolton's (1986) relationship and best fit values of  $Q$  and  $R$  for conventional scale triaxial tests (calculated from data presented by Fox 2011).

	$\phi_c$ (deg.)	$Q$	$R$	
	39	7.82	-1.53	
	$I_D$	Predicted $\phi_p$ (deg.)	Measured $\phi_p$ (deg.)	$\Delta \phi_p$ (deg.)
U32-100 LS	0.32	45.7	39.9	-5.8
U57-100 LS	0.57	47.3	44.4	-2.9
U75-100 LS	0.75	48.4	47.3	-1.1
U34-200 LS	0.34	45.2	39.8	-5.4
U60-200 LS	0.6	46.3	43.9	-2.4
U83-200 LS	0.83	47.3	45.9	-1.4
U46-400 LS	0.46	44.8	39.5	-5.3
U64-400 LS	0.64	45.2	41.6	-3.6
U83-400 LS	0.83	45.7	42.7	-3.0
			Average Difference	3.4

Table 6.20: Comparison of measured and predicted values of  $\phi_p$  for the large-scale weathered *MWR* material using Bolton's (1986) relationship and best fit values of  $Q$  and  $R$  for conventional scale triaxial tests (calculated from data presented by Fox 2011).

	$\phi_c$ (deg.)	$Q$	$R$	
	38	6.40	-0.65	
	$I_D$	Predicted $\phi_p$ (deg.)	Measured $\phi_p$ (deg.)	$\Delta \phi_p$ (deg.)
W63-100 LS	0.63	41.7	39.3	-2.4
W76-100 LS	0.76	42.1	41.3	-0.8
W102-100 LS	1.02	42.7	42.1	-0.6
W71-200 LS	0.71	40.6	38.2	-2.4
W83-200 LS	0.83	40.7	39.6	-1.1
W95-200 LS	0.95	40.8	40.4	-0.4
W87-400 LS	0.87	39.0	37.7	-1.3
W96-400 LS	0.96	38.9	38.8	-0.1
W105-400 LS	1.05	38.9	39.2	0.3
			Average Difference	1.1

### 6.7.3 Particle Breakage

Comparison of particle breakage between conventional and large-scale triaxial tests is limited to comparison of the initial and post test gradations for each material at each scale of testing. Initial and post test gradations (indicating the gradation of maximum change from the initial for the range of tests considered) for conventional and large-scale triaxial tests are presented on Figures 6.24 and 6.25 for the unweathered and weathered *MWR* materials, respectively. Post test gradations show that the shift in the particle size distribution for both materials is relatively constant in shape for both materials with the conventional scale tests having a slightly higher magnitude of shift, especially in the weathered material.

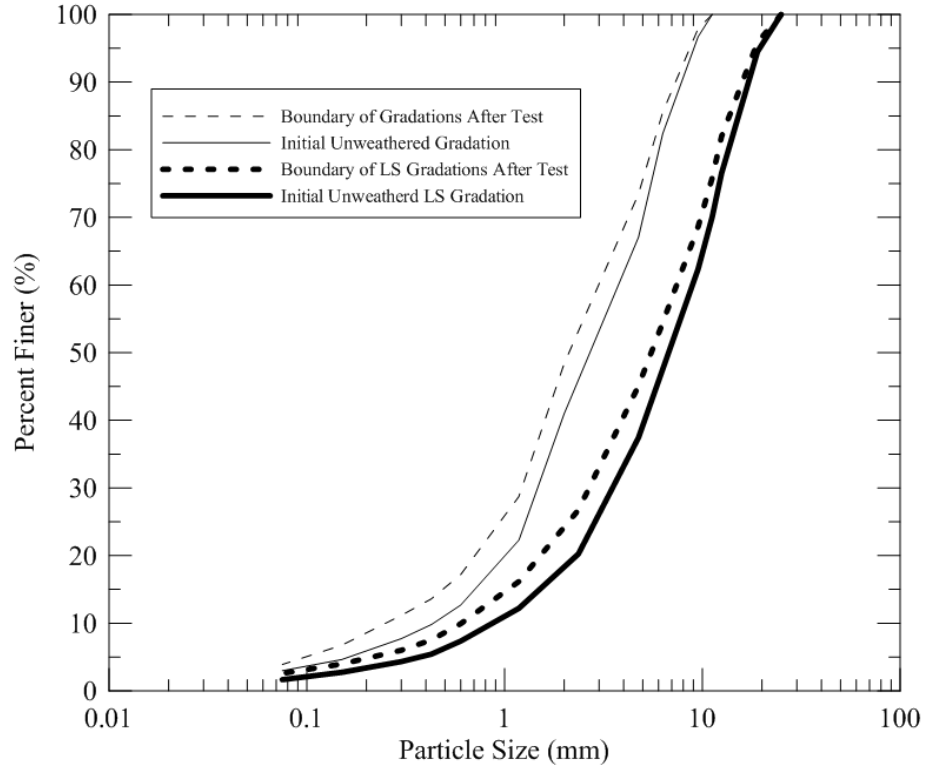


Figure 6.24: Initial and post test gradations for conventional and large-scale triaxial tests on unweathered *MWR* specimens (Fox 2011).

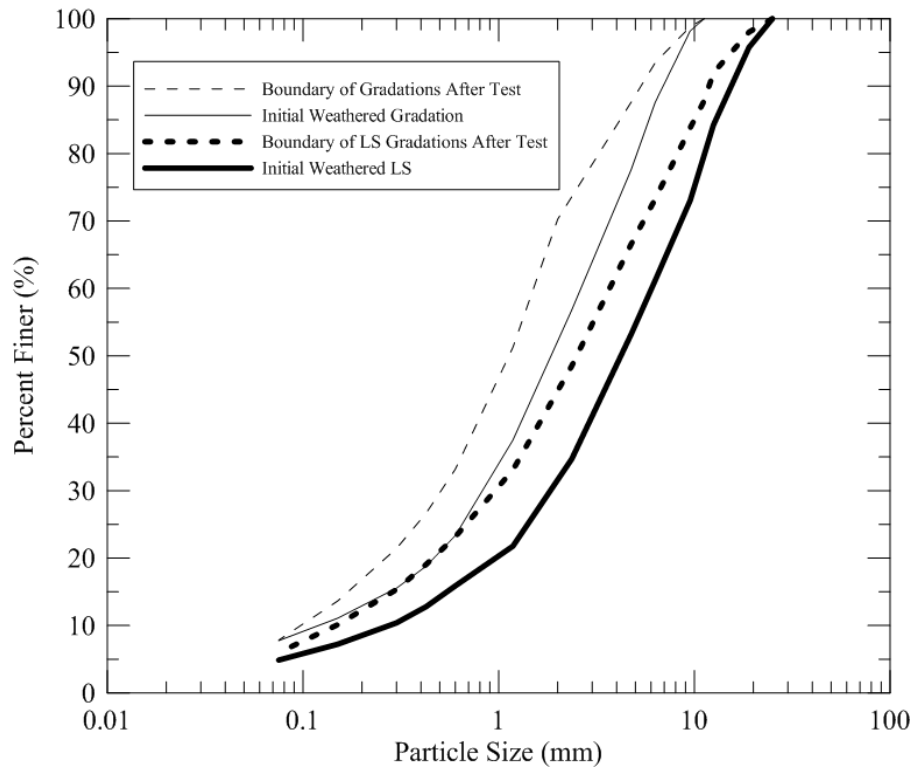


Figure 6.25: Initial and post test gradations for conventional and large-scale triaxial tests on weathered *MWR* specimens (Fox 2011).

#### 6.7.4 Fractal Dimension

The initial  $D$  for the large-scale specimens tested by Fox (2011) was 2.53 and 2.79 for the unweathered and weathered *MWR* material, respectively. Both conventional and large-scale triaxial test results show a change in  $D$  in the weathered material approximately two times that of the unweathered indicating a greater propensity for particle breakage for the  $p'$  levels used in the tests. The evolution of  $D$  for conventional and large-scale tests is plotted on Figure 6.26 for comparison. With the initial  $D$  possibly being a function of particle size, the comparison of the presented results in Figure 6.25 should be the path to a stable  $D$ . For both materials, the path from  $p' = 0$  kPa to  $p' = 400$  kPa appear parallel. Additionally, both materials show little effect of  $D_R$  on the evolution of  $D$ . Therefore, with parallel paths and the insignificant effect of  $D_R$ , it is postulated that the  $p'$  required for a conventional scale specimen to reach a truly stable  $D$  is the same as the  $p'$  required for a large-scale specimen. Equipment limitations during both studies prevented testing above  $p' = 400$  kPa and, as a result, this hypothesis cannot be confirmed. To show the similarity between the evolutions of  $D$  for the two materials, Figure 6.27 shows the evolution of  $D$  normalized with respect to the initial  $D$  of the model gradation. Values of the measured  $D$  and  $\Delta D$  for large-scale triaxial tests are presented in Table 6.21.

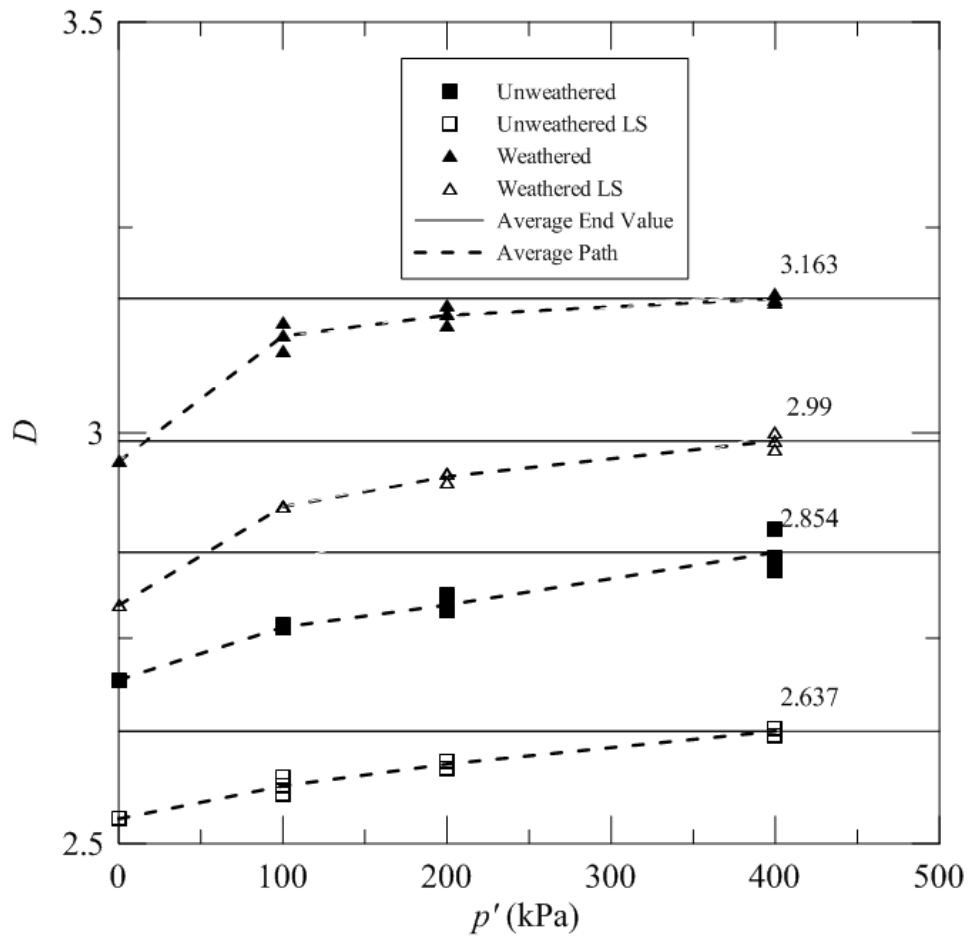


Figure 6.26: Evolution of the fractal dimension ( $D$ ) for the unweathered and weathered *MWR* materials in conventional and large-scale triaxial testing (From data obtained by Fox 2011).

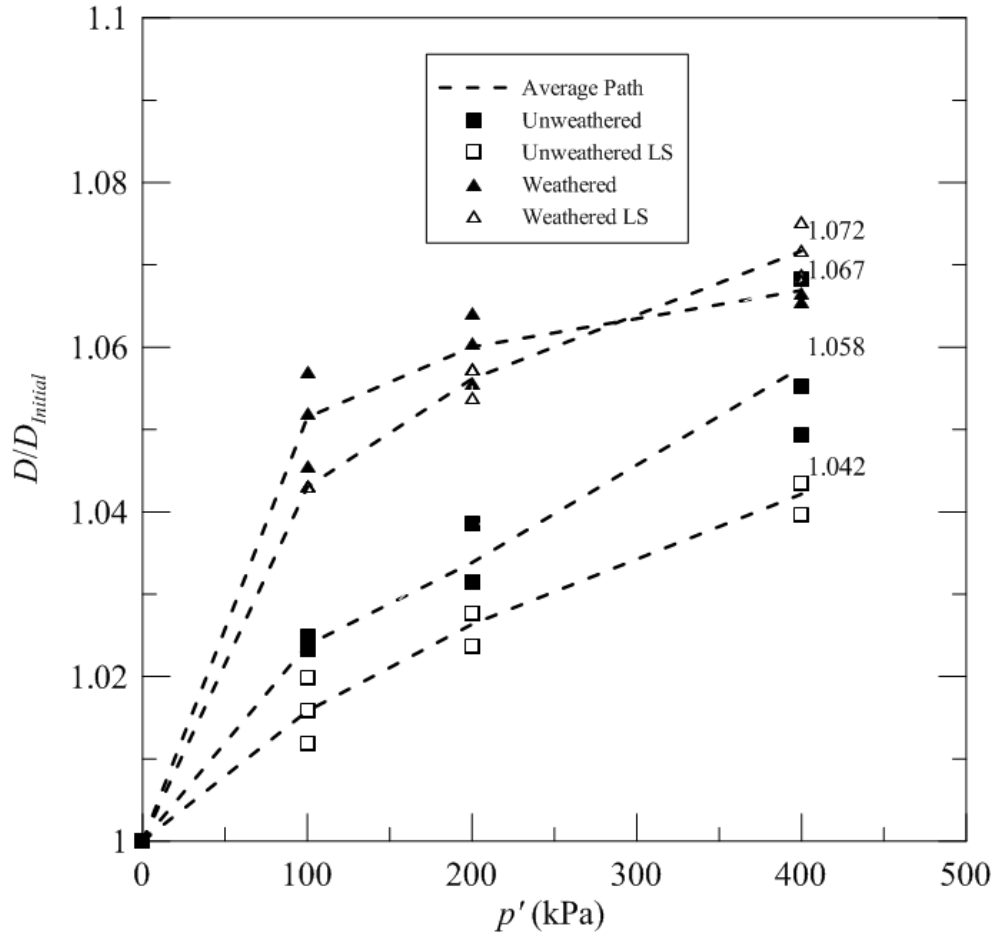


Figure 6.27: Evolution of the fractal dimension ( $D$ ) for the unweathered and weathered  $MWR$  materials in conventional and large-scale triaxial testing normalized with respect to  $D_{Initial}$  (From data obtained by Fox 2011).

Table 6.21: Values of  $D_{final}$  and  $\Delta D$  determined for each *LSTX* test (Fox 2011)

Test	$D_{Initial}$	$D_{final}$	$\Delta D$
U32-100 LS	2.53	2.56	0.03
U57-100 LS	2.53	2.57	0.04
U75-100 LS	2.53	2.58	0.05
U34-200 LS	2.53	2.59	0.06
U60-200 LS	2.53	2.60	0.07
U83-200 LS	2.53	2.60	0.07
U46-400 LS	2.53	2.64	0.11
U64-400 LS	2.53	2.64	0.11
U83-400 LS	2.53	2.63	0.10
W63-100 LS	2.79	2.91	0.12
W76-100 LS	2.79	2.91	0.12
W102-100 LS	2.79	2.91	0.12
W71-200 LS	2.79	2.95	0.16
W83-200 LS	2.79	2.95	0.16
W95-200 LS	2.79	2.94	0.15
W87-400 LS	2.79	2.98	0.19
W96-400 LS	2.79	2.99	0.20
W105-400 LS	2.79	3.00	0.21

### 6.7.5 Surface Energy

Fox (2011) evaluated the modified Granta – Gravel work equation as described in Section 6.6. Table 6.23 presents values of  $\Gamma_{se}$  and  $dS$  calculated for each triaxial test for both the unweathered and weathered *MWR* materials in *LSTX* testing. Fox (2011) reports values of  $\Gamma_{se}$  ranging between 8 and 24 J/m<sup>2</sup> for the unweathered material and 8 and 15 J/m<sup>2</sup> for the weathered material. These values correlate extremely well with the values of  $\Gamma_{se}$  determined for the conventional scale specimens tested in the present study (7.2 – 23.7 J/m<sup>2</sup> for the unweathered material and 3.7 – 6.8 J/m<sup>2</sup> for the weathered material). These results indicate that surface energy is an intrinsic characteristic of a given material and may be independent of particle size. Increasing values of  $dS$  are not comparable

because the surface area of a specific specimen is dependent on the scale of the specimen itself (i.e. the amount of material within the specimen).

Table 6.22: Values of  $\Gamma_{se}$  and  $dS$  determined for each *LSTX* test (Fox 2011)

Test	$\Gamma_{se}$ (J/m <sup>2</sup> )	$dS$ (m <sup>2</sup> )
U32-100 LS	8	3
U57-100 LS	8	3
U75-100 LS	13	3
U34-200 LS	22	4
U60-200 LS	19	5
U83-200 LS	20	5
U46-400 LS	21	7
U64-400 LS	24	8
U83-400 LS	13	8
W63-100 LS	8	8
W76-100 LS	9	9
W102-100 LS	5	14
W71-200 LS	15	6
W83-200 LS	6	18
W95-200 LS	9	18
W87-400 LS	7	21
W96-400 LS	9	20
W105-400 LS	8	22

## CHAPTER 7: CONCLUSIONS

### 7.1 Summary

The present study was developed to systematically investigate the mechanical behavior of unweathered and weathered mine waste rock (*MWR*) in conventional scale triaxial testing. Results of the study were compared to large-scale triaxial test results presented by Fox (2011) for the same *MWR* materials at the same levels of  $p'$ . Model gradations were created for each material following the parallel gradation approach developed by Lowe (1964) such that the particle size distribution curve for each model gradation was exactly parallel to the material collected in the field and large-scale specimens. The parallel gradation technique was used in an effort to make the fabric of the material independent of sample size and maximum particle size in order to quantitatively and qualitatively analyze the effect of sample scaling and, correspondingly, maximum particle size on the mechanical response of a given geomaterial. The main conclusions ascertained during the course of the present study are presented in the following sections.

### 7.2 Specimen Preparation and Uniformity

Specimen reconstitution was performed in accordance with the preparation technique outlined by Fox (2011) which is consistent with the rigid, thin-walled tube technique outlined in ASTM D 4254 (Method B) except specimens were reconstituted in two identical lifts instead of a single lift. An experimental program was conducted to test the uniformity of triaxial test specimens before triaxial testing was conducted. Tables 4.6 and 4.7 outline the results of the experimental program designed to evaluate specimen

uniformity in conventional scale triaxial test specimens. Results of the experimental program indicate that specimen uniformity was consistently better in conventional scale triaxial test specimens compared to that of large-scale triaxial test specimens. Coefficients of variation (*COV*) for the  $D_R$  measured in each lift was 4.1% and 2.5% for “loose” and “dense” conventional scale triaxial specimens, respectively, compared to 15.3% and 8.0% for “loose” and “dense” large-scale triaxial test specimens, respectively.

### 7.3 Isotropic Compression

The range of critical state parameters  $\kappa$ ,  $\nu_{\kappa}$ ,  $\lambda$  and  $N$  determined after isotropic compression for unweathered and weathered *MWR* materials were shown to be similar in comparison between conventional and large-scale triaxial testing (Table 6.12). The relatively constant range of  $\kappa$ ,  $\nu_{\kappa}$ ,  $\lambda$  and  $N$  determined over the similar ranges of  $D_{R, Initial}$  to which specimens were reconstituted suggests that the compressibility of the materials during isotropic compression is relatively independent of sample size and maximum particle size. A large number of variables may exist, such as fines content, particle strength and mineralogy, which may vary between specimen scales. These varying parameters may influence the observed compressibility of specimens at different scales. Compressibility often increases as fines content increases, the slight increase in compressibility of conventional scale specimens may be explained by the increase in fines content though the parallel gradation technique. Therefore, the isotropic compression data presented in this study also suggests the individual grain properties between conventional and large-scales are relatively constant for the two *MWR* materials tested (which is unlikely true for all geomaterials).

## 7.4 Drained Monotonic Axisymmetric Compression

### 7.4.1 Typical Stress – Strain – Volumetric Response

Stress-strain-volumetric responses were very similar between conventional and large-scale triaxial specimens. Specimens in both conventional and large-scale triaxial testing generally exhibited strain softening behavior for the unweathered material where strain hardening behavior was observed for the weathered material. The strain – volumetric response of both materials also showed similarities between conventional and large-scale tests. The unweathered material tended towards a more dilative behavior compared to the contractive behavior exhibited by the weathered material for the range of soil states tested. Volumetric responses of each material are plotted on Figures 6.17 and 6.18. Data presented suggests that general (i.e. dilative or contractive) stress-strain-volumetric behavior is independent of scale and maximum particle size for a given material although the conventional unweathered specimens appeared to be a bit more dilative than their large-scale counterparts. The presented data also suggests that compressibility and frictional characteristics during monotonic loading increase with decreasing particle size. These results may be attributed to increased particle breakage during monotonic loading, increased  $FC$  and increased fines plasticity among other factors.

For the conventional and large-scale triaxial tests, the peak dilatancy rate  $(-\delta\varepsilon_p/\delta\varepsilon_a)_{max}$  was one order of magnitude higher for the unweathered  $MWR$  material than that of the weathered  $MWR$  material. Average values of  $(-\delta\varepsilon_p/\delta\varepsilon_a)_{max}$  for conventional scale triaxial tests were 0.259 and 0.024 for the unweathered and weathered material, respectively, whereas large-scale triaxial tests indicated average values of  $(-\delta\varepsilon_p/\delta\varepsilon_a)_{max}$  equal to 0.122

and 0.026 for the unweathered and weathered material, respectively. These results suggest fines content ( $FC$ ), nature of the fines (i.e. plasticity and particle shape) and particle breakage may significantly affect the measured values of  $(-\delta\varepsilon_p/\delta\varepsilon_a)_{max}$  during monotonic loading of  $MWR$  materials.

#### 7.4.2 Critical State Friction Angle

The critical state friction angle ( $\phi_c$ ) was determined to be  $39^\circ$  for the unweathered material and  $38^\circ$  for the weathered material in conventional scale triaxial testing. The final value of  $\phi_c$  was determined by analyzing tests reconstituted to relatively low levels of  $D_R$  at the highest levels of  $p'$ , which generally exhibited mechanical behavior that most nearly meets the critical state criteria ( $\delta v/\delta\varepsilon_q = \delta p'/\delta\varepsilon_q = \delta q/\delta\varepsilon_q = 0$ ). The final values of  $\phi_c$  determined in the study presented by Fox (2011) were  $38^\circ$  for the unweathered material and  $36^\circ$  for the weathered material. Results suggest that  $\phi_c$  increases slightly (by  $1 - 2^\circ$ ) with decreasing sample size and maximum particle size.

#### 7.4.3 Stress – Dilatancy Relationship

Critical state parameters  $Q$  and  $R$  were determined to be 7.82 and -1.53 for the unweathered material and 6.40 and -0.65 for the weathered material tested in conventional scale triaxial tests. Fox (2011) presented values of  $Q$  and  $R$  equal to 10.8 and 1.17 for the unweathered material and 8.50 and 0.73 for the weathered material tested in large-scale triaxial tests. Results indicate that both  $Q$  and  $R$  increase with increasing particle size. With respect to the values of  $Q$ , which is intrinsically related to the strength of a material's individual grains, data suggests that particle strength increases with

increasing particle size for both materials. Also, the use of Bolton's (1986) stress – dilatancy relationship indicates greater accuracy in predicting  $\phi_p$  using large-scale test results.  $\phi_c$ ,  $Q$  and  $R$  values obtained from large-scale specimens predicted  $\phi_p$  with an average difference equal to  $0.7^\circ$  for the unweathered material and an average difference equal to  $0.5^\circ$  with a for the weathered material.  $\phi_c$ ,  $Q$  and  $R$  values obtained from conventional scale specimens gave an average difference equal to  $1.5^\circ$  for the unweathered material and an average deviation equal to  $1.0^\circ$  for the weathered material. Using  $\phi_c$ ,  $Q$ , and  $R$  parameters determined in conventional scale triaxial tests, Bolton's relationship predicted values of  $\phi_p$  for large-scale triaxial tests differing  $3.4^\circ$  from measured values, on average, for the unweathered material where the average difference for the weathered material was only  $1.1^\circ$ . Predictions of  $\phi_p$  using Bolton's relationship were shown to become more accurate as  $D_R$  increased. Results indicate that conventional triaxial tests should not be used to characterize the strength characteristics of large-scale materials.

### 7.5 Particle Breakage and Fractal Dimensions

Post test gradations indicate a slightly larger propensity for particle breakage in the conventional scale triaxial tests compared to that of large-scale triaxial tests. However, the shift in the particle-size distribution is similar in shape for both materials indicating the relative amount of particle breakage experienced by the mean particle size is scale invariant for materials exhibiting the same fabric but different maximum particle sizes.

The fractal dimension ( $D$ ) was shown to evolve in somewhat parallel paths for both conventional and large-scale tests suggesting the same  $p'$  would be required to achieve a stable  $D$  for both conventional and large-scale tests. In both scales, the value of  $D$  was shown to be independent of  $D_R$  and highly dependent on the value of initial confining stress. Total changes in  $D$  were approximately twice as large for the weathered material as the unweathered material in both scales. Although the initial  $D$  may be dependent on the scale of the initial particle-size distribution, results suggest the evolution of  $D$  is independent of sample size and maximum particle size.

#### 7.6 Surface Energy

Values of surface energy ( $\Gamma_{se}$ ) were shown to be within the same range in both conventional and large-scale triaxial tests. Results presented indicate that surface energy is an intrinsic property of a given material and is independent of sample size and maximum particle size. In both cases, values of  $\Gamma_{se}$  were found to be consistent with published values of  $\Gamma_{se}$  in the literature.

#### 7.7 Parallel Gradation Technique

The present study illustrates the suitability of implementing the parallel gradation technique to accurately test the mechanical response of geomaterials with large maximum particle sizes. Although results indicate that large-scale triaxial testing provides more accurate values of  $\phi_c$  than conventional scale tests, the range of deviation is quite small. Moreover, the similarities in mechanical responses between conventional and large-scale tests allows the practicing geotechnical engineer to qualitatively and semi-quantitatively

analyze geomaterials with large maximum particle sizes in conventional scale laboratory settings without the need for specialized large-scale equipment for some practical purposes. However, it must be reiterated that the conventional scale triaxial testing did produce consistently unconservative values (even if ever so slightly) of  $\phi_c$  (and  $\phi_p$ ) compared to the values obtained during large-scale testing. As such, relying on conventional tests alone to accurately characterize the mechanical behavior of geomaterials containing large particle sizes may lead to unconservative estimations of material strength. Finally, for practical purposes, the results of this study suggest that an empirical correlation may be developed to estimate large-scale behavior using conventional scale triaxial tests given additional data collected for a range of testing scales.

### 7.8 Suggestions for Future Work

The following research topics concerning the mechanical behavior of *MWR* are suggested:

1. Further research on the role that particle shape plays in affecting the values of limiting void ratios measured for *MWR* materials with large particle sizes.
2. Further research on the evolution of a stable fractal dimension ( $D$ ) and the potential for a normalized relationship relating specimens with parallel gradations at both large and small scales.
3. Further research in the use of the shape factors  $\beta_s$  and  $\beta_v$  and the influence that specimen scaling (i.e. with the parallel gradation) technique may have on measured values of  $\beta_s$ ,  $\beta_v$ ,  $dS$  and correspondingly,  $D$ .

4. Further research on the mechanical behavior of *MWR* materials at higher levels of  $p'$  similar to those that might be found in large *MWR* impoundments.
5. Further systematic research on the effect of *FC* on the mechanical behavior of *MWR* at varying scales to better allow evaluation of the mechanical behavior of field materials in geotechnical laboratories.
6. Further research regarding the effect of mineralogy as well as the effect of chemical and physical weathering on the mechanical behavior of *MWR* materials at both large and small scales.
7. The data presented in Section 6.7.1 may suggest that particle breakage is relatively constant in specimens scaled using the parallel gradation technique and that have similar individual grain properties between scales. No conclusive data was measured or obtained to support this hypothesis during the course of this study and further research into the relative magnitude and effect of particle breakage on the critical state parameters  $\kappa$ ,  $\nu_{\kappa}$ ,  $\lambda$  and  $N$  determined after isotropic compression is suggested.
8. Further testing in an effort to develop an empirical correlation to estimate large-scale behavior using conventional scale triaxial tests.

## LIST OF REFERENCES

- Ashby, M. F. and Jones, D. R. H. (1986) *Engineering Materials II*, Oxford: Pergamon Press.
- Ashby, M. F. and Jones, D. R. H. (1980) *Engineering Materials I*, Oxford: Pergamon Press.
- ASTM D 4767-04 *Standard Test Method for Undrained Triaxial Compression Test on Cohesive Soils*. ASTM International.
- ASTM D 2487-10 *Standard Practice for Classification of Soil for Engineering Purposes (Unified Soil Classification System)* ASTM International.
- ASTM D 2488-09 *Standard Practice for Description and Identification of Soils*. ASTM International.
- ASTM D 6913-04 *Standard Test Method for Particle-size Distribution of Soils Using Sieve Analysis* ASTM International.
- ASTM D 4253-00 *Standard Test Method for Maximum Index Density and Dry Unit Weight of Soils Using a Vibratory Table*. ASTM International.
- ASTM D 4318-10 *Standard Test Method for Liquid Limit, Plastic Limit, and Plasticity Index of Soils*. ASTM International.
- ASTM D 4254-00 *Standard Test Method for Minimum Index Density and Dry Unit Weight of Soils and Calculation of Relative Density*. ASTM International.
- ASTM D 421-85 *Standard Practice Dry Preparation of Soil Samples for Particle-Size Analysis and Determination of Soil Constants*. ASTM International.
- ASTM D 422-62 *Standard Test Method for Particle Size Analysis of Soils*. ASTM International.
- ASTM D 854-02 *Standard Test Method for Specific Gravity of Solids by Water Pycnometer*. ASTM International.
- ASTM C 127-07 *Standard Test Method for Density, Relative Density and Absorption of Coarse Aggregate*. ASTM International.
- Baxter, D. Y. (2000) *Mechanical Behavior of Soil-Bentonite Cutoff Walls*, PhD. Dissertation, *Virginia Polytechnic Institute and State University*. USA.

- Been, K. and Jefferies, M. G. (2000) Implications for critical state theory from isotropic compression of sand, *Geotechnique*, Vol. 50, No. 4, 419-429.
- Been, K. and Jefferies, M. G. (1985) A state parameter for sands, *Geotechnique*, Vol. 35, No. 2, 99-112.
- Bohn, H.L., McNeal, B.L., O' Connor, G.A. (2001) Soil Chemistry. Wiley Interscience, Wiley & Sons, New York.
- Bolton, M. D., Nakata, Y., and Chen, Y. P. (2008) Micro- and macro-mechanical behavior of DEM crushable materials, *Geotechnique*, Vol. 58, No. 6, 471-480.
- Bolton, M. D. (1986) The strength and dilatancy of sands, *Geotechnique*, Vol. 36, No. 1, 65-78.
- Bolton M.D. and Lee D.M. (1993) Back-analysis of a pilot scale shear test on coarse granular fill, *Proc. Int. Conf. on Engineered Fills*, Newcastle University, Thomas Telford, London, 214-225.
- Brace, W. F. and Walsh, J. B. (1962) Some direct measurements of the surface energy of quartz and orthoclase. *Am. Miner.* Vol. 47, 1111-1122.
- Bozzano, F., Gaeta, M. and Marcoccia, S. (2005) Weathering of Valle Ricca Stiff and Jointed Clay. *Engineering Geology*. Vol. 84, 161-182.
- Carraro, J. A. H., Prezzi, M., and Salgado, R. (2009) Shear Strength and Stiffness of Sands Containing Plastic and Nonplastic Fines, *Journal of Geotechnical and Geoenvironmental Engineering*, Vol. 135, No. 9, 1167-1178.
- Carraro, J. A. H. (2004) Mechanical Behavior of Silty and Clayey Sands, PhD. Dissertation. *Purdue University*, USA.
- Chang, N., Hermann, G. and Clayton, C. (2011) The Effect of Fabric on the Behavior of Gold Tailings, *Geotechnique*, Vol. 61, No. 3, 187-197.
- Cho, G. C., Dodds, J. and Santamarina, J. C. (2006) Particle Shape Effects on Packing Density, Stiffness and Strength, *Journal of Geotechnical and Geoenvironmental Engineering*, Vol. 132, No. 5, 591-602.
- Corey, A. T. (1994) *Mechanics of Immiscible Fluids in Porous Media*. Water Resources Publications, LLC, Colorado.
- Coop, M. R., Sorensen, K. K., Bodas Freitas, T., and Georgoutsos, G. (2004) Particle breakage during shearing of a carbonate sand, *Geotechnique*, Vol. 54, No. 3, 157-163.

- Das, B. M. (2006) *Principles of Geotechnical Engineering*. 6<sup>th</sup> Ed., Thomson Canada Limited. Canada.
- De Josselin de Jong, G. (1976 ) Rowe's Stress-Dilatancy Relation Based on Friction, *Geotechnique*, Vol. 26, No. 3, 527-534.
- Essington, M. E. (2004) *Soil and Water Chemistry*, New York: CRC Press.
- Forootan-Rad, P. and Moavenzadeh, F. (1968) Crack Initiation and Propagation in Rock, *MIT. Department of Civil Engineering Report*, R68-29, p. 126
- Fox, Z. P. (2011) Critical State, Dilatancy and particle Breakage of Mine Waste Rock. Master's Thesis. *Colorado State University*, USA.
- Friedman, M., Handin, J. and Alani, G. (1972) Fracture-Surface Energy of Rocks. *Int. J. Rock Mech. Min. Sci.*, Vol. 9, 757-766.
- Frost, R. J. (1973) Some testing experiences and characteristics of boulder-gravel fill in earth dams, *ASTM STP 523*, 207-233.
- Frost, J. D. and Park, J. Y. (2003) A Critical Assessment of the Moist Tamping Technique. *J. Geotechnical Testing*. ASTM, Vol. 26, No. 1, 1-14.
- Frydman, S., Zeitlen, J.G., and Alpan, I. (1973) The Membrane Effect in Triaxial Testing of Granular Soils, *Journal of Testing and Evaluation*, Vol. 1, No. 1, 37-41.
- Fumagalli, E. (1969) Tests on cohesionless materials for rockfill dams, *Journal of Soil Mechanics and Foundations*, ASCE, Vol. 95, No. 1, 313-332.
- Gilman J. J. (1960) Direct measurement of surface energies of crystals. *J. Appl. Phys.* Vol. 31, 2208-2218.
- Hardin, B. O. (1985) Crushing of soil particles, *Journal of Geotechnical Engineering*, Vol. 111, No. 10, 1177-1192.
- Harr, M E. (1977) *Mechanics of particulate media*, McGraw Hill: New York.
- Head, K. H. (1986). *Manual of Soil Laboratory Testing* Vol. 3, Pentech Press Limited: London.
- Henkel, D. J. and Gilbert, G. D. (1952) The Effect of the Rubber membrane on the Measure Triaxial compression Strength of Clay Samples, *Geotechnique*, Vol. 3, 20-29.

- Holtz, W. G., and Gibbs, H. J. (1956) Triaxial shear tests on pervious gravelly soils, *Journal of Soil Mechanics and Foundations Division, ASCE*, Vol. 82, No. SM1, Proceedings Paper 867, 1-22.
- Indraratna, B. and Salim, W. (2002) Modeling of particle breakage of coarse aggregate incorporating strength and dilatancy *Geotechnical Engineering*, Vol. 155, No. 4, 243-252.
- Indraratna, B., Ionescu, D., and Christie, H.D. (1998) Shear Behavior of Railway Ballast Based on Large-scale Triaxial Tests, *Journal of Geotechnical and Geoenvironmental Engineering*, Vol. 124, No. 5, 439-449.
- Indraratna, W. B., Wijewardena, L.S.S., and Balasubramaniam, A.S. (1993) Large-scale Testing of Greywacke Rockfill, *Geotechnique*, Vol. 43, No. 1, 37-51.
- Jory, J (1999) Stratigraphy and host-rock controls of gold deposits in the northern Carlin trend. *Gold Deposits of the Carlin Trend*, 20-34.
- Karimpour, H. and Lade, P. V. (2010) Time effects relate to crushing in sand, *Journal of Geotechnical and Geoenvironmental Engineering*, Vol. 136, No. 9, 1209-1219.
- Kuhn, M. R. and Mitchell, J. K. (1993) New Perspectives on Soil Creep. *Journal of Geotechnical Engineering*. ASCE, Vol. 119, No. 3, 507-524.
- Lade, P. V. and Karimpour, H. (2010) Time Effects Related to Crushing in Sand. *Journal of Geotechnical and Geoenvironmental Eng.* ASCE, Vol. 136, No. 9, 1209-1219.
- Lade, P. V. (1994) Creep effects on static and cyclic instability of granular soils, *Journal of Geotechnical Engineering*, Vol. 120, No. 2, 404-419.
- Lade, P. V., Yamamuro, J. A. and Bopp, P. A. (1998) Influence of Time Effects on Instability of Granular Materials, *Computers and Geotechnics*, Vol. 20, No. 3/4, 179-193.
- Lade, P. V., Yamamuro, J. A. and Liggio, C. D. (2009) Effects of Fines Content on Void Ratio, Compressibility, and Static Liquefaction of Silty Sand, *Geomechanics and Engineering*, Vol. 1, No. 1, 1-15.
- Lambe, T. W., and Whitman, R. V., (1969) *Soil Mechanics*, John Wiley and Sons, New York.
- LaRochelle, P., Leroueli, S., Trak, B., Blais-Leroux, L., and Tavenas, F. (1988) Observational Approach to Membrane and Area Corrections in Triaxial Tests, *Advanced Triaxial Testing of Soils and Rock*, ASTM, STP 977, 715-731.

- Lee, D. M. (1992) The angles of friction of granular fills, Ph.D. dissertation, *Cambridge University, UK*.
- Leslie, D. D. (1969) Relationships between Shear Strength, Gradation, and Index Properties on Rockfill Materials *Proceedings, 7<sup>th</sup> International Conference on Soil Mechanics and Foundation Engineering*, Mexico City, 201-210.
- Leps, T. M. (1970) Review of Shearing Strength of Rockfill, *Journal of Soil Mechanics and Foundations Division*, ASCE, Vol. 96, No. SM 4, 1159-1170.
- Lowe, J. (1964) Shear strength of coarse embankment dam materials, *Proceedings from the 8<sup>th</sup> International Congress on Large Dams*, Vol. 3, 745-761.
- Mandelbrot, B. B. (1982) *The fractal geometry of nature*, W. H. Freeman.
- Marachi, N. D., Chan, C. K., and Seed, H. B. (1972) Evaluation of Properties of Rockfill Materials, *Journal of Soil Mechanics and Foundation Engineering*, ASCE, Vol. 98, No. SM1, 95-114.
- Marachi, N. D. (1969) "Strength Characteristics of Rockfill Materials" *Seventh International Conference on Soil Mechanics and Foundation Engineering*, Mexico City, 217-224.
- Marsal, R. J. (1973) *Mechanical Properties of Rockfill, Embankment-dam Engineering*, John Wiley & Sons: New York.
- Marsal, R. J. (1969) Particle Breakage in Coarse Granular Soils, *Proceedings, 7<sup>th</sup> International Conference on Soil Mechanics and Foundation Engineering*, Mexico City, 155-166.
- Marsal, R. J. (1969) Shear Strength of Rockfill Samples, *Proceedings, 7<sup>th</sup> International Conference on Soil Mechanics and Foundation Engineering*, Mexico City, 225-234.
- Marsal, R. J. (1967) Large-scale Testing of Rockfill Materials, *Journal of Soil Mechanics and Foundation Engineering Division*, ASCE, Vol. 93, SM2, 27-43.
- McDowell, G. R. (2003) Micromechanics of creep in granular materials, *Geotechnique*, Vol. 53, No. 10, 915-916.
- McDowell, G. R. and Khan, J. J. (2003) Creep of granular geomaterials, *Granular Matter*, Vol. 5, 115-120.
- McDowell, G. R. and Harireche, O. (2002) Discrete element modeling of soil particle fracture, *Geotechnique*, Vol. 52, No. 2, 131-135.

- McDowell, G. R., Nakata, Y., and Hoyodo, M. (2002) On the plastic hardening of sand, *Geotechnique*, Vol. 52, No. 5, 349-358.
- McDowell, G. R. and Bolton, M. D. (1998) On the micromechanics of crushable aggregates, *Geotechnique*, Vol. 48, No. 5, 667-679.
- McDowell, G. R., Bolton, M. D., and Robertson, D. (1996) The Fractal Crushing of Granular Materials, *Journal of Mechanical Physics of Solids*, Vol. 44, No. 12, 2079-2102.
- Mitchel, J. K. and Soga, K. (2005) *Fundamentals of Soil Behavior*. 3<sup>rd</sup> Edition, John Wiley and Sons, New Jersey.
- Miura, N. and O-hara, S. (1979) Particle crushing of decomposed granite soil and shear stresses, *Soils and Foundations*, Vol.19, No. 4, 1-14.
- Muir-Wood, D. (1990) *Soil behavior and critical state soil mechanics*, Cambridge University Press: Cambridge.
- Nakayama, J. (1965) Direct Measurement of Fracture Energies of Brittle Heterogeneous Materials. *Journal of the American Ceramic Society*. Vol. 48, No. 11, 583-587.
- Neves, E. M. (1990) *Advances in Rockfill Structures*. NATO ASI series.
- Oda, M. (1972) Initial Fabrics and Their Relations to Mechanical properties of Granular Material, *J. Japanese Soc. Of Soil Mech. and Foundation Eng.*, Vol. 12, No. 1, 17-36.
- Perkins T.K. and Bartlett L. E. (1963), Surface Energies of Rocks Measured During Cleavage. *Soc. Petrol Engrs. J.* Vol. 3, No. 4, 307.
- Pitman, T. D., Robertson, P. K. and Segoo, D. C. (1994) Influence of Fines on the Collapse of Loose Sands. *Canadian Geotech. J.* Vol. 31, 728-739.
- Reynolds, O. (1885) On the dilatancy of media composed of rigid particles in contact, with experimental illustrations, *Philosophical Magazine*, Series 5, Vol. 20, 469-481.
- Roscoe, K. H., Schofield, A. N. and Thurairajah, A. (1963) Yield of clays on states wetter than critical, *Geotechnique*, Vol. 13, 211-240.
- Rowe, P. W. (1962) The Stress-Dilatancy Equation for an Assembly of Particles in Contact, *Proceedings of the Royal Society of London. Series A. Mathematical and Physical Sciences*, Vol. 269, No. 1339, 500-527.

- Salgado, R. (2008) *The Engineering of Foundations*, McGraw-Hill Book Company: New York.
- Salgado, R., Bandini, P., and Karim, A. (2000) Strength and Stiffness of Silty Sand, *Journal of Geotechnical and Geoenvironmental Engineering*, Vol. 126, No. 5, 451-462.
- Santhanan A. T. and Gupta Y. P. (1968) Cleavage surface energy of calcite. *Int. Journal Rack Mech. Min. Sci.*, Vol. 5, 252-259.
- Schofield, A. N. and Wroth, C. P. (1968) *Critical State Soil Mechanics*, McGraw-Hill Book Company: New York.
- Sevi A. F. (2008), Physical Modeling of Railroad Ballast Using the Parallel Gradation Scaling Technique Within the Cyclical Triaxial Framework, PhD. Dissertation. *Missouri University of Science and Technology*. USA.
- Shaevich, R. B. (2007) Measurement of the specific free surface energy of solids. *Measurement Techniques*, Vol. 50, No. 10, 1121-1123.
- Sitharam, T. G. and Nimbkar, M. S. (2000) Micromechanical modeling of granular materials: effect of particle size and gradation, *Geotechnical and Geological Engineering*, Vol. 18, 91-117.
- Skempton, A.W. (1954). The Pore-Pressure Coefficients A and B. *Geotechnique*, Vol. 4, 143- 147.
- Tarantino, A. and Hyde, A. F. L. (2005) An experimental investigation of work dissipation in crushable materials, *Geotechnique*, Vol. 55, No. 8, 575-584.
- Taylor, D. W. (1948) *Fundamentals of Soil Mechanics*, John Wiley and Sons: New York.
- Townsend, F. C.(1973) Comparisons of Vibrated Density and Standard Compaction Tests on Sands with Varying Amounts of Fines, *Evaluation of Relative Density and Its Role in Geotechnical Projects Involving Cohesionless Soils, ASTM STP 523*, American Society for Testing and Materials, 348-363.
- Turcotte, D. L. (1986) Fractals and fragmentation, *Journal of Geophysical Research*, Vol. 91, No. B2, 921-926.
- Ueng, T. S. and Chen T. J. (2000) Energy Aspects of Particle Breakage in Drained Shear of Sands, *Geotechnique*, Vol. 50, No. 1, 65-72.

- Vaid, Y. P., Sivathayalan, S., and Stedman, D. (1999) Influence of specimen reconstitution method on the undrained response of sand, *Geotechnical Testing Journal*, Vol. 22, No. 33, 187-196.
- Vallerga, B. A., Seed, H. B., Monismith, C. L., and Cooper, R. S. (1957) "Effect of Shape, Size and Surface Roughness of Aggregate Particles on the Shear Strength of Granular Materials" *ASTM, STP 212*, 63-74.
- Varadarajan, A., Sharma, K. G., Venkatachalam, K., and Gupta, A. K. (2003) Testing and modeling two rockfill materials, *Journal of Geotechnical and Geoenvironmental Engineering*, Vol. 129, No. 3, 206-218.
- Wood, F.M., Yamamuro, J.A. and Lade, P.V. (2008): Effect of depositional method on the undrained response of silty sand. *Canadian Geotechnical Journal*, Vol. 45 No.11, 1525–1537.
- Yamamuro, J.A., Wood, F.M. and Lade, P.V. (2008): Effect of depositional method on the microstructure of silty sand. *Canadian Geotechnical Journal*, Vol. 45 No.11, 1538–1555.
- Yimsiri, S. and Soga, K. (2010). DEM analysis of soil fabric effects on behavior of sand. *Geotechnique*. Vol. 60, No. 6, 483-495.
- Zeller, J. and Wulliman, R. (1957) The shear strength of the shell materials for the GoSchenenalp Dam, Switzerland, *Proceedings of the 4<sup>th</sup> Institution of the Journal of Soil Mechanics and Foundation Engineering*, London, 2, 399-404.

## APPENDIX A: X-RAY DIFFRACTION RESULTS

As mentioned in Chapter 4, H & M Analytical based out of Allentown, NJ completed X-Ray diffraction (*XRD*) testing on the unweathered and weathered *MWR* materials in order to quantitatively characterize each material's mineralogy. Samples tested were created to model the fine and coarse fraction of each material. Tests were run on a Panalytical X'Pert Pro diffractometer using Cu radiation at 45KV/40mA and a scan over the range of 3° - 90° with a step size of 0.01576° and a counting time of 500 seconds per step. Once the diffraction patterns had been collected, Powder Diffraction File (PDF) published by the International Centre for Diffraction Data was used to identify the phases. After the phases were identified, they were quantified with the aid of a Rietveld refinement, which is a whole pattern fitting procedure and is considered the gold standard of quantitative analysis with a typical accuracy of about 1%. The Rietveld refinement is a standardless analysis which accounts for intensity, peak shape, and peak location to attain a minimal residual error between the calculated expected pattern and the observed diffraction pattern. A total of 14 phases, or constituents, were identified for the two *MWR* materials and numbered as tabulated in Table A.1. A detailed list of the identified constituents and their molecular formulas are tabulated in Table A.1. Figures A.1 through A.20 below provide detailed results from the *XRD* tests conducted by H & M Analytical, Inc.

Table A.1: Phases identified through *XRD* testing and their molecular formula (H & M Analytical report dated December 29, 2011).

Phase	Molecular Formula	Phase Number in Figures
Quartz	SiO <sub>2</sub>	1
Pyrite	FeS <sub>2</sub>	2
Gypsum	Ca(SO <sub>4</sub> )(H <sub>2</sub> O) <sub>2</sub>	3
Rutile	TiO <sub>2</sub>	4
Anatase	TiO <sub>2</sub>	5
Siderite	FeCO <sub>3</sub>	6
Muscovite	KAl <sub>2</sub> ((AlSi <sub>3</sub> )O <sub>10</sub> )(OH) <sub>2</sub>	7
Kaolinite	Al <sub>2</sub> Si <sub>2</sub> O <sub>5</sub> (OH) <sub>4</sub>	8
Magnetite	(Fe,Ti,Mn) <sub>3</sub> O <sub>4</sub>	9
Goethite	FeO(OH)	10
Phengite	K(Al,Mg) <sub>2</sub> (Si,Al) <sub>4</sub> O <sub>10</sub> (OH) <sub>2</sub>	11
Calcite	Ca(CO) <sub>3</sub>	12
Dolomite	CaMg((CO) <sub>3</sub> ) <sub>2</sub>	13
Barite	Ba(SO <sub>4</sub> )	14



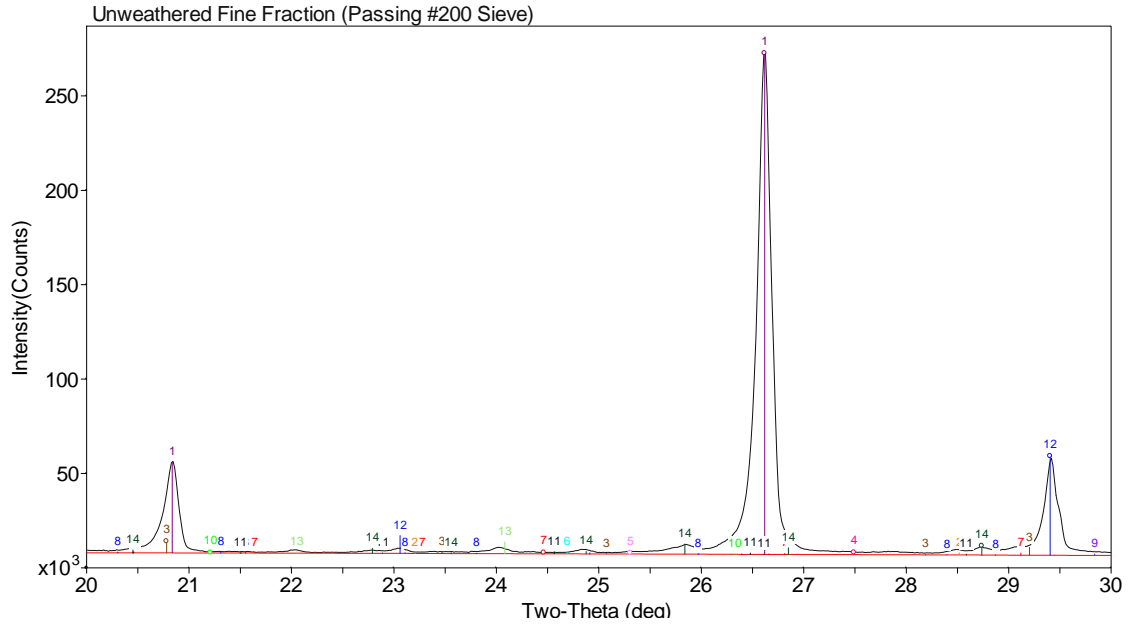


Figure A.3: Exploded view showing the phase identification for the unweathered fine fraction sample (H & M Analytical report dated December 29, 2011).

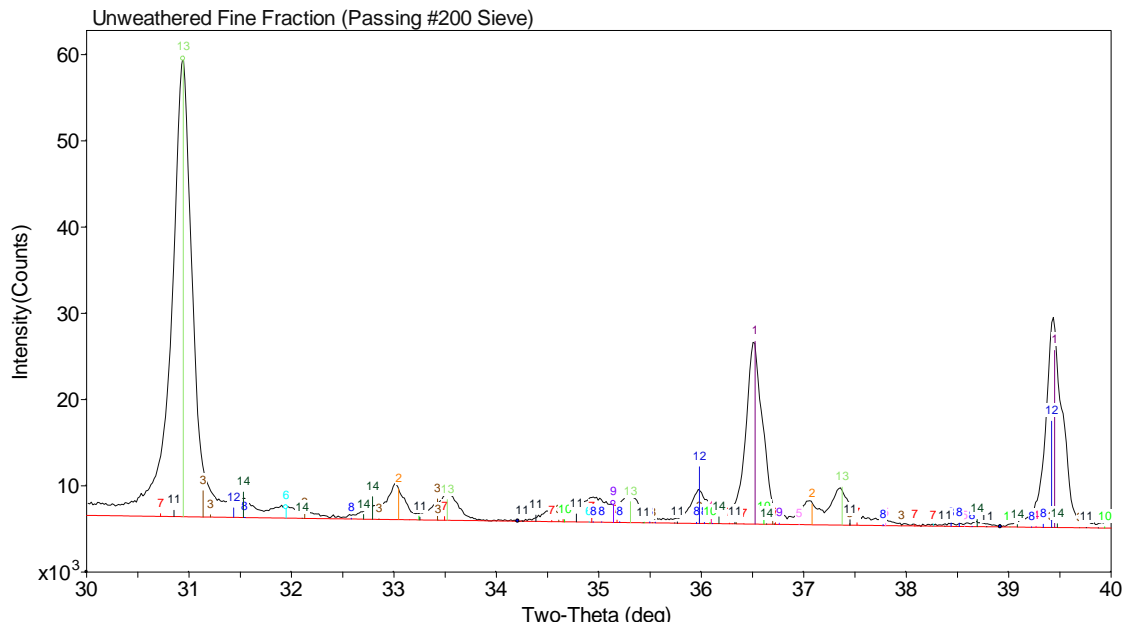


Figure A.4: Exploded view showing the phase identification for the unweathered fine fraction sample (H & M Analytical report dated December 29, 2011).

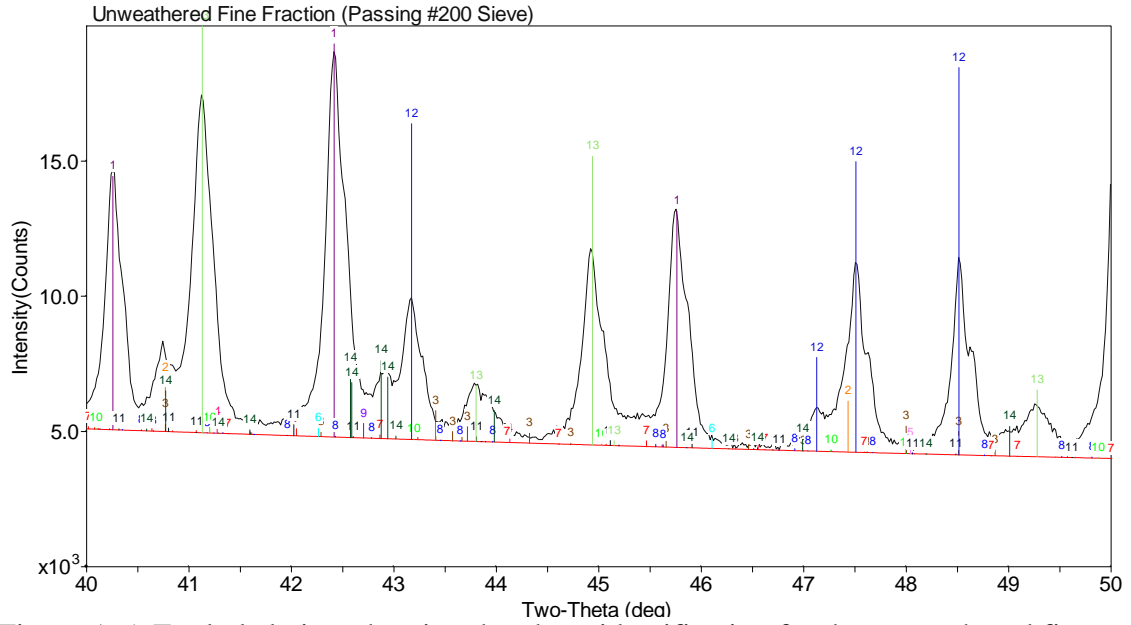


Figure A.5: Exploded view showing the phase identification for the unweathered fine fraction sample (H & M Analytical report dated December 29, 2011).

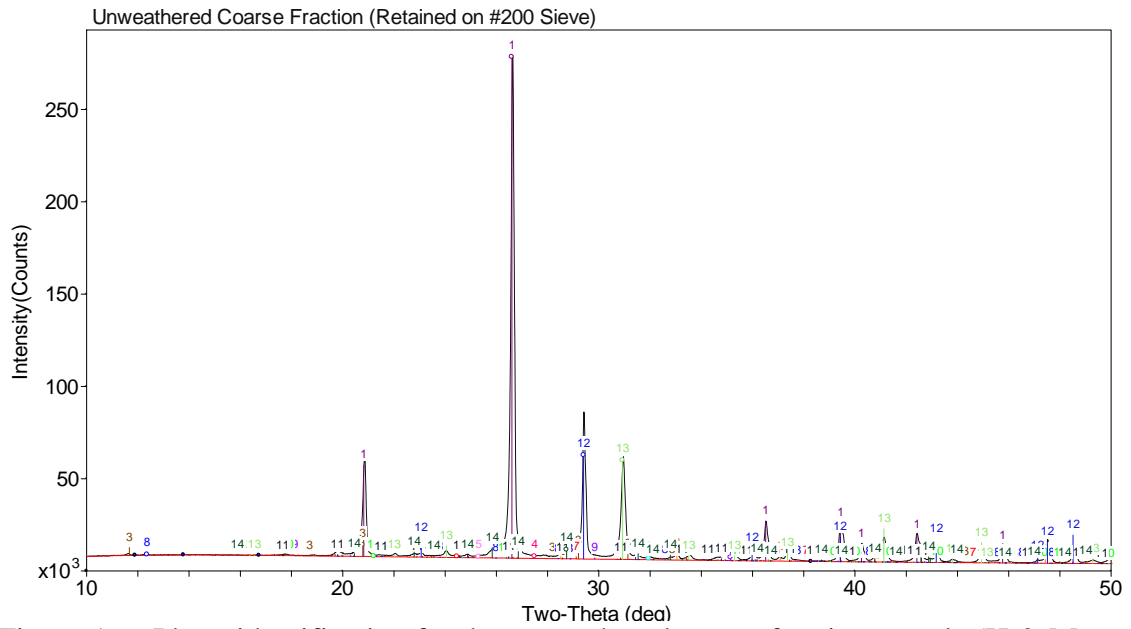


Figure A.6: Phase identification for the unweathered coarse fraction sample (H & M Analytical report dated December 29, 2011).

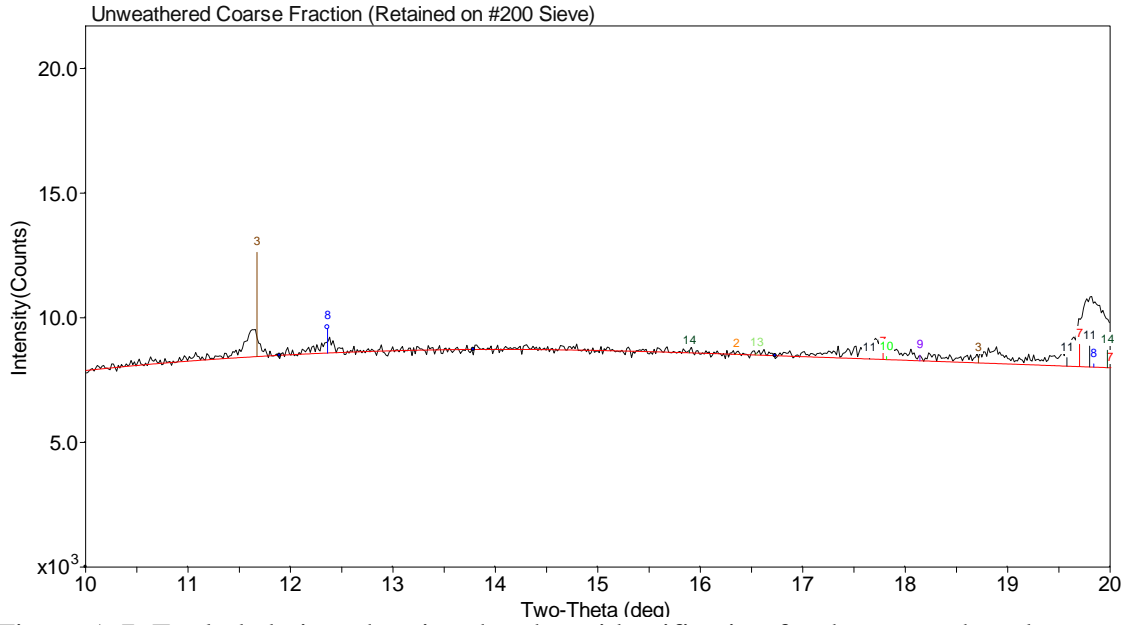


Figure A.7: Exploded view showing the phase identification for the unweathered coarse fraction sample (H & M Analytical report dated December 29, 2011).

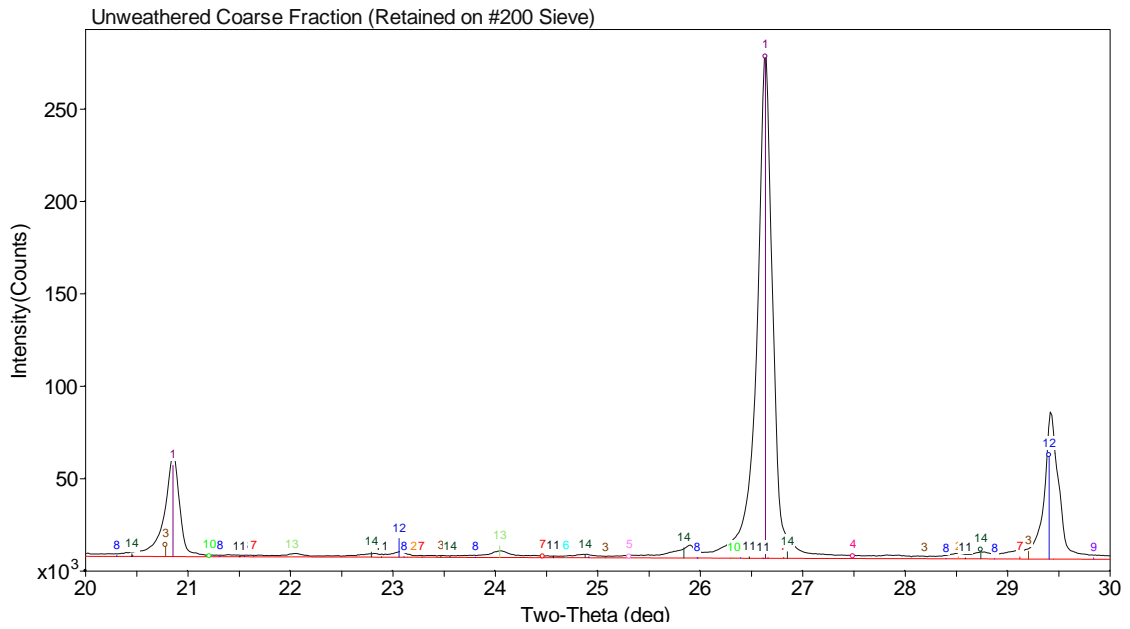


Figure A.8: Exploded view showing the phase identification for the unweathered coarse fraction sample (H & M Analytical report dated December 29, 2011).

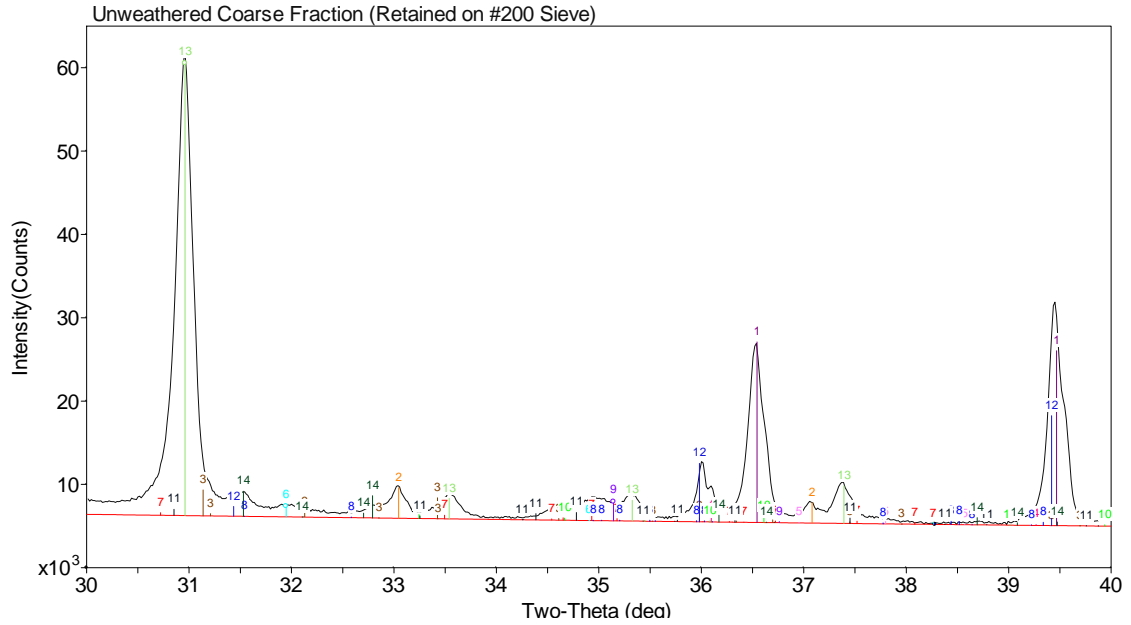


Figure A.9: Exploded view showing the phase identification for the unweathered coarse fraction sample (H & M Analytical report dated December 29, 2011).

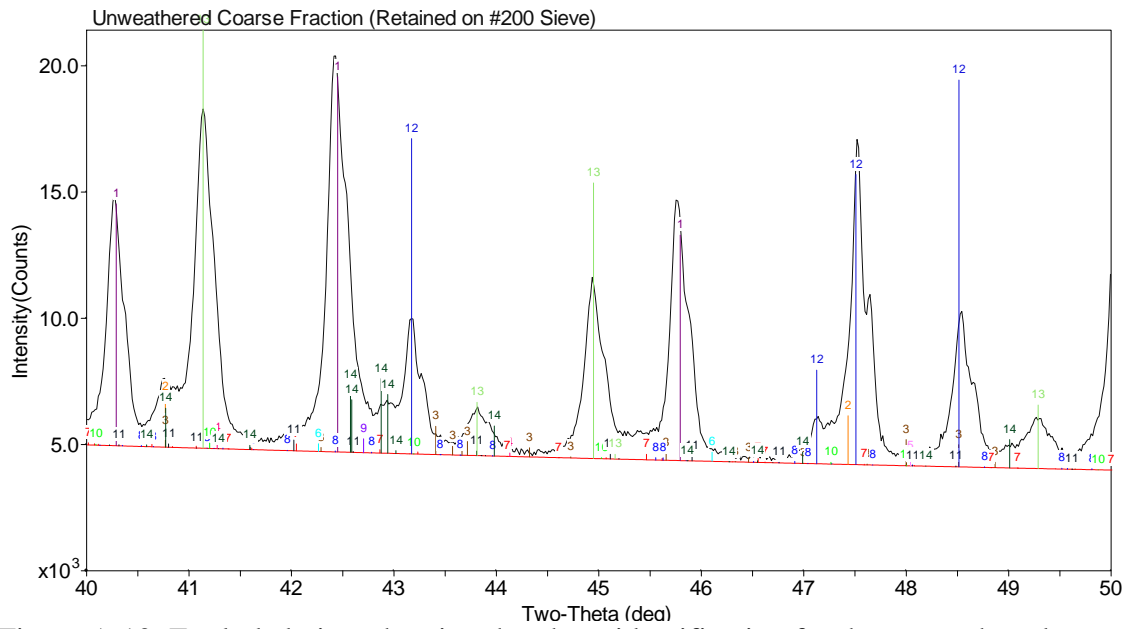


Figure A.10: Exploded view showing the phase identification for the unweathered coarse fraction sample (H & M Analytical report dated December 29, 2011).

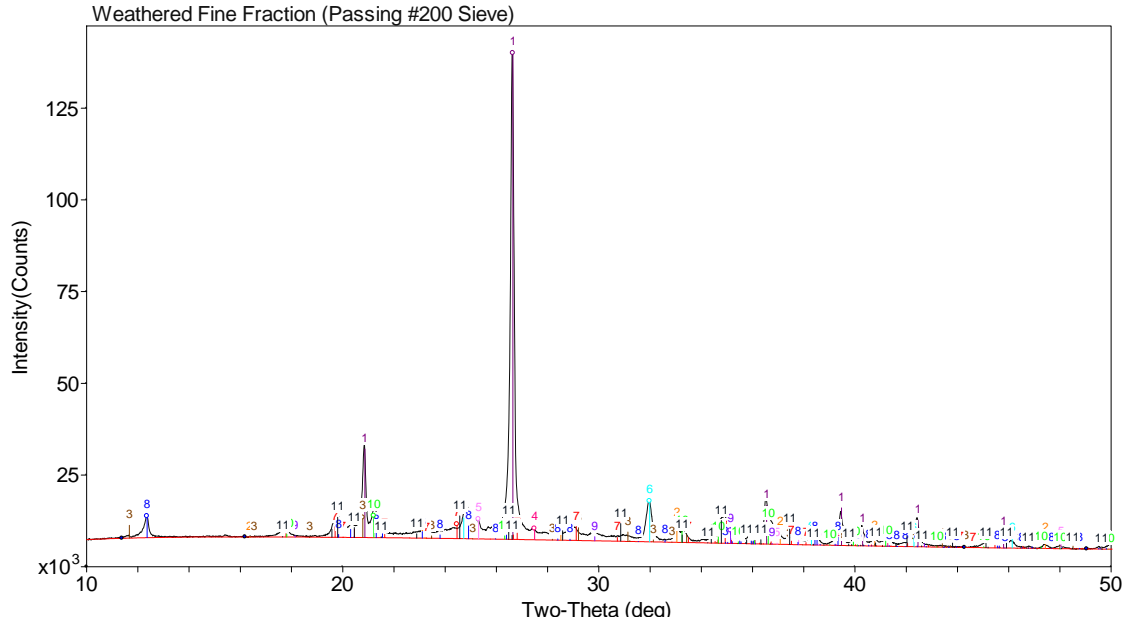


Figure A.11 Phase identification for the weathered fine fraction sample (H & M Analytical report dated December 29, 2011).

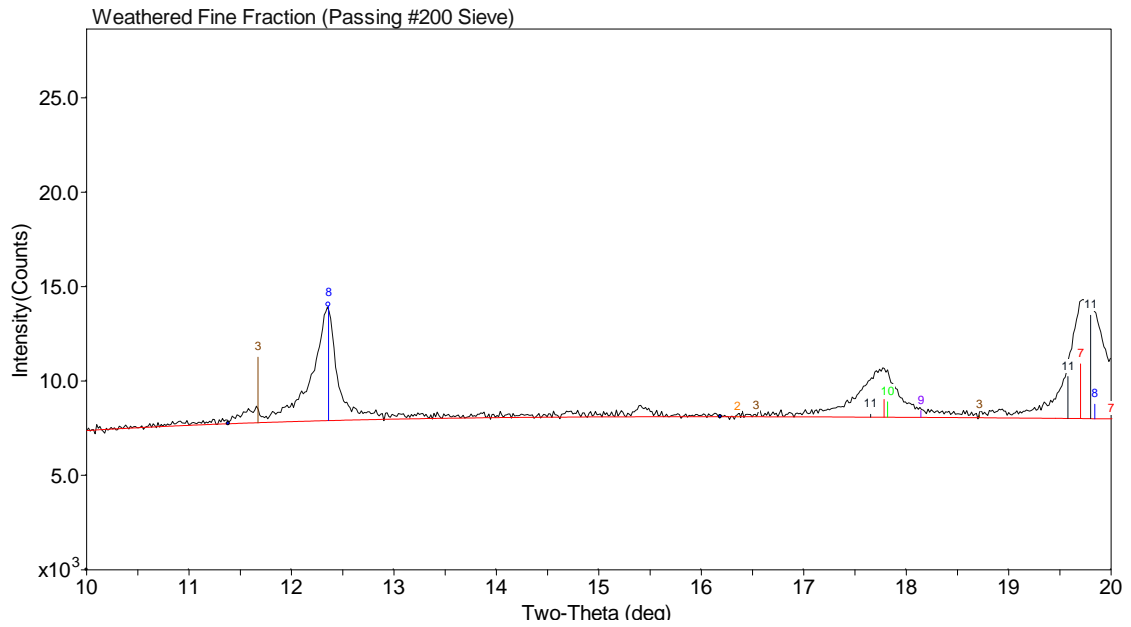


Figure A.12: Exploded view showing the phase identification for the weathered fine fraction sample (H & M Analytical report dated December 29, 2011).

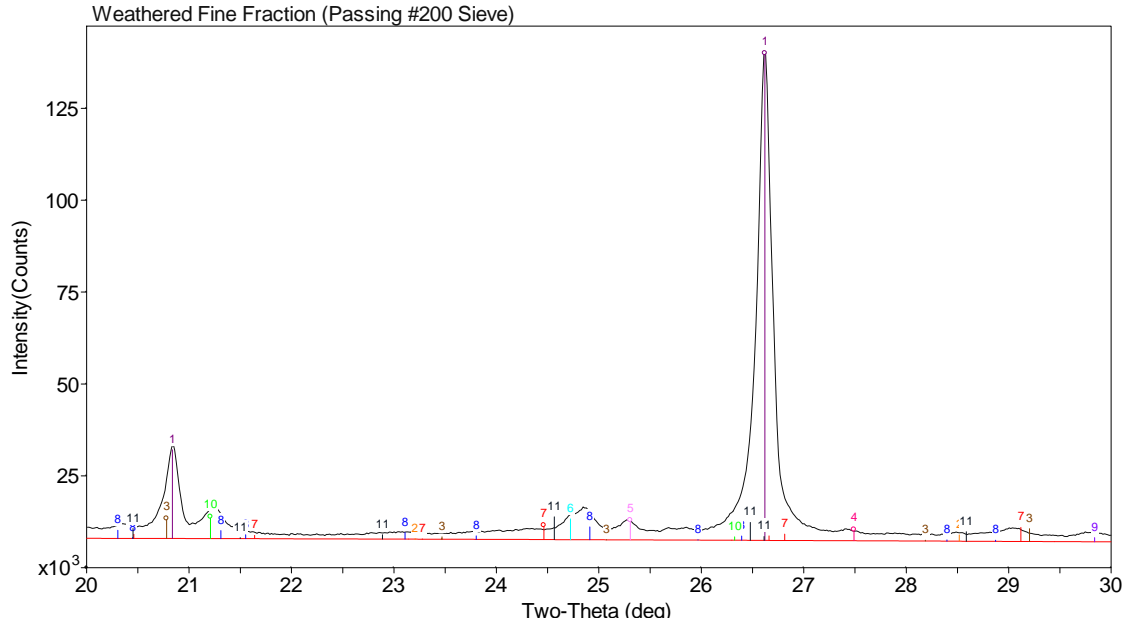


Figure A.13: Exploded view showing the phase identification for the weathered fine fraction sample (H & M Analytical report dated December 29, 2011).

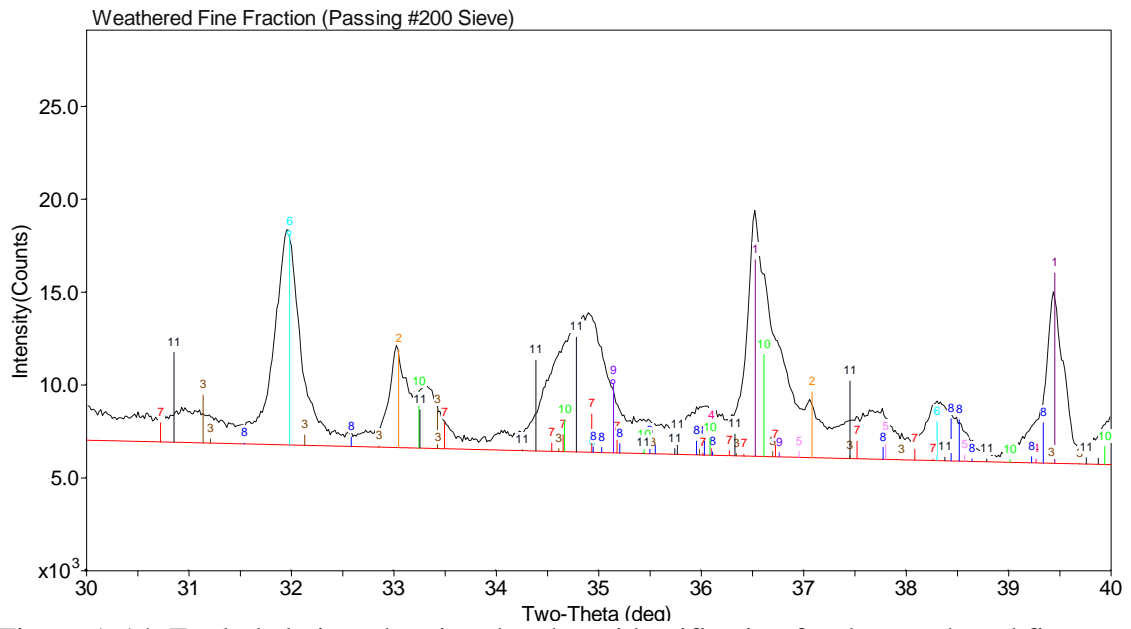


Figure A.14: Exploded view showing the phase identification for the weathered fine fraction sample (H & M Analytical report dated December 29, 2011).

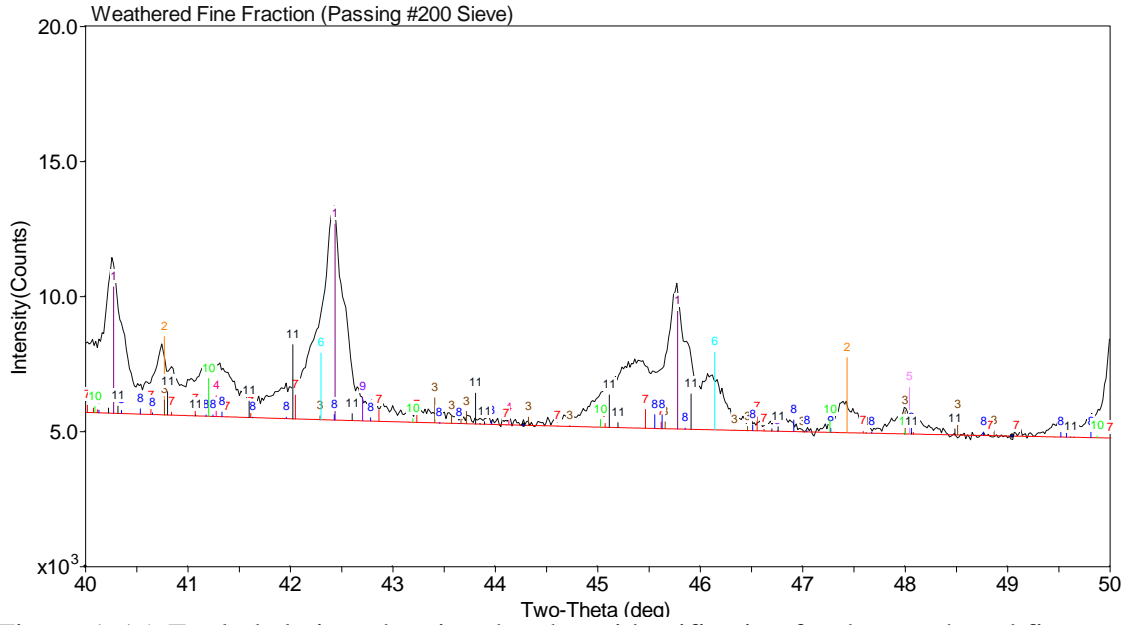


Figure A.15: Exploded view showing the phase identification for the weathered fine fraction sample (H & M Analytical report dated December 29, 2011).

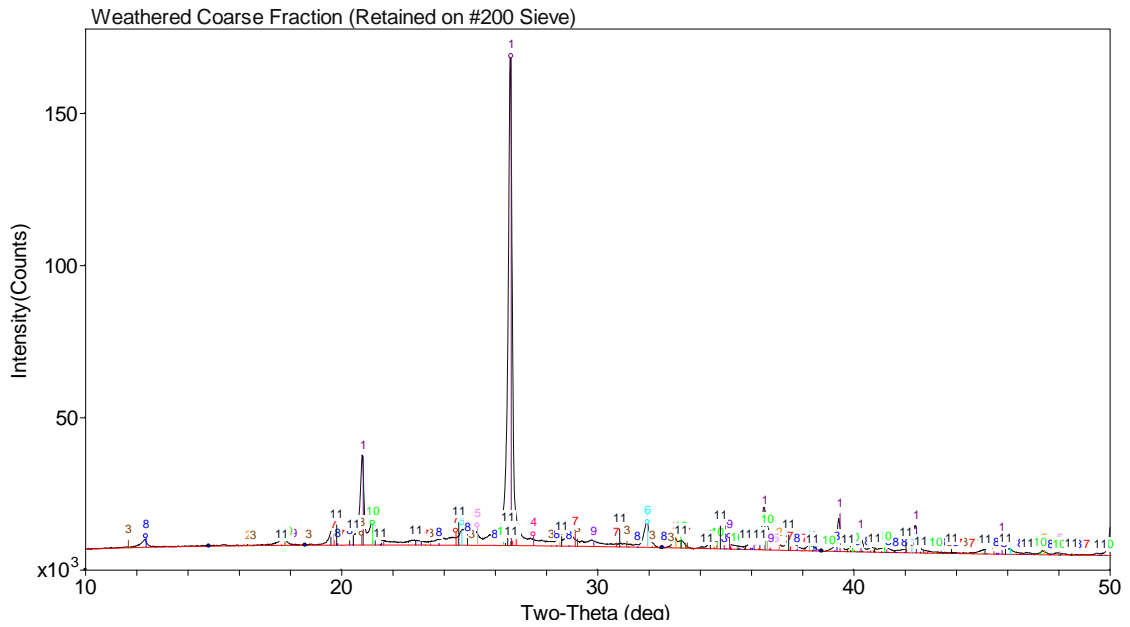


Figure A.16: Phase identification for the weathered coarse fraction sample (H & M Analytical report dated December 29, 2011).

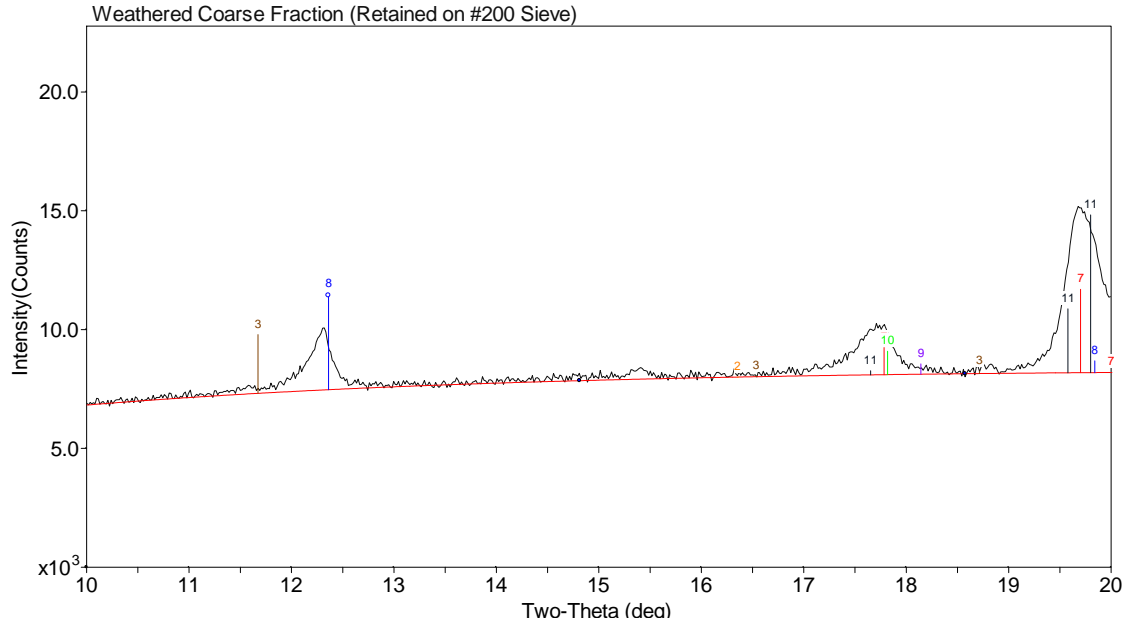


Figure A.17: Exploded view showing the phase identification for the weathered coarse fraction sample (H & M Analytical report dated December 29, 2011).

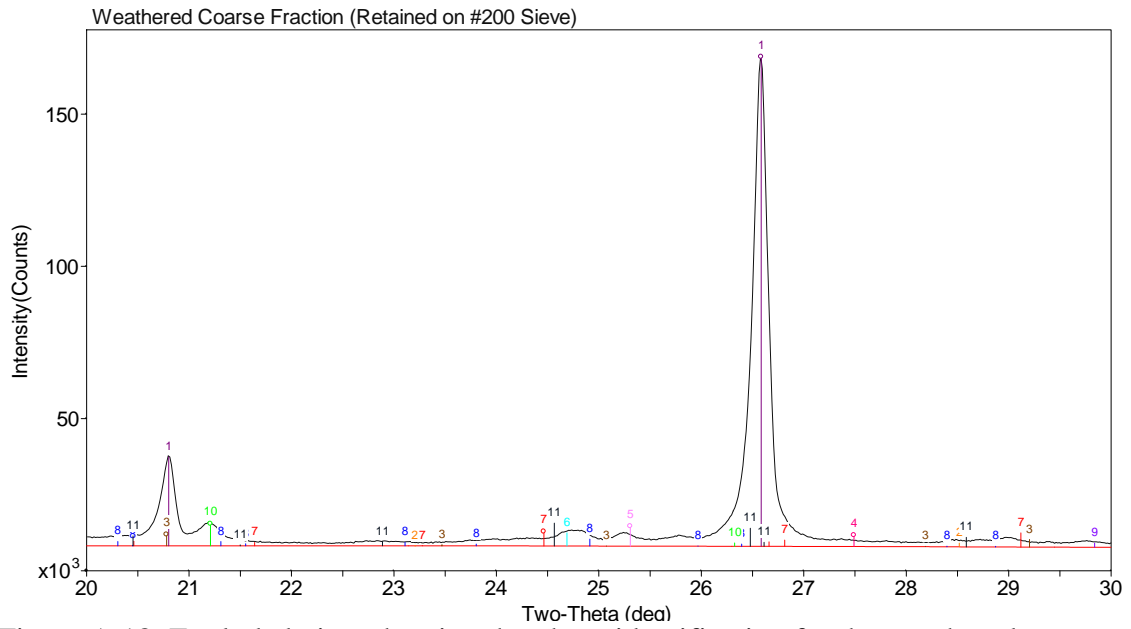


Figure A.18: Exploded view showing the phase identification for the weathered coarse fraction sample (H & M Analytical report dated December 29, 2011).

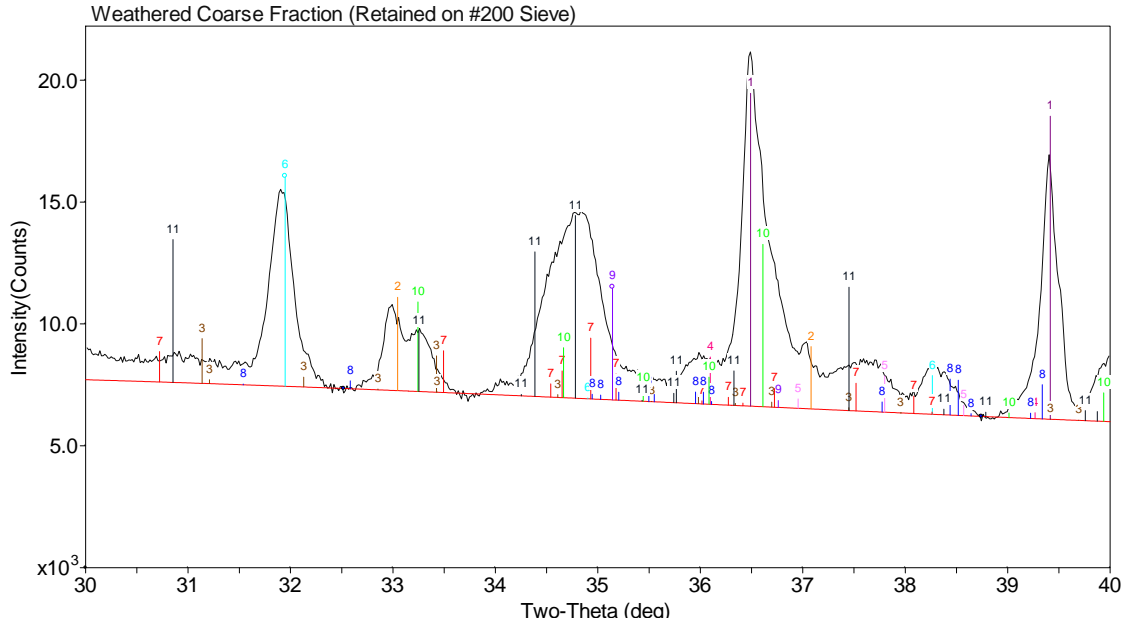


Figure A.19: Exploded view showing the phase identification for the weathered coarse fraction sample (H & M Analytical report dated December 29, 2011).

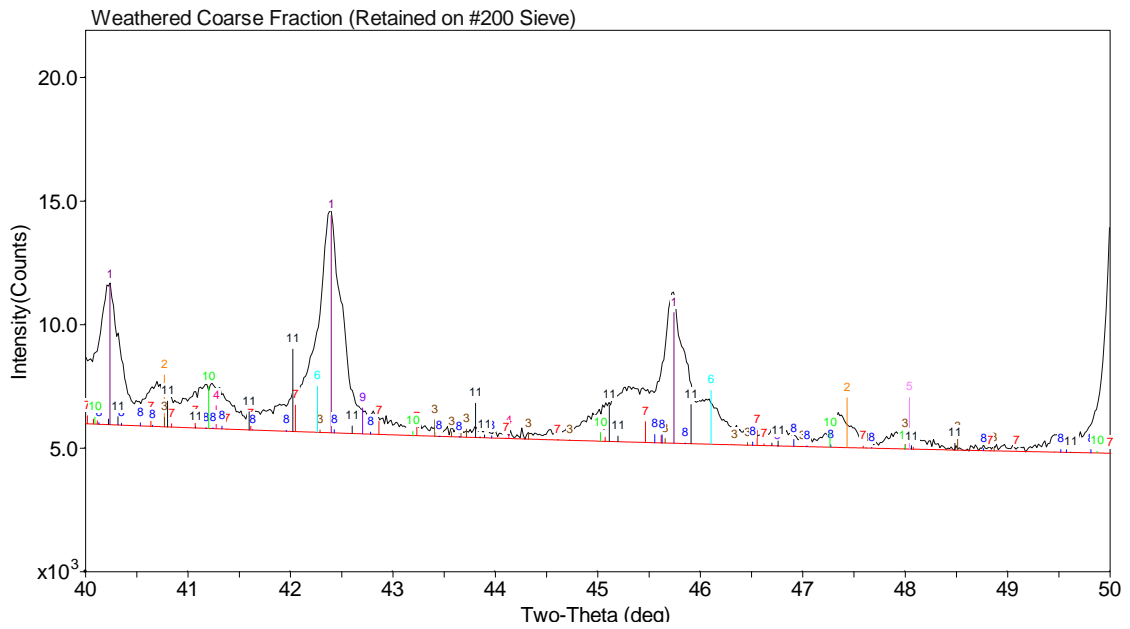


Figure A.20: Exploded view showing the phase identification for the weathered coarse fraction sample (H & M Analytical report dated December 29, 2011).

## APPENDIX B: PARTICLE SIZE DISTRIBUTIONS

Pre and post test particle-size distributions for each triaxial specimen tested are presented below.

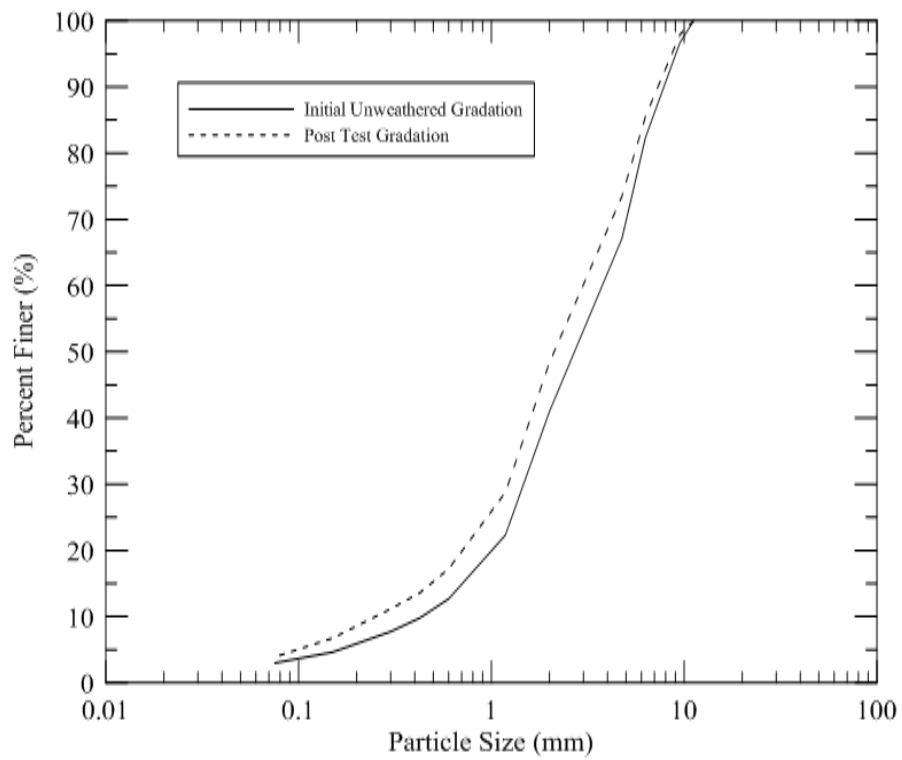


Figure B.1: Pre and post test particle size distribution for specimen U75-400.

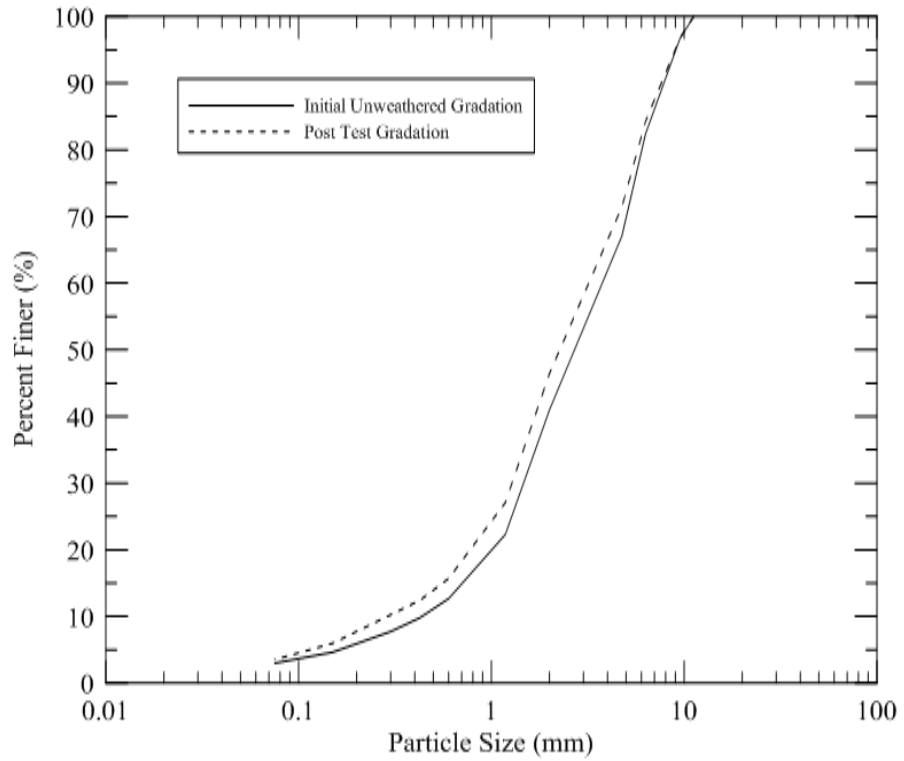


Figure B.2: Pre and post test particle size distribution for specimen U77-200.

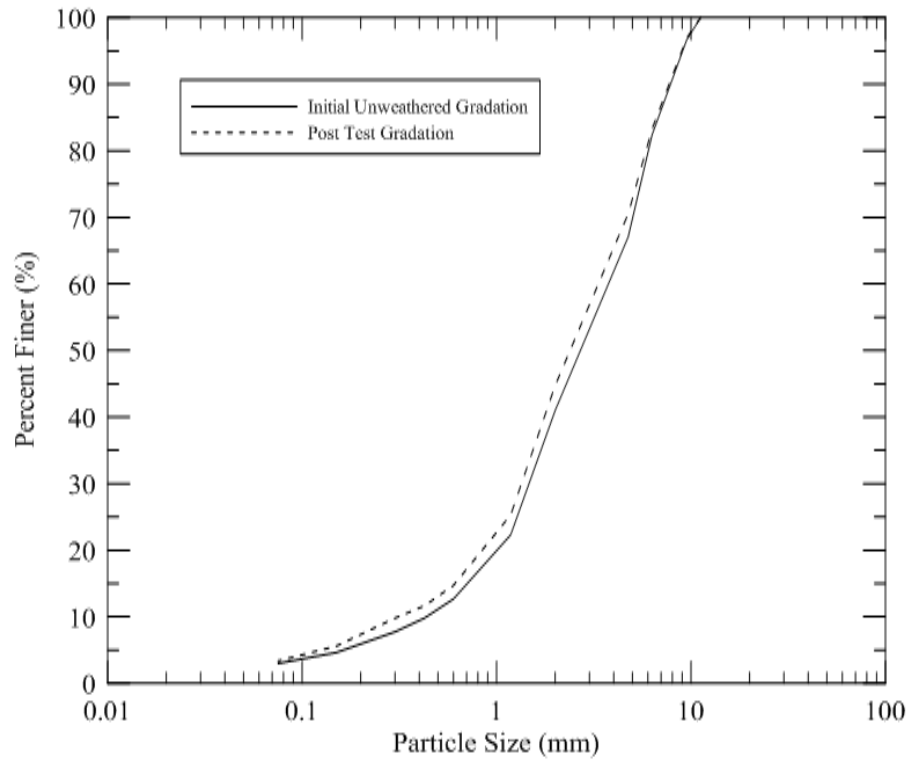


Figure B.3: Pre and post test particle size distribution for specimen U70-100.

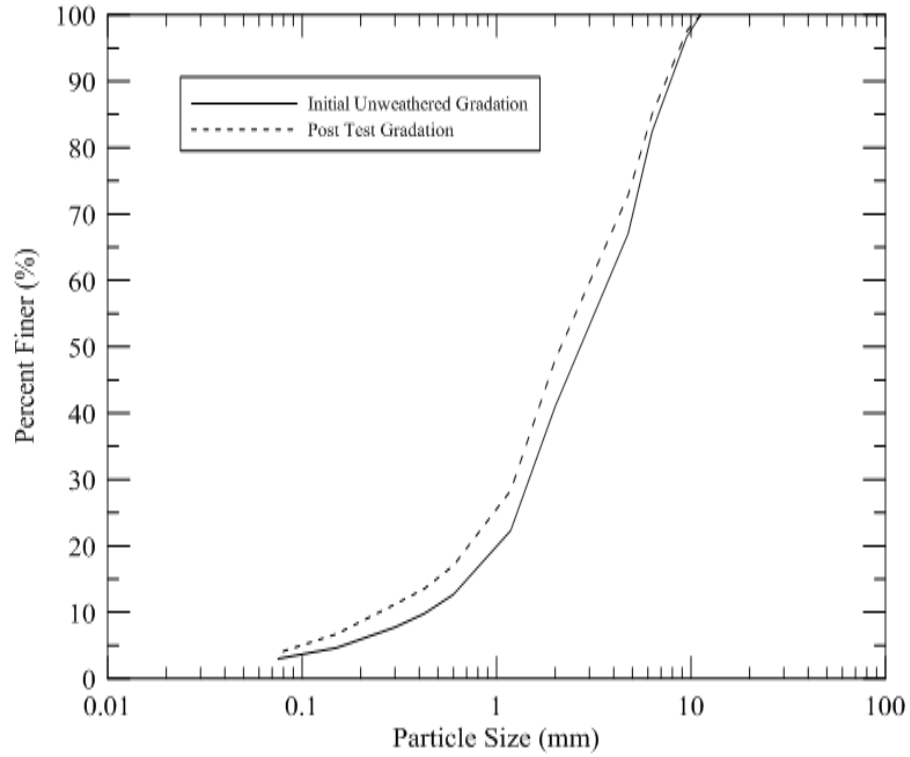


Figure B.4: Pre and post test particle size distribution for specimen U68-400.

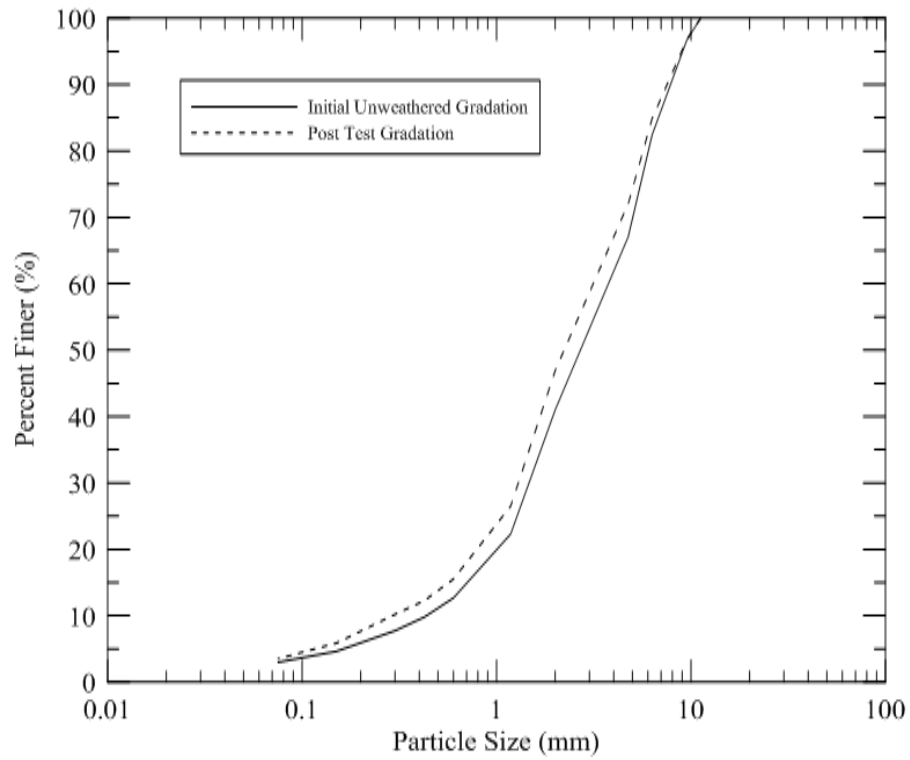


Figure B.5: Pre and post test particle size distribution for specimen U54-200.

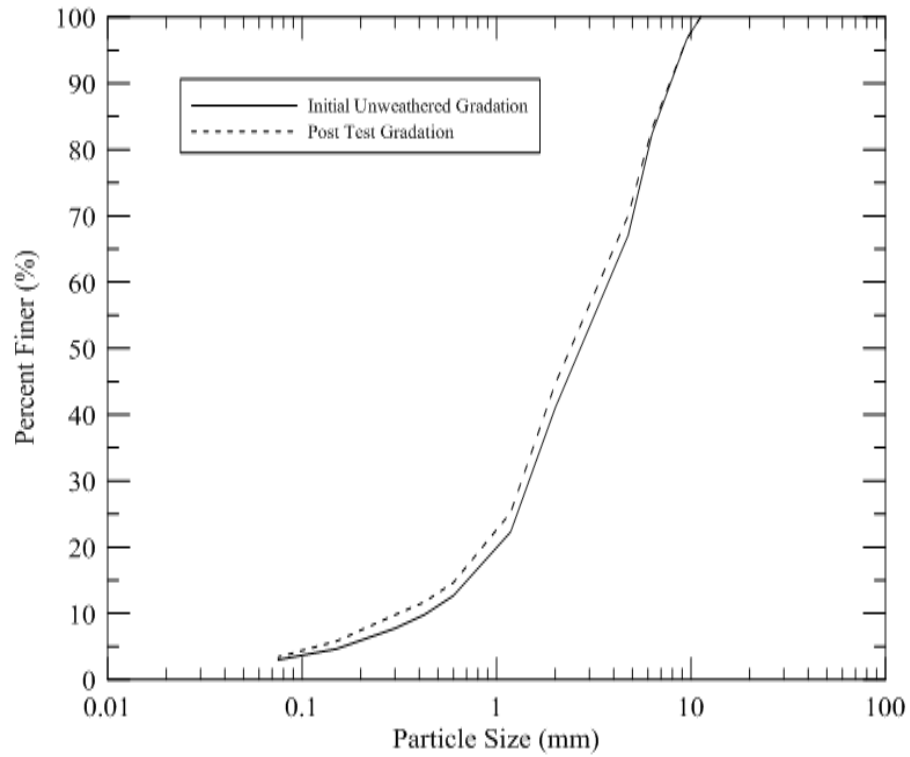


Figure B.6: Pre and post test particle size distribution for specimen U50-100.

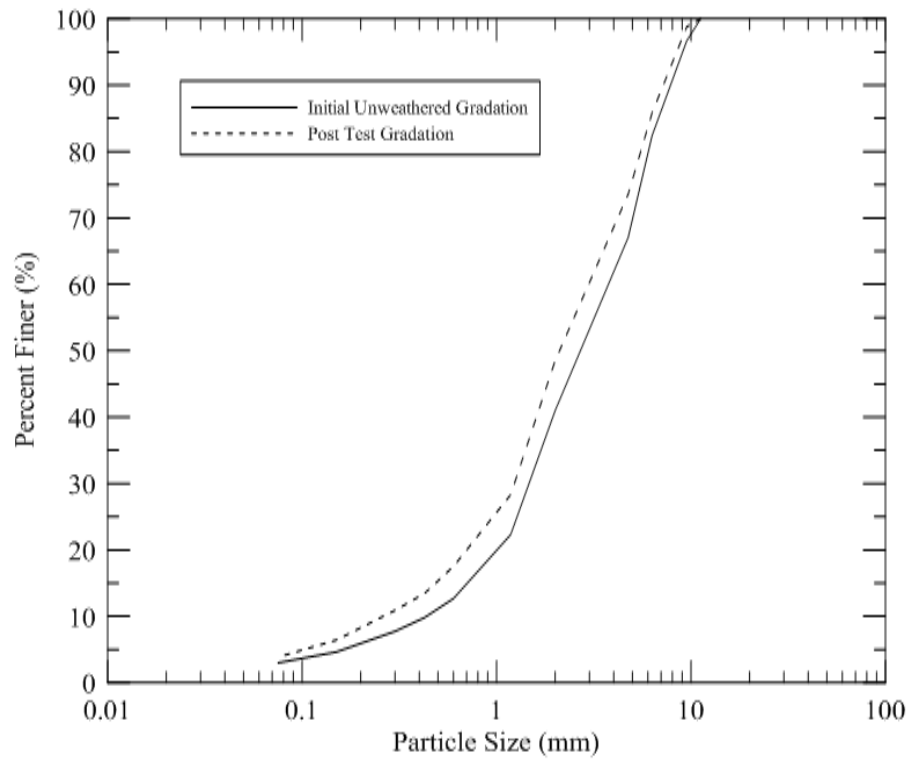


Figure B.7: Pre and post test particle size distribution for specimen U42-400.

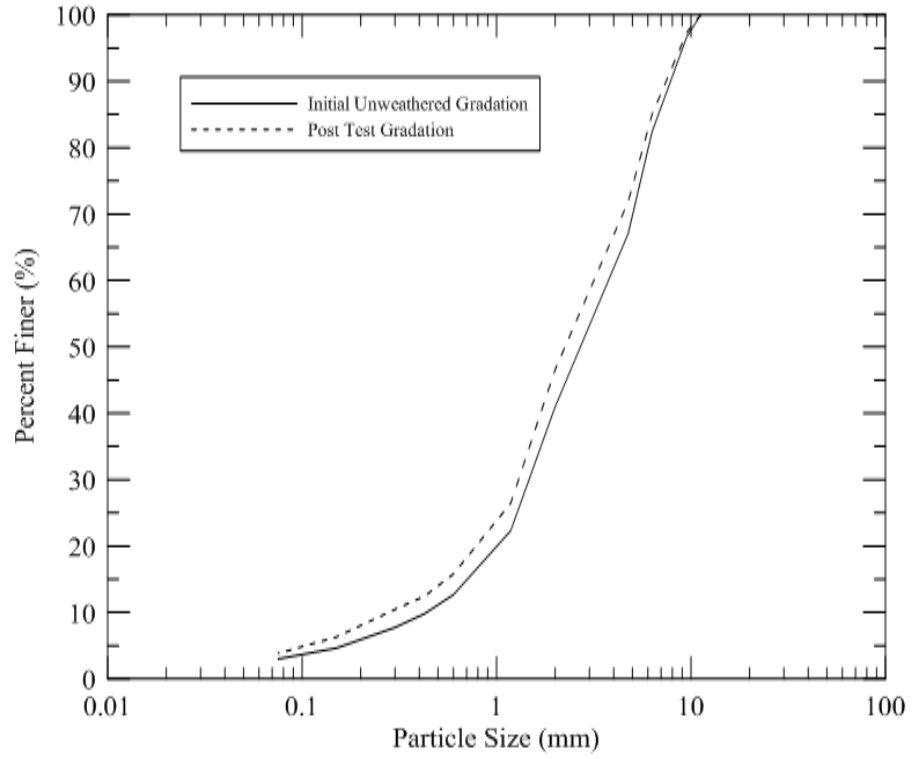


Figure B.8: Pre and post test particle size distribution for specimen U40-200.

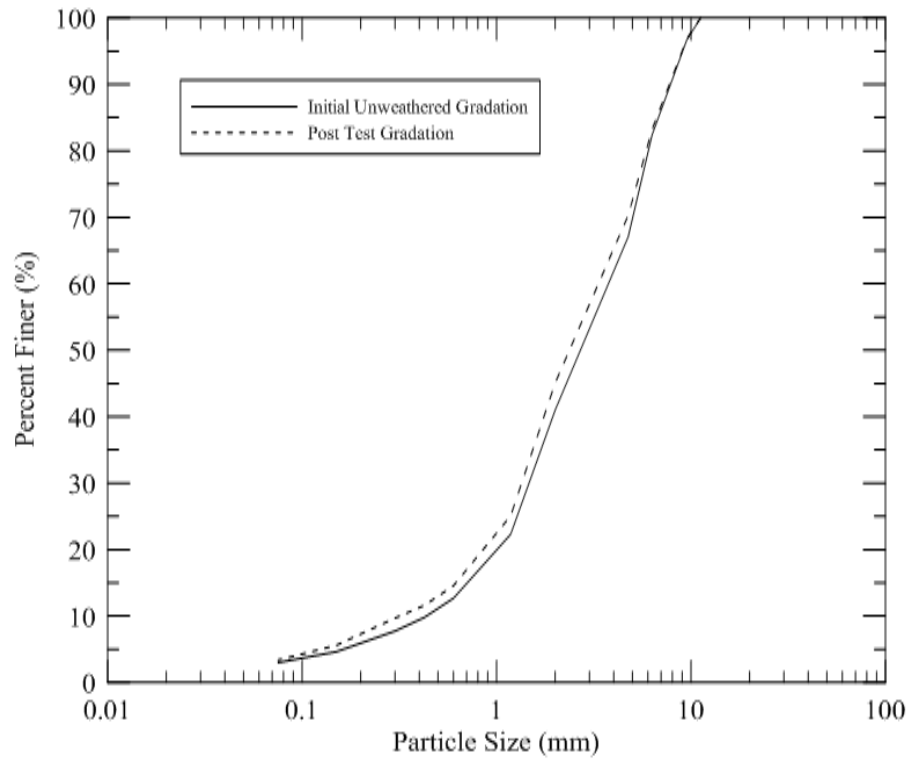


Figure B.9: Pre and post test particle size distribution for specimen U26-100.

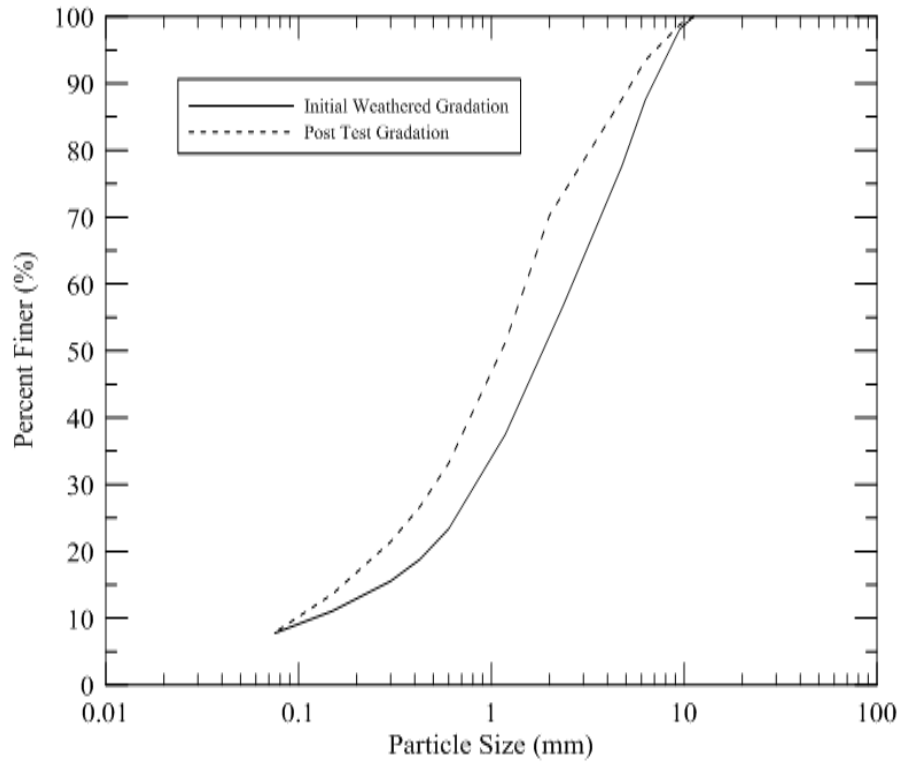


Figure B.10: Pre and post test particle size distribution for specimen W92-400.

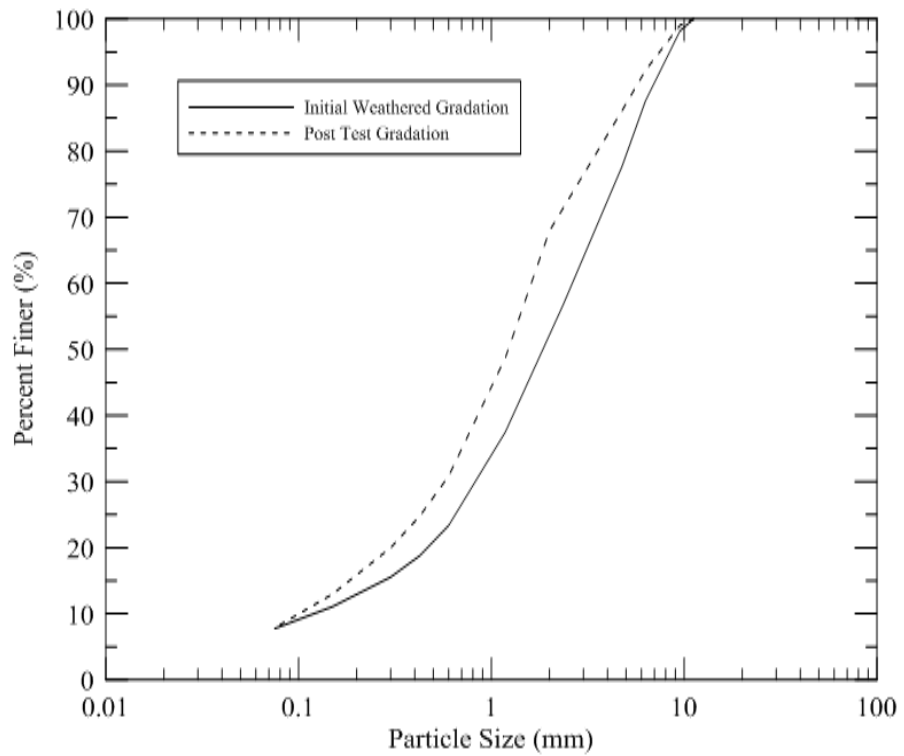


Figure B.11: Pre and post test particle size distribution for specimen W83-200.

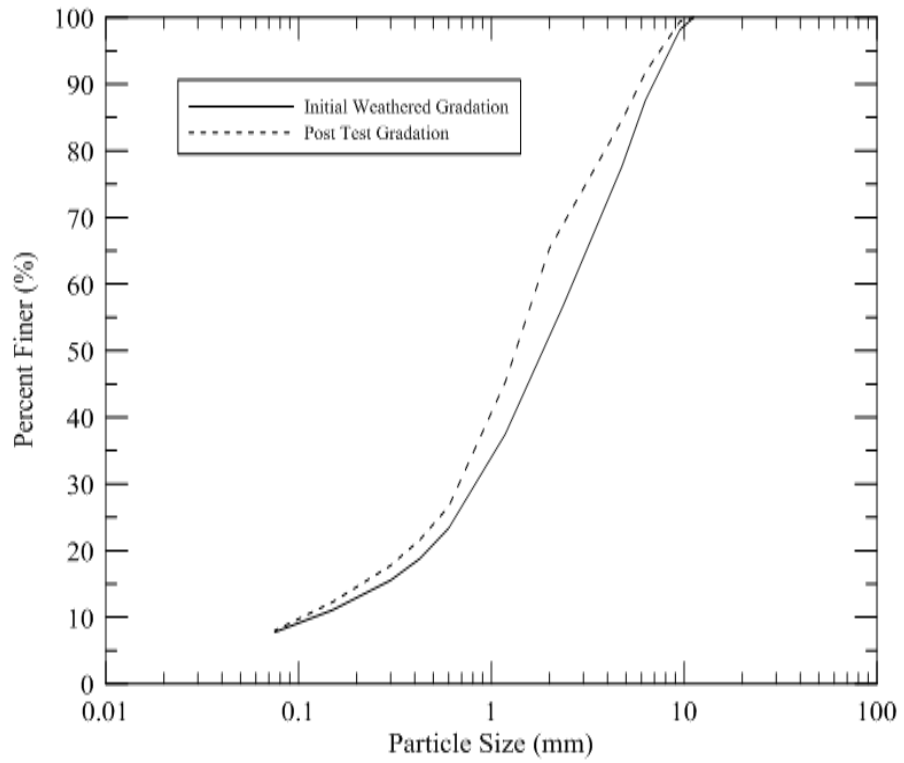


Figure B.12: Pre and post test particle size distribution for specimen W78-100.

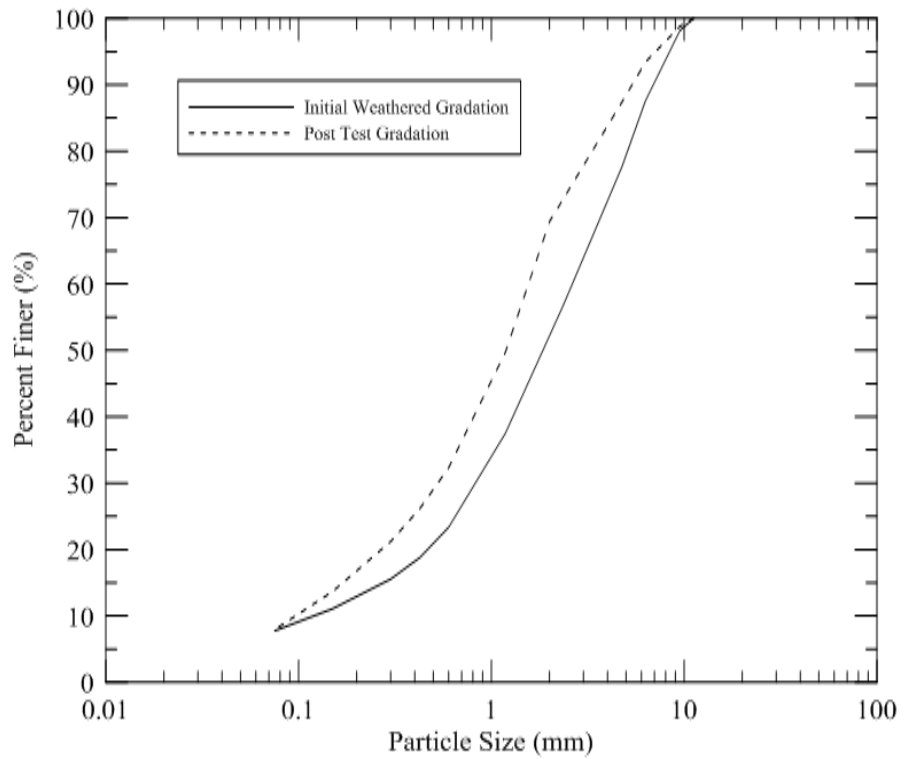


Figure B.13: Pre and post test particle size distribution for specimen W76-400.

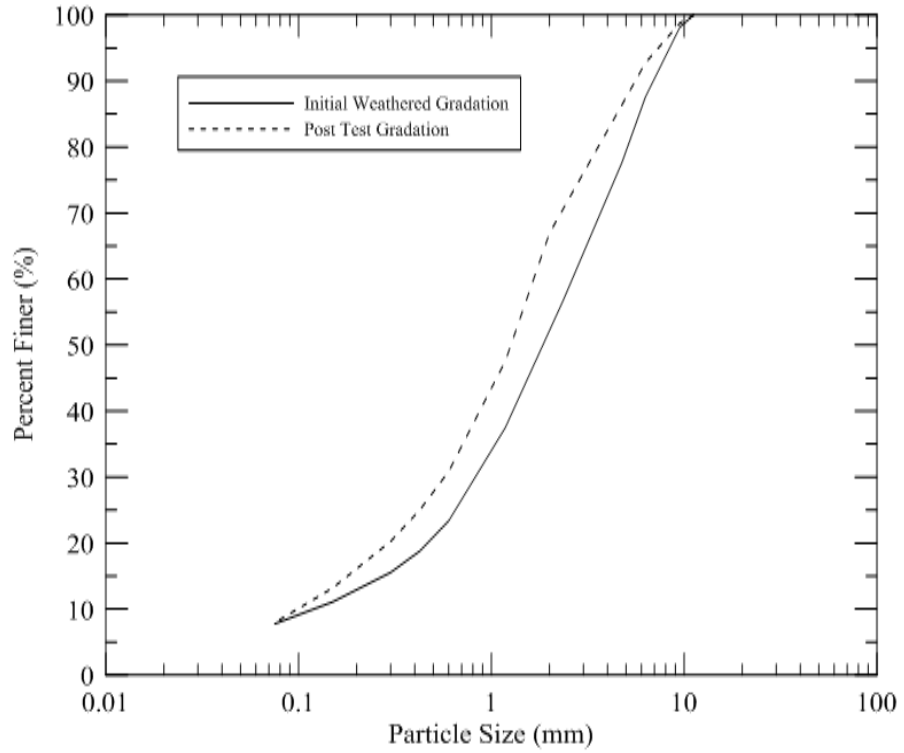


Figure B.14: Pre and post test particle size distribution for specimen W72-200.

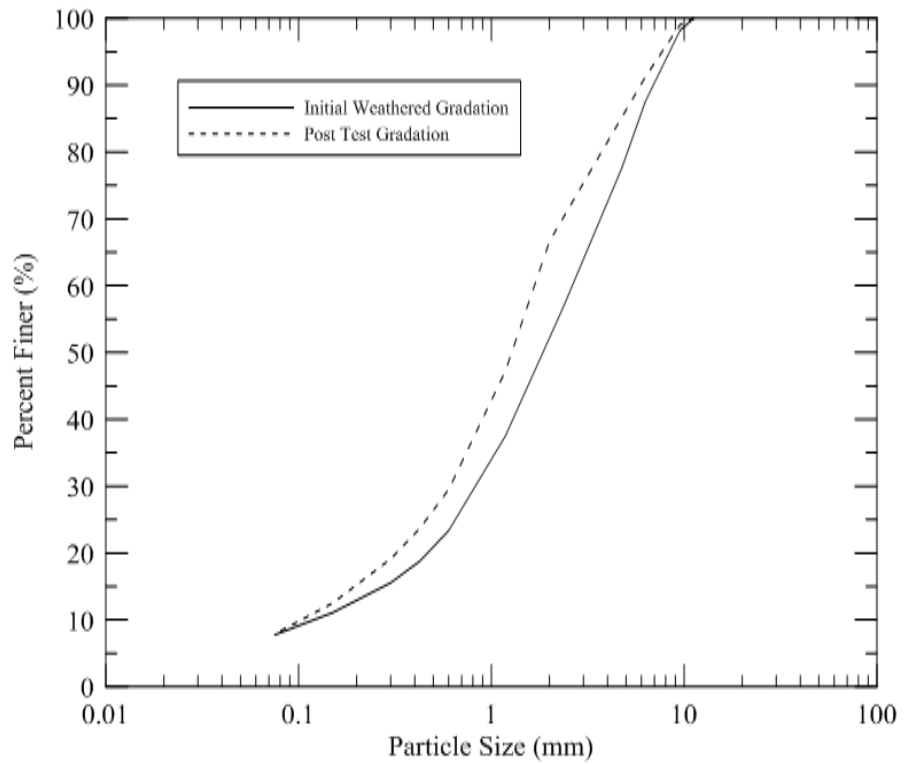


Figure B.15: Pre and post test particle size distribution for specimen W61-100.

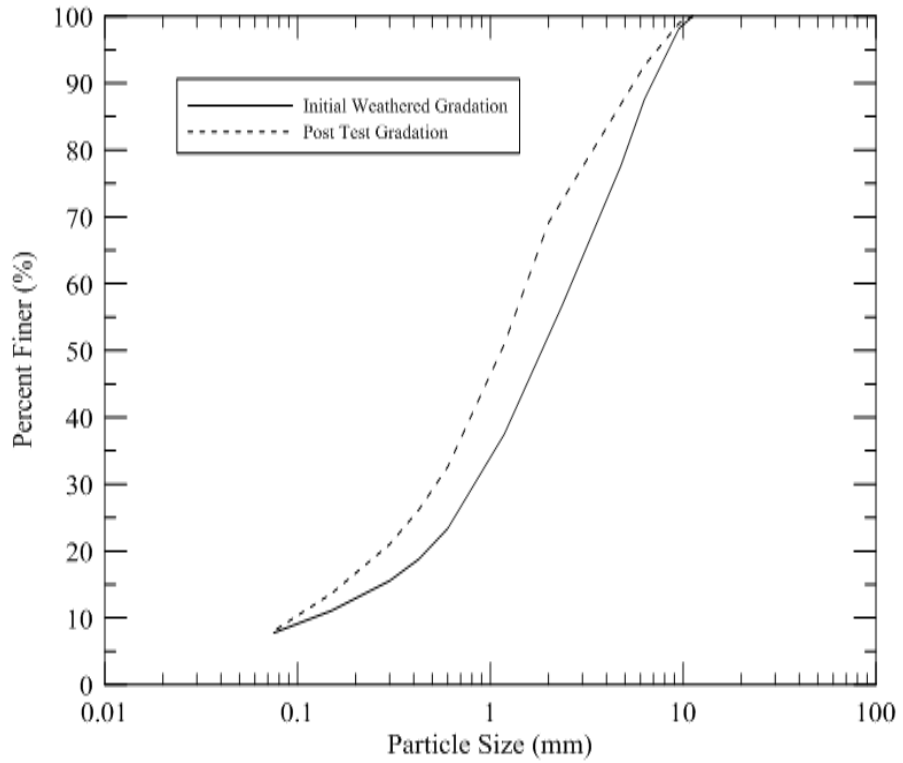


Figure B.16: Pre and post test particle size distribution for specimen W55-400.

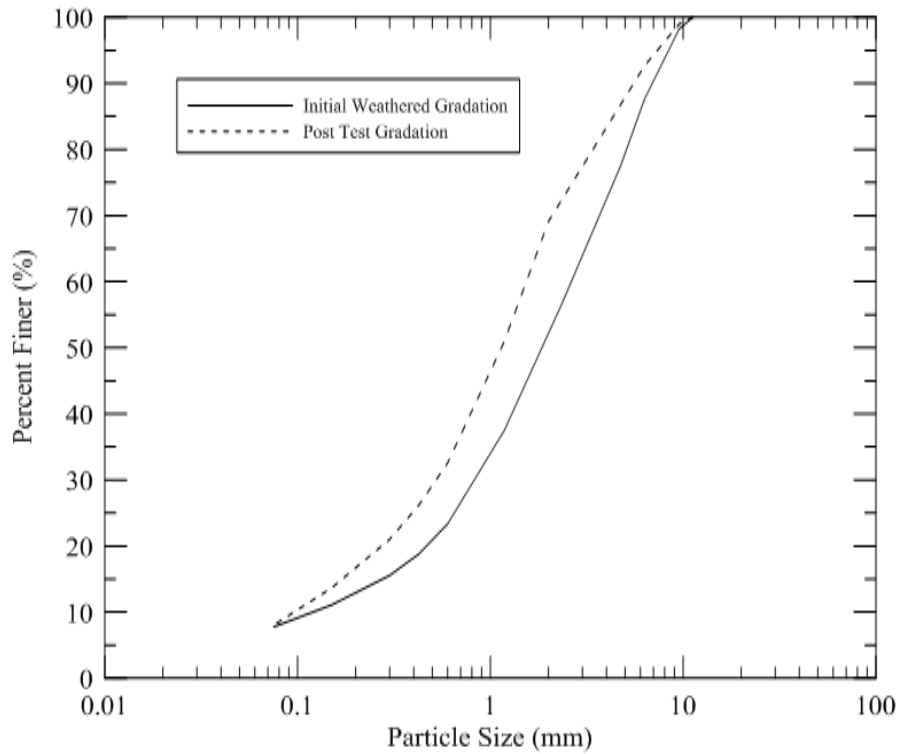


Figure B.17: Pre and post test particle size distribution for specimen W44-200.

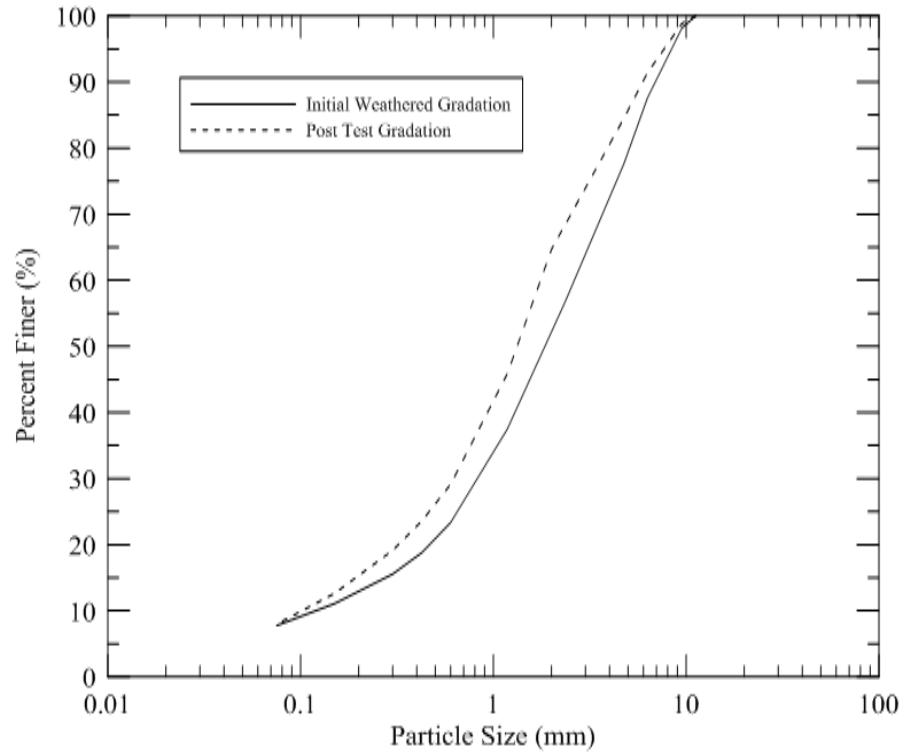


Figure B.18: Pre and post test particle size distribution for specimen W34-100.

## APPENDIX C: TRIAXIAL TEST RESULTS

In order to allow a more detailed analysis of the data presented in this study, a complete set of triaxial test results are provided below on an individual basis on Figures C.1 through C.18.

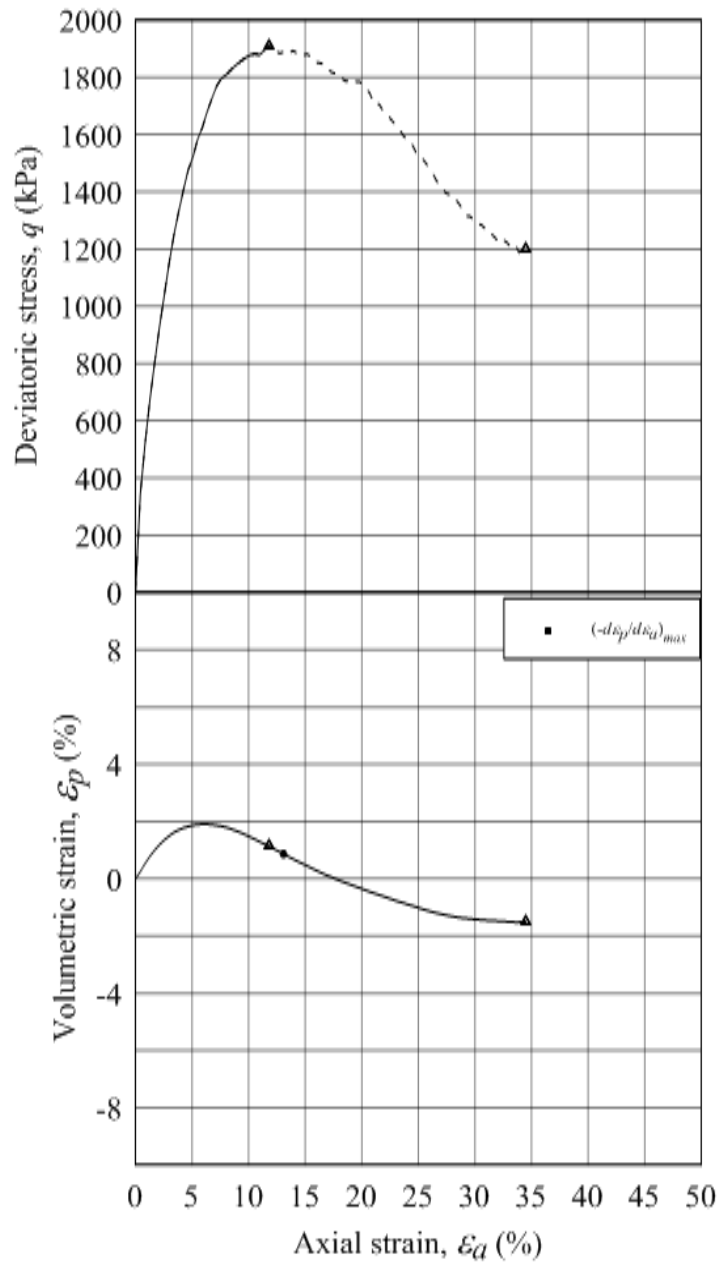


Figure C.1: Deviatoric stress and volumetric strain versus axial strain for specimen U75-400.

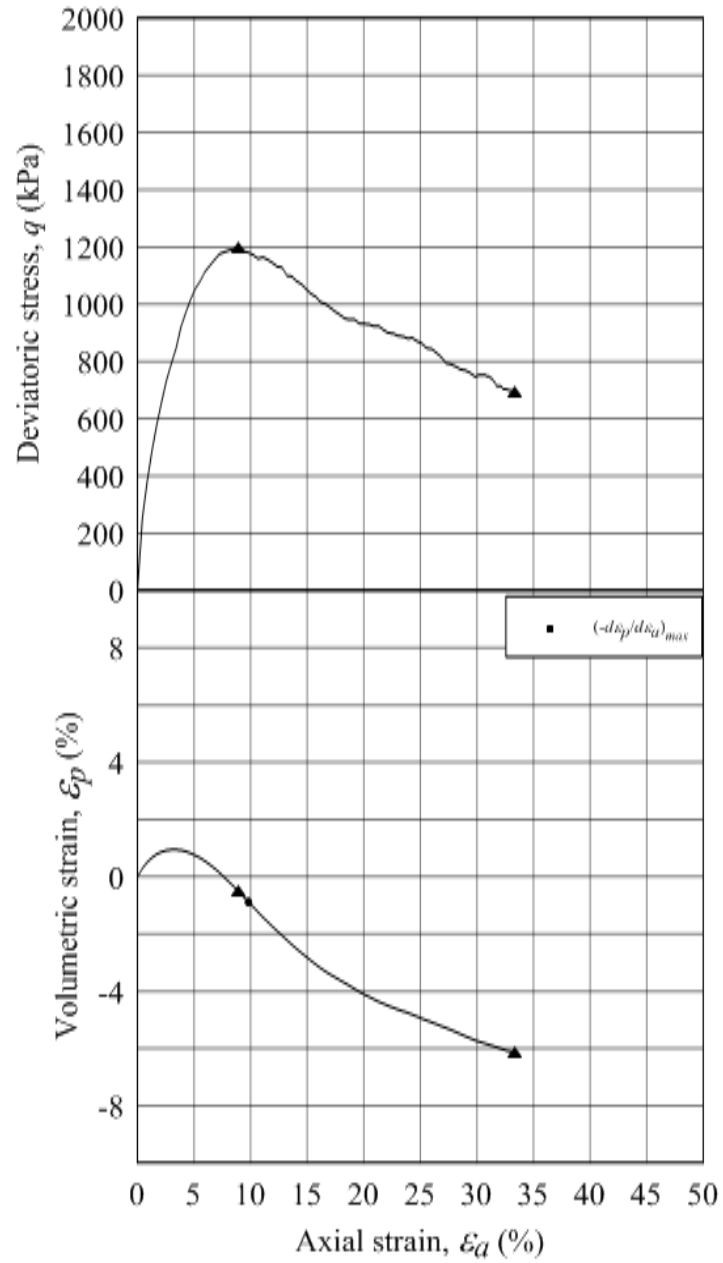


Figure C.2: Deviatoric stress and volumetric strain versus axial strain for specimen U77-200.

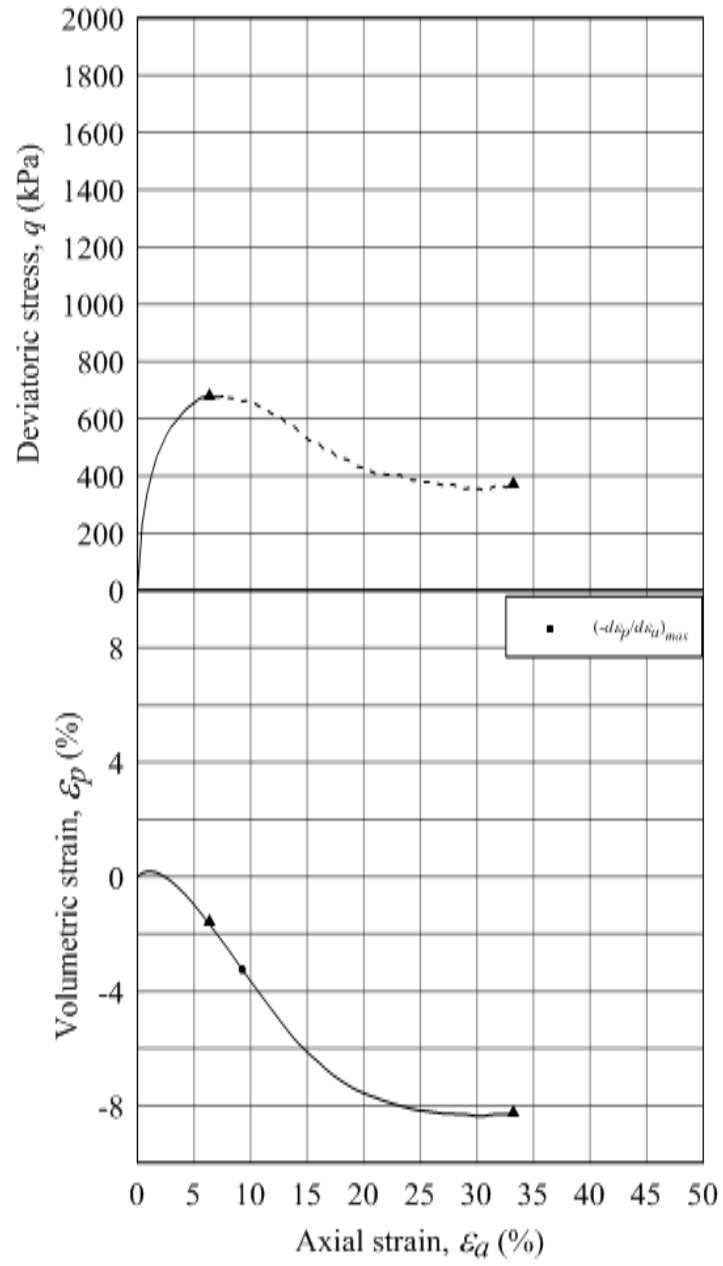


Figure C.3: Deviatoric stress and volumetric strain versus axial strain for specimen U70-100.

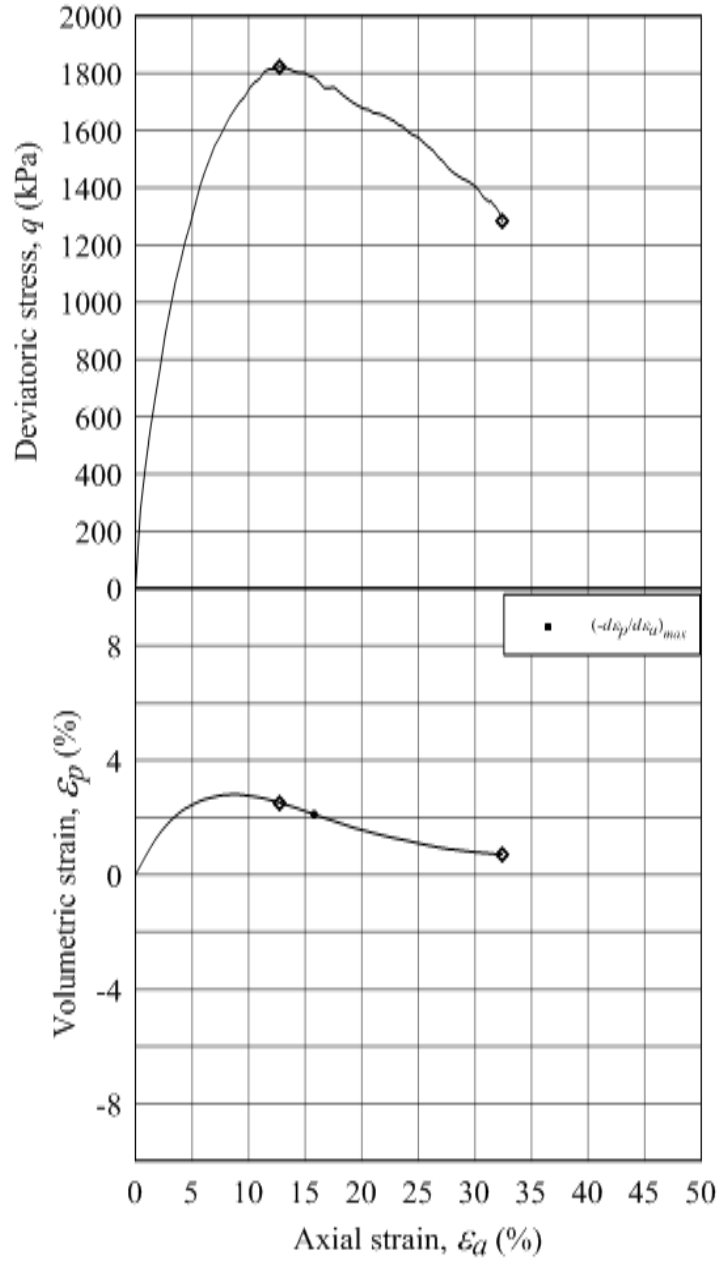


Figure C.4: Deviatoric stress and volumetric strain versus axial strain for specimen U68-400.

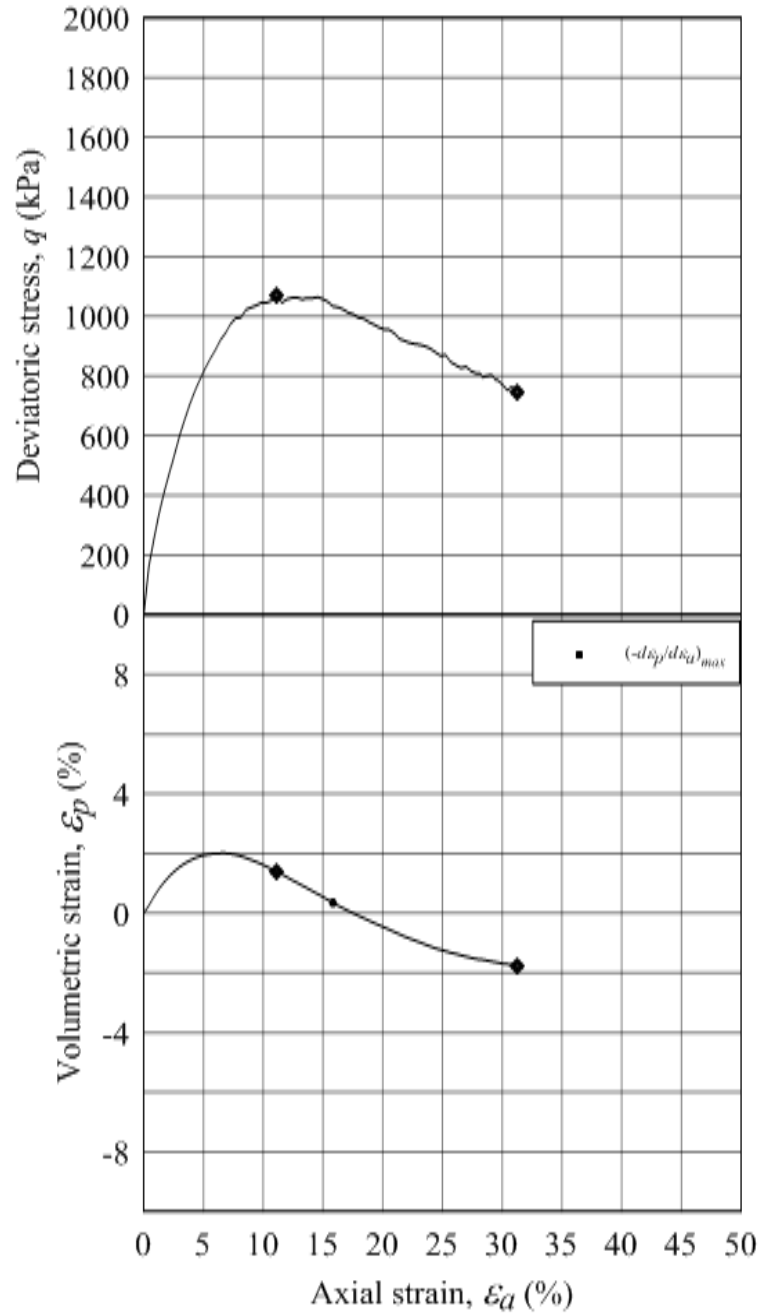


Figure C.5: Deviatoric stress and volumetric strain versus axial strain for specimen U54-200.

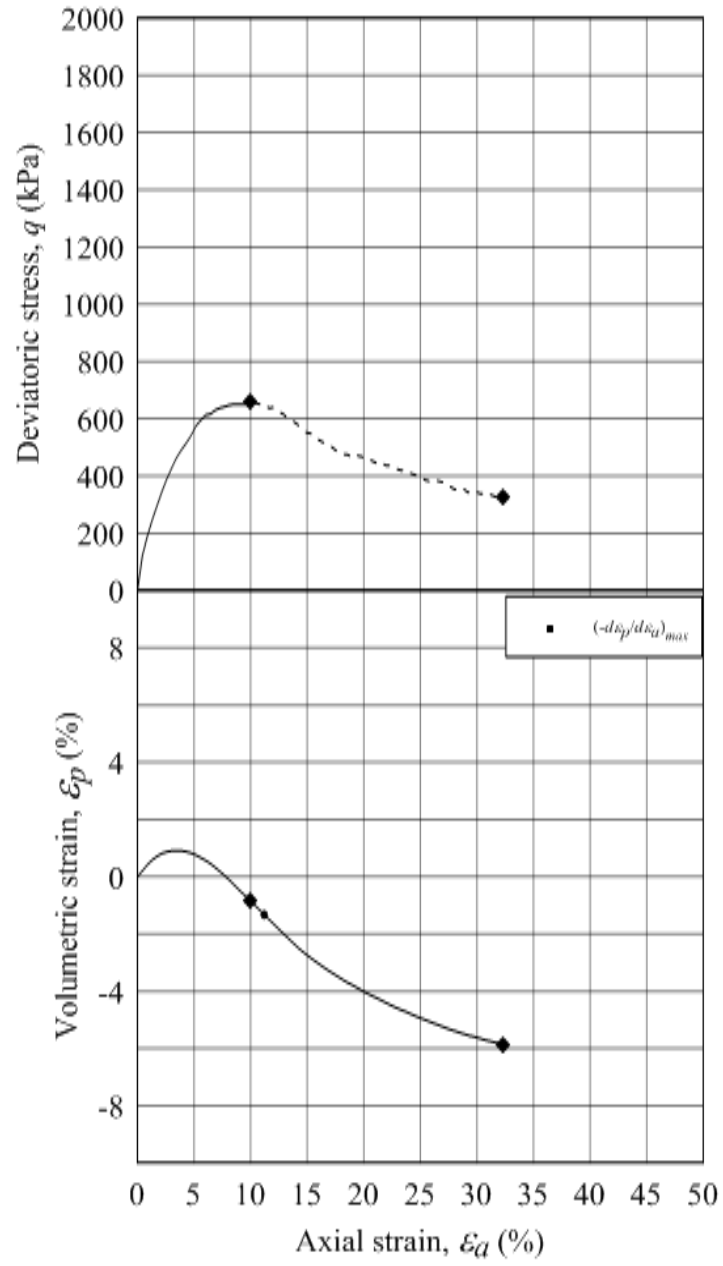


Figure C.6: Pre Deviatoric stress and volumetric strain versus axial strain for specimen U50-100.

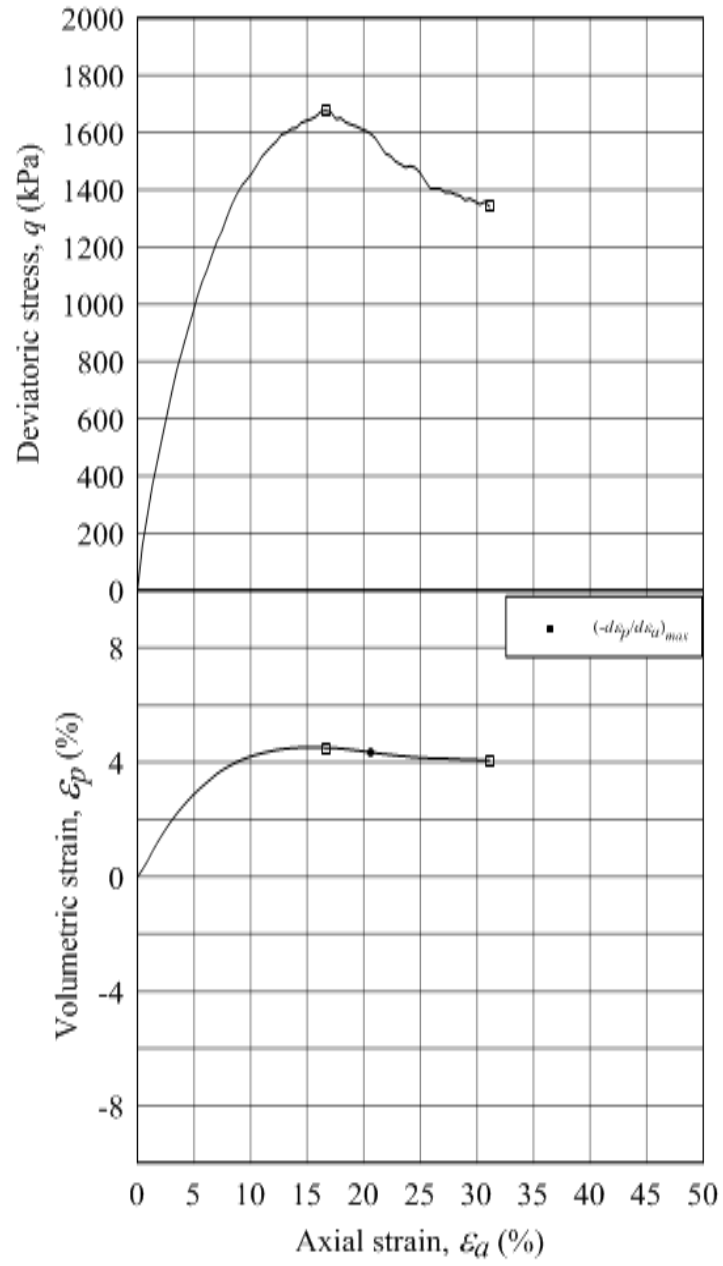


Figure C.7: Deviatoric stress and volumetric strain versus axial strain for specimen U42-400.

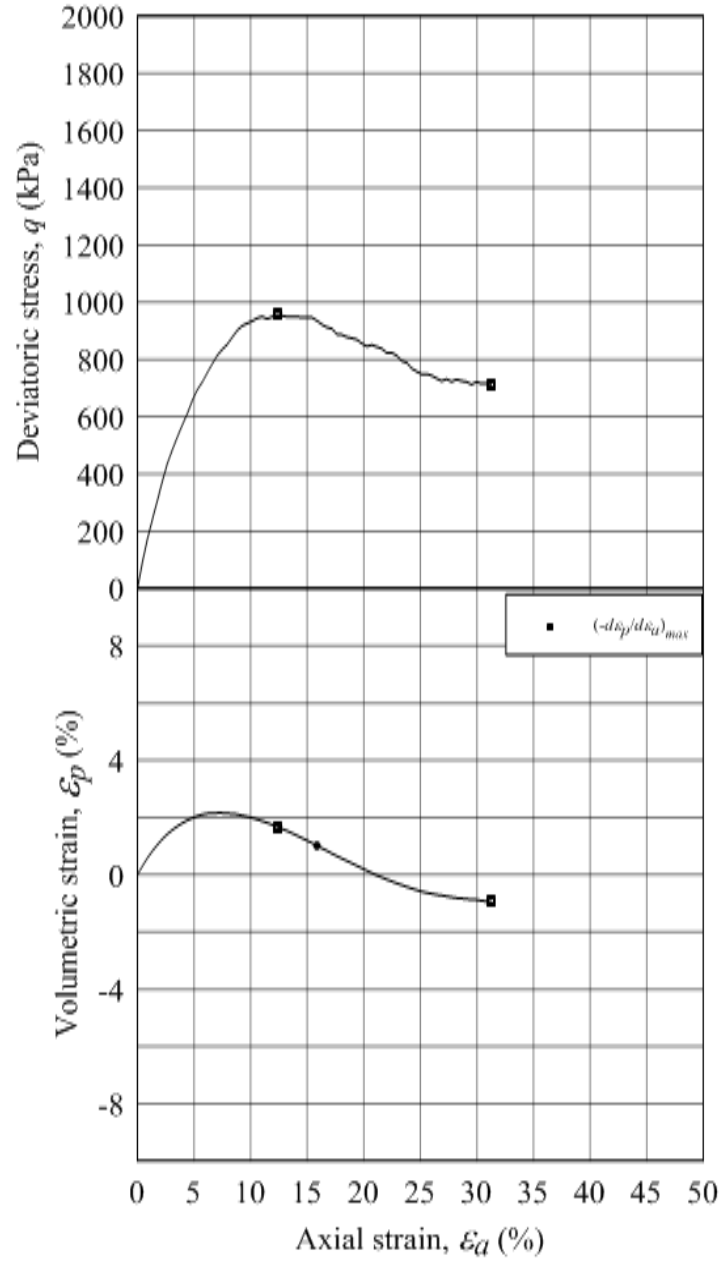


Figure C.8: Deviatoric stress and volumetric strain versus axial strain for specimen U40-200.

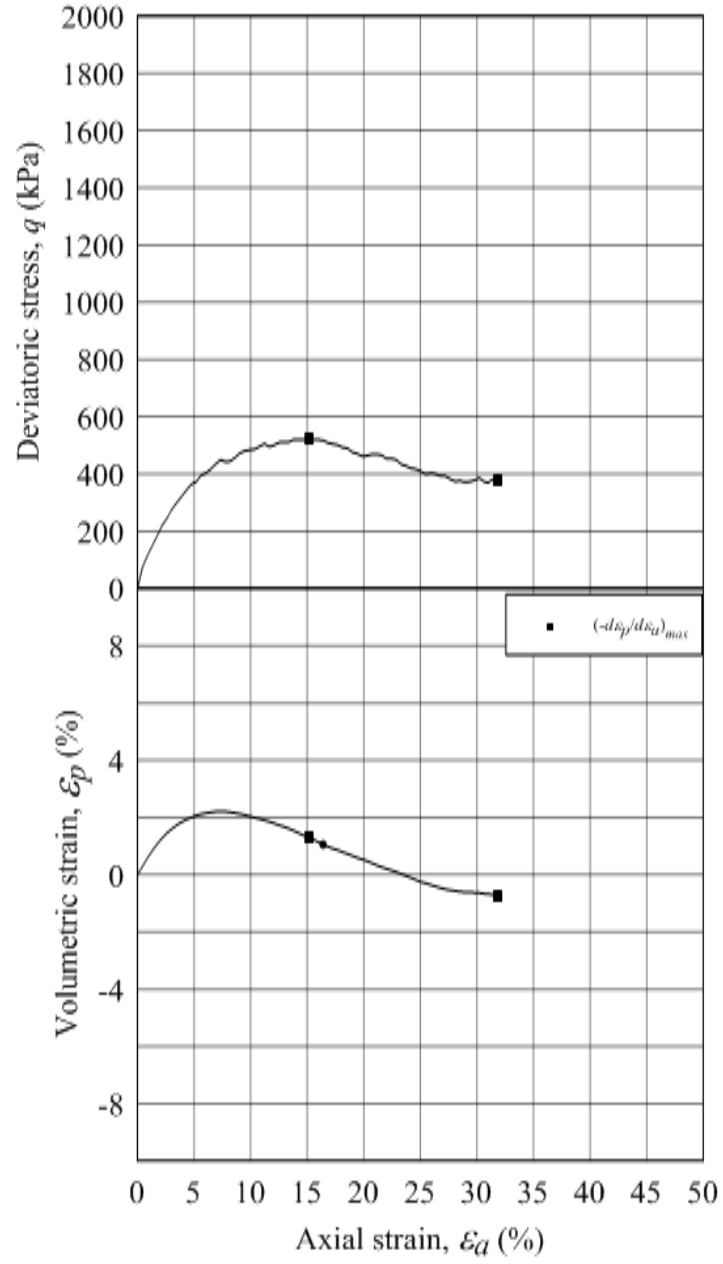


Figure C.9: Deviatoric stress and volumetric strain versus axial strain for specimen U26-100.

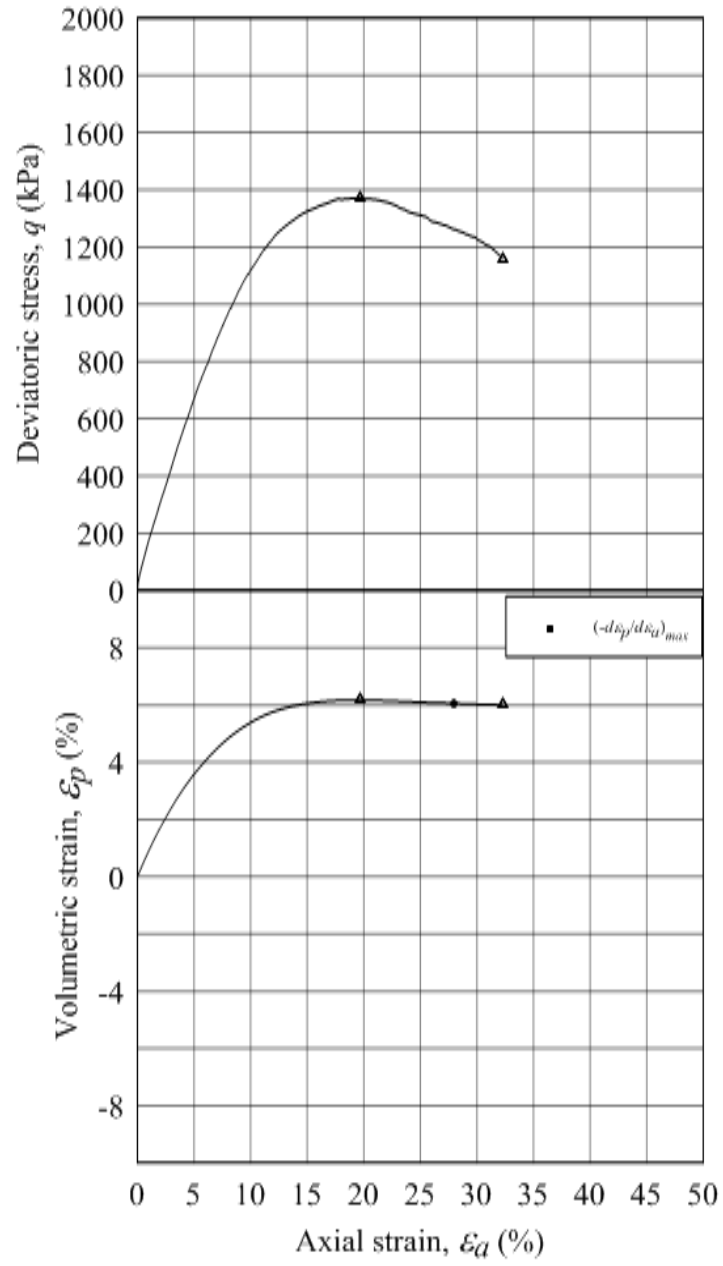


Figure C.10: Deviatoric stress and volumetric strain versus axial strain for specimen W92-400.

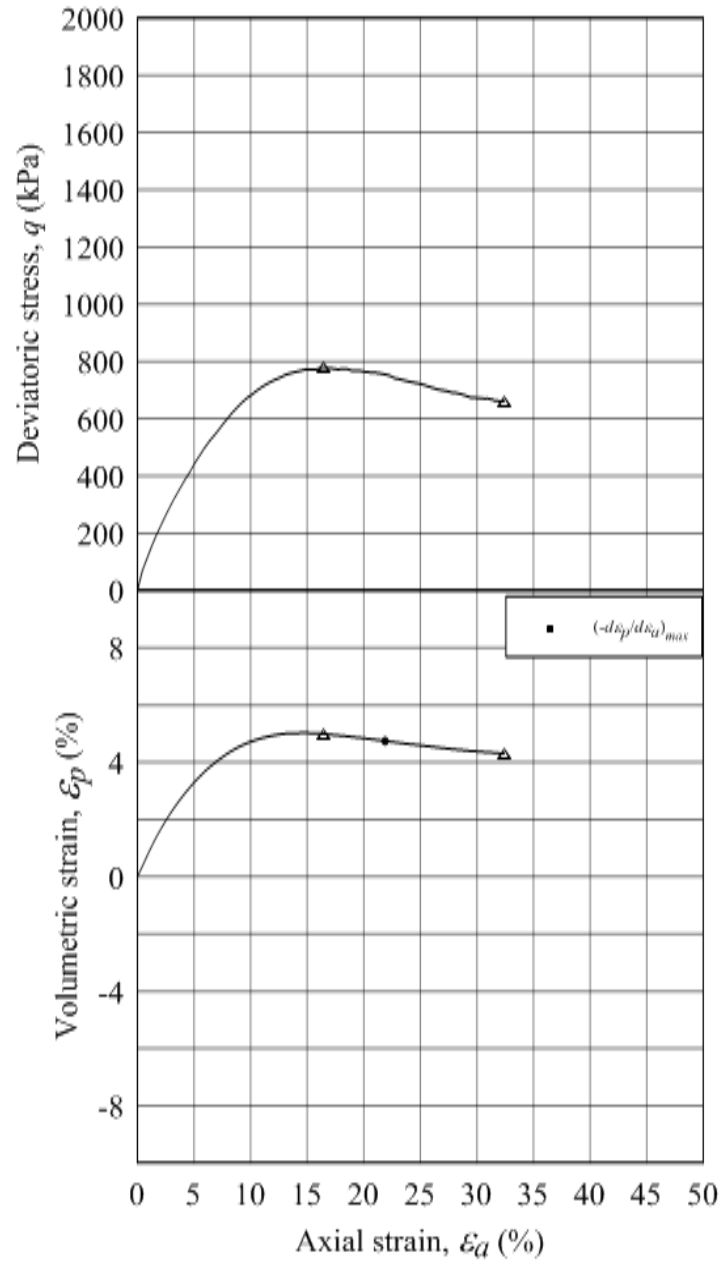


Figure C.11: Deviatoric stress and volumetric strain versus axial strain for specimen W83-200.

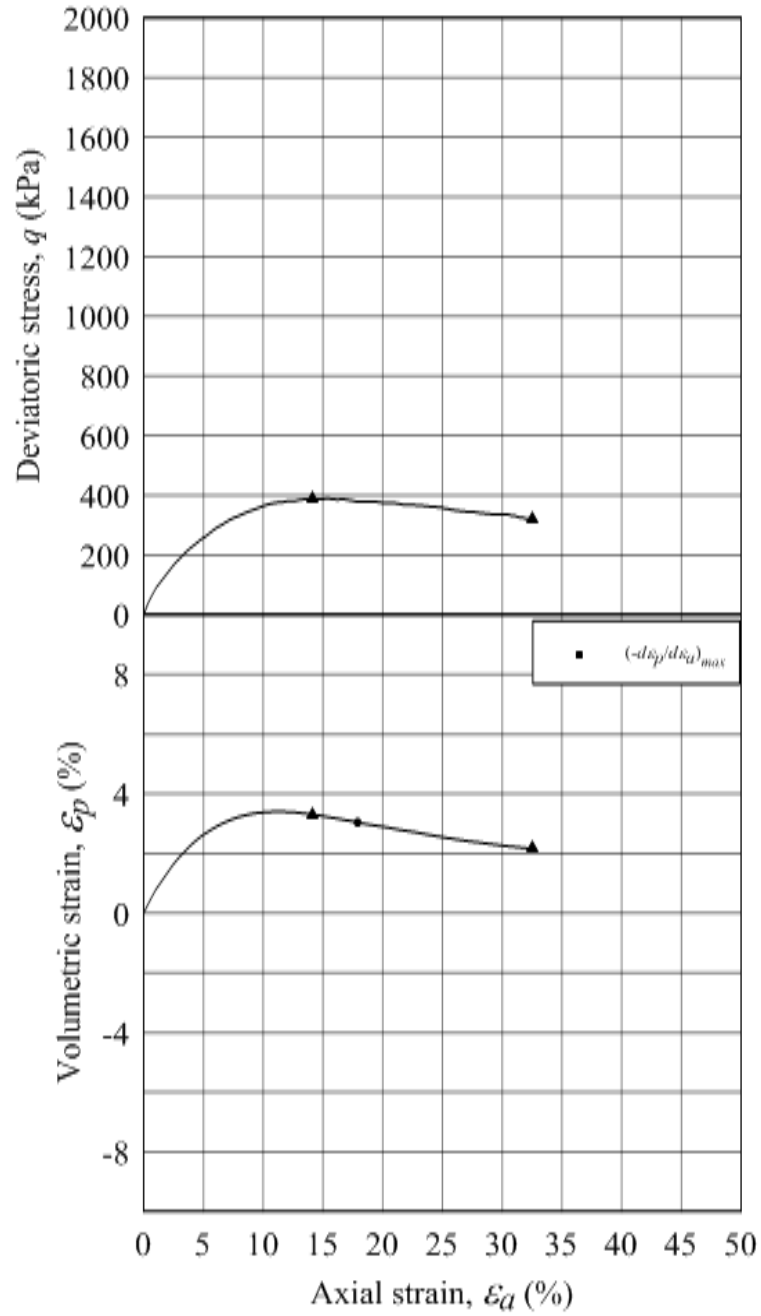


Figure C.12: Deviatoric stress and volumetric strain versus axial strain for specimen W78-100.

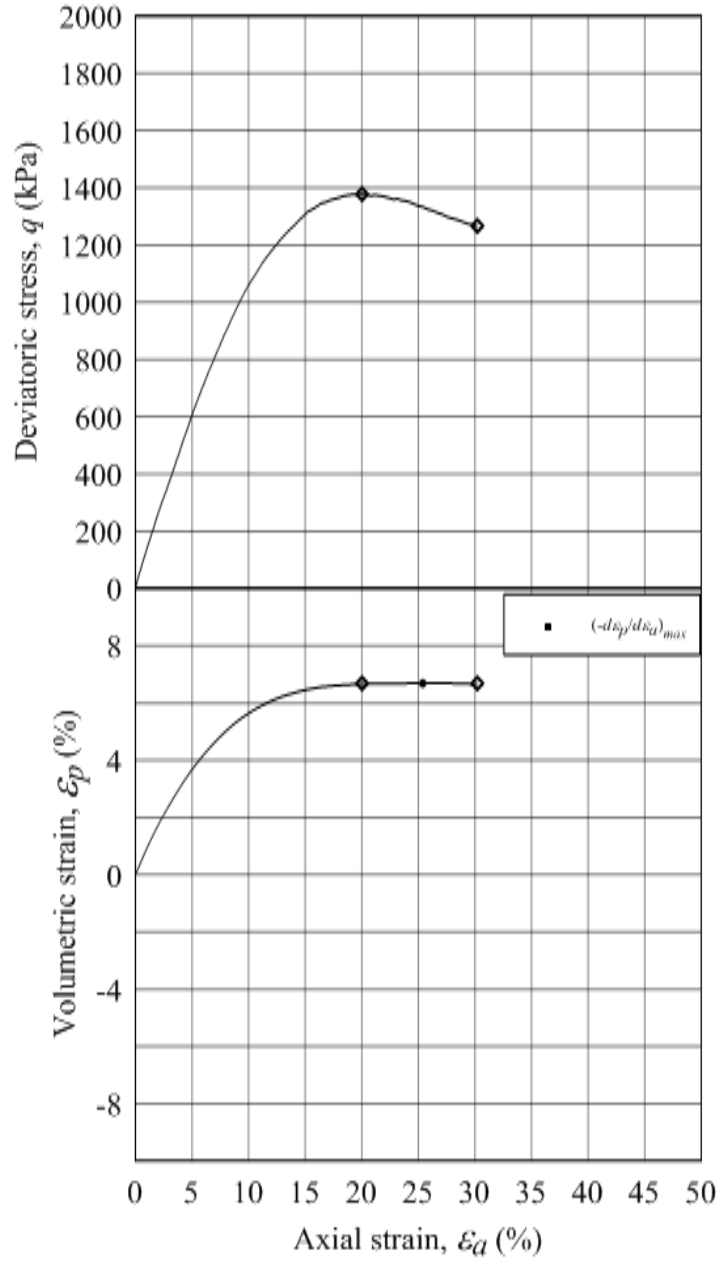


Figure C.13: Deviatoric stress and volumetric strain versus axial strain for specimen W76-400.

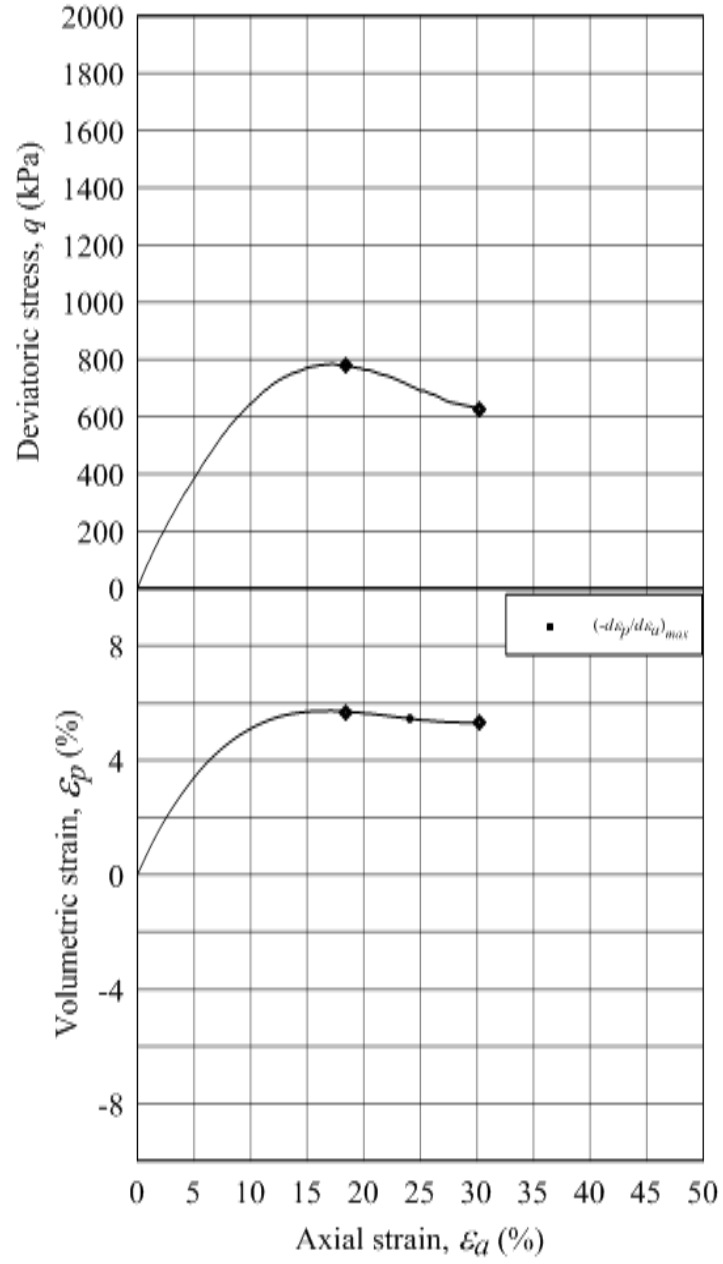


Figure C.14: Deviatoric stress and volumetric strain versus axial strain for specimen W72-200.

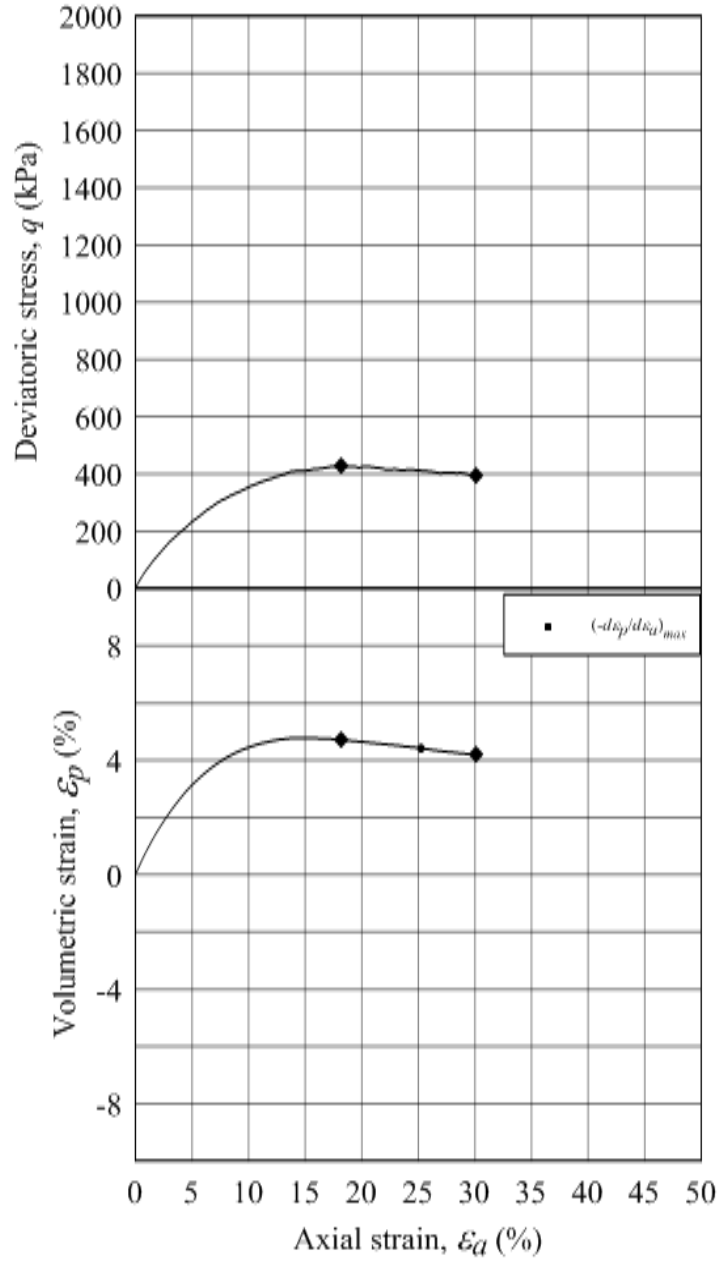


Figure C.15: Deviatoric stress and volumetric strain versus axial strain for specimen W61-100.

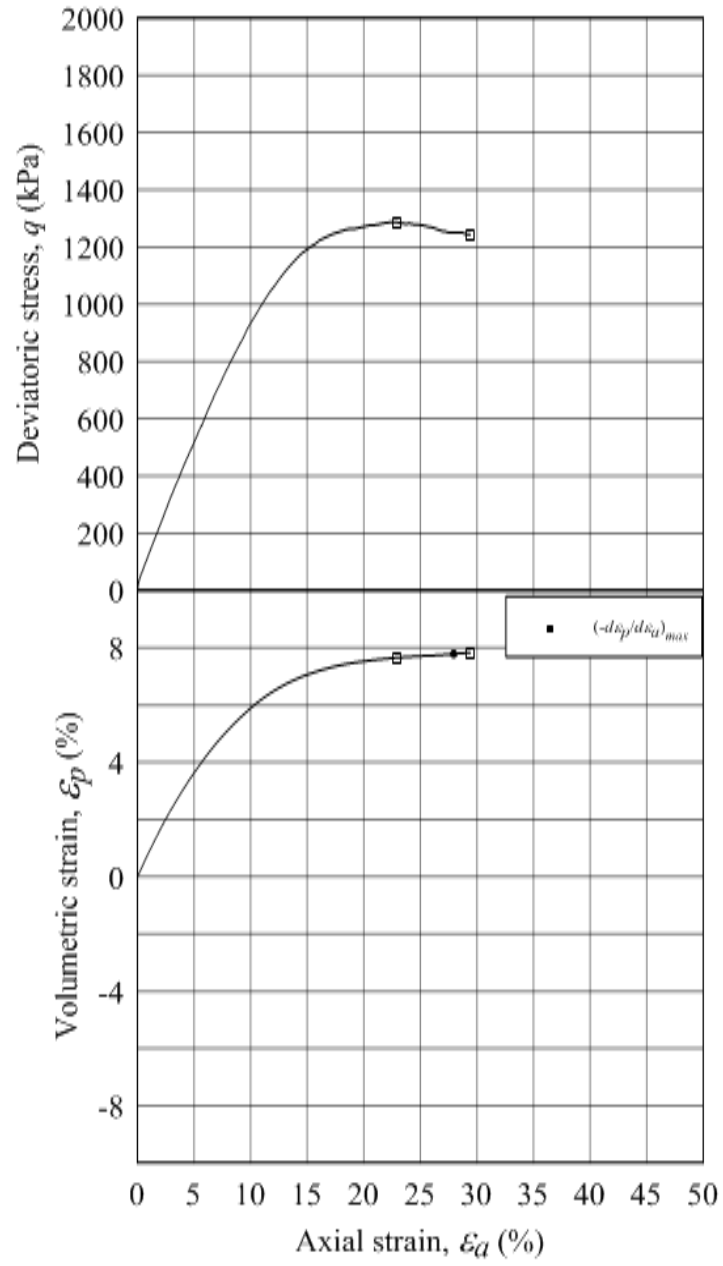


Figure C.16: Deviatoric stress and volumetric strain versus axial strain for specimen W55-400.

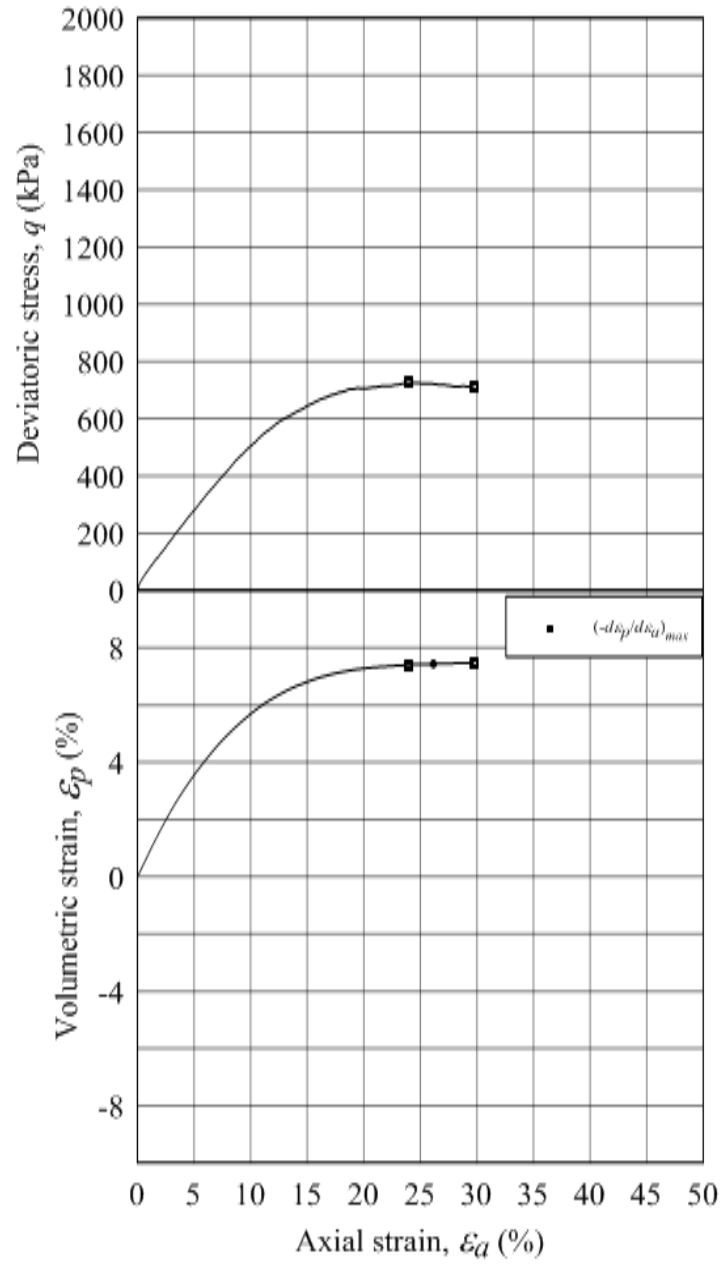


Figure C.17: Deviatoric stress and volumetric strain versus axial strain for specimen W44-200.

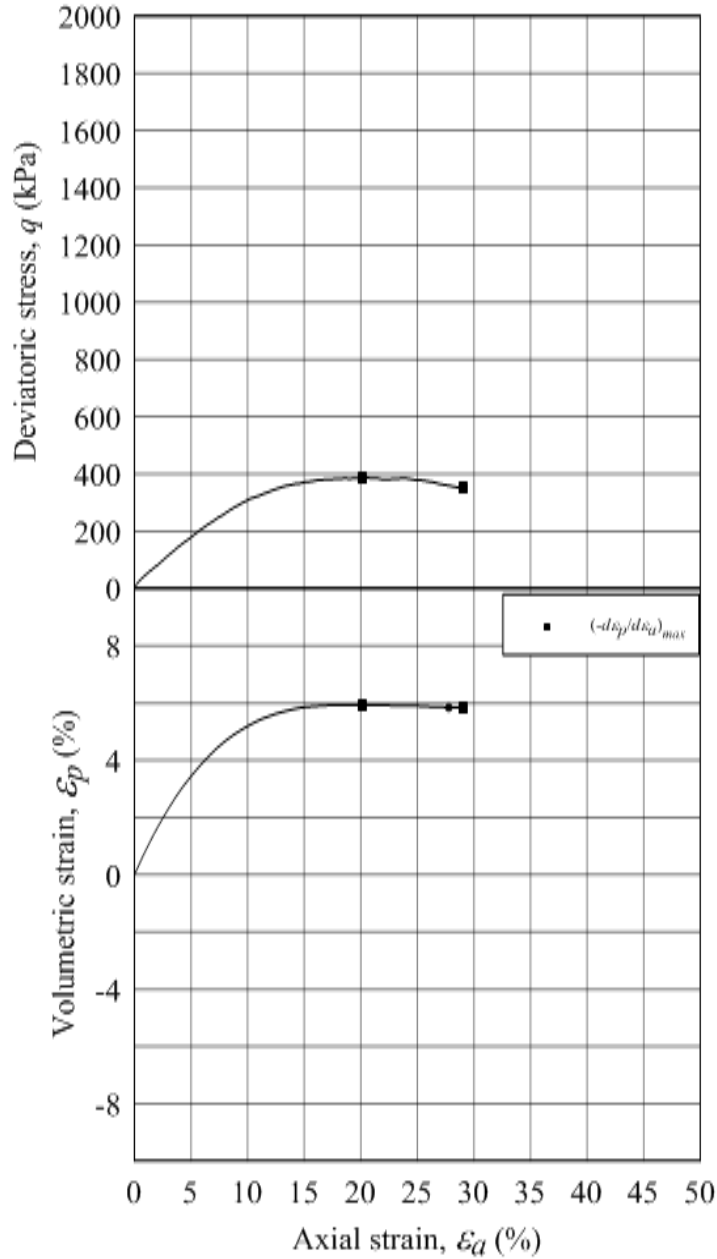


Figure C.18: Deviatoric stress and volumetric strain versus axial strain for specimen W34-100.

Back pressure saturation was completed as discussed in Chapter 4. Generally back pressure values necessary to achieve a minimum  $B$  value of 0.98 were larger for the weathered material than that of the unweathered material. Back pressure saturation data for the unweathered and weathered  $MWR$  materials are presented on Figures C.19 through C.24.

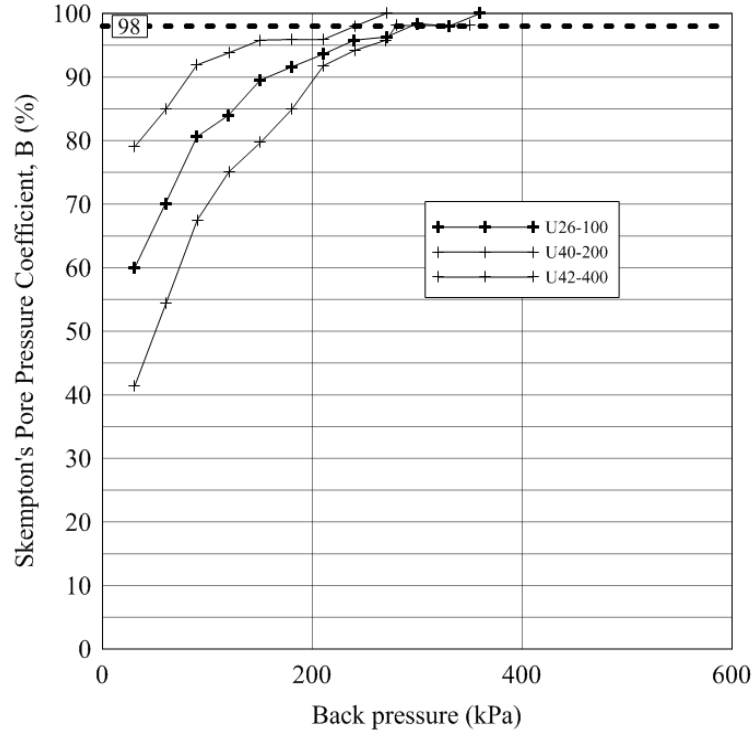


Figure C.19: Back pressure saturation data for specimens U42-400, U40-200 and U26-100.

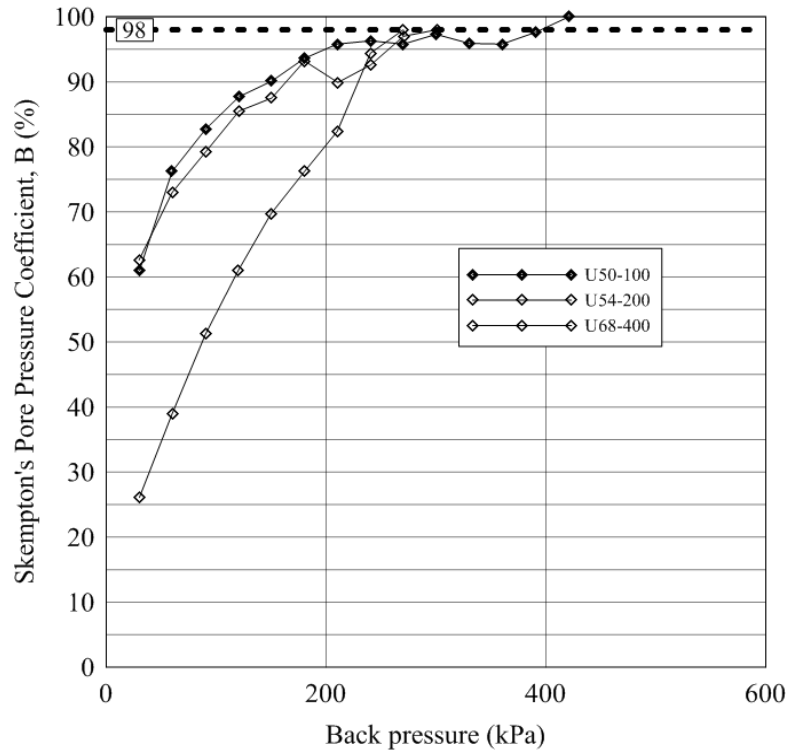


Figure C.20: Back pressure saturation data for specimens U68-400, U54-200 and U50-100.

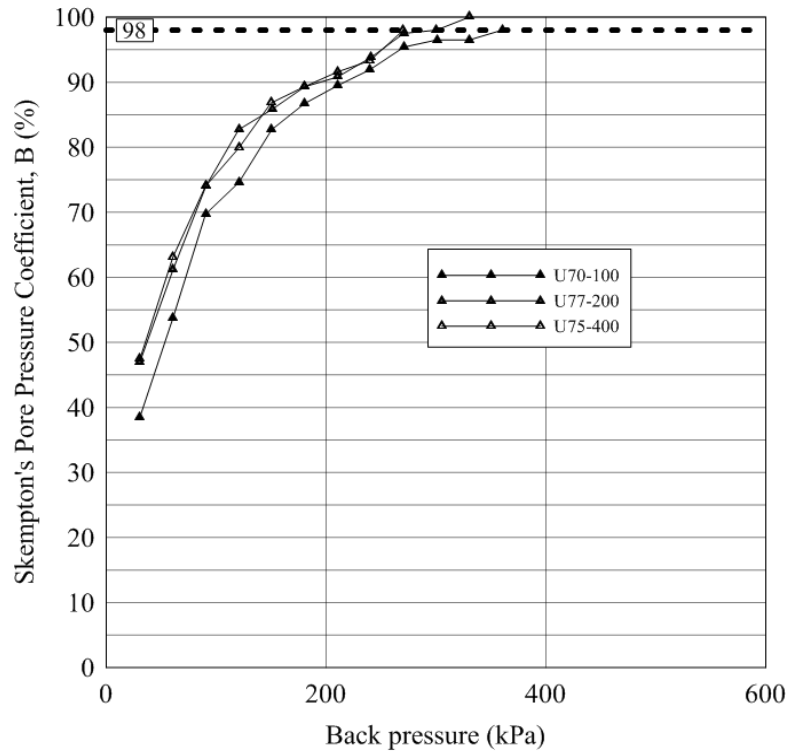


Figure C.21: Back pressure saturation data for specimens U75-400, U77-200 and U70-100.

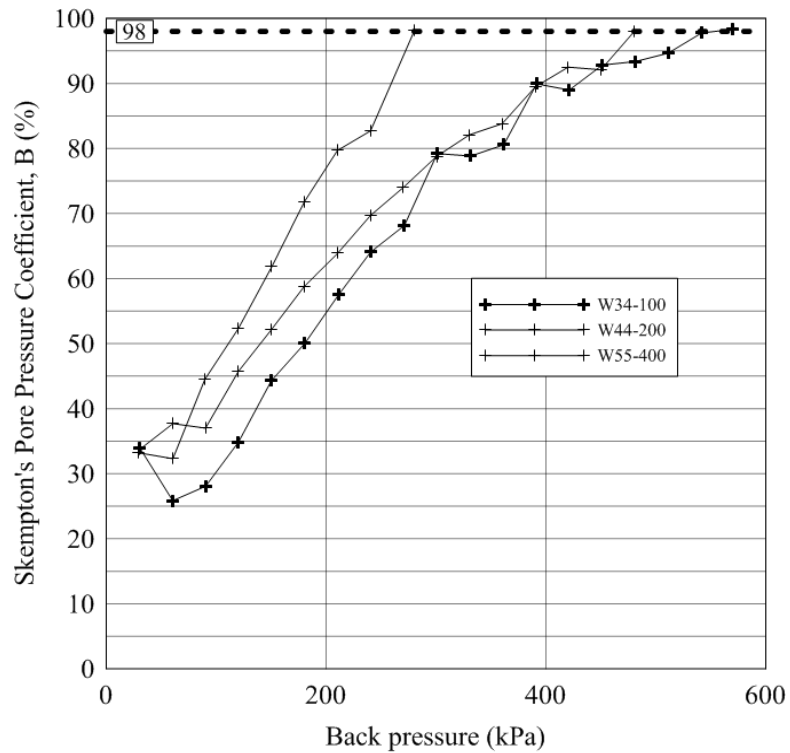


Figure C.22: Back pressure saturation data for specimens W55-400, W44-200 and W34-100.

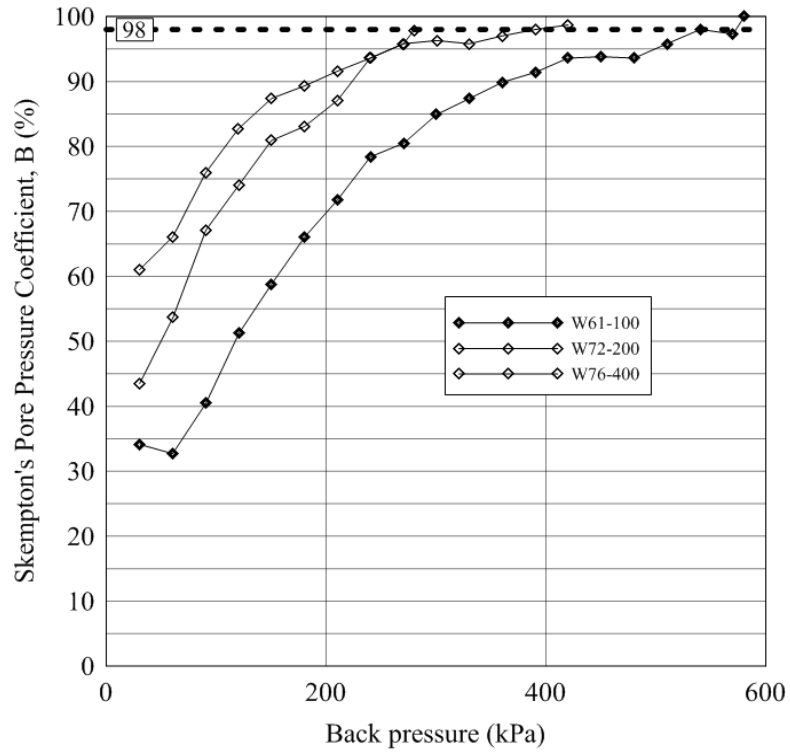


Figure C.23: Back pressure saturation data for specimens W76-400, W72-200 and W61-100.

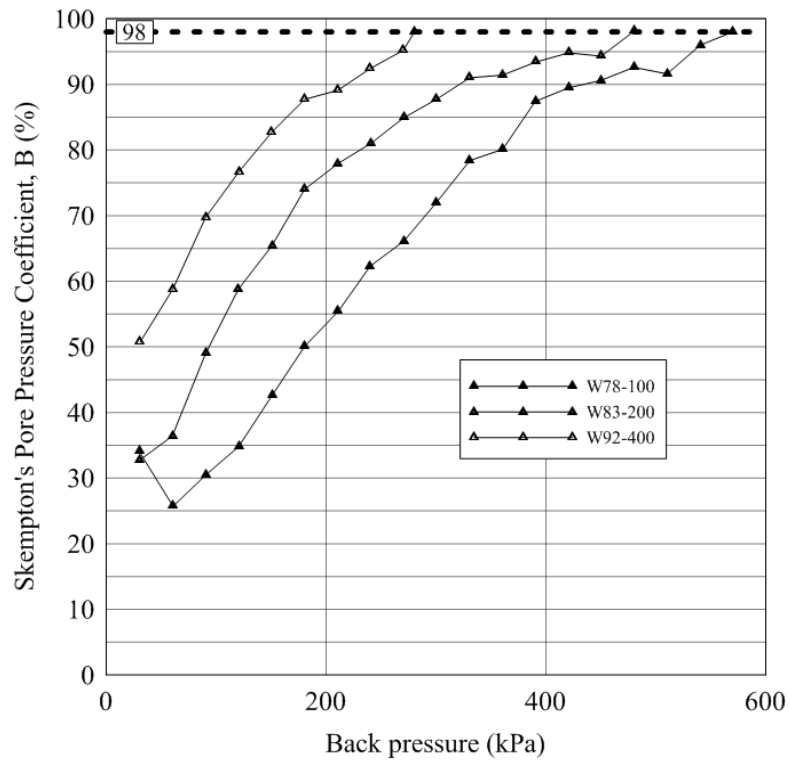


Figure C.24: Back pressure saturation data for specimens W92-400, W83-200 and W78-100.

## APPENDIX D: FRACTAL DIMENSIONS

As previously discussed in Chapter 3 and 4, the fractal dimension ( $D$ ) was determined for each specimen before and after triaxial testing. Determining  $D$  was accomplished by assuming values of the shape factors  $\beta_s$  and  $\beta_v$  equal to those determined using data presented by Marsal (1973) for angular rockfill. Section 4.2.10 expands on the assumptions made in the determination of  $D$ . Using the shape factors, a simple power law can be applied through Equation 3.30 in order to determine  $D$ . Using the parallel gradation technique (Lowe 1964), the initial  $D$  for each material was constant at 2.70 and 2.97 for the unweathered and weather material, respectively. Figures D.1 and D.2 show the initial regression of  $D$  for the unweathered and weathered materials, respectively, while Figures D.3 through D.20 are regressions for the determination of  $D$  after each specific triaxial test. Final values of  $D$  for each test are tabulated in Tables 5.3 and 5.4.

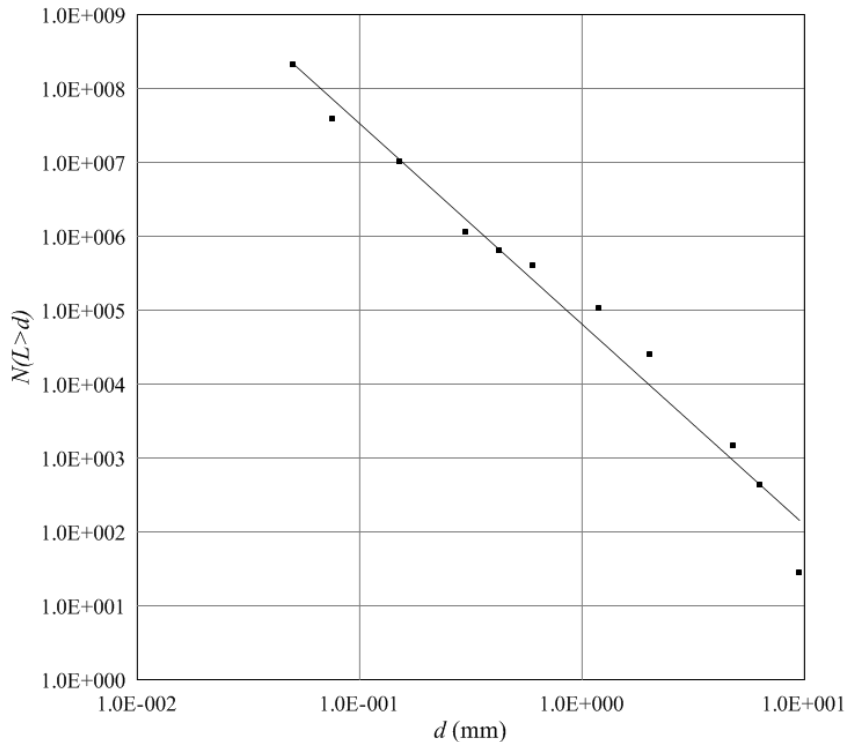


Figure D.1: Initial regression of  $D$  for the unweathered material ( $D = 2.70$ ).

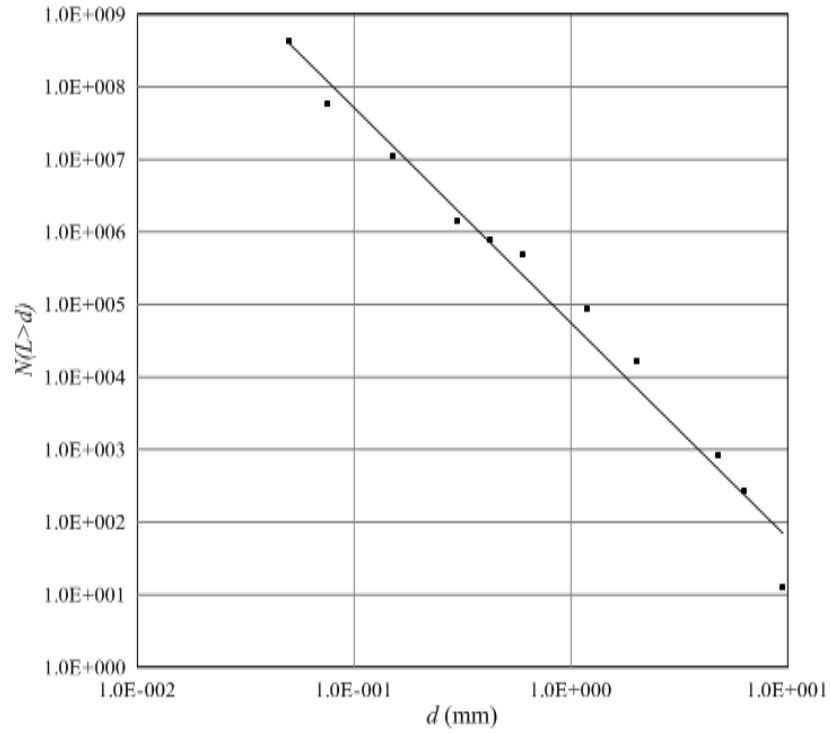


Figure D.2: Initial regression of  $D$  for the unweathered material ( $D = 2.97$ ).

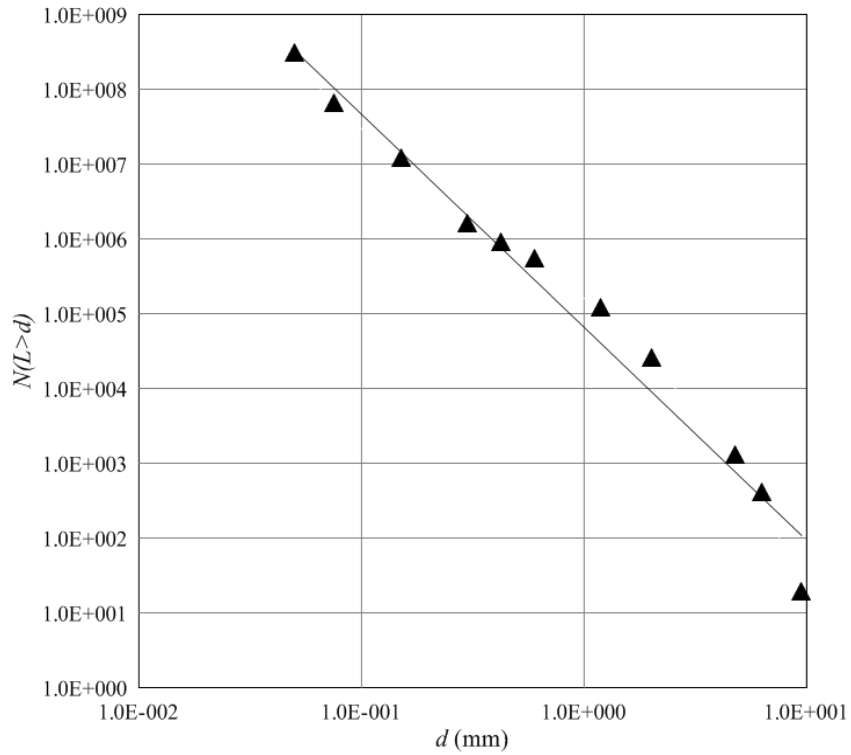


Figure D.3: Post test regression of  $D$  for specimen U75-400.

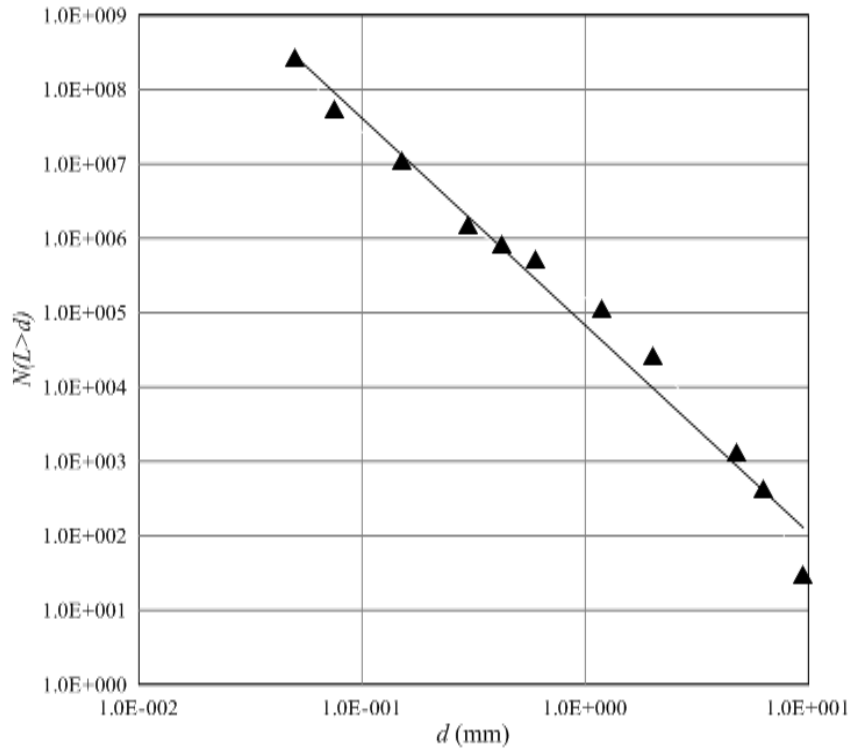


Figure D.4: Post test regression of  $D$  for specimen U77-200.

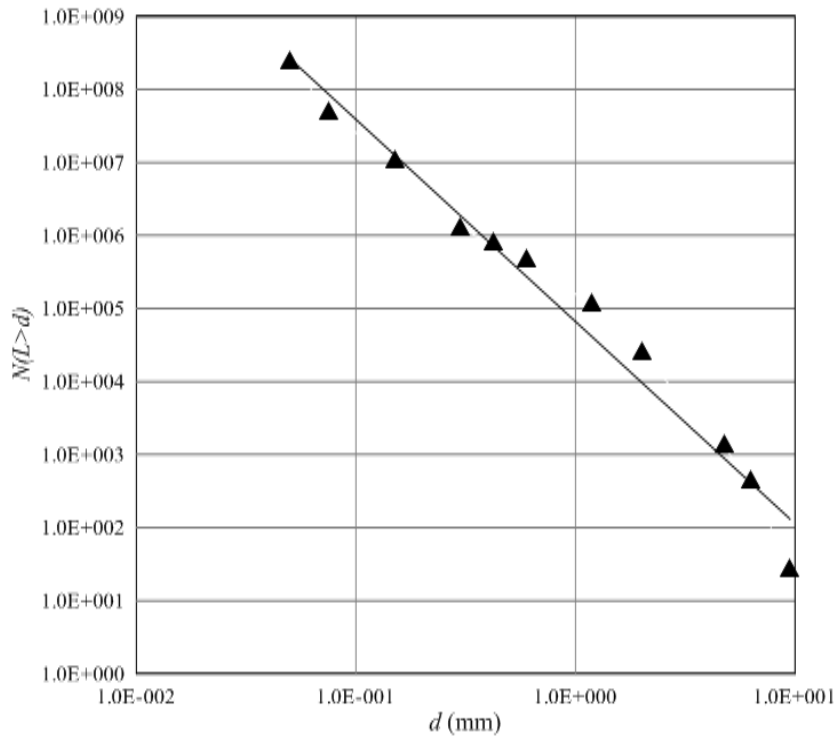


Figure D.5: Post test regression of  $D$  for specimen U70-100.

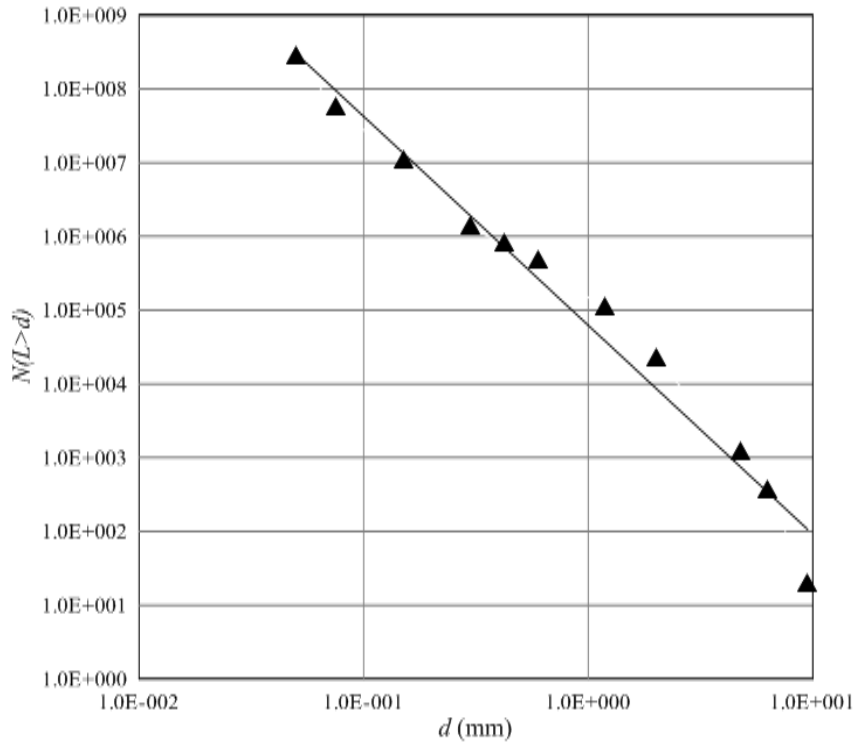


Figure D.6: Post test regression of  $D$  for specimen U68-400.

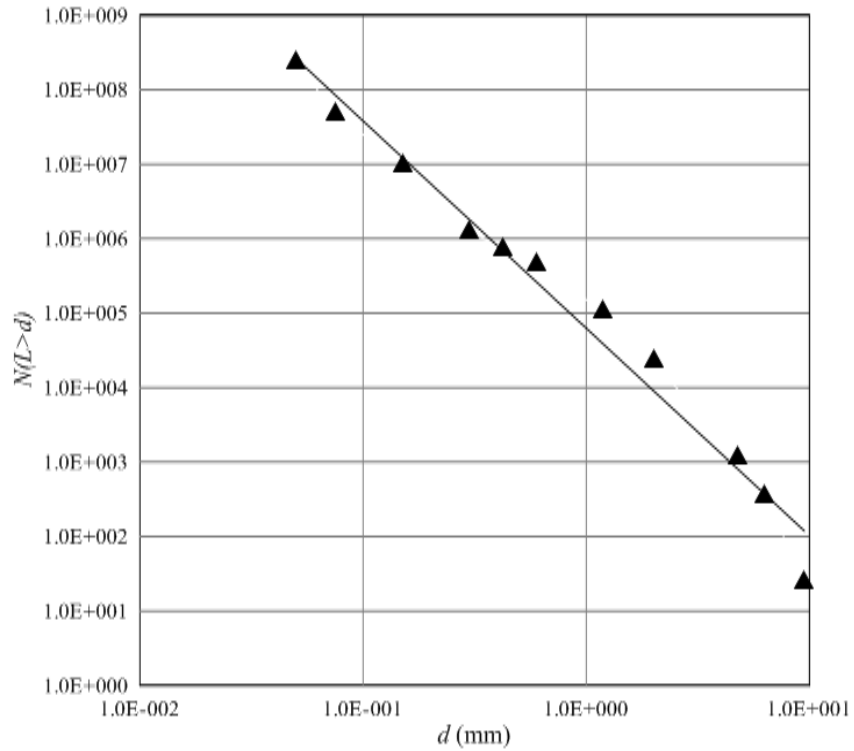


Figure D.7: Post test regression of  $D$  for specimen U54-200.

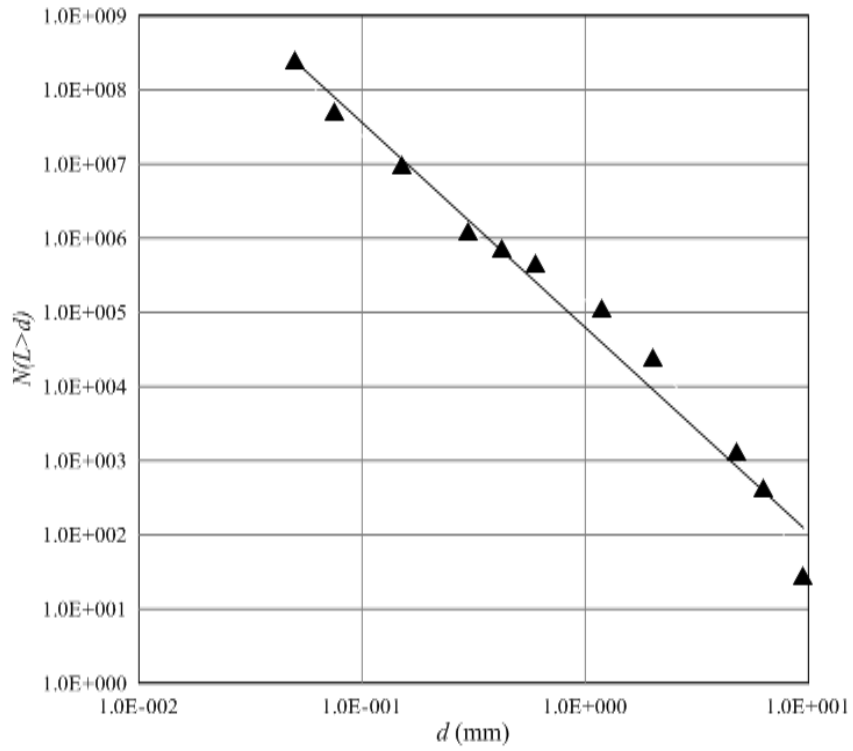


Figure D.8: Post test regression of  $D$  for specimen U50-100.

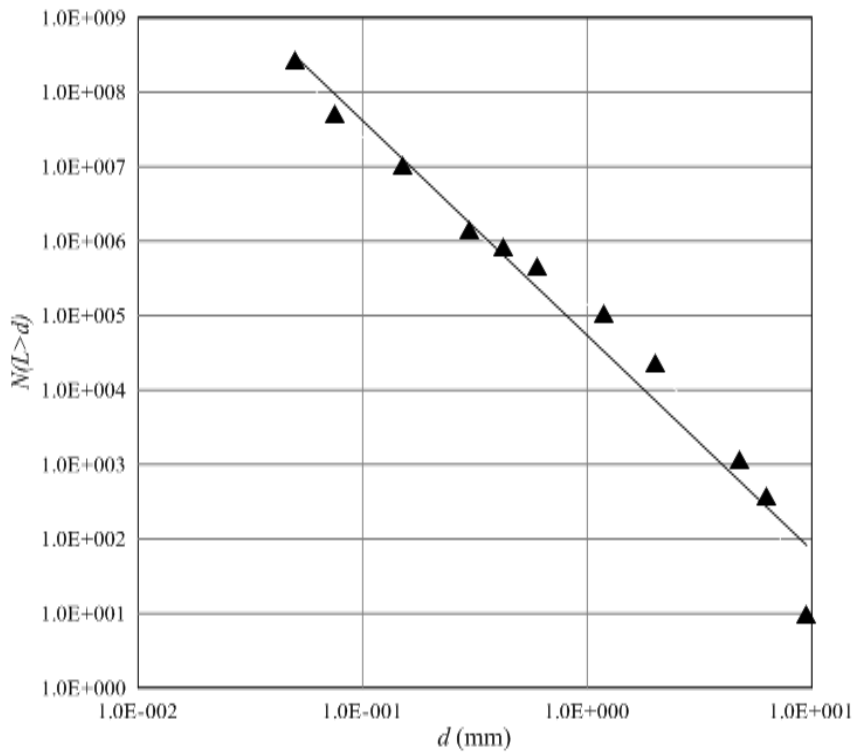


Figure D.9: Post test regression of  $D$  for specimen U42-400.

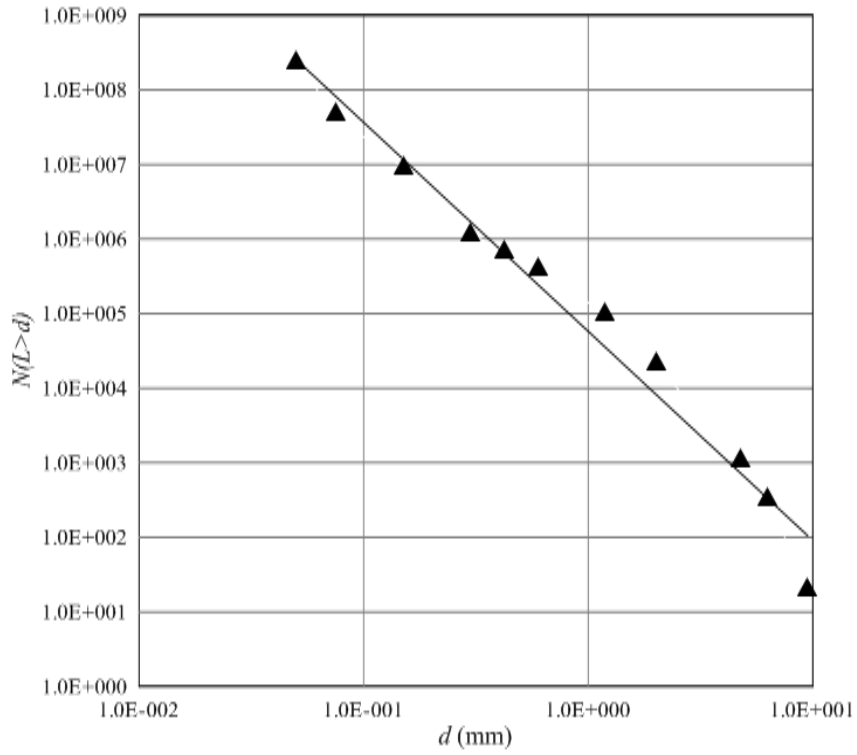


Figure D.10: Post test regression of  $D$  for specimen U40-200.

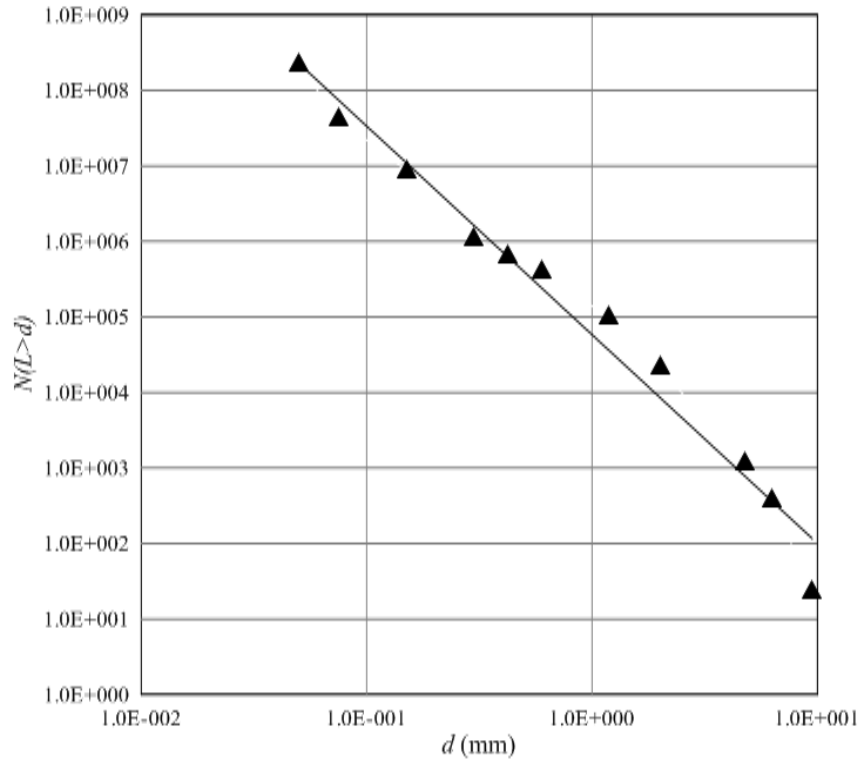


Figure D.11: Post test regression of  $D$  for specimen U26-100.

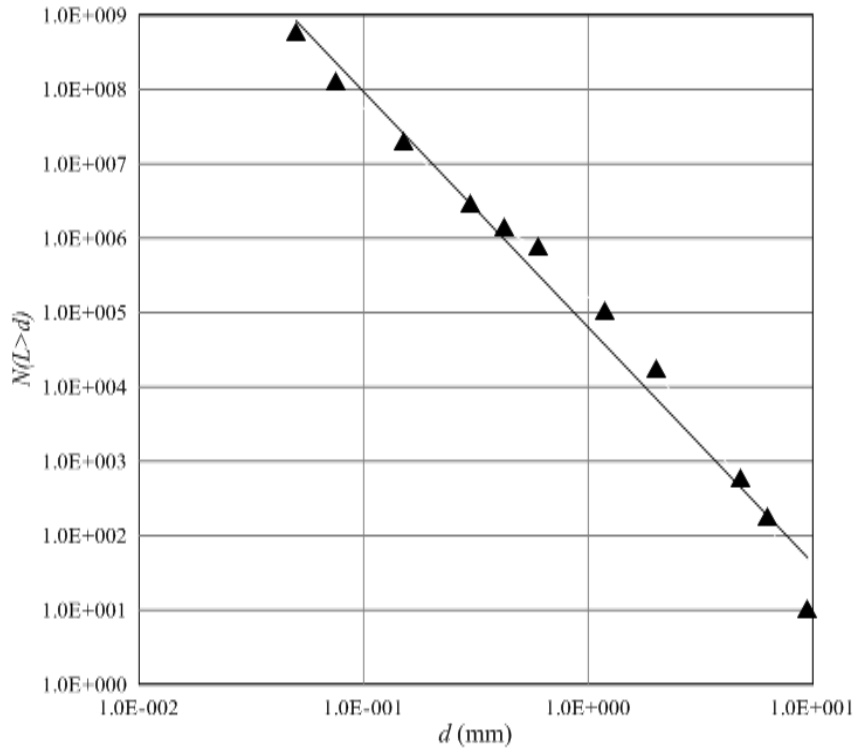


Figure D.12: Post test regression of  $D$  for specimen W92-400.

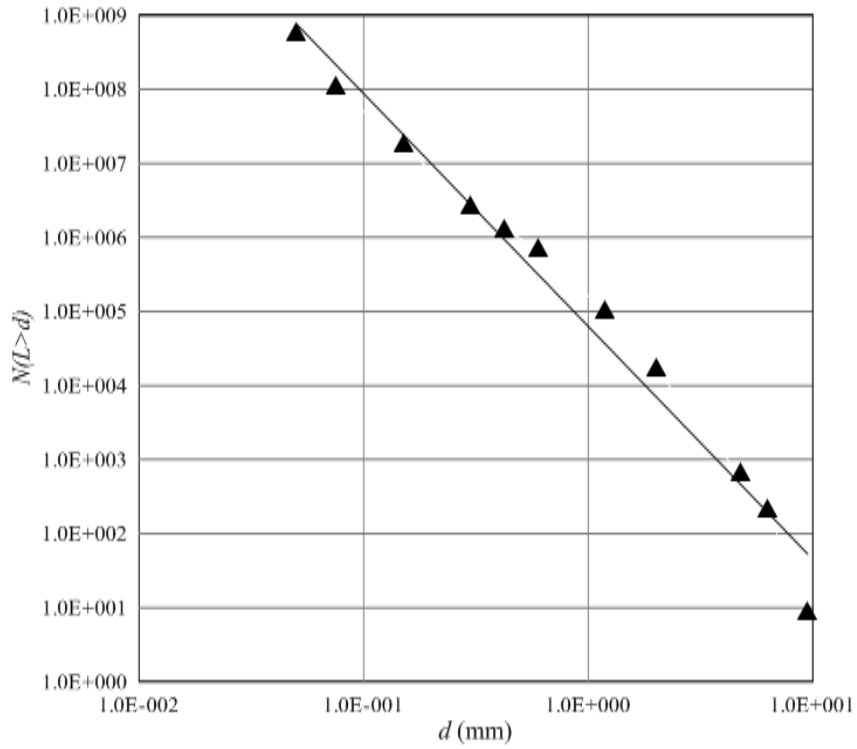


Figure D.13: Post test regression of  $D$  for specimen W83-200.

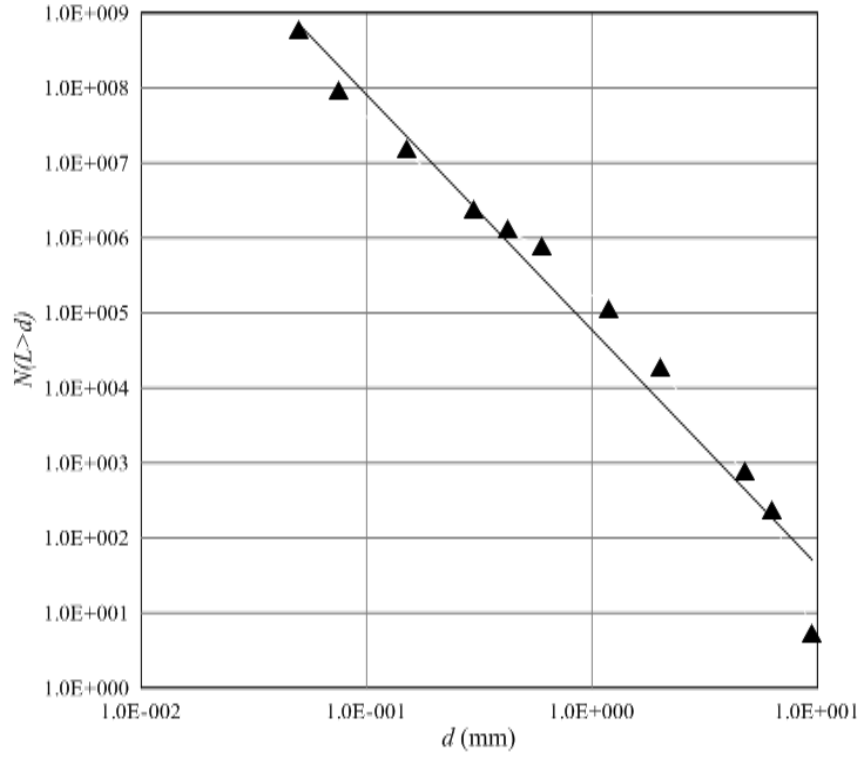


Figure D.14: Post test regression of  $D$  for specimen W78-100.

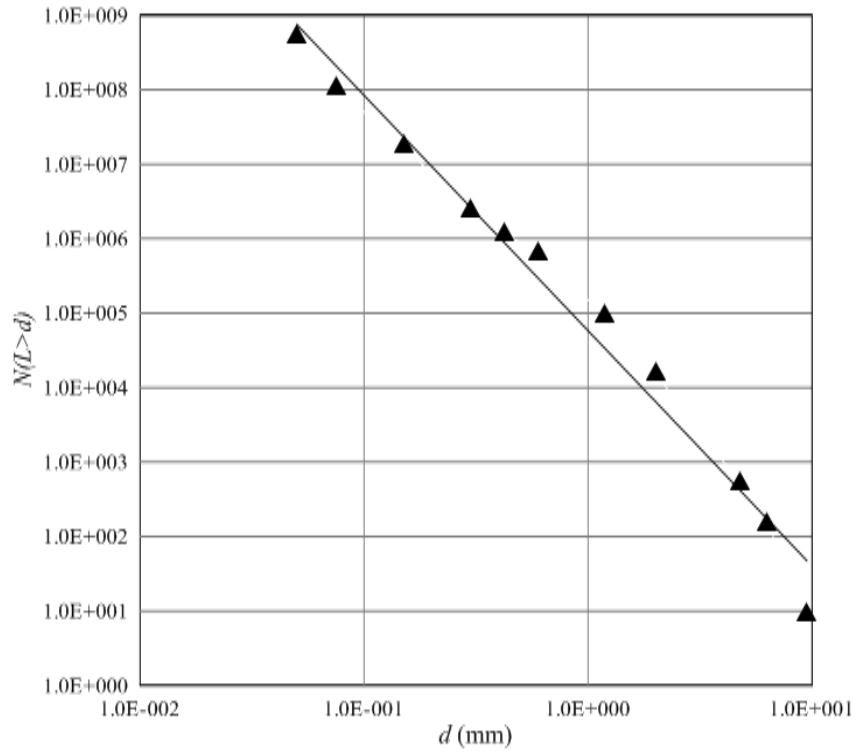


Figure D.15: Post test regression of  $D$  for specimen W76-400.

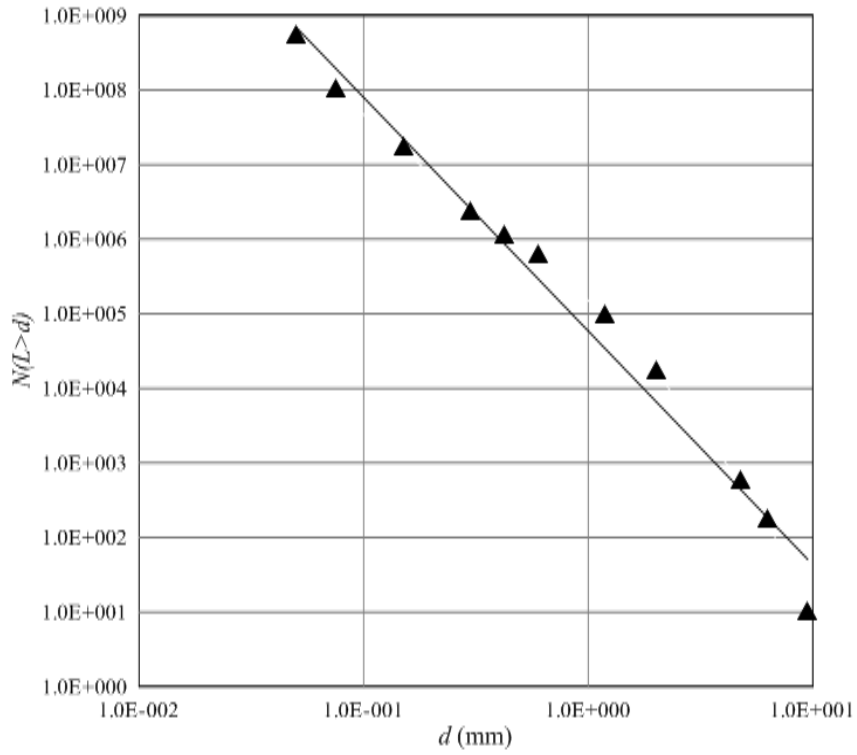


Figure D.16: Post test regression of  $D$  for specimen W72-200.

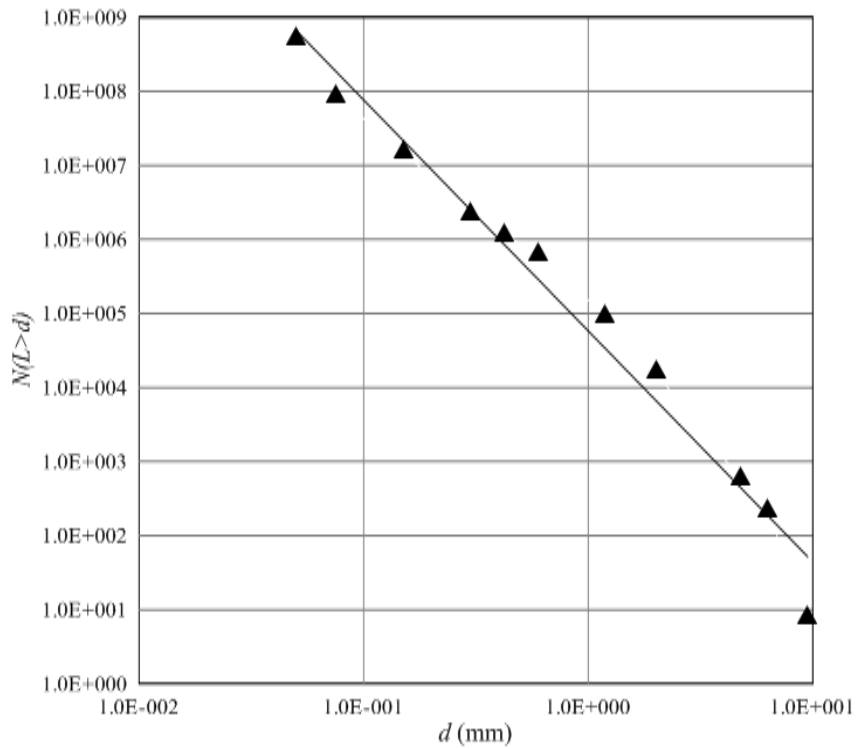


Figure D.17: Post test regression of  $D$  for specimen W61-100.

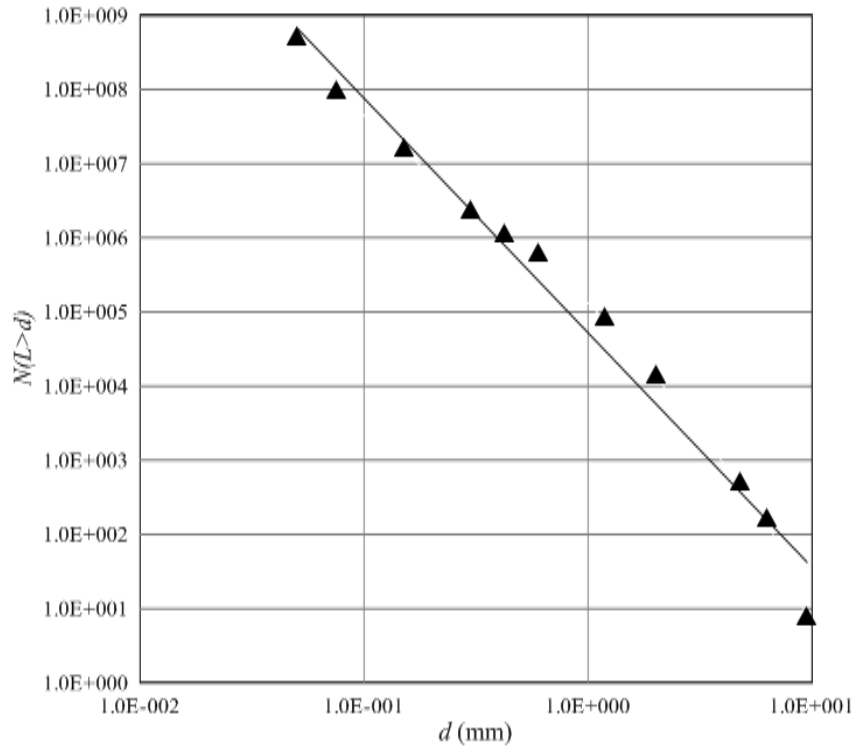


Figure D.18: Post test regression of  $D$  for specimen W55-400.

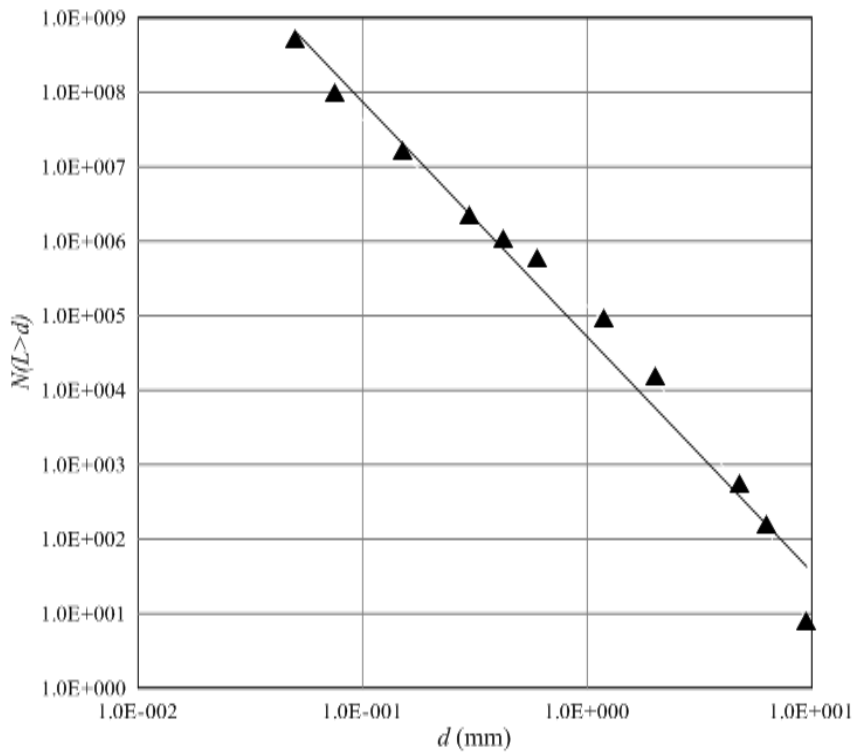


Figure D.19: Post test regression of  $D$  for specimen W44-200.

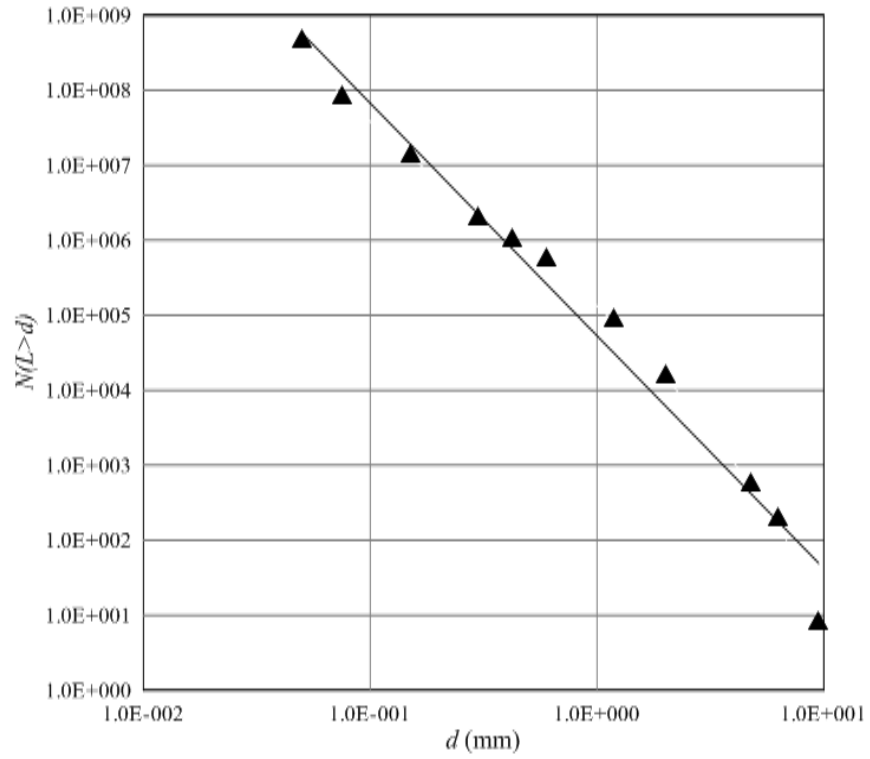


Figure D.20: Post test regression of  $D$  for specimen W34-100.

## APPENDIX E: SCANNING ELECTRON MICROSCOPY IMAGES

In an effort to characterize the relative impact of fines on the mechanical behavior of the *MWR* materials tested in this study, scanning electron microscopy (*SEM*) was completed on samples of the fines (material passing the #200 sieve) for both the and weathered *MWR* materials. The *SEM* analysis was conducted using Colorado State University's JEOL JSM-6500F Scanning Electron Microscope. The microscope operates at 0.5 to 30 kV with an ultimate resolution of 1.5 nm and a magnification range of 10X to 400,000X. A photograph of the JEOL JSM-6500F Scanning Electron Microscope used to capture microphotographs of the *MWR* fines used in this study is presented on Figure E.1.

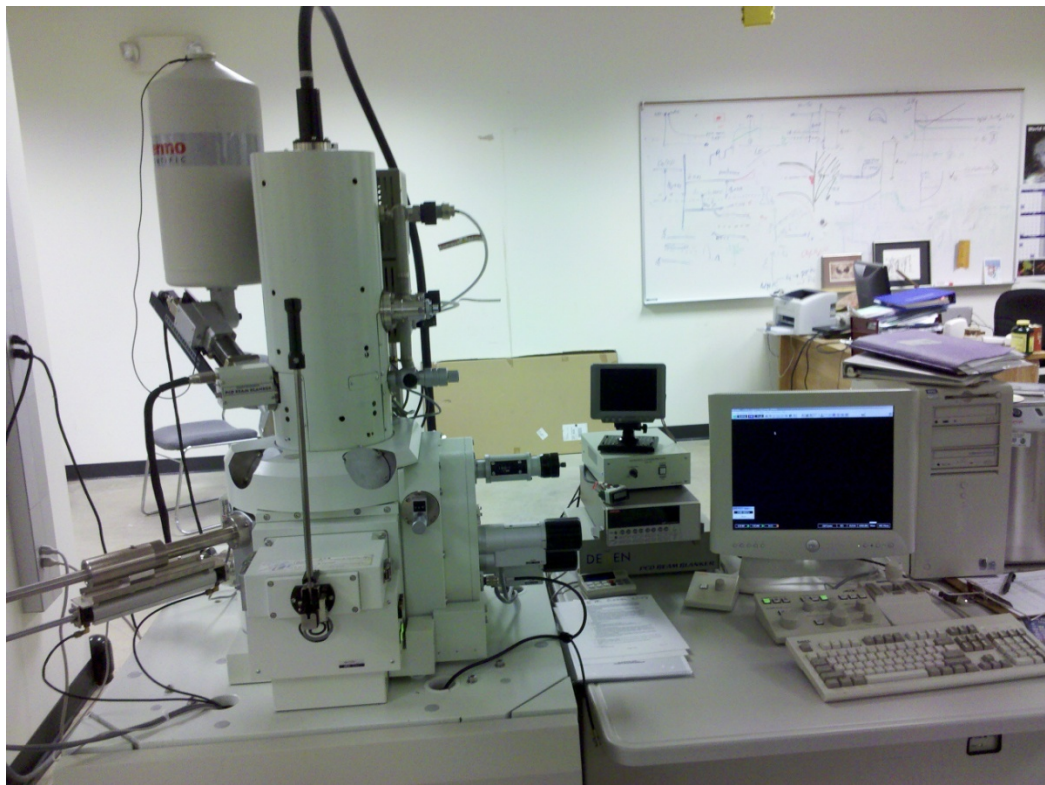


Figure E.1: Photograph of the JEOL JSM-6500F Scanning Electron Microscope used to capture microphotographs of *MWR* fines used in the present study.

Microphotographs were taken at a range of different magnifications ranging from 100X to 10,000X for both *MWR* materials. *SEM* conducted on unweathered *MWR* fines

primarily showed prismatic particles with sharp and slightly rounded edges with very little plate like particles. *SEM* conducted on weathered *MWR* fines showed a large increase in plate like particles compared to that of the unweathered. Based on *XRD* results presented in Chapter 4 and Appendix A, the plate like particles in the weathered material are likely a mixture of kaolin clay and muscovite (mica). Increased soil plasticity in the weathered material compared to that of the unweathered material also supports the claim that a significant portion of the plate like particles are indeed low plasticity kaolin clay.

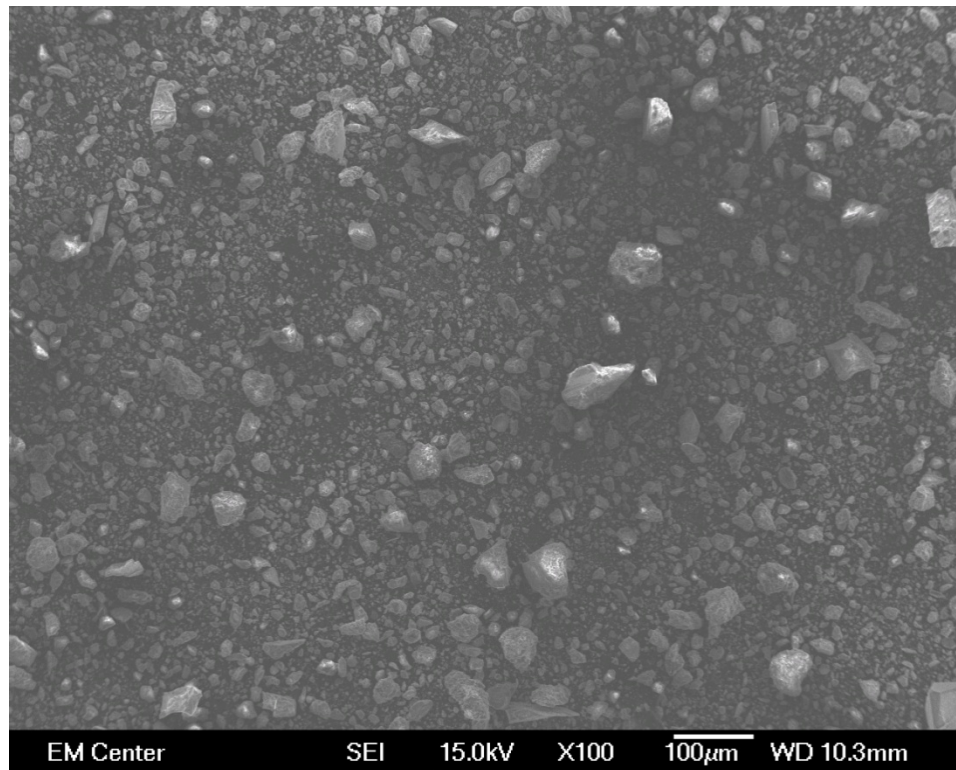


Figure E.2: Microphotograph of the unweathered fines at 100X magnification.

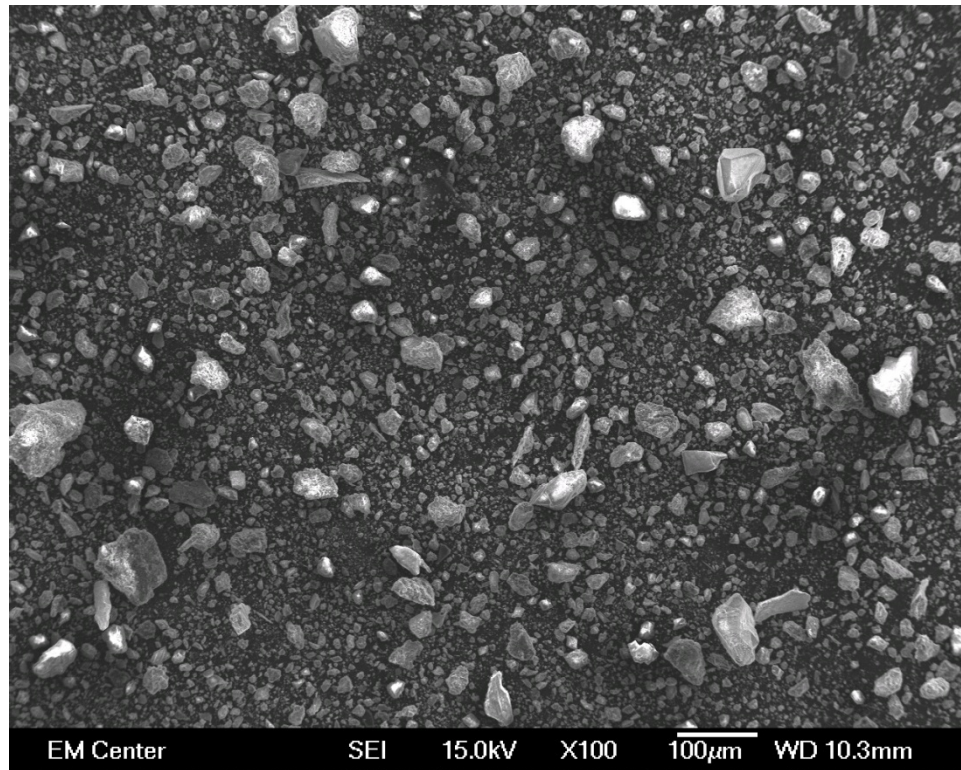


Figure E.3: Microphotograph of the unweathered fines at 100X magnification.

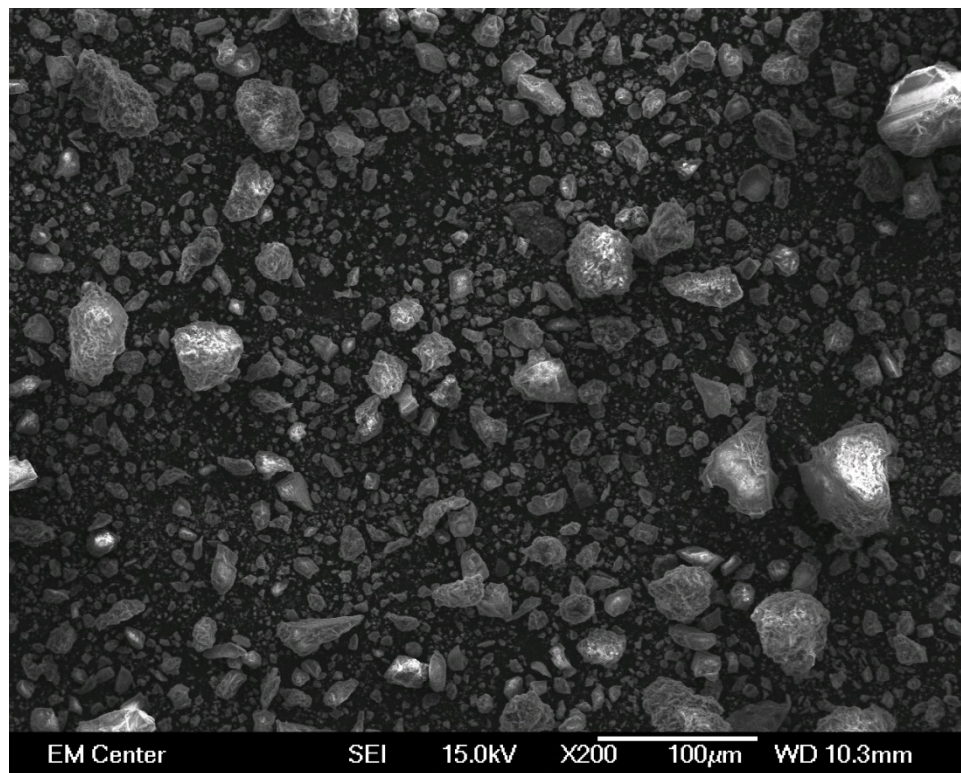


Figure E.4: Microphotograph of the unweathered fines at 200X magnification.

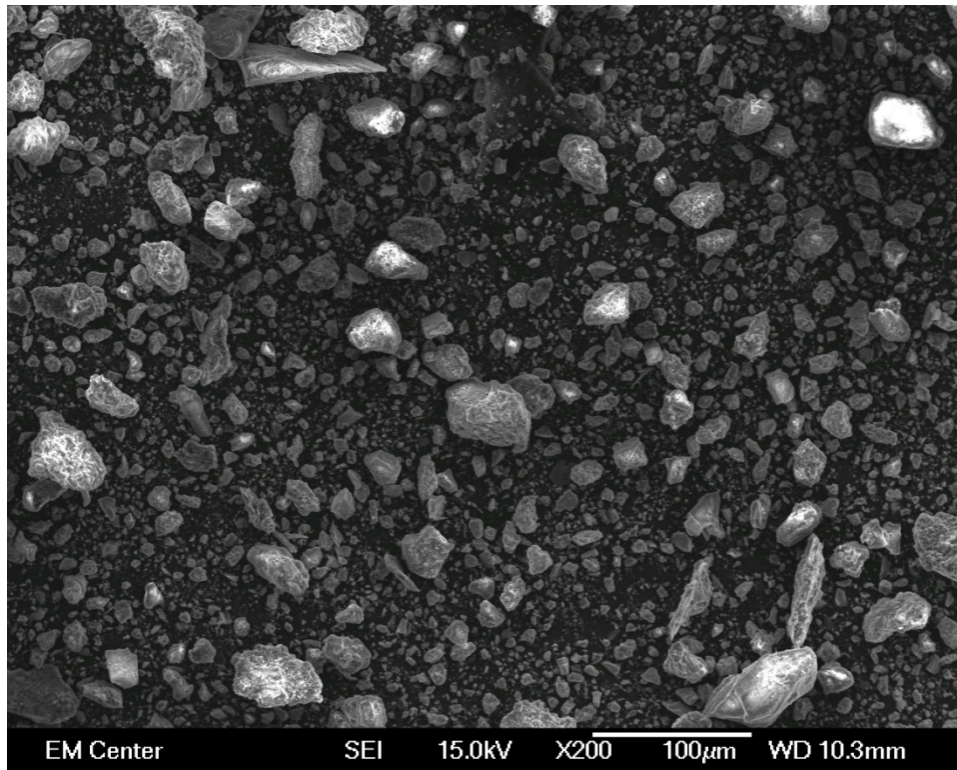


Figure E.5: Microphotograph of the unweathered fines at 200X magnification.

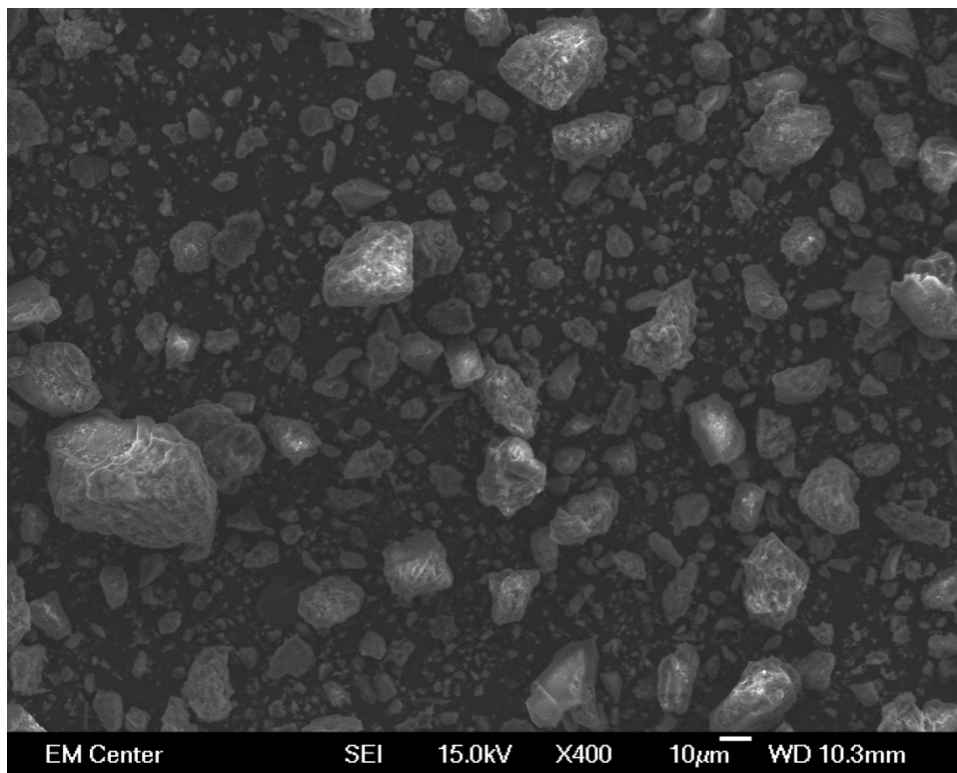


Figure E.6: Microphotograph of the unweathered fines at 400X magnification.

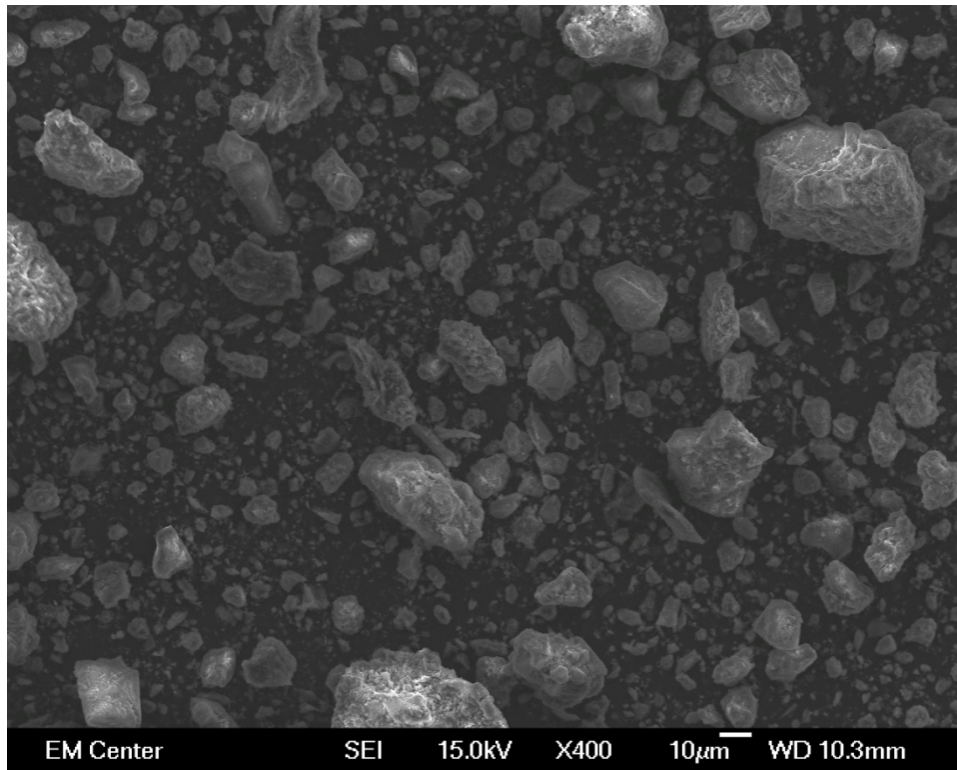


Figure E.7: Microphotograph of the unweathered fines at 400X magnification.

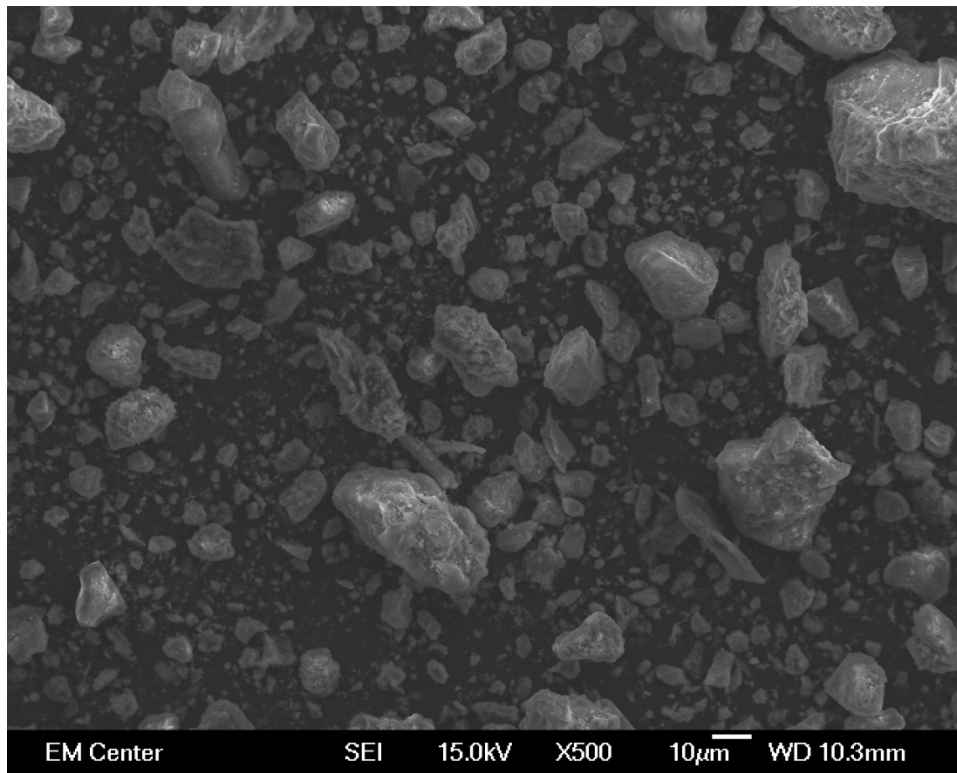


Figure E.8: Microphotograph of the unweathered fines at 500X magnification.

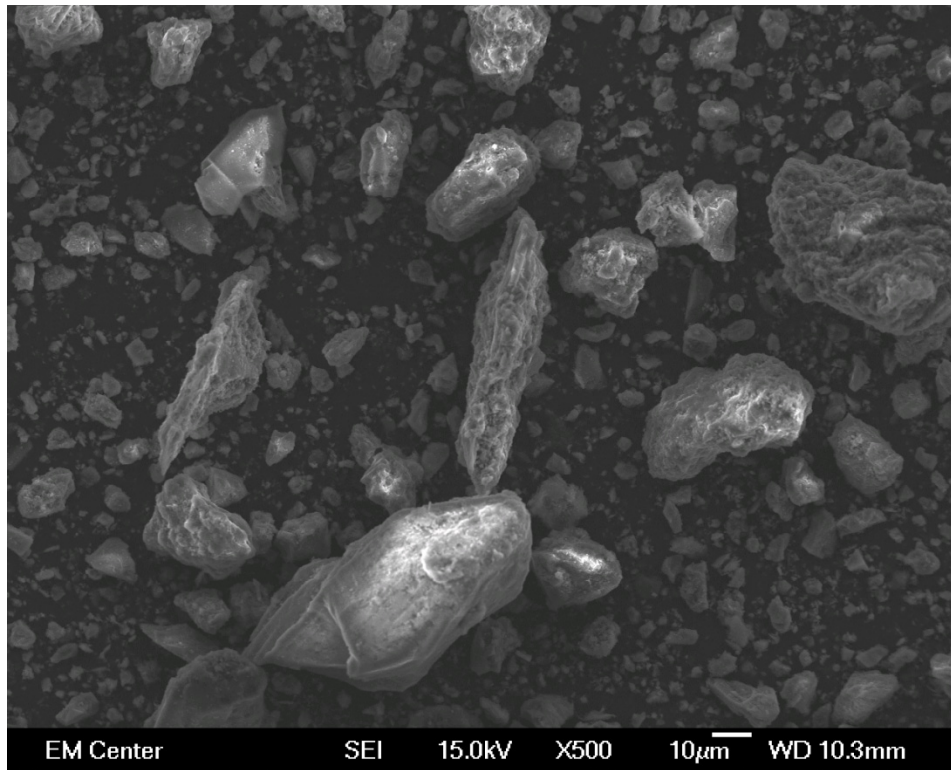


Figure E.9: Microphotograph of the unweathered fines at 500X magnification.

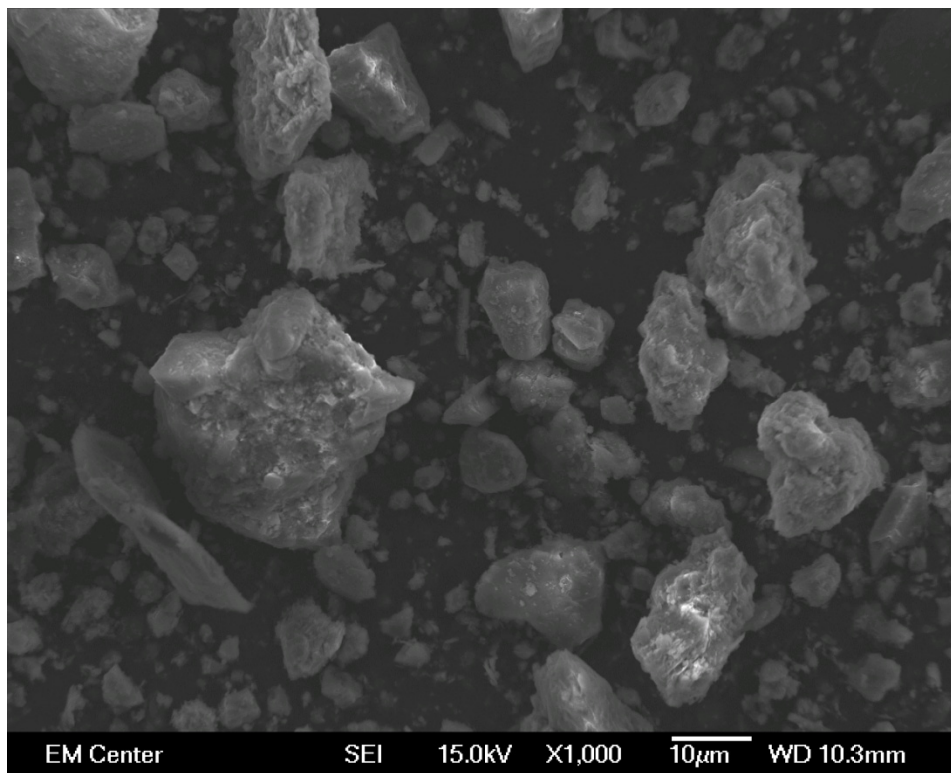


Figure E.10: Microphotograph of the unweathered fines at 1,000X magnification.

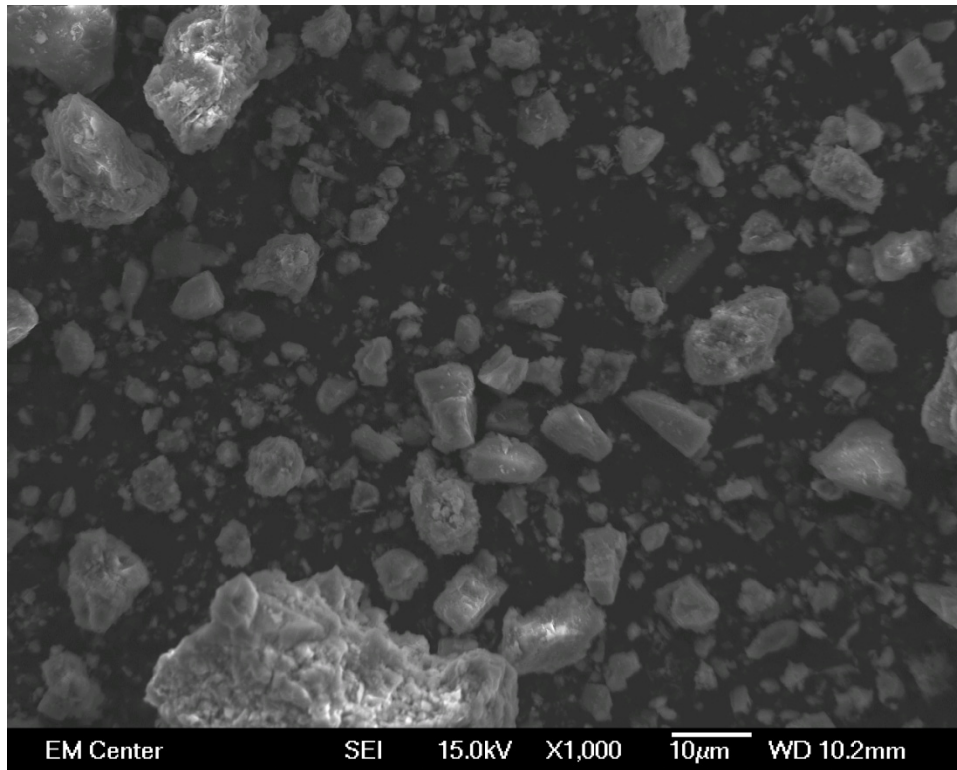


Figure E.11: Microphotograph of the unweathered fines at 1,000X magnification.

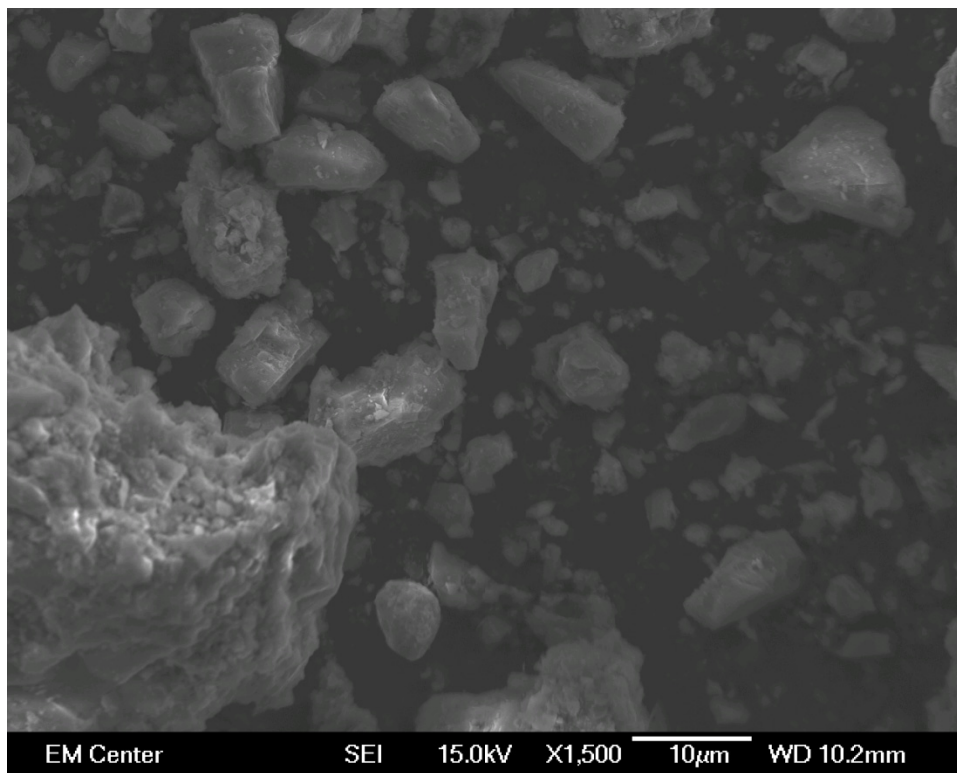


Figure E.12: Microphotograph of the unweathered fines at 1,500X magnification.

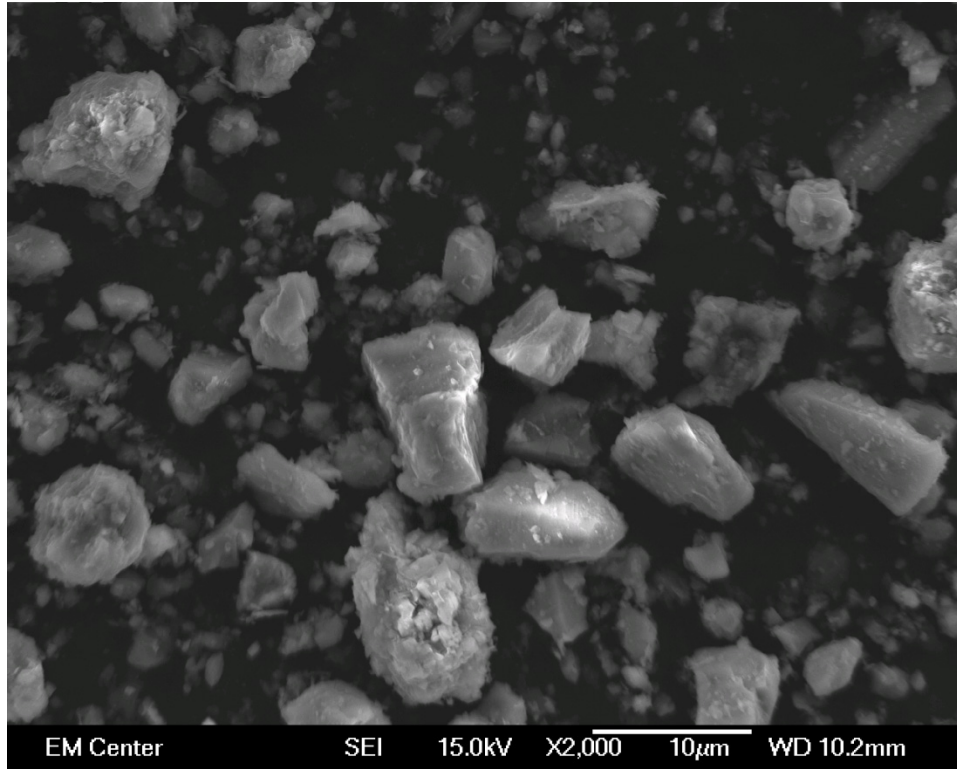


Figure E.13: Microphotograph of the unweathered fines at 2,000X magnification.

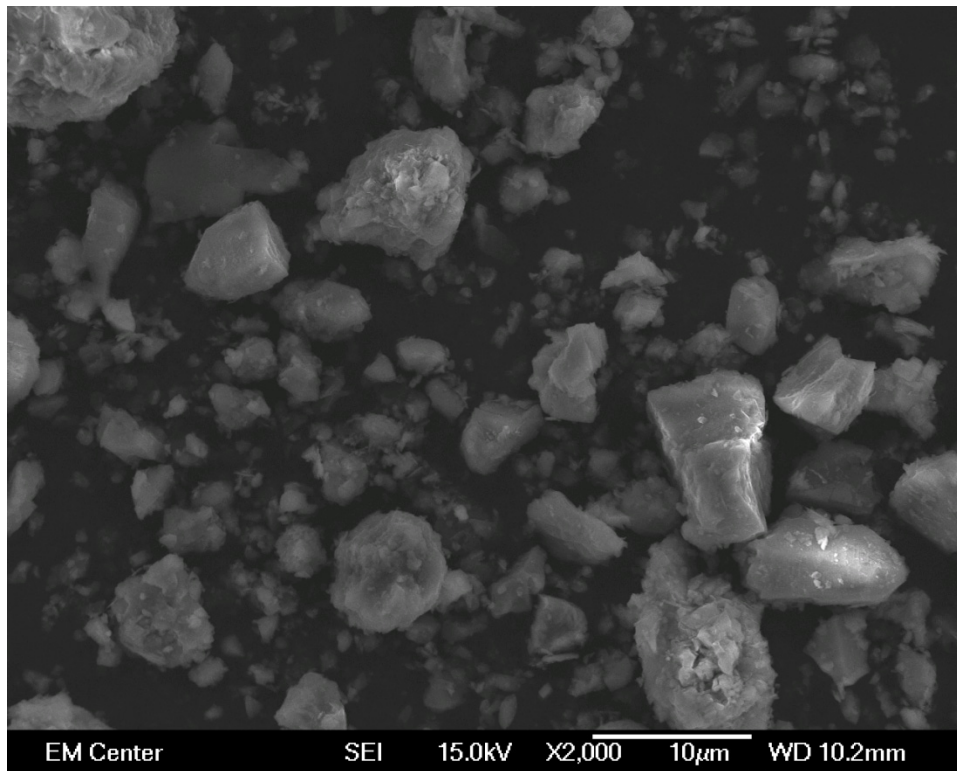


Figure E.14: Microphotograph of the unweathered fines at 2,000X magnification.

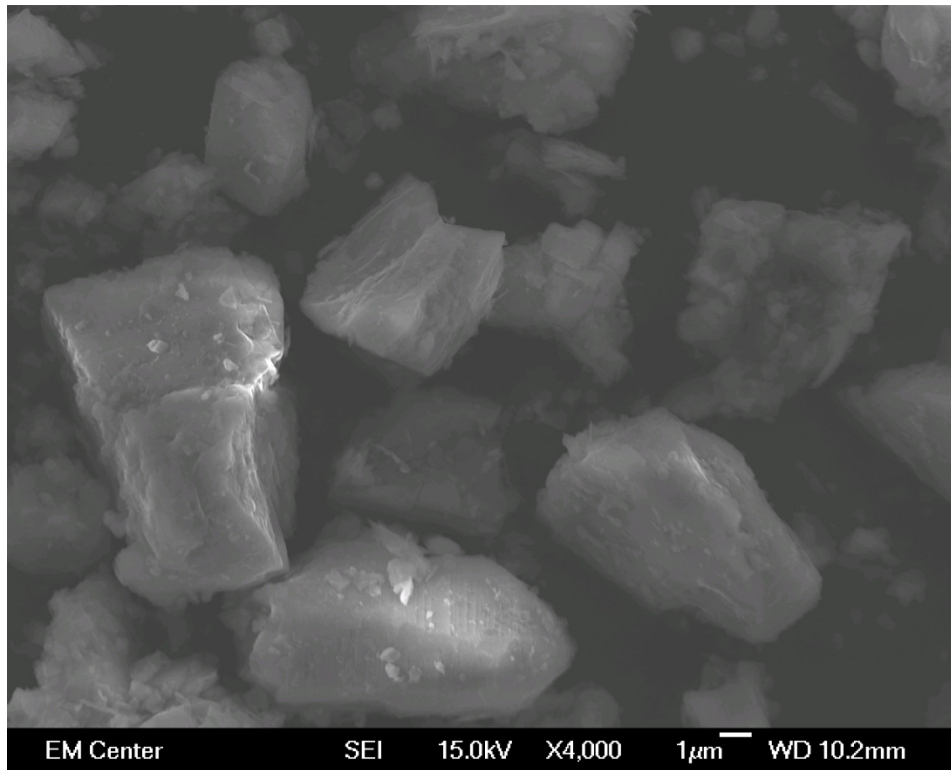


Figure E.15: Microphotograph of the unweathered fines at 4,000X magnification.

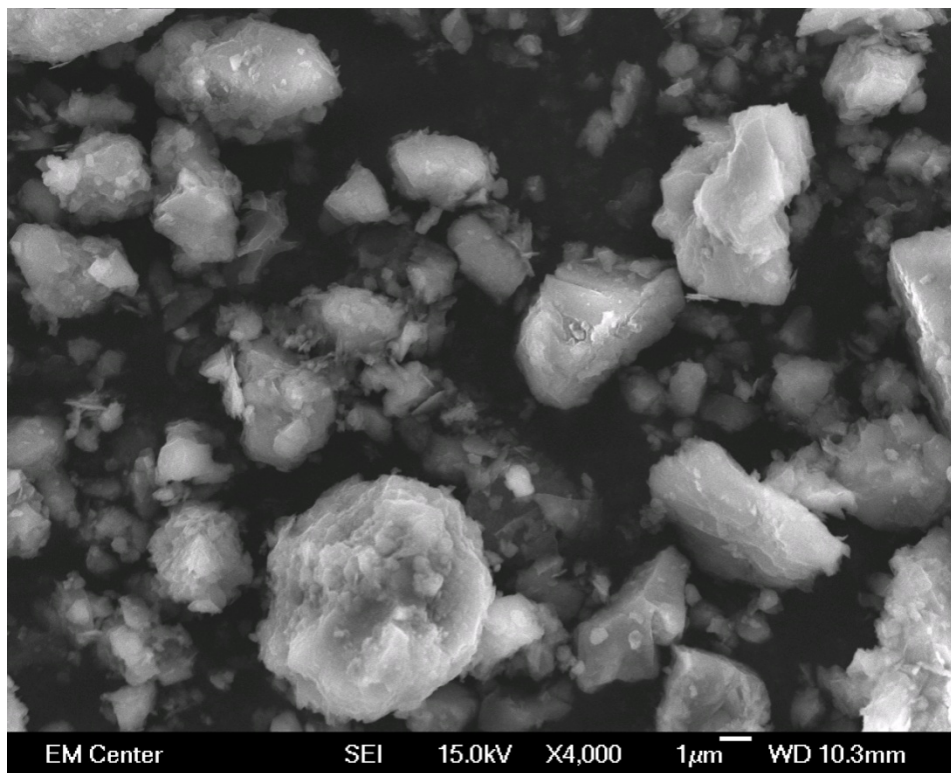


Figure E.16: Microphotograph of the unweathered fines at 4,000X magnification.

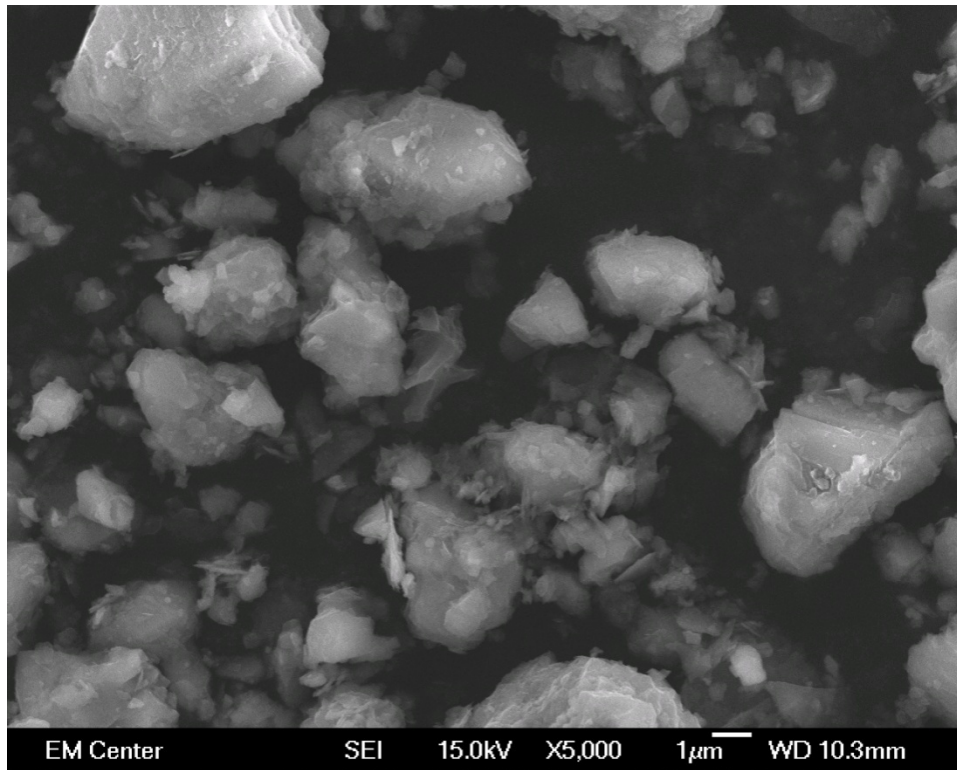


Figure E.17: Microphotograph of the unweathered fines at 5,000X magnification.

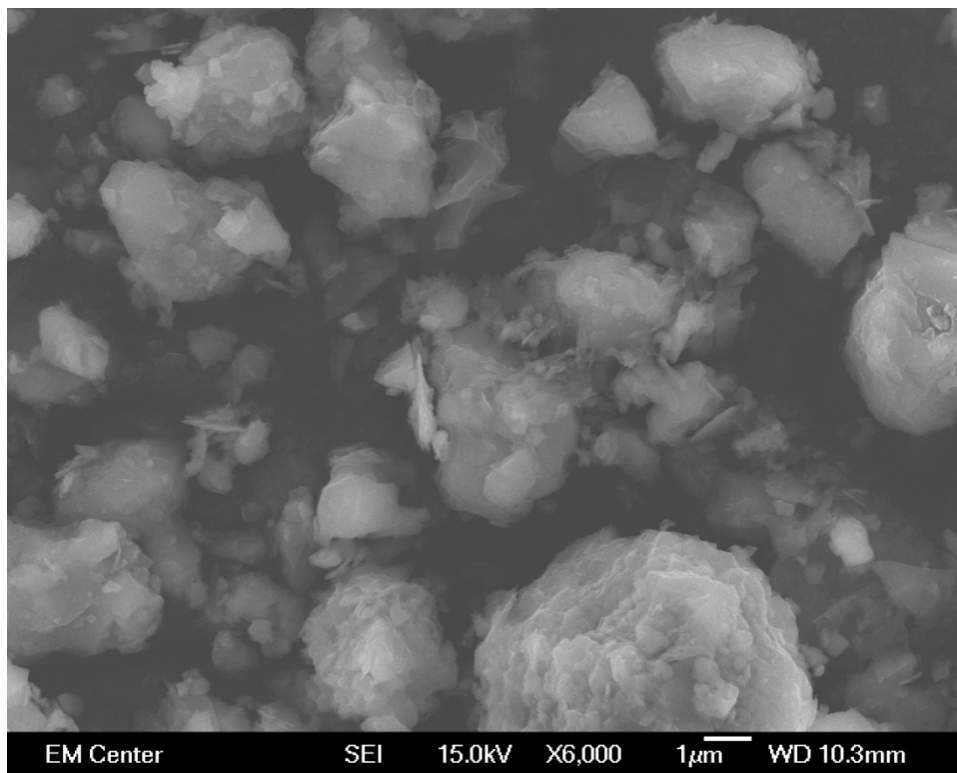


Figure E.18: Microphotograph of the unweathered fines at 6,000X magnification.

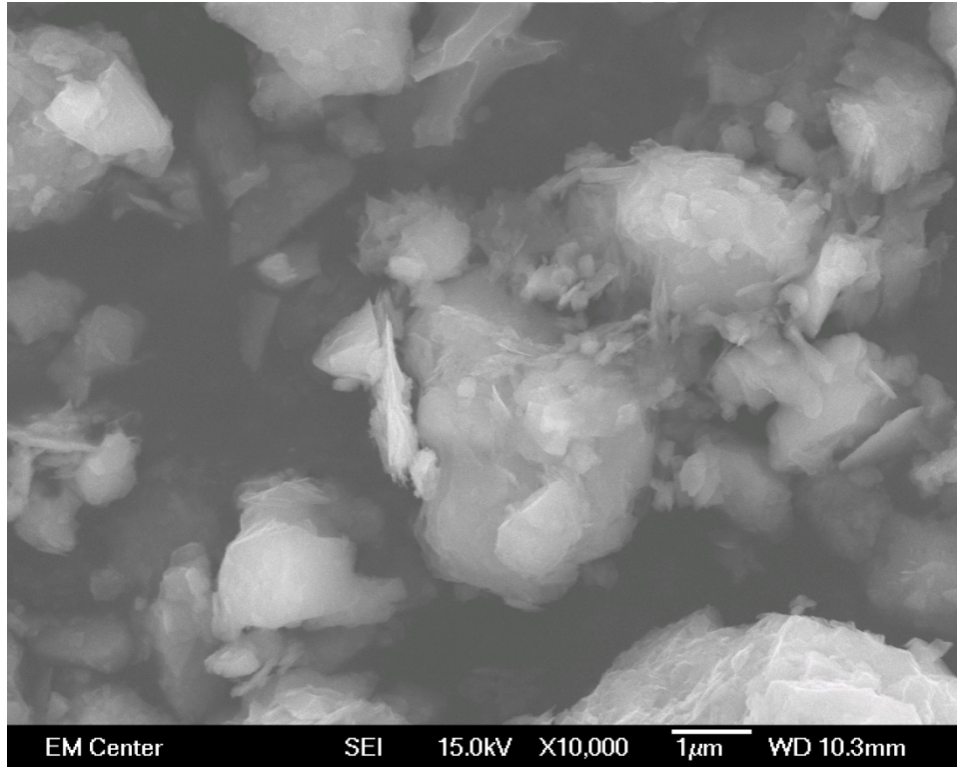


Figure E.19: Microphotograph of the weathered fines at 10,000X magnification.

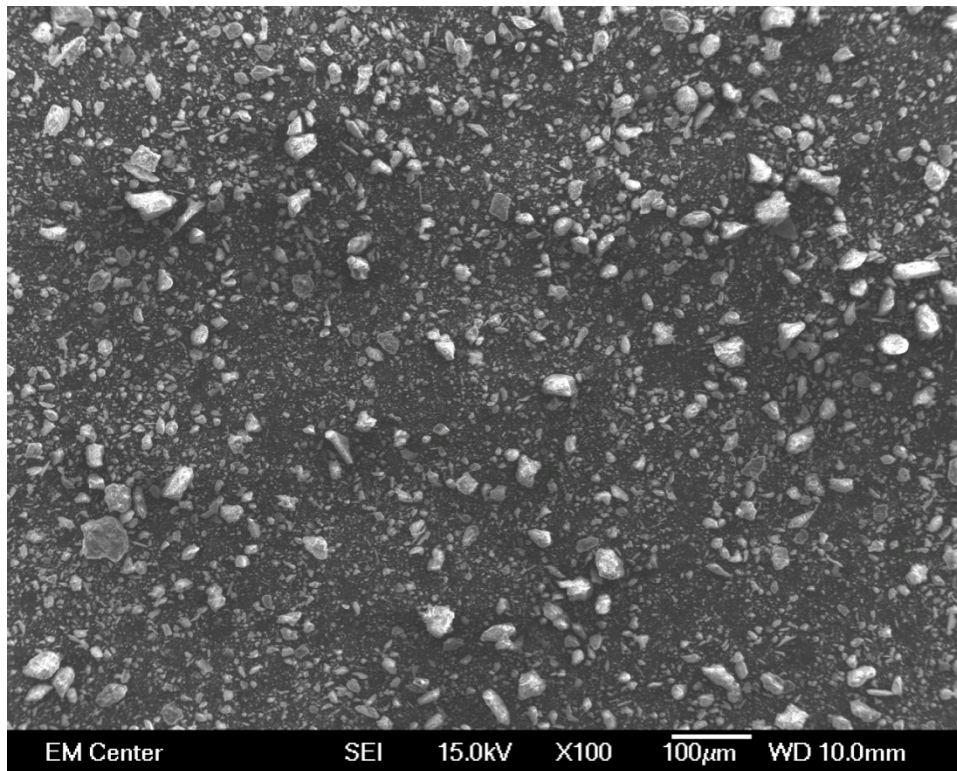


Figure E.20: Microphotograph of the weathered fines at 100X magnification.

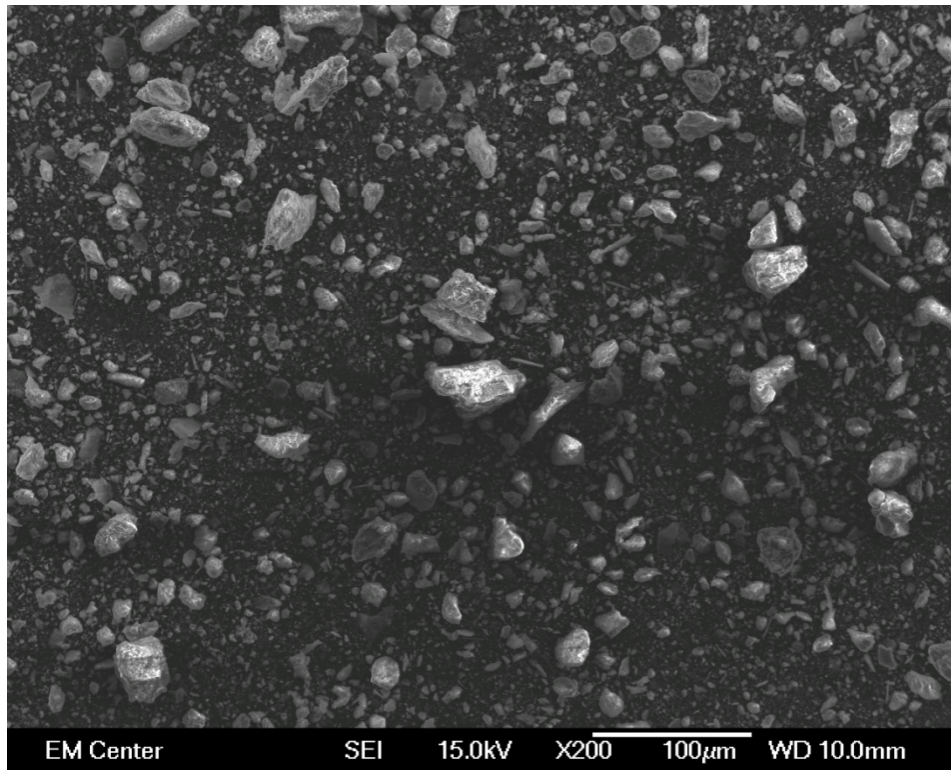
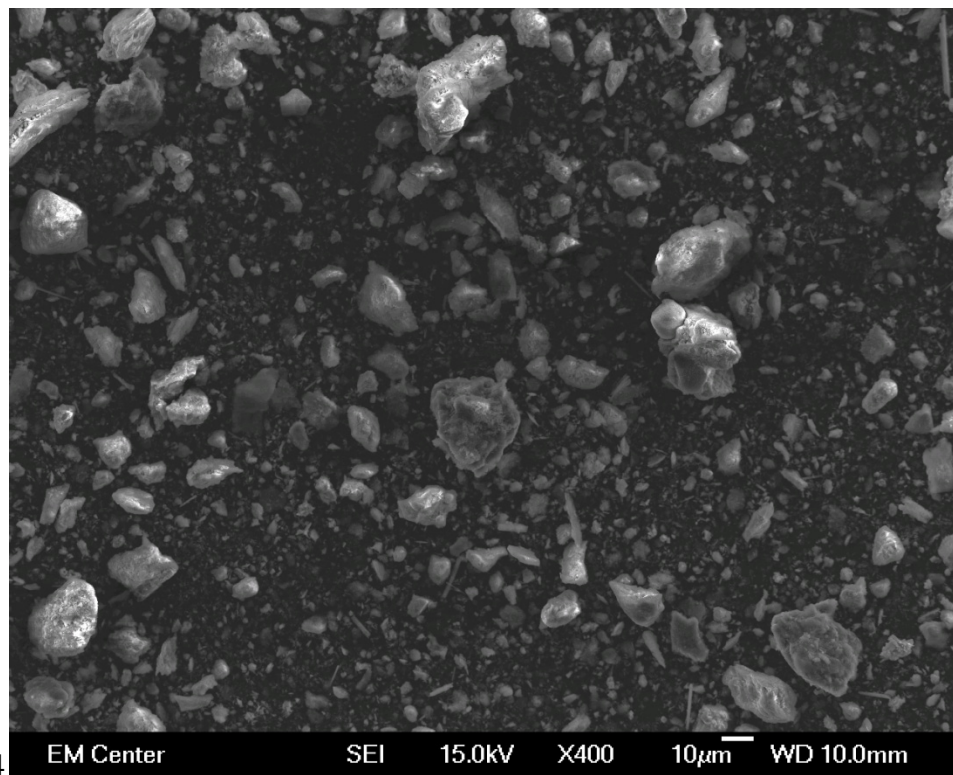


Figure E.21: Microphotograph of the weathered fines at 200X magnification.



4 Figure E.22: Microphotograph of the weathered fines at 400X magnification.

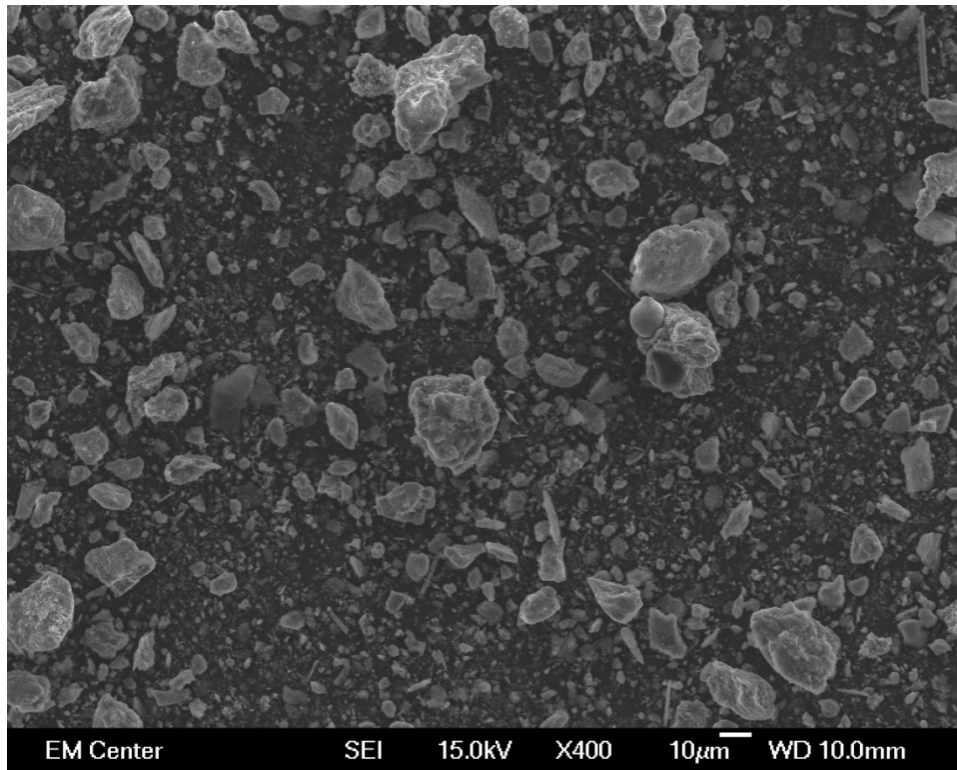


Figure E.23: Microphotograph of the weathered fines at 400X magnification.

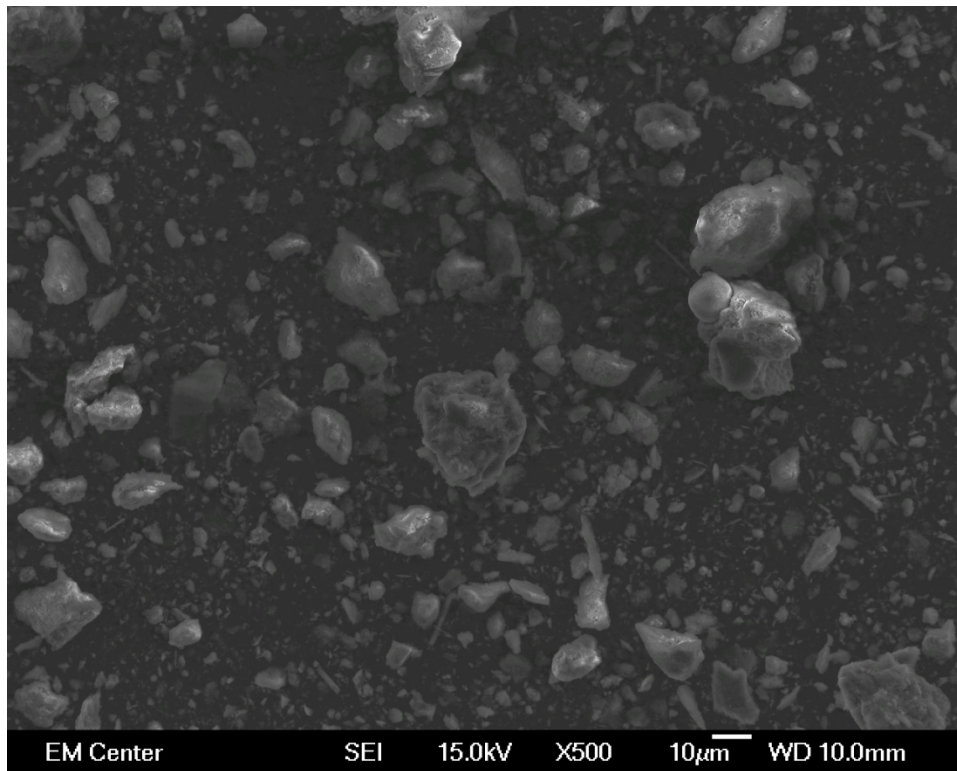


Figure E.24: Microphotograph of the weathered fines at 500X magnification.

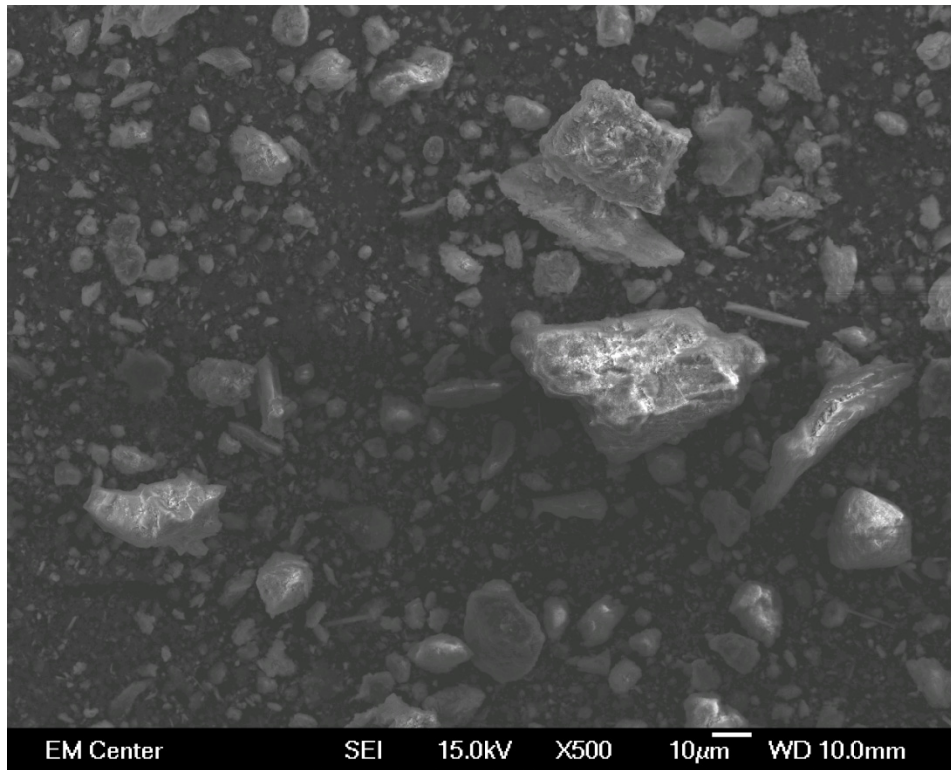


Figure E.25: Microphotograph of the weathered fines at 500X magnification.

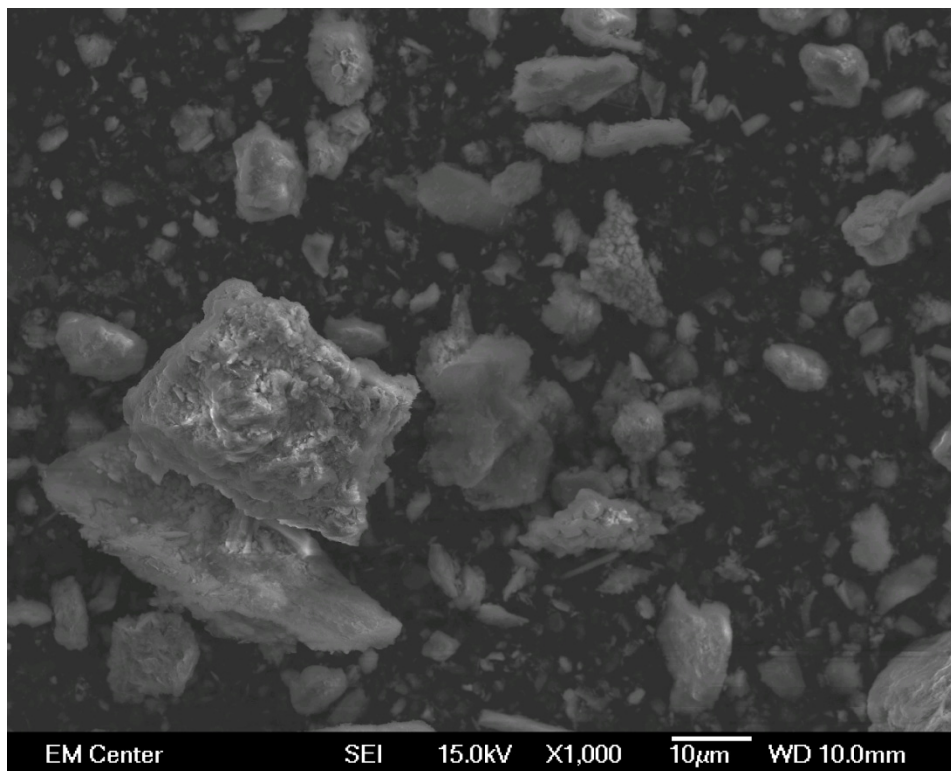


Figure E.26: Microphotograph of the weathered fines at 1,000X magnification.

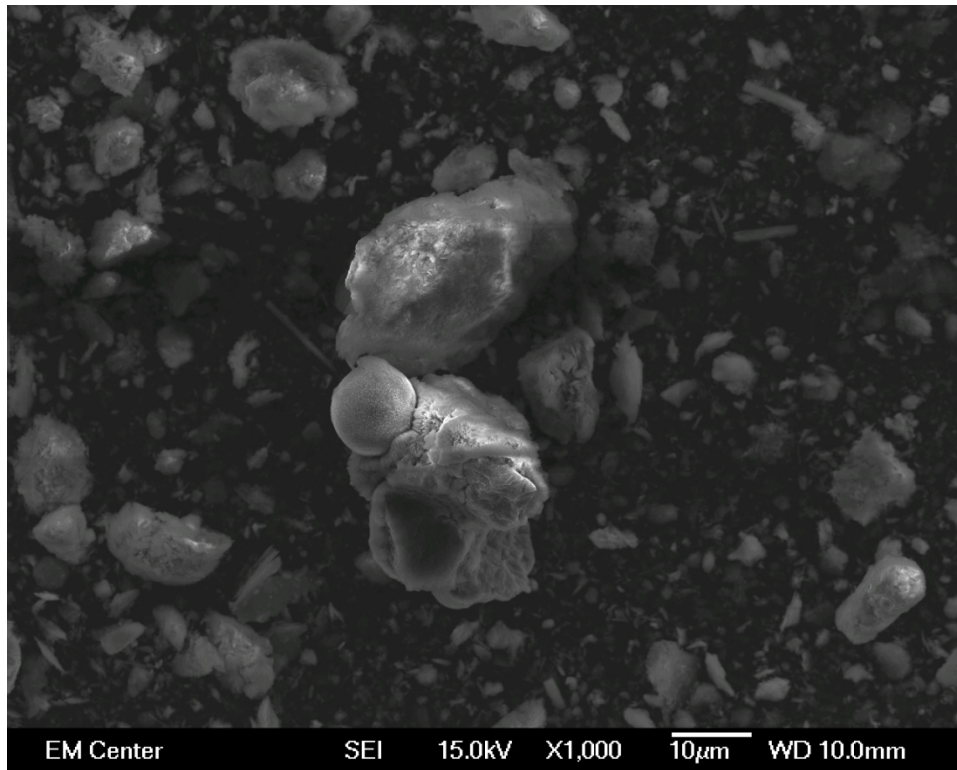


Figure E.27: Microphotograph of the weathered fines at 1,000X magnification.

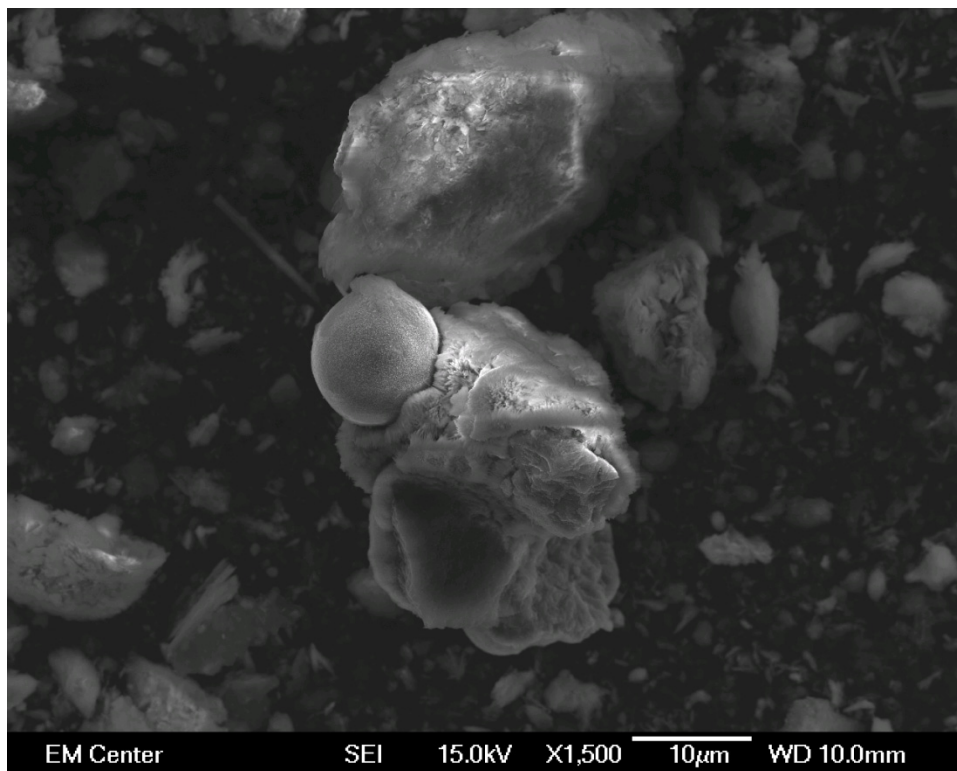


Figure E.28: Microphotograph of the weathered fines at 1,500X magnification.

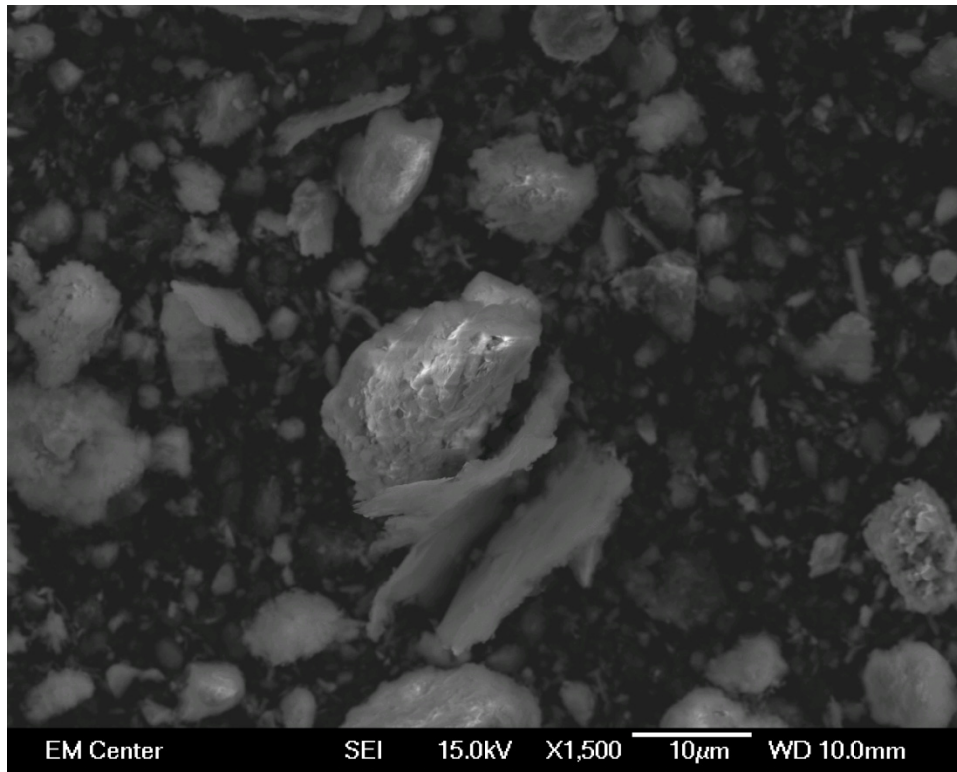
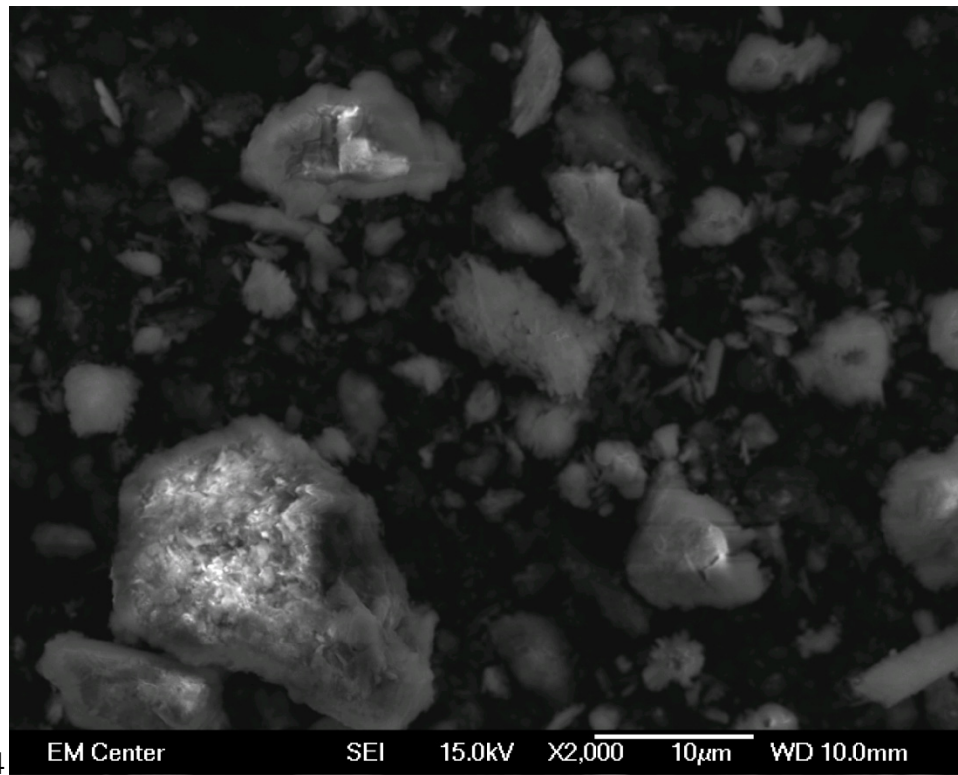


Figure E.29: Microphotograph of the weathered fines at 1,500X magnification.



4 Figure E.30: Microphotograph of the weathered fines at 2,000X magnification.



Figure E.31: Microphotograph of the weathered fines at 2,000X magnification.

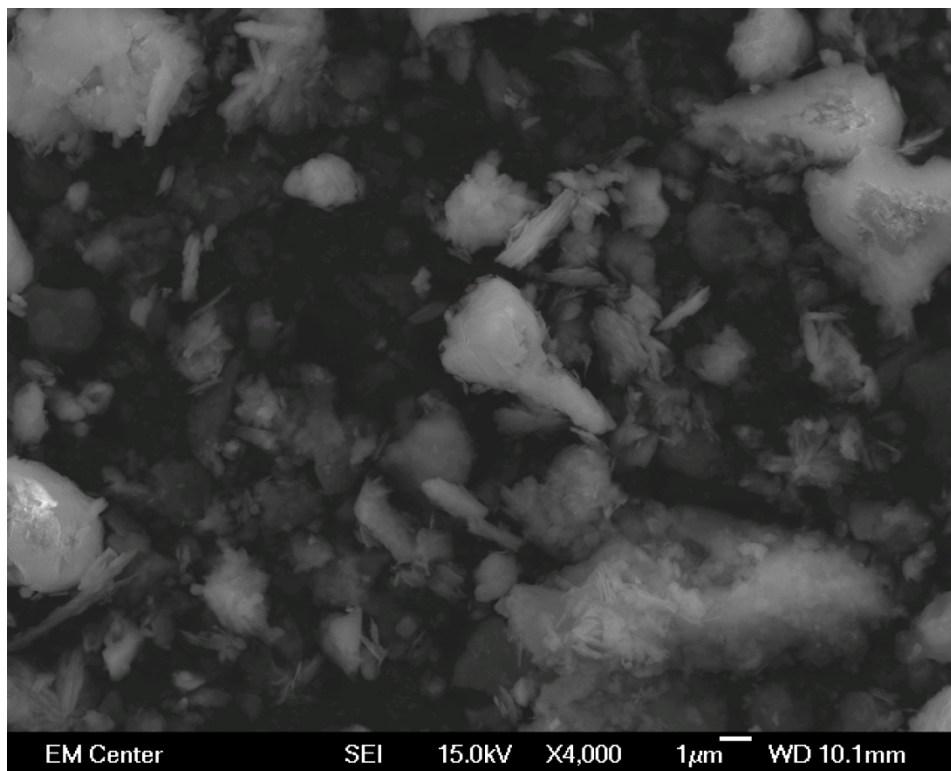


Figure E.32: Microphotograph of the weathered fines at 4,000X magnification.

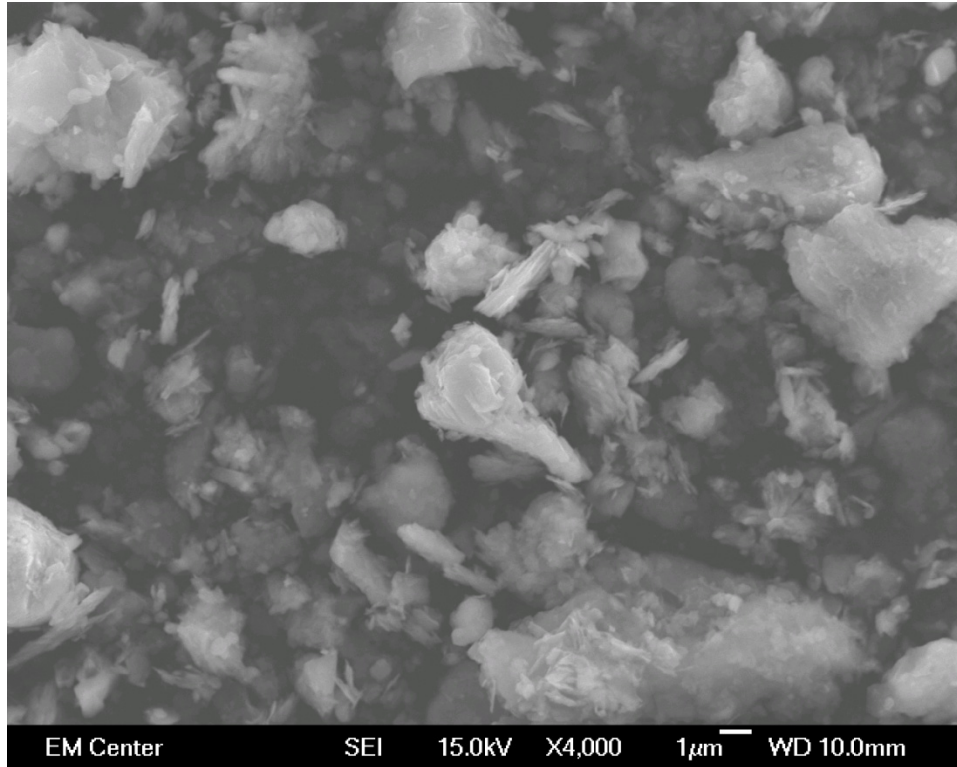


Figure E.33: Microphotograph of the weathered fines at 4,000X magnification.

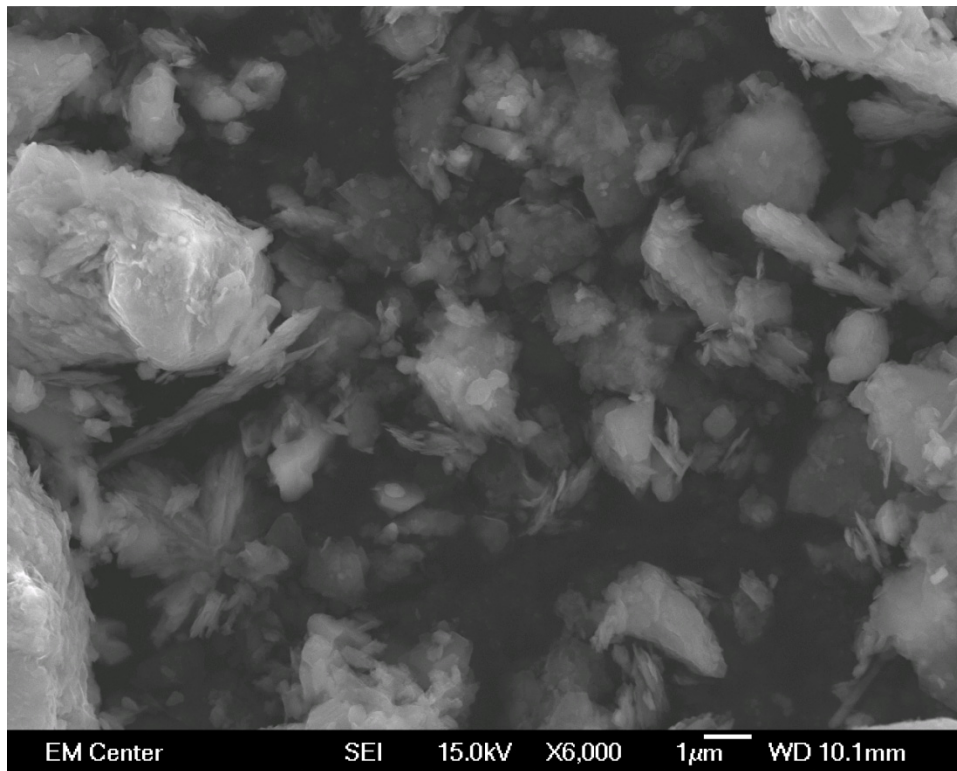


Figure E.34: Microphotograph of the weathered fines at 6,000X magnification.

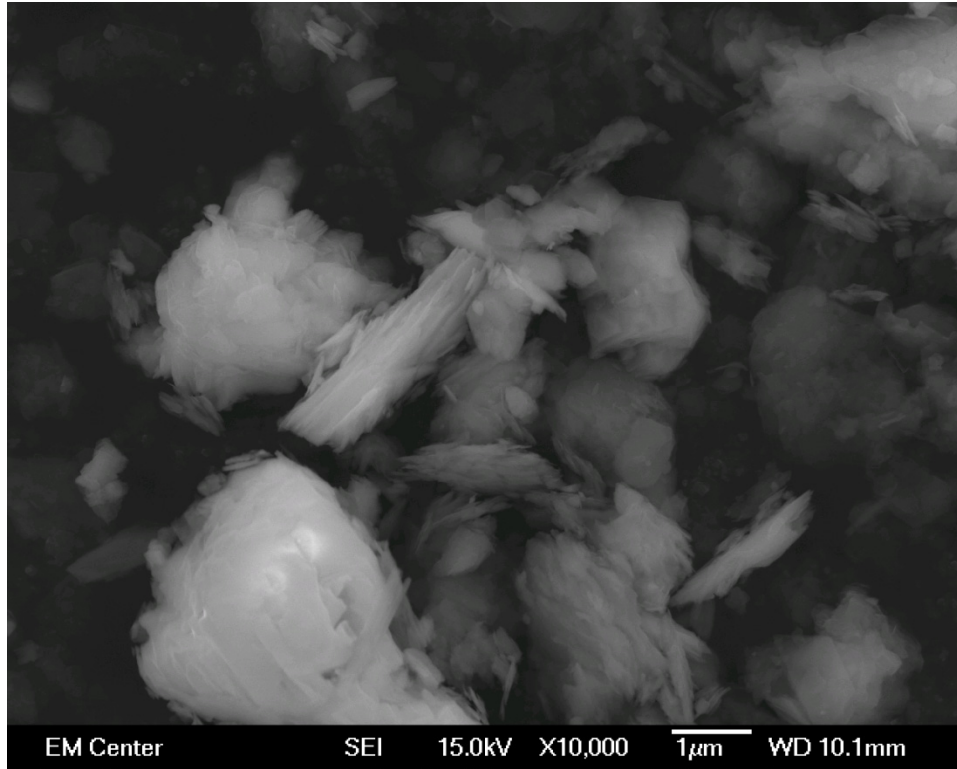


Figure E.35: Microphotograph of the weathered fines at 10,000X magnification.

## APPENDIX F: CALIBRATIONS AND CALIBRATION VERIFICATIONS

Ensuring accuracy and precision of instruments used in laboratory testing is pivotal to characterizing the reliability of laboratory test results. Although equipment limitations inhibited the actual calibration of transducers, a thorough transducer verification program was conducted at the beginning of this test program. Verification of the transducer calibrations was completed to in an effort to obtain the most reliable and accurate test results possible. The verification process consisted of comparing values measured using the transducers supplied by ELE International, Inc. against known values produced by calibrated equipment. Accuracy of the transducer is defined as the absolute value of the deviation between the transducer and the “standard” calibrated equipment divided by the range of measured values. The accuracy of the transducer was taken to be the maximum value of accuracy measured over three separate verification trials. Table 4.5 summarizes the results of the proceeding verification analyses for each transducer used in the course of this study.

Six pressure transducers were used in the present study to conduct conventional scale triaxial tests. The pressure transducers were verified using a Martel T140 – 100 PSI (Serial No. 9771033) with a capacity of 700 kPa and resolution of 0.01 kPa. Although the pressure transducers had a range of 1,700 kPa, the panel board only had a pressure rating to 1,034 kPa and an air supply capable of delivering 700 kPa. Therefore verification of the pressure transducer calibrations was determined over the tested 0 – 700 kPa range only. Three trials were conducted where the pressure was increased from 0 to

700 kPa in gradual increments. Tables F.1 through F.6 summarize the results of the verification test conducted for each pressure transducer.

Table F.1: Verification of calibration for pressure transducer PT14850.

Pore Pressure Transducer PT14850						
Standard (kPa)	Trial 1 (kPa)	Accuracy	Trial 2 (kPa)	Accuracy	Trial 3 (kPa)	Accuracy
0.0	0.0	0.00%	0.0	0.00%	0.0	0.00%
51.7	50.6	0.15%	50.9	0.12%	50.7	0.14%
100.2	99.1	0.16%	99.3	0.13%	99.2	0.15%
151.1	150.0	0.15%	150.3	0.12%	150.1	0.14%
205.6	204.9	0.10%	204.7	0.13%	204.8	0.12%
257.3	256.4	0.13%	256.1	0.17%	256.3	0.15%
303.2	302.5	0.10%	302.3	0.13%	302.4	0.12%
354.2	353.6	0.08%	353.4	0.12%	353.5	0.10%
404.0	403.5	0.07%	403.3	0.10%	403.4	0.09%
448.6	448.2	0.06%	448.4	0.03%	448.3	0.04%
504.9	504.3	0.08%	504.6	0.05%	504.4	0.07%
552.0	552.1	0.01%	552.3	0.04%	552.2	0.02%
606.3	606.1	0.03%	606.3	0.00%	606.2	0.01%
654.2	654.4	0.03%	654.7	0.06%	654.5	0.05%
699.4	700.1	0.10%	700.3	0.13%	700.2	0.11%
Maximum Accuracy						0.17%

Table F.2: Verification of calibration for pressure transducer PT14868.

Pore Pressure Transducer PT14868						
Standard (kPa)	Trial 1 (kPa)	Accuracy	Trial 2 (kPa)	Accuracy	Trial 3 (kPa)	Accuracy
0.0	0.0	0.00%	0.0	0.00%	0.0	0.00%
53.1	53.5	0.06%	53.7	0.09%	53.6	0.07%
108.2	108.4	0.03%	108.6	0.06%	108.5	0.04%
160.5	160.9	0.06%	161.1	0.09%	161.0	0.07%
207.2	207.5	0.04%	207.6	0.04%	207.6	0.05%
256.8	256.8	0.00%	256.9	0.01%	256.9	0.01%
300.8	300.8	0.00%	300.9	0.01%	300.9	0.02%
352.7	352.4	0.05%	352.5	0.04%	352.5	0.03%
412.0	411.8	0.03%	411.9	0.02%	411.9	0.01%
450.7	450.5	0.03%	450.7	0.00%	450.6	0.02%
510.6	509.2	0.19%	510.1	0.07%	510.0	0.08%
567.5	566.0	0.22%	566.9	0.10%	566.8	0.10%
609.6	607.4	0.31%	608.3	0.19%	608.2	0.19%
654.1	651.9	0.31%	652.8	0.19%	652.7	0.20%
711.9	709.4	0.35%	710.3	0.22%	710.2	0.24%
Maximum Accuracy						0.35%

Table F.3: Verification of calibration for pressure transducer PT14869.

Pore Pressure Transducer PT14869						
Standard (kPa)	Trial 1 (kPa)	Accuracy	Trial 2 (kPa)	Accuracy	Trial 3 (kPa)	Accuracy
0.0	0.0	0.00%	0.0	0.00%	0.0	0.00%
53.1	53.5	0.05%	53.7	0.09%	53.6	0.07%
108.2	108.4	0.03%	108.6	0.06%	108.5	0.04%
160.5	160.9	0.05%	161.1	0.09%	161.0	0.07%
207.2	207.4	0.02%	207.3	0.00%	207.3	0.01%
256.8	257.0	0.03%	256.9	0.02%	256.8	0.00%
300.8	300.4	0.05%	300.6	0.02%	300.5	0.04%
352.7	352.2	0.07%	352.4	0.04%	352.3	0.06%
412.0	411.0	0.14%	411.2	0.11%	411.1	0.13%
450.7	449.6	0.16%	448.9	0.26%	449.7	0.15%
510.6	508.8	0.25%	508.1	0.35%	508.9	0.24%
567.5	565.3	0.32%	564.6	0.42%	565.4	0.30%
609.6	608.8	0.11%	606.7	0.41%	606.6	0.42%
654.1	653.5	0.09%	651.1	0.43%	651.0	0.44%
711.9	708.9	0.42%	708.3	0.51%	708.2	0.53%
Maximum Accuracy						0.53%

Table F.4: Verification of calibration for pressure transducer PT14763.

Pore Pressure Transducer PT14763						
Standard (kPa)	Trial 1 (kPa)	Accuracy	Trial 2 (kPa)	Accuracy	Trial 3 (kPa)	Accuracy
0.0	0.0	0.00%	0.0	0.00%	0.0	0.00%
51.7	50.7	0.14%	51.0	0.11%	50.8	0.12%
100.2	99.0	0.17%	99.3	0.13%	99.2	0.15%
151.1	149.9	0.17%	150.1	0.14%	150.0	0.15%
205.6	204.8	0.11%	204.9	0.10%	205.0	0.09%
257.3	257.3	0.00%	257.5	0.03%	257.4	0.02%
303.2	302.6	0.08%	303.5	0.04%	303.4	0.03%
354.2	354.1	0.01%	355.0	0.11%	354.9	0.10%
404.0	404.0	0.00%	404.9	0.12%	404.8	0.11%
448.6	448.3	0.04%	449.2	0.08%	449.1	0.08%
504.9	505.1	0.02%	505.2	0.05%	505.1	0.03%
552.0	552.3	0.04%	552.4	0.06%	552.3	0.05%
606.3	606.1	0.03%	606.3	0.01%	606.1	0.02%
654.2	655.1	0.13%	655.2	0.14%	655.2	0.14%
699.4	701.0	0.23%	701.3	0.27%	701.4	0.28%
Maximum Accuracy						0.28%

Table F.5: Verification of calibration for pressure transducer PT14764.

Pore Pressure Transducer PT14764						
Standard (kPa)	Trial 1 (kPa)	Accuracy	Trial 2 (kPa)	Accuracy	Trial 3 (kPa)	Accuracy
0.0	0.0	0.00%	0.0	0.00%	0.0	0.00%
51.7	50.8	0.12%	51.1	0.09%	50.9	0.09%
100.2	100.0	0.03%	100.3	0.01%	100.1	0.01%
151.1	151.1	0.00%	151.3	0.03%	151.2	0.03%
205.6	206.5	0.12%	206.4	0.11%	206.4	0.12%
257.3	257.0	0.04%	256.9	0.05%	256.8	0.04%
303.2	302.9	0.04%	303.1	0.01%	303.0	0.01%
354.2	355.1	0.12%	355.0	0.11%	355.0	0.12%
404.0	405.1	0.16%	405.0	0.14%	404.9	0.16%
448.6	449.2	0.08%	449.4	0.11%	449.2	0.11%
504.9	505.5	0.09%	505.6	0.10%	505.7	0.11%
552.0	552.4	0.06%	552.4	0.06%	553.2	0.18%
606.3	606.6	0.04%	606.6	0.04%	607.4	0.15%
654.2	654.2	0.00%	655.1	0.12%	655.0	0.12%
699.4	699.2	0.03%	700.1	0.10%	700.0	0.10%
Maximum Accuracy						0.18%

Table F.6: Verification of calibration for pressure transducer PT14851.

Pore Pressure Transducer PT14851						
Standard (kPa)	Trial 1 (kPa)	Accuracy	Trial 2 (kPa)	Accuracy	Trial 3 (kPa)	Accuracy
0.0	0.0	0.00%	0.0	0.00%	0.0	0.00%
51.7	50.8	0.12%	51.0	0.10%	50.9	0.10%
100.2	100.3	0.01%	100.5	0.04%	100.4	0.04%
151.1	152.1	0.14%	152.2	0.16%	152.1	0.16%
205.6	205.8	0.03%	205.8	0.03%	205.9	0.04%
257.3	257.1	0.04%	257.1	0.03%	257.1	0.03%
303.2	303.1	0.02%	303.9	0.11%	303.9	0.11%
354.2	353.8	0.05%	354.7	0.07%	354.6	0.07%
404.0	403.1	0.13%	404.0	0.01%	403.9	0.01%
448.6	449.1	0.06%	449.2	0.09%	449.1	0.09%
504.9	505.1	0.03%	505.3	0.06%	505.2	0.06%
552.0	552.2	0.02%	552.4	0.05%	552.2	0.05%
606.3	606.5	0.02%	606.8	0.07%	606.9	0.08%
654.2	655.3	0.16%	654.4	0.03%	654.5	0.16%
699.4	699.8	0.06%	699.2	0.02%	700.0	0.09%
Maximum Accuracy						0.16%

Two volume change transducers were used during the course of this study. Each volume change transducer had a capacity of 90 ml. Verification of the volume change transducers was completed manually by measuring the change in volume entering the volume change transducer through a calibrated burette constructed by ELE International, Inc. Tables F.7 and F.8 summarize the results of the calibration verification for the volume change transducers used in this study.

Table F.7: Verification of calibration for volume change transducer VC27-1641.

Volume Change Transducer VC27-1641						
Standard (ml)	Trial 1 (ml)	Accuracy	Trial 2 (ml)	Accuracy	Trial 3 (ml)	Accuracy
0.00	0.00	0.00%	0.00	0.00%	0.00	0.00%
10.00	10.17	0.19%	10.15	0.17%	10.16	0.18%
20.00	20.10	0.11%	20.08	0.09%	20.06	0.07%
30.00	30.15	0.17%	30.16	0.18%	30.15	0.17%
40.00	40.02	0.02%	40.04	0.04%	40.03	0.03%
50.00	50.00	0.00%	50.00	0.00%	50.01	0.01%
60.00	59.97	0.03%	60.01	0.01%	60.05	0.06%
70.00	69.97	0.03%	70.05	0.06%	69.95	0.06%
80.00	80.00	0.00%	80.04	0.04%	80.02	0.02%
90.00	89.83	0.19%	89.85	0.17%	89.87	0.14%
Maximum Accuracy						0.19%

Table F.8: Verification of calibration for volume change transducer VC27-1642.

Volume Change Transducer VC27-1642						
Standard (ml)	Trial 1 (ml)	Accuracy	Trial 2 (ml)	Accuracy	Trial 3 (ml)	Accuracy
0.00	0.00	0.00%	0.00	0.00%	0.00	0.00%
10.00	10.11	0.12%	10.13	0.14%	10.12	0.13%
20.00	20.07	0.08%	20.04	0.04%	20.12	0.13%
30.00	30.16	0.18%	30.14	0.16%	30.08	0.09%
40.00	40.10	0.11%	40.00	0.00%	40.01	0.01%
50.00	50.05	0.06%	50.04	0.04%	49.95	0.06%
60.00	60.05	0.06%	60.02	0.02%	60.07	0.08%
70.00	70.01	0.01%	70.10	0.11%	70.01	0.01%
80.00	80.05	0.06%	80.06	0.07%	80.00	0.00%
90.00	90.03	0.03%	89.88	0.13%	90.09	0.10%
Maximum Accuracy						0.19%

A single load cell was used during the course of this study during drained monotonic axisymmetric compression of triaxial test specimens. Verification of the calibration for

the load cell consisted of comparison between measured values of the load cell and a calibrated 9,000 N capacity proving ring (Serial No. 2544) manufactured by ELE International, Inc. Although the capacity for both the load cell and the proving ring are in units of N, the most current calibration of the proving ring was set to read in pounds-force (lbf). Accordingly, the readout of the load cell was set to imperial units in order to facilitate calibration verification. Table F.9 summarizes the results of the calibration verification for the load cell used in this study.

Table F.9: Verification of calibration for load cell LC404303.

Load Cell LC404303						
Standard (lbf)	Trial 1 (lbf)	Accuracy	Trial 2 (lbf)	Accuracy	Trial 3 (lbf)	Accuracy
0	0	0.00%	0	0.00%	0	0.00%
66.38	67.73	0.07%	68	0.08%	67.73	0.07%
132.21	133	0.04%	133.56	0.07%	133	0.04%
198.51	199.5	0.05%	198.95	0.02%	199.5	0.05%
265.28	264.76	0.03%	266.48	0.06%	264.76	0.03%
525.86	527.07	0.06%	526.94	0.05%	527.07	0.06%
788.94	788.13	0.04%	788.12	0.04%	788.13	0.04%
1043.89	1045.51	0.08%	1044.94	0.05%	1045.51	0.08%
1298.61	1297.96	0.03%	1297.04	0.08%	1297.96	0.03%
1555.67	1556.42	0.04%	1556.42	0.04%	1556.42	0.04%
1805.92	1807.5	0.08%	1806.44	0.03%	1807.5	0.08%
Maximum Accuracy						0.08%

Similar to the load cell, only one axial displacement transducer was used in the course of this study. The displacement transducer had a range of 50 mm and a resolution of 0.01 mm. The calibration verification for the displacement transducer was achieved using a Mitutoyo Corporation micrometer (Serial No. 350-352) with a capacity of 25.4 mm. Because the capacity of the micrometer is approximately half of that of the displacement transducer, each verification trial was completed over a different absolute range of the

transducer in order to verify the entire capacity of the transducer. Table F.10 summarizes the results of the calibration verification for the axial displacement transducer.

Table F.9: Verification of calibration for displacement transducer AD27-1617.

Displacement Transducer AD27-1617						
Standard (mm)	Trial 1 (mm)	Accuracy	Trial 2 (mm)	Accuracy	Trial 3 (mm)	Accuracy
0	0	0.00%	0	0.00%	0	0.00%
0.1	0.1015	0.08%	0.1013	0.06%	0.1014	0.07%
0.2	0.2014	0.07%	0.2012	0.06%	0.2013	0.06%
0.3	0.3018	0.09%	0.3018	0.09%	0.3016	0.08%
0.4	0.4013	0.06%	0.4017	0.08%	0.4015	0.08%
0.5	0.501	0.05%	0.5009	0.05%	0.5008	0.04%
0.6	0.6005	0.03%	0.6	0.00%	0.6001	0.00%
0.7	0.7002	0.01%	0.7	0.00%	0.7	0.00%
0.8	0.8	0.00%	0.8003	0.01%	0.7998	0.01%
0.9	0.8996	0.02%	0.8994	0.03%	0.8991	0.05%
1	0.9987	0.06%	0.9983	0.09%	0.9985	0.07%
Maximum Accuracy						0.09%

In order to apply the area and membrane corrections discussed in Chapter 4, the elastic modulus was determined for the membranes used during triaxial testing according to the procedure outlined by Head (1986). Tables F.10 and F.11 summarize the results of four trials for each thickness of membrane used.

Table F.10: Determination of the Elastic Modulus for the 0.3-mm-thick membranes used during triaxial tests.

Thickness (mm)	0.3							
Width (mm)	15.3							
A (m <sup>2</sup> )	9.72E-06							
Trial 1								
Mass (g)	Length (mm)	$\Delta L$ (mm)	F (N)	L (m)	$\Delta L$ (m)	E (kPa)	$\epsilon_a$ (%)	Average E (kPa)
0	38.84	0	0.00	0.03884	0	--	--	824.58
20.15	39.72	0.88	0.20	0.03972	0.00088	898	2.3%	
100.15	43.78	4.94	0.98	0.04378	0.00494	795	12.7%	
180.15	47.89	9.05	1.77	0.04789	0.00905	781	23.3%	
Trial 2								
Mass (g)	Length (mm)	$\Delta L$ (mm)	F (N)	L (m)	$\Delta L$ (m)	E (kPa)	$\epsilon_a$ (%)	Average E (kPa)
0	38.69	0	0.00	0.03869	0	--	--	796.38
21.33	39.66	0.97	0.21	0.03966	0.00097	859	2.5%	
101.33	44.22	5.53	0.99	0.04422	0.00553	716	14.3%	
181.33	47.39	8.7	1.78	0.04739	0.0087	814	22.5%	
Trial 3								
Mass (g)	Length (mm)	$\Delta L$ (mm)	F (N)	L (m)	$\Delta L$ (m)	E (kPa)	$\epsilon_a$ (%)	Average E (kPa)
0	38.9	0	0.00	0.0389	0	--	--	836.35
20.56	39.8	0.9	0.20	0.0398	0.0009	897	2.3%	
100.56	44.02	5.12	0.99	0.04402	0.00512	771	13.2%	
180.56	47.34	8.44	1.77	0.04734	0.00844	840	21.7%	
Trial 4								
Mass (g)	Length (mm)	$\Delta L$ (mm)	F (N)	L (m)	$\Delta L$ (m)	E (kPa)	$\epsilon_a$ (%)	Average E (kPa)
0	38.9	0	0.00	0.0389	0	--	--	820.66
20.48	39.77	0.87	0.20	0.03977	0.00087	925	2.2%	
100.48	44.03	5.13	0.99	0.04403	0.00513	769	13.2%	
180.48	48.13	9.23	1.77	0.04813	0.00923	768	23.7%	
Average E (kPa) for Trials 1-4								819.49

Table F.11: Determination of the Elastic Modulus for the 0.6-mm-thick membranes used during triaxial tests.

Thickness (mm)	0.6							
Width (mm)	15.3							
A (m <sup>2</sup> )	1.94E-05							
Trial 1								
Mass (g)	Length (mm)	$\Delta L$ (mm)	F (N)	L (m)	$\Delta L$ (m)	E (kPa)	$\epsilon_a$ (%)	Average E (kPa)
0	39.56	0	0.00	0.03956	0	--	--	939.88
75.56	40.94	1.38	0.74	0.04094	0.00138	1097	3.5	
155.56	43.16	3.6	1.53	0.04316	0.0036	866	9.1	
235.56	45.07	5.51	2.31	0.04507	0.00551	857	13.9	
Trial 2								
Mass (g)	Length (mm)	$\Delta L$ (mm)	F (N)	L (m)	$\Delta L$ (m)	E (kPa)	$\epsilon_a$ (%)	Average E (kPa)
0	39.22	0	0.00	0.03922	0	--	--	915.74
78.61	40.73	1.51	0.77	0.04073	0.00151	1034	3.85	
158.61	42.76	3.54	1.56	0.04276	0.00354	890	9.03	
238.61	44.98	5.76	2.34	0.04498	0.00576	823	14.69	
Trial 3								
Mass (g)	Length (mm)	$\Delta L$ (mm)	F (N)	L (m)	$\Delta L$ (m)	E (kPa)	$\epsilon_a$ (%)	Average E (kPa)
0	39.38	0	0.00	0.03938	0	--	--	901.78
77.15	40.9	1.52	0.76	0.0409	0.00152	1012	3.86	
157.15	43.28	3.9	1.54	0.04328	0.0039	804	9.90	
237.15	44.7	5.32	2.33	0.0447	0.00532	889	13.51	
Trial 4								
Mass (g)	Length (mm)	$\Delta L$ (mm)	F (N)	L (m)	$\Delta L$ (m)	E (kPa)	$\epsilon_a$ (%)	Average E (kPa)
0	39.46	0	0.00	0.03946	0	--	--	914.92
77.15	40.89	1.51	0.76	0.04089	0.00151	1019	3.83	
157.15	43.12	3.74	1.54	0.04312	0.00374	838	9.50	
237.15	44.71	5.33	2.33	0.04471	0.00533	887	13.53	
Average E (kPa) for Trials 1-4							918.08	